Durcissement des superalliages monocristallins : des mécanismes physiques à la modélisation continue

Aurélien Vattre

MINES
ParisTech

ED n°432 : Sciences des Métiers de l'Ingénieur

THESE

pour obtenir le grade de
Docteur de l'Ecole Nationale Supérieure des Mines de Paris
Spécialité Sciences et Génie des Matériaux

présentée et soutenue publiquement par

Aurélien VATTRE

le 17 décembre 2009

**Durcissement des superalliages monocristallins:
des mécanismes physiques à la modélisation continue
-
Strength of single crystal superalloys:
from dislocation mechanisms to continuum micromechanics**

Jury

M.	S. FOREST	Président	Mines Paris - ParisTech
M.	J. De HOSSON	Rapporteur	Rijksuniversiteit Groningen
M.	G. EGGELER	Rapporteur	Ruhr-Universität Bochum
M.	C. FRESSENGEAS	Rapporteur	Université Paul Verlaine
M.	B. FEDELICH	Examinateur	BAM
M.	L. DUPUIS	Examinateur	CEA
M.	A. ROOS	Encadrant de thèse	ONERA
M.	B. DEVINCRE	Directeur de thèse	CNRS/ONERA

ONERA The French Aerospace Lab
29, avenue de la Division Leclerc, 92322 Châtillon Cedex

_____

Résumé

Ce présent travail s'inscrit dans le cadre de la modélisation multi-échelles de la plasticité cristalline des superalliages monocristallins à base nickel. Dans ce contexte, une transition d'informations recueillies à l'échelle mésoscopique justifiant physiquement un modèle micromécanique est mise en évidence.

Un couplage entre une simulation par dynamique des dislocations et la méthode des éléments finis, le Modèle Discret-Continu (MDC) est utilisé afin de reproduire les interactions entre dislocations et précipités. Une première application a pour objet de décrire des effets d'échelle induits par une variation de la largeur du couloir de matrice sur les propriétés mécaniques. La relation entre les microstructures simulées de dislocations, la contrainte d'écoulement et la déformation plastique est appréhendée. Une seconde étude traite l'influence de l'orientation du chargement sur le comportement mécanique du superalliage. Les interactions entre les systèmes primaires et déviés sont discutées et leur rôle majeur dans la localisation de la déformation plastique dans les couloirs de matrice est démontré. Par ailleurs, l'écrantage des interactions élastiques à longues portées associées aux réseaux de dislocations d'interface explique l'origine du faible taux d'écrouissage observé pour des essais orientés $\langle 111 \rangle$ à hautes températures.

Fortes des interprétations faites à l'échelle des dislocations, deux modélisations de nature très différentes sont développées. Une première évoque dans sa formulation une loi de durcissement dictée par une densité de dislocations géométriquement nécessaires. La formation et l'évolution des microstructures de dislocations sont étudiées : la comparaison avec les résultats obtenus avec le MDC montre les faiblesses de cette approche continue. On justifie ainsi le développement d'un second modèle micromécanique par homogénéisation, pour lequel la réponse globale du matériau est déterminée en considérant les rôles de la microstructure et des interactions mécaniques entre constituants. Dans ce modèle, les mécanismes locaux sont décrits de manière physique et les lois d'écrouissage sont écrites en termes de densités de dislocations mobiles. Il a été identifié à 850 et 950°C, et validé avec succès sur le superalliage CMSX-4 monocristallin.

Abstract

The present work deals with crystal plasticity of single crystal nickel-base superalloys. In this context, a scale transition of transferring information from mesoscale towards a physically justified micromechanical model is shown.

A numerical coupling between dislocation dynamic simulations and the finite element method, the so-called Discrete-Continuous Model (DCM) is used in order to take into account the mutual interactions between dislocations and precipitates. In a first application, the dependence of the mechanical properties on the channel width is investigated. The relationship between simulated microstructures of dislocation, flow stress and plastic strain is then analysed. A second set of calculations addresses the anisotropic mechanical response of single crystal superalloys. Analyses of dislocation interactions show the crucial role of one active slip system and its collinear system in the strain localisation in the form of slip bands. Furthermore, screening of long-range elastic interactions associated to the interfacial dislocation network explain the origin of the low hardening rate observed in $\langle 111 \rangle$-oriented specimens at high temperatures.

From these interpretations at the dislocation scale, two different modeling approaches are developed. On the one hand, one model uses the geometrically necessary dislocations in a hardening law. Both the formation and the evolution of the dislocation microstructures are analysed: comparison with results obtained by the DCM shows some short comings of this continuous approach. Then, a second micromechanical model based on a homogenisation procedure is justified. Its global response is determined by the microstructure and the mechanical interactions between its subdomains. In this micromechanical model, the local mechanisms are physically described and the constitutive laws are written in terms of mobile dislocation densities. It has been identified at 850 and 950°C, and successfully validated on the single crystal superalloy CMSX-4.

Remerciements

Je n'aurais jamais cru rencontrer autant de difficultés à ce stade du manuscrit pour écrire les remerciements: son écriture est un exercice périlleux étant donné qu'il s'agit d'oublier personne... Il est alors nécessaire de soigner la qualité de cette page, et je commencerai donc par remercier tous ceux que j'aurais malencontreusement omis dans la suite du discours.

Durant ces 3 années, une grande liberté m'a été offerte pour explorer des domaines passionnants de la Métallurgie Physique et de la Mécanique, dont le recouvrement m'a pleinement fasciné. Du coup, le présent travail est le fruit d'une aventure commune entre le Département Matériaux et Structures Métalliques (ONERA), le Laboratoire d'Etudes des Microstructures (CNRS/ONERA) et le Bundesanstalt für Materialforschung und -prüfung (BAM-Berlin). J'ai donc pu profiter des riches expériences de ces trois laboratoires, sans quoi cette thèse n'aurait été une réussite. Je mesure aujourd'hui la chance que j'ai eue de pouvoir travailler sous cette association de couleurs. Je reviendrai dessus...

En premier lieu, je tiens à remercier particulièrement les membres de mon jury qui ont accepté de lire et corriger les 200 pages de ce mémoire. Cela m'a permis de prendre un peu de recul sur les travaux qui m'ont animé pendant trois années de ma vie. Je remercie donc Samuel Forest pour avoir accepté de présider mon jury de soutenance, et d'avoir été très tôt un prépondérant interlocuteur enthousiaste pour discuter de mes travaux.
I thank Professors Jeff De Hosson and Gunther Eggeler for accepting to report my doctoral thesis. Their attendances in the jury were a great honor for me.
Je remercie fortement Claude Fressengeas d'avoir accepté de rapporter sur ce travail, et d'avoir pris le temps de discuter de tout, forcément de sciences, mais également d'autres sujets.
Je remercie Laurent Dupuy d'avoir accepté d'examiner mon travail.

Cette thèse a donc été l'objet d'une collaboration étroite avec le BAM, et plus précisément avec Bernard Fedelich. Je me souviens du premier e-mail envoyé à Bernard le 11 décembre 2006. Je n'espérais pas vivre une si riche expérience: elle m'a fait bénéficier de sa culture mécanicienne dans un environnement d'une dimension humaine incommensurable. Je le remercie donc de son ouverture, des conseils prodigués, de sa rigueur, de tous ces moments passés ensemble à travailler. Vielen Dank.

Il est maintenant temps de me consacrer à mes deux encadrants proches, Arjen Roos et Benoit Devincre. Merci de m'avoir entraîné dans cette aventure intellectuelle. Je remercie Arjen de son enthousiasme et de sa rigueur rédactionnelle. Merci également à Benoit de m'avoir fait confiance dans ce parcours et m'avoir transmis des bribes de tes connaissances. J'ai adoré l'ensemble des discussions scientifiques ou non, animées ou pas, que nous avons pu partager et je soulignerai vos réelles disponibilités. Votre complémentarité était idéale !

Je remercie également l'ensemble du personnel de l'union des 3 laboratoires présentés qui m'a donné la possibilité d'accomplir la tâche qui m'incombait: Frédéric Feyel et Vincent Chiaruttini qui m'ont non seulement souvent adressé des conseils avisés concernant ZéBuLoN, mais également débuggé pas mal de situations. J'adresse également mes remerciements à Frank Gallerneau, Pierre Caron et Jean-Louis Chaboche avec lesquels j'ai toujours apprécié nos discussions autour des thématiques qui éveillaient ma

Contents

Frequently used symbols

μ	Shear modulus
ν	Poisson's ratio
$\boldsymbol{\alpha}$	Nye's dislocation tensor
α	Constant in Taylor relation (2.52) or Orowan relation (3.79)
$\boldsymbol{\beta},\ \boldsymbol{\beta}^{e/p}$	Total, elastic and plastic distortions
$\boldsymbol{\varepsilon},\ \boldsymbol{\varepsilon}^{e/p}$	Total, elastic and plastic strains
$\dot{\gamma}^g$	Plastic strain rate on glide system g
γ^{APB}	AntiPhase Boundary (APB) energy
$\mathcal{N}$	Number of mobile segments
Γ	Line tension
τ^g	Resolved shear stress on glide system g
$\tau_{eff},\ \tau_{\mathrm{APB}},\ \tau_{KW}$	Effective, APB, and Kear-Wilsdorf stresses
$\tau_{gK}^{\mathrm{Orowan}}$	Orowan critical shear stress on glide system g in the channel K
ρ^g	Total dislocation density on glide system g
ρ_m	Mobile dislocation density on glide system g
ρ_{GND}^g	Geometrically necessary dislocation density on glide system g
ρ_{SSD}^g	Statistically stored dislocation density on glide system g
∇	Gradient operator
$\boldsymbol{\Omega}_{IJ}$	Influence tensors
A	Swept area
a^{gr}	Forest strength interaction matrix
B	Drag coefficient
$\mathbf{m}^g$	Slip direction of glide system g
$\mathbf{n}^g$	Normal slip plane of glide system g
$\mathbf{b}$	Burgers vector
v	Average dislocation velocity
APB	AntiPhase Boundary
(C)RSS	(Critical) Resolved Shear Stress
DCM	Discrete-Continuous Model
DD	Dislocation Dynamics
FE	Finite Elements
IP	Integration Point

Introduction

Les turboréacteurs sont des systèmes de propulsion essentiellement utilisés dans l'aviation. Il s'agit des plus anciens systèmes de moteurs à réaction. L'inventeur français Maxime Guillaume dépose en mai 1921 un brevet concernant son principe "Propulsion par réaction sur l'air". Il sera ensuite développé indépendamment par deux ingénieurs dans les années 1930: par Sir Frank Whittle en Grande-Bretagne et Haus von Ohain en Allemagne. Ce dernier fait voler le premier turboréacteur, le HeS3, sur le Heinkel He 178 en Août 1939 (figure 1 a).

(a)
(b)

Figure 1 - (a) Premier vol d'un avion à turboréacteur en Août 1939, le Heinkel He 178. (b) Cinquante ans plus tard, le Dassault Rafale, dont le premier vol a été effectué en Juillet 1986, est équipé du turboréacteur M88-2 construit par la Snecma.

Au début du XXI$^\text{e}$ siècle le rapport coût/efficacité du réacteur le rend particulièrement attractif pour les avions de transport du haut subsonique (0,7 < Mach < 1). C'est pour celà qu'il est utilisé sur les avions civils des familles Airbus A3xx, ou Boeing B7xx. Par ailleurs, parce qu'il est le seul capable de couvrir les domaines allant du subsonique au supersonique (Mach $\geqslant$ 1), les turboréacteurs équipent aujourd'hui les avions de combat comme le Dassault Rafale (figure 1 b). L'industrie du turboréacteur est un secteur majeur de l'aéronautique et s'avère donc être un facteur important dans le développement économique, de la technologie de pointe et de la recherche appliquée.

Problématique industrielle et motivation académique

Les turboréacteurs d'aujourd'hui sont des machines d'une extrême complexité regroupant un grand nombre de sous-systèmes. La fabrication et l'exploitation des turboréacteurs nécessitent des connaissances techniques parmi les plus pointues dans les domaines tels que la mécanique des fluides, la thermodynamique, l'automatique, l'acoustique ou encore la science des matériaux. A bord d'un avion, civil ou militaire, le turboréacteur n'est pas seulement un organe propulsif. Il fournit aussi toute l'énergie disponible à bord sous forme électrique, hydraulique et pneumatique et alimente le système de pressurisation et de conditionnement d'air. Le groupe moteur est ainsi souvent appelé "générateur de puissance"

ou "powerplant". Si le rendement et la fiabilité de ces moteurs se sont considérablement améliorés depuis leurs débuts, leur coût est très important et représente en général pour un avion civil le tiers du coût total de l'appareil.

Un turboréacteur comporte un ou plusieurs étages de compresseur, une chambre de combustion et une turbine (figure 2). De grandes quantités d'air sont aspirées par le compresseur qui va graduellement augmenter sa pression. L'air comprimé est ensuite envoyé dans une chambre à combustion. Là, il est mélangé à du kérosène de manière à constituer un mélange explosif, et est brûlé. Ce mélange, après combustion, produit une grande quantité de gaz chauds violemment éjectés vers la tuyère. Ces gaz entraînent simultanément une turbine qui récupère une partie de l'énergie cinétique des gaz et la convertit en énergie mécanique afin d'entraîner le fonctionnement de la soufflante et du compresseur. La turbine haute pression, dont les ailettes sont soumises au flux des gaz de combustion les plus chauds, est la pièce la plus compliquée sur les plans de l'aérodynamique et de la tenue des matériaux.
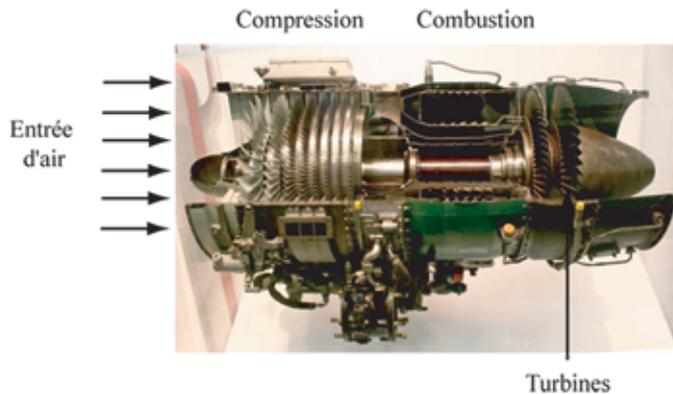
Figure 2 - Turboréacteur J85-GE-17A de General Electric illustrant son principe de fonctionnement.

En raison de nombreux facteurs tels que la température élevée des gaz brûlés, les forts gradients thermiques présents, la corrosion à chaud, la fatigue vibratoire, ainsi que les contraintes induites par la géométrie complexe, les aubes de turbines sont les pièces qui subissent les sollicitations les plus endommageantes. Par ailleurs, ce sont les aubes qui conditionnent le rendement du réacteur. Il semble donc naturel qu'une préoccupation des motoristes porte sur l'amélioration du rendement des turbomachines, c'est-à-dire l'obtention d'une température de sortie des gaz brûlés la plus élevée possible. La recherche de cette température optimale a donc conduit très rapidement au problème technologique qu'est la tenue des composants à haute température. C'est ainsi que des solutions visant à améliorer la durée de vie des aubes de turbine se sont dessinées. Le développement de nouveaux alliages constitue un axe de recherche principal et d'importants progrès ont été réalisés sur les matériaux constituant les aubes.

Alors qu'apparaissent les premiers turboréacteurs dans les années 1930, les superalliages existaient déjà. C'est en France qu'ont été mis au point pour la première fois en 1929 les aciers au chrome-nickel additionnés de titane, qui sont à la base des superalliages. Cette découverte est liée à deux noms Pierre Chevenard et Xavier Wache. Par la suite le fer a été substitué par le cobalt puis par le nickel avec notamment l'INCONEL destiné à la forge, ce qui lui conférait de meilleures propriétés mécaniques. Les recherches sur de nouvelles compositions chimiques d'alliages et de nouveaux modes d'élaboration sont très importantes dans les années 1950 et 1960. La chimie des superalliages à base nickel, principalement destinés aujourd'hui aux aubes monocristallines de turbine à gaz, a évolué de manière significative depuis le développement des alliages de première génération dérivés des matériaux à grains colonnaires. Les grains étant des sites privilégiés pour l'amorçage de fissures, les aubes monocristallines ont été mises au point, par croissance cristalline à partir d'un germe sélectionné. L'utilisation du monocristal et la performance d'ensemble des seconde et troisième générations d'alliages caractérisée par l'addition de quantités croissantes de rhénium, ont permis d'augmenter notablement la température d'entrée du gaz dans la turbine.

Avec le développement accru des superalliages monocristallins à base nickel, les industries aéronautiques ont mené (et mènent), en étroite relation avec de nombreux laboratoires de recherche, des études afin d'approfondir les connaissances dans les domaines reliant la composition, la microstructure et le comportement en service des aubes monocristallines. La maîtrise et, a fortiori, la prédiction et l'optimisation des processus de conception des matériaux et des structures passent par la prise en compte de phénomènes et mécanismes intervenant à différentes échelles, en espace comme en temps. Depuis l'échelle atomistique et parmi toute la gamme d'échelles possibles, il est essentiel de déterminer la (ou les) échelle(s) pertinente(s), c'est-à-dire celle(s) où agissent les mécanismes déterminants et dominants pour l'analyse et la compréhension des propriétés macroscopiques observées. Comprendre, modéliser et simuler chacune des échelles ainsi que leurs interactions constituent l'un des enjeux majeurs des approches dites multi-échelles.

L'approche multi-échelles

La mise en oeuvre de telles approches requiert des investigations couplées de nature expérimentale, théorique et numérique. De part leur (micro)structures, les superalliages s'intègrent parfaitement dans cette logique. Ces matériaux, à vocation industrielle, sont l'illustration parfaite de l'apport de l'analyse multi-échelles à la compréhension du comportement mécanique. Du point de vue de la compréhension des phénomènes, la démarche multi-échelles permet de tisser le lien entre le comportement des constituants élémentaires et le comportement macroscopique. Sur les aspects expérimentaux, l'enjeu reste la détermination de l'échelle pertinente qui ouvre la voie à l'analyse des mécanismes réellement responsables des effets aux plus grandes échelles.

Se pose ainsi le problème de la définition des échelles qui est implicitement contenu dans la dénomination "multi-échelles". Qu'est-ce que l'échelle microscopique ? Qu'est-ce que l'échelle macroscopique ? Existe t-il une échelle intermédiaire mésoscopique ? Ceci reflète bien la préoccupation liée au problème du choix des échelles, autrement dit: jusqu'à quel système physique est-il nécessaire de descendre pour rendre compte des propriétés mécaniques d'un matériau ? La réponse à cette dernière question sera fondamentalement différente selon l'interlocuteur et évoluera d'une école à l'autre. Le physicien du solide répondra que la dislocation individuelle est représentative de l'échelle microscopique et que l'échelle macroscopique peut être représenté par le monocristal. Pour le mécanicien, l'échelle microscopique est assurée par la matrice, tandis que l'échelle macroscopique peut correspondre à la structure. En somme, comme le remarque Zaoui [ZAO01]: "l'enjeu est alors que le *macro* du physicien ne soit plus trop éloigné du *micro* du mécanicien". Cette définition montre que l'accord sous-jacent des échelles entre les deux protagonistes est d'autant plus délicat qu'elle dépend du matériau étudié, et se doit naturellement d'être fondée sur des résultats expérimentaux (figure 3 a).

Les échelles caractéristiques dans ce mémoire sont définies de la manière suivante:

* L'échelle microscopique: cette échelle permet de mettre en évidence la propriété individuelle des dislocations. La microscopie électronique en transmission est aujourd'hui l'outil le mieux adapté pour ce travail (~ 1 nm).

* L'échelle mésoscopique: cette échelle correspond au comportement collectif de l'ensemble des dislocations où la notion de densité de dislocations commence à avoir un sens. Elle peut ainsi mettre en évidence l'interaction des dislocations avec la microstructure (~ 1 μm).

* L'échelle macroscopique: cette échelle est propre au travail de l'ingénieur et au calcul de structures qui vise la conception et le dimensionnement de pièces comme les aubes de turbines (~ 1 mm$-$m).

Ainsi du point de vue de la modélisation (figure 3 b), l'effort se décline selon ces mêmes trois échelles plébiscités par l'expérience:

(a)

(b)
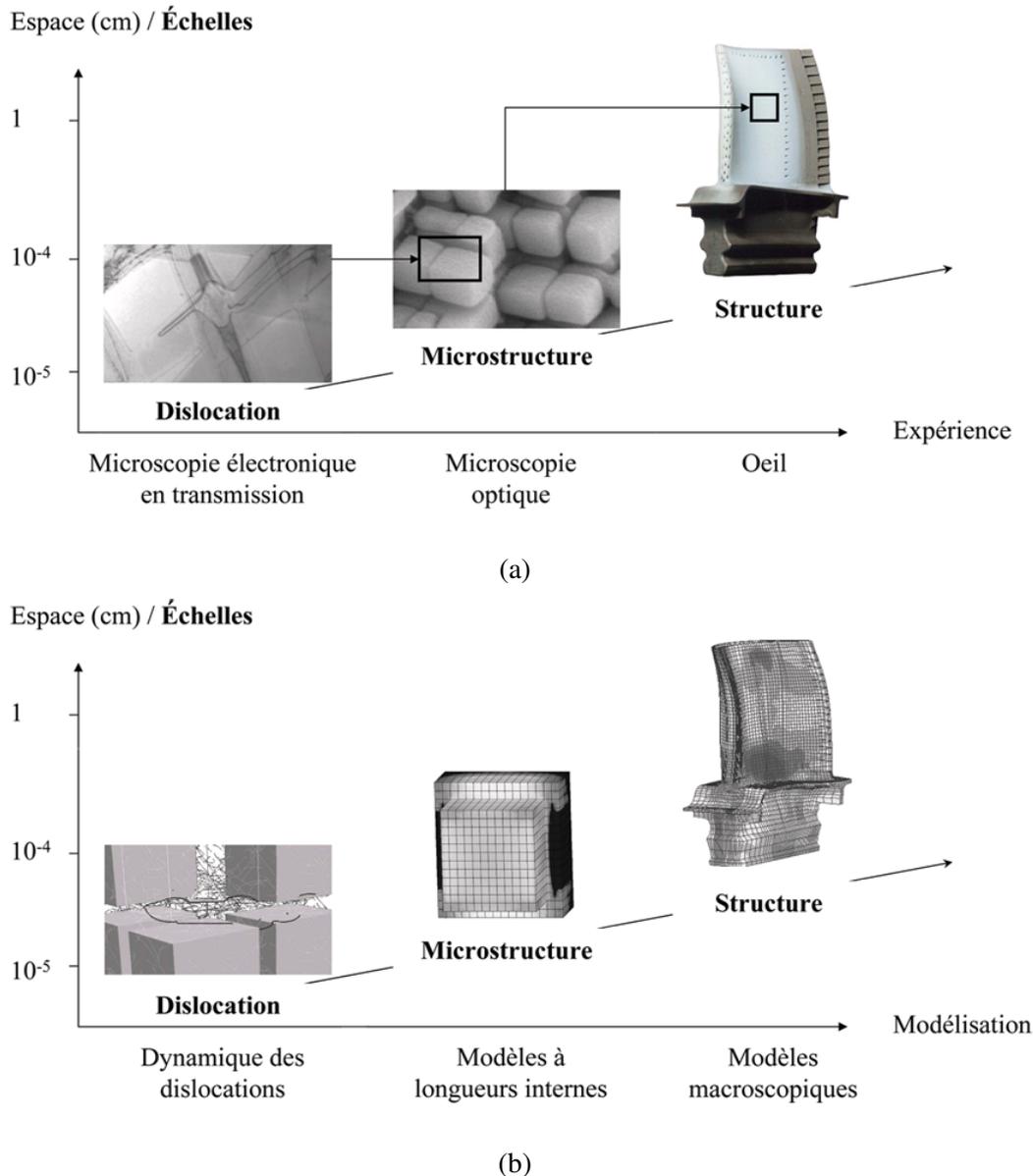
Figure 3 - Approche multi-échelles de la plasticité des superalliages monocristallins: de la dislocation individuelle à l'aube de turbine d'un point de vue (a) de l'expérience et (b) de la modélisation.

* L'échelle microscopique de la dislocation: l'objectif est de comprendre l'origine microscopique des phénomènes observés à l'échelle macroscopique. Pour cela, les simulations de dynamique des dislocations s'avèrent être un outil d'une grande importance.

* L'échelle mésoscopique de la microstructure: l'objectif à cette échelle est de faire le lien entre le *macro* du physicien et le *micro* du mécanicien. Cette échelle est dont capitale et résume parfaitement la formule de Zaoui. Selon les problèmes posés, il faut combiner, de façon séquentielle ou couplée, différentes techniques de simulations, discrètes et/ou continues telles que des simulations massives de dynamique des dislocations ou des modèles continus de plasticité à longueur interne.

* L'échelle macroscopique de la structure: l'objectif est de rendre accessible la simulation numérique des structures. Il s'agit alors de développer un modèle macroscopique et d'en identifier ses paramètres de manière à reproduire et à prévoir le comportement complexe et la tenue de la structure étudiée.

La combinaison expérience/modélisation est nécessaire dans la volonté de mieux comprendre et prendre en compte la microstructure des matériaux, permettant ainsi d'accroître le caractère prédictif des modèles macroscopiques actuels. En conclusion, la stratégie développée dans ce mémoire permet à la fois de mettre en évidence les mécanismes physiques élémentaires dominants aux échelles les plus fines, et ainsi, de nourrir les modélisations du comportement du superalliage monocristallin aux échelles supérieures.

Plan du manuscrit

Ce mémoire est composé de trois chapitres:

Le chapitre 1 présente à la fois le matériau étudié, et plus particulièrement les mécanismes de déformation à hautes températures du superalliage monocristallin à base nickel, ainsi que l'approche multi-échelles de la plasticité dominée par le mouvement collectifs des dislocations dans les couloirs de matrice. Ce chapitre met en évidence qu'améliorer la compréhension et la modélisation du comportement mécanique des superalliages monocristallins requiert davantage l'examen des relations entre les différentes échelles qu'un affinement de la connaissance à chaque échelle séparément. Finalement, deux questions dédiées à la plasticité des superalliages monocristallins à 850°C demeurant aujourd'hui ouvertes sont posées: l'une concerne les effets de taille des couloirs de matrice et l'autre de l'influence de l'orientation du chargement sur le comportement mécanique du superalliage.

Le chapitre 2 est consacré à la description de l'outil numérique à la base des études présentées dans ce mémoire. Ce chapitre traite la plasticité discrète fondée sur un couplage entre les simulations de dynamique des dislocations et la méthode des éléments finis. L'adaptation qui a été nécessaire pour le traitement de la plasticité en présence d'interfaces est précisée, et les résultats des problèmes posés au précédent chapitre sont présentés. Pour chacun des problèmes, les microstructures de dislocations obtenues sont analysées dans un premier temps et comparées si possible avec les résultats expérimentaux existants. Les mécanismes microscopiques qui sont à l'origine de leur formation sont également détaillés. Dans un second temps, les caractéristiques mécaniques macroscopiques qui résultent du comportement de la microstructure de dislocations sont mises en évidence.

Le chapitre 3 concerne deux modélisations continues de nature différentes. Une première partie évoque un modèle à longueur interne dont une loi de durcissement est dictée par une densité de dislocations géométriquement nécessaires. Ce modèle est alors qualifié d'intermédiaire dans la mesure où il permet d'établir des bases physiques dans le développement d'un modèle cristallin à l'échelle supérieure. Ainsi une seconde partie met à profit l'étude des microstructures de dislocation menée aux échelles les plus fines pour améliorer un modèle micromécanique d'écrouissage cinématique, validé sur une large gamme de type et d'orientation de chargement. Ce modèle est fondé sur une procédure d'homogénéisation, pour lequel la réponse globale du matériau est déterminée en considérant les rôles de la microstructure et des interactions mécaniques entre constituants. Ce chapitre a pour objectif de montrer les nouvelles avancées sur la formulation des lois de plasticité cristalline obtenue par échange d'informations pertinentes à travers la transition d'échelles précédemment définie.

Ce mémoire est rédigé en anglais car il résulte d'une étroite collaboration entre le Laboratoire d'Etudes des Microstructures (CNRS−ONERA), le Département Matériaux et Structures Métalliques (ONERA) et le Bundesanstalt für Materialforschung und -prüfung (BAM, Berlin) pour le chapitre 3.

State of the art

Contents

Introduction

Le premier chapitre intitulé "Etat de l'Art" repose sur trois parties. La première partie 1.1 est dédiée à la présentation du matériau étudié durant le travail de thèse, le superalliage monocristallin à base nickel. Un superalliage ou alliage haute performance est un alliage métallique présentant une excellente résistance mécanique et une bonne résistance au fluage à haute température (typiquement 0,7 à 0,8 fois sa température de fusion en K), ainsi qu'une bonne résistance à la corrosion et à l'oxydation. Le développement des superalliages a été très intense dans les années 1950 et 1960 lorsque Versnyder [VER60] a montré l'intérêt de leur utilisation pour les aubes de turbine haute pression. Un nouvel essor technologique est franchi avec l'avènement des premiers monocristaux en 1970 [VER70], et ce n'est qu'à partir de 1980 qu'apparaissent les superalliages monocristallins dont la composition est spécifiquement étudiée pour sa forme monocristalline.

La seconde partie 1.2 porte sur une étude bibliographique des actuelles modélisations de la plasticité cristalline traversant différentes échelles de résolution: de la dynamique des dislocations à la mécanique des milieux continus. Elle traite ainsi de la plasticité multi-échelles: à différentes échelles de résolution, diverses approches permettent de modéliser la plasticité d'un matériau. Chaque modèle tend à devenir de plus en plus performant, et il est aujourd'hui pensable de "remonter" les échelles d'espace et de temps de manière continue en réalisant par exemple des simulations atomiques ou par dynamique des dislocations, afin d'asseoir un modèle à l'échelle supérieure.

Enfin, une troisième et dernière partie est tournée vers une présentation non exhaustive de problèmes aujourd'hui ouverts sur la modélisation du comportement des superalliages monocristallins. Deux de ces problèmes illustrent les effets de taille et de l'orientation du chargement sur le comportement mécanique de ces alliages. En effet, dans le cadre d'une étude sur les superalliages, un objectif visé par la mécanique des matériaux hétérogènes doit être de prévoir le comportement du superalliage à partir de la seule connaissance du comportement de chacune des phases, et de la morphologie des constituants. Par ailleurs, une modélisation appliquée sur une pièce de géométrie complexe comme l'aube de turbine doit être capable de rendre compte de l'anisotropie du comportement.

1.1   Single crystal nickel-based superalloys

1.1.1   Introduction

Over the later part of the twentieth century, the performance of the superalloys was improved drastically by a concerted period of alloy and process development. Figure (4) provides a perspective for turbine blading, which has occurred since the first superalloys began to appear in the 1940s. Cast rather than wrought materials are currently preferred since a better creep performance is then obtained. The introduction of improved casting methods, and later the introduction of processing by directional solidification, enabled significant improvements. This was due to the columnar microstructures that were produced in which the transverse grain boundaries were eliminated. Once this development occurred, it was quite natural to remove the grain boundaries completely, so that monocrystalline (single crystal) superalloys were produced. This allowed, in turn, the removal of grain-boundary strengthening elements such as boron (B) and carbon (C) which had traditionally been added. The fatigue life is then improved [STR80].

Nowadays, single crystal superalloys are being used in increasing quantities in the gas turbine engine. The improvements have been made in a period of approximately 15 years between 1980 and 1995, primarily as a consequence of a better appreciation of the physical factors which confer high-temperature strength to these materials. Table (1.1) lists the compositions of common nickel-based superalloys, including those used in single crystal form. As many as 9 different alloying additions are added. The so-called first generation single crystal superalloys, such as AM1, Rene N4 or SRR99, contain appreciable quantities of the hardening elements aluminum (Al), titanium (Ti), and tantalum (Ta). Second-generation alloys, such as PWA 1484, Rene N5 or CMSX-4, is characterised by a 3 wt% concentration of rhenium
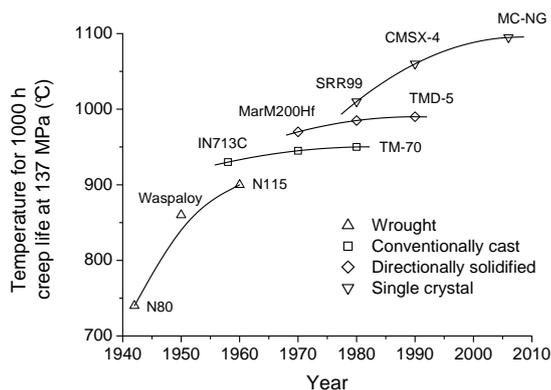
Figure 4 - Evolution of the high-temperature performance of superalloys over a 70 year period since their emergence in the 1940s [REE06].

(Re), which is increased to about 6 wt% for the third-generation alloys such as CMSX-10 or Rene N6. In addition, the modern alloys are characterised by significantly lower concentrations of chromium (Cr) and higher concentrations of Al and Re. Concentrations of Ti and molybdenum (Mo) are at very modest levels. The period since 2000 has seen the emergence of the fourth-generation single crystal superalloys, such as MC-NG, which are characterised by additions of ruthenium (Ru).

1.1.2 Microstructure and defects

1.1.2.1 The γ phase

Although nickel alone is not endowed with a distinctly high modulus of elasticity or low diffusivity, the γ NiAl matrix is favoured by most gas turbine designers for the most severe temperature and time excursions. It is remarkable that some of these alloys can be used at 0.9 T_M (with T_M the melting point) and for times up to 100,000 h at somewhat lower temperatures. The basic reasons for this endurance must be attributed to the high tolerance of nickel for alloying without phase instability, and the tendency, at high temperatures, to form Al_2O_3-rich phases with exceptional resistance to oxidation.

The γ phase exhibits the face-centered cubic (fcc) structure, and in nearly all cases it forms a continuous matrix phase in which the other phases reside. It contains significant concentrations of elements such as Co, Cr, Mo, Ru, and Re.

The fcc structure consists of close-packed planes, stacked with periodicity equal to three. The perfect lattice can be denoted ABCABCABCABC..., where each A, B or C represents a close-packed layer. The lattice vector is $\frac{a}{\sqrt{2}}$, with a is the length of the side of the unit cell.

From a crystallographic point of view, the slip system in a fcc metal such as Ni is $\frac{a}{2}\langle 1\bar{1}0\rangle\{111\}$. Hence the Burgers vector is $\frac{a}{\sqrt{2}}$. However, this statement does not properly respect the micromechanics of deformation. Glide of an $\frac{a}{2}\langle 1\bar{1}0\rangle\{111\}$ dislocation occurs by the passage of two partial dislocations, which, although in close proximity to each other, are separated by a distance which depends on the force of their elastic repulsion and the energy of the planar stacking fault so produced. This implies that the $\frac{a}{2}\langle 1\bar{1}0\rangle\{111\}$ dislocations are dissociated. Electron microscopy confirms that the reaction is accompanied by the creation of an Intrinsic Stacking Fault (ISF) in the $(1\bar{1}1)$ plane according to the following form

$$\frac{a}{2}\langle 110\rangle\{\bar{1}11\} \longrightarrow \frac{a}{6}\langle 211\rangle\{\bar{1}11\} + \text{ISF} + \frac{a}{6}\langle 12\bar{1}\rangle\{\bar{1}11\} \tag{1.1}$$

where each dislocation on the right-hand side of the equation is a Shockley partial [DEC84].

Alloy	Cr	Co	W	Mo	Re	Al	Ti	Ta	Hf	Ru	Density
AM1	7.8	6.5	5.7	2	-	5.2	1.1	7.9	-	-	8.6
CMSX-2	8	4.6	7.9	0.6	-	5.6	1	6	-	-	8.6
Rene N4	9	8	6	2	-	3.7	4.2	4	-	-	8.56
SRR99	8	5	10	-	-	5.5	2.2	3	-	-	8.56
AM3	8	5.5	5.7	2	-	6	2	3.5	-	-	8.25
PWA1484	5	10	6	2	3	5.6	-	8.7	0.1	-	8.95
Rene N5	7	8	5	2	3	6.2	-	7	0.2	-	8.7
CMSX-4	6.5	9	6	0.6	3	5.6	1	6.5	0.1	-	8.7
CMSX-10	2	3	5	0.4	6	5.7	0.2	8	0.03	-	9.05
Rene N6	4.2	12.5	5.4	1.4	5.4	5.75	-	7.2	0.15	-	8.97
MC-NG	4	-	5	1	4	6	0.5	5	0.1	0.1	8.75

Table 1.1: The compositions (in weight%) of some common single crystal nickel-based superalloys [MSM]. The alloys from AM1 to AM3 belong to the first-generation alloys. Re-containing alloys are labelled second generation (such as the PWA1484, Rene N5, and CMSX-4 alloys). The CMSX-10 and Rene N6 alloys belong to the third generation, and MC-NG to the fourth. A review of the evolution of the chemistry of these classes of alloys, focusing on the advantages and drawbacks, can be found in [CAR99]. The Ni content balances the whole composition. Density is expressed in g/cm^3.

1.1.2.2 The γ' phase

The γ' Ni_3Al phase displays the primitive cubic, $L1_2$, crystal structure, with Al atoms at the cube corners and Ni atoms at the centres of the faces (see figure 5). Remarkably, the strength of γ' increases as temperature increases, reaching a maximum at around 800°C [SIM72]. This phase contributes not only through its intrinsic strength, but also because in the γ/γ' alloys it forces Orowan bypassing, as will be explained further on.
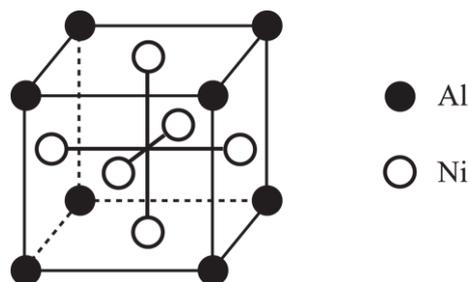
Figure 5 - $L1_2$ unit cell. Arrangement of Ni and Al atoms in the ordered Ni_3Al phase.

An early question was about the precise geometry of a dislocation gliding through an ordered lattice. Marcinkowski *et al.* [MAR61] first observed in the Transmission Electron Microscope (TEM) that dislocations in $L1_2$ ordered Cu_3Au contained two components, or superpartials, which were held together by a strip of AntiPhase Boundary (APB). They obtained the direct evidence for a hypothesis proposed by Köhler and Seitz, that dislocations in superlattice structures would propagate more readily if they existed in groups coupled by an APB. In other words, they predicted that the ordered structure of most intermetallics would require a superdislocation, i.e. a pair of dislocations separated by a strip of material with the ordering of the atoms exactly out-of-plane with respect to the normal structure, the APB. Experimentally, it is now established that the $a\langle10\bar{1}\rangle$ superdislocations are dissociated into two $\frac{a}{2}\langle10\bar{1}\rangle$

ordinary dislocations bordering the APB on $\{111\}$ planes according to the following reaction:

$$a\langle 10\bar{1}\rangle \longrightarrow \frac{a}{2}\langle 10\bar{1}\rangle + \text{APB} + \frac{a}{2}\langle 10\bar{1}\rangle \tag{1.2}$$

Moreover, the $\frac{a}{2}\langle 10\bar{1}\rangle$ dislocations split further into two superlattice Shockley partials $\frac{a}{6}\langle 112\rangle$, just as for a dislocation in the γ phase (see relation 1.1), according to

$$\frac{a}{2}\langle 10\bar{1}\rangle \longrightarrow \frac{a}{6}\langle 2\bar{1}\bar{1}\rangle + \text{SISF} + \frac{a}{6}\langle 11\bar{2}\rangle \tag{1.3}$$
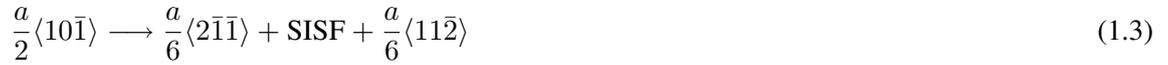
where the Superlattice Intrinsic Stacking Fault (SISF) contains a fault in the stacking sequence but maintains the condition among the nearest neighbouring atoms [DEC04].

However, in practice, the dissociations are usually even more complicated than those given in relations (1.2) and (1.3). This is because the superdislocations dissociate on both $\{111\}$ and $\{010\}$, which distinct segments of it lying on each of the two planes. For instance, it is possible for the APB, or segments of it, to cross-slip to a cube plane $\{010\}$. This configuration is expected to be sessile, since the cube plane is not a glide plane for γ'. This configuration is termed a Kear-Wilsdorf (KW) lock, after those who discovered it in $L1_2$ crystal structures [KEA62]. The behaviour of the KW lock is central to the understanding of the anomalous yield effect displayed by $L1_2$ compounds and Ni_3Al in particular. This point is considered in greater detail in section 1.1.3.

1.1.2.3 The $\gamma + \gamma'$ alloys

The microstructures of the two-phase superalloys of interest contain γ' precipitates which are cuboïdal in form (see figure 6 a). Analysis of these structures using TEM confirms that a distinct cube-cube orientation relation exists between the γ' precipitates and γ matrix in which they reside, according to

$$\begin{aligned}
\{100\}_\gamma &\;//\; \{100\}_{\gamma'} \\
\langle 010\rangle_\gamma &\;//\; \langle 010\rangle_{\gamma'}
\end{aligned} \tag{1.4}$$

which is referred to as the cube-cube orientation relationship.
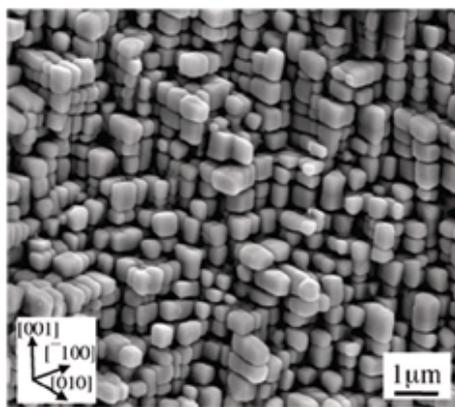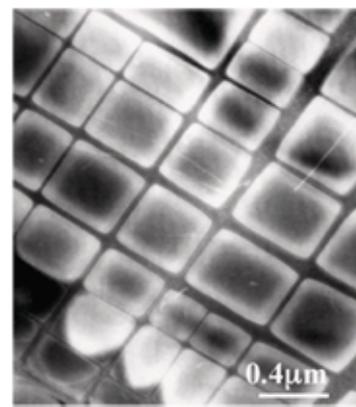
(a)   (b)

Figure 6 - Morphology of the cuboïdal γ' phase in the superalloy after a complete heat treatment in (a) 3- and (b) 2- dimensional view [XIN09].

The γ/γ' interfaces have the $\langle 100 \rangle$ directions as normal plane. Provided that the lattice misfit δ, defined as

$$\delta = 2 \times \left[\frac{a^{\gamma'} - a^{\gamma}}{a^{\gamma'} + a^{\gamma}} \right] \qquad (1.5)$$

between the a^{γ} and $a^{\gamma'}$ lattice parameters of the respective disordered γ and ordered γ' phases, is not too large, the γ/γ' interface remains coherent and the interfacial energy remains low. The γ' precipitates align along the elastically soft $\langle 100 \rangle$ direction (see figure 6 b).

The microstructures of the superalloys are found to depend critically on the coherency of the γ/γ' interface. Ricks *et al.* [RIC83] have studied the development of γ' precipitates in a number of different nickel-based superalloys during heat treatment, identifying correlations between the morphology, size and sign of the γ/γ' misfit. It was shown that the morphological development occurs in the sequence spheres↦cubes↦arrays of cubes. No substantial difference in this respect was found between positive and negative misfitting alloys. Interestingly, both the size at which the γ' particles depart from the spherical morphology and the severity of the heat treatment required to form the cuboïdal arrays were found to be sensitive to the lattice misfit. The results suggest that when the magnitude of the misfit δ is small, this minimises the interfacial energy so that γ' coarsening is restricted. As a consequence, the γ' particles must grow to a larger size before the cuboïdal form is found [BRU02].

In practice, δ roughly ranges between -0.5% and 0.5%, depending on the temperature and on the mean chemical composition. The chemistry of the successive generations of alloys evolved in order to increase the amount of γ' precipitates, which has reached 70% in the latest generation, and consequently the strengthening effects.

1.1.3   Strengthening effects

1.1.3.1   Overview of precipitation hardening

The mechanical properties of single crystal nickel-based superalloys strongly depend on the microstructure, which, in turn, is controlled by the chemical composition and the processing conditions. This is particularly the case for the yield stress, which is a sensitive function of the distribution of the γ' phase. The strength of the nickel-base superalloys is a function of four distinct mechanisms, including:

* ∗ Solid-solution strengthening.

* ∗ Misfit strengthening.

* ∗ Orowan strengthening.

* ∗ Order strengthening.

The strength of commercial superalloys arises from the combination of these hardening contributions. These strengthening mechanisms are considered to be independent and additive [POL92].

1.1.3.2   Solid-solution strengthening

Solid-solution strengthening is generally distinguishable from precipitation-strengthening by the relatively low content of precipitate-forming elements such as aluminum, titanium, or niobium. Solid-solution strengthening is caused partly by lattice distortion, and therefore increases with atomic size difference, up to a maximum of about 10%. Atomic clustering [FLE63] or short range order can also strengthen the matrix [PET99]. For the specific case of a nickel-based superalloy, the chemical force acting on dislocations has been investigated and calculated by post mortem and *in-situ* TEM [SAA04]. At room-temperature it was estimated that the shear stress to move the dislocation corresponds to a friction stress of the order of 100 MPa.

1.1.3.3 Misfit strengthening

As mentioned in section 1.1.2, a difference in the distribution of the alloying elements between the two phases results in slight difference in their lattice parameters, which is often expressed by the coherency (mismatch) parameter δ given by relation (1.5). A consequence of a non-zero δ are coherency stresses, which are present even when the externally applied load is zero. For instance, in a CMSX-4 single crystal superalloy it has been reported that $\delta = -2.3 \ 10^{-3}$ at room temperature [GLA94]. Assuming that the γ/γ' interfaces remain into elastic coherence, it follows that the precipitates are constrained in a state of hydrostatic tension.

In order to estimate the coherency stress field, several Finite Element (FE) analyses can be found in the literature, using isotropic [GLA89] or anisotropic [POL92] elasticity, or anisotropic viscoplasticity [NOU95]. All these studies show qualitatively that in the case of a negative lattice parameter, the precipitate is in tension and the matrix channels in compression.

Hence, the residual internal stress field exerts a (back-) force on dislocations during tensile testing. Nembach and Neite [NEM85] have extensively reviewed the experimental evidence bearing on lattice misfit effects on the strength of superalloys. It was concluded that there is no convincing experimental proof that misfit affects the flow stress of γ'-hardened alloys and that lattice misfits of the magnitude found in commercial alloys do not make a significant contribution to strength.

1.1.3.4 Orowan strengthening

The origin of strengthening mechanisms is complex since the matrix/precipitate interfaces, the size and spacing of the precipitates play an important role. For example, comparing the creep behaviour at $1000°$C of γ phase, γ' phase, and a mixture of the two phases, Nathal *et al.* [NAT89] found for the two-phase alloy a decrease in creep rate of about a factor of 1000 relative to γ' alone.

Creep tests of nickel-base superalloy single crystals were coupled with stereo TEM by Pollock and Argon [POL92]. For their alloys with a γ' volume fraction ~ 67 % and precipitate size ~ 0.5 μm, they found that for creep at $850°$C the γ' was essentially dislocation-free and undeformable. As a result, dislocations are forced to move through the narrow channels between precipitates, ultimately forming complex network and thereby constituting the principal cause for the high creep resistance. The dislocation structure developed during early stages of primary creep at $850°$C and 552 MPa is shown in figure (7 a). No dislocations appear within those precipitates that extend through the foil thickness. The visible dislocations occur in matrix channels that are contained within the foil: in vertical channels (lower part of the figure) and in horizontal channels (upper part of the figure).

Gliding dislocation can bow between precipitates and bypass them, leaving dislocation segments at interfaces. This mechanism has been emphasised by Carry and Strudel [CAR77], and the effect of this process on the yield stress can be described by the Orowan bowing model [ORO48]. The increment in flow stress due to bowing is given by consideration of the radius of curvature R to which a flexible dislocation line can be bent by an applied stress τ^{Orowan}. Considering that the value of R is half the precipitate spacing d, τ^{Orowan} is also defined by

$$\tau^{\text{Orowan}} \approx \sqrt{\frac{2}{3}} \frac{\mu b}{d} \qquad (1.6)$$

with μ the shear modulus, b the magnitude of the Burgers vector, and $\sqrt{\frac{3}{2}} \, d$ the width of the channels in a $\{111\}$ octahedral plane. Dislocation loops leave behind segments pressed against the interfaces which may have a pure screw or $\pm 60°$ mixed character, depending on the channel direction.

<div align="center">(a)   (b)</div>
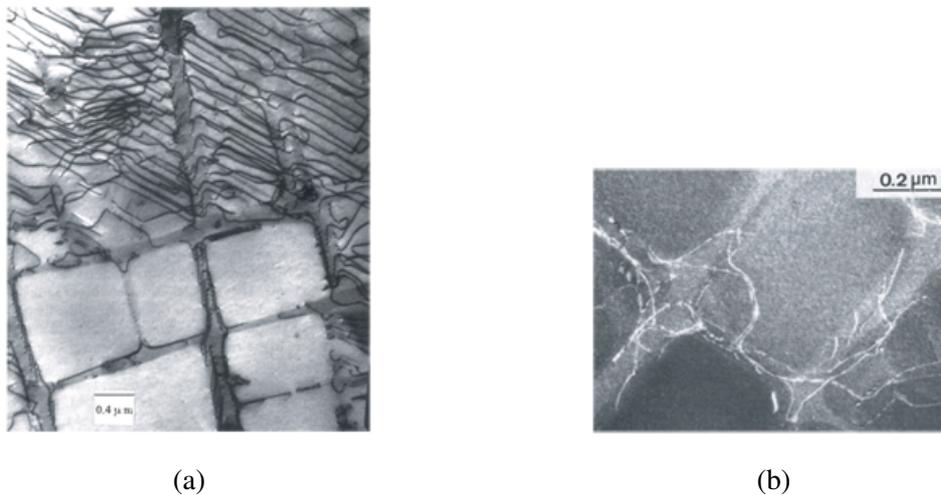
Figure 7 - (a) Dislocation structures developed during primary creep at 850°C of a single crystal super-alloy, CMSX-3 [POL92]. Dislocations appear in the matrix channels and bow out between the γ' precipitates. (b) Conventional transmission electron microscopy micrographs showing the (bowing-assisted) cutting process of ordered γ' precipitates by pairs of dislocations in AM1 at 950°C [POU89].

1.1.3.5 Order strengthening

A $\frac{a}{2}\langle 1\bar{1}0\rangle\{111\}$ dislocation travelling in a γ channel cannot enter the γ' phase without the formation of an APB, and therefore the dislocations must travel through the γ' structure in pairs, with a second $\frac{a}{2}\langle 1\bar{1}0\rangle\{111\}$ dislocation removing the APB introduced by the first (see reaction 1.2). This is supported by evidence from TEM [POU89] (see figure 7 b). The associated APB energy γ^{APB} represents a barrier which must be overcome if precipitate cutting is to occur. Although detailed calculations are required for an estimate, the precipitate-cutting stress is expected to be of the order $\frac{\gamma^{\mathrm{APB}}}{b}$.

Even though APB energy determinations have been the object of several studies or reviews [NAB97], according to which the main influences on APB energy are the chemical composition and temperature, their influence is not well established. The APB energy of the pure Ni_3Al compound was estimated to be around 170 mJ.m^{-2} [DIM91]. The addition of 1 at% Ta increases this energy to 250 mJ.m^{-2} [BAL91], which reduces considerably the probability of formation of superdislocations capable to shear a γ' precipitate. The cutting stress associated to $\gamma^{\mathrm{APB}} = 250$ mJ.m^{-2} is then approximately 1000 MPa. For the case of strongly coupled dislocations, i.e. when the precipitates are large and the volume fraction is high, this cutting regime is considered in detail in section 2.4.2, where it will be studied by dislocation dynamics simulations.

1.1.3.6 Temperature dependence of strengthening

The nickel alloys exhibit a remarkable characteristic: the yield stress does not decrease strongly with increasing temperature, as is the case for most other alloy systems. In fact, for many superalloys the yield stress increases with increasing temperature, typically up to temperatures of about 800°C [BEA69]. Figure (8 a) shows some typical data for a number of single crystal alloys, tested along the $\langle 001\rangle$ orientation. The peak stress of beyond 1000 MPa is about 50 times greater than the flow stress of pure Ni. This confirms that considerable metallurgical strengthening effects are at play. For temperatures beyond 800°C (until about 1200°C), the yield stress decreases quickly.

In a first attempt to rationalise this behaviour, Davies and Stoloff [DAV65] studied the yield properties of Ni-Al binary alloys between -200 and 800°C. The TEM images indicated that the micromechanism of deformation was Orowan looping at 850°C, but precipitate cutting was observed for material subjected
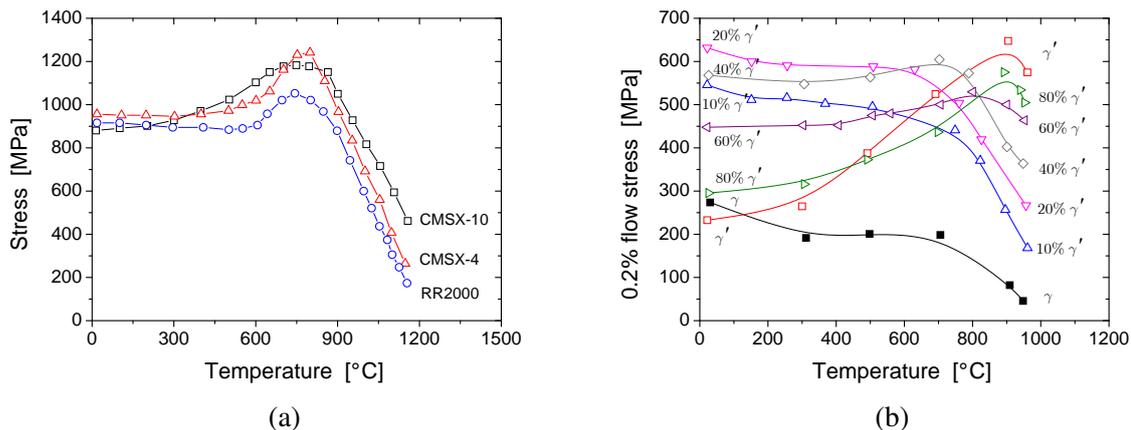
Figure 8 - Variation of the yield stress with temperature of (a) a number of single crystal superalloys with temperature [REE06], and (b) NiAlCr alloys containing various volume fractions of γ' phase [BEA69].

to the 700°C treatment. This is an evidence that the constant yield stress displayed by the Ni-14%Al alloy heat treated at 700°C is due to deformation of the γ' phase.

Further work reported by Piearcey *et al.* [PIE67] sheds light on the role of γ' in the deformation of superalloys. The MarM200 alloy, which contains a γ' volume fraction $f \approx 0.60$, was tested in single crystal form and revealed a similar curve to those of the more modern single crystals given in figure (8 a). Also tested was single crystal cube-oriented Ni$_3$Al, alloyed such that its composition matched that found in MarM200. The results confirm that at and beyond the peak stress, the behaviour of the alloy is determined by the strength of the γ' phase. Furthermore, from ambient temperature up to the temperature associated with the peak stress, the γ' imparts an increasing fraction of the strength as the temperature increases. Similar experiments were carried out by Beardmore *et al.* [BEA69]. The temperature dependence of the yield stress was determined for a number of alloys with varying amounts of γ' precipitates (see figure 8 b). Once again, the yield stress of the alloy consisting of 100% γ' displayed a strong positive dependence on the temperature, up to about 800°C (see red curve in figure 8 b). Above the temperature corresponding to the peak stress, the yield stress of a two-phase $\gamma + \gamma'$ alloys obeys a rule of mixtures, i.e. it corresponds to the weighted average of the values for the γ and γ' phases. This contrasts strongly with the behaviour at low temperatures, where the two-phase alloys are very much stronger than the rule of mixtures would predict.

The anomalous yielding effect is discussed in detail in section 2.4.2. Upon deformation, the anisotropy of the APB energy and further contribution from the elastic anisotropy combine to promote the cross-slip of segments of the γ' superdislocations from the $\{111\}$ slip plane to the cross-slip plane $\{001\}$. The cross-slipped segments are sessile so they resist further deformation. As mentioned above, these are known as KW locks. The hardening is increasingly prevalent as the temperature rises, due to a component of the cross-slipping process which is thermally activated.

Beyond the peak stress, which occurs typically around $800-850°C$, slip-line trace analysis on deformed single crystals has shown that the slip mode changes to $\frac{a}{2}\langle 1\bar{1}0\rangle\{001\}$, i.e. the so-called cube slip dominates [STA75].

1.2 Multiscale plasticity

1.2.1 Introduction

The mathematical concept of dislocations in elastic continua was first studied by Volterra [VOL07]. Each dislocation is seen as a cut, followed by a relative displacement and then a reattachment of the material of

the two sides of the cut. In materials science, the concept of dislocations was independently introduced by Orowan, Polany and Taylor [TAY34] in 1934, who used dislocations to explain plastic deformation of single crystals. The existence of dislocations was first confirmed directly by Hirsch *et al.* [HIR60] by TEM images around 1950. Figure (9) illustrates a early of the history of dislocations since 1907 and the definition of Volterra's dislocation to the first direct observation of dislocations.

V. Volterra   **G.I. Taylor**   **M. Polanyi**   **E. Orowan**   **P.B. Hirsch**

1860 - 1940   **1886 - 1975**   **1891 - 1976**   **1891 - 1976**   **1920 -**

Figure 9 - The early of the history of dislocation theory. 1907: Definition of Volterra's dislocation (or isolated defect) by the mathematician V. Volterra; 1934: Discovery of the concept of crystal dislocation introduced by Orowan, Polany and Taylor; 1956: First published observations of dislocations by transmission electron microscopy.

In crystalline materials, dislocation glide in slip planes gives rise to plastic deformation. A dislocation is thus an elementary carrier of crystal plasticity. Therefore, modelling the plasticity of crystalline materials involves the understanding of dislocation properties, which are closely related to the atomic structure of their dislocation cores and their long-range elastic fields. Many models have been developed to understand the plasticity of metals. Since the features of plasticity vary in size and time, the models also vary widely in length and time scales, as depicted in figure (10).

In this thesis most attention is given to discrete simulations and continuum mechanics, with a special emphasis on Dislocation Dynamics (DD) (see section 2.1), and homogenisation techniques (see section
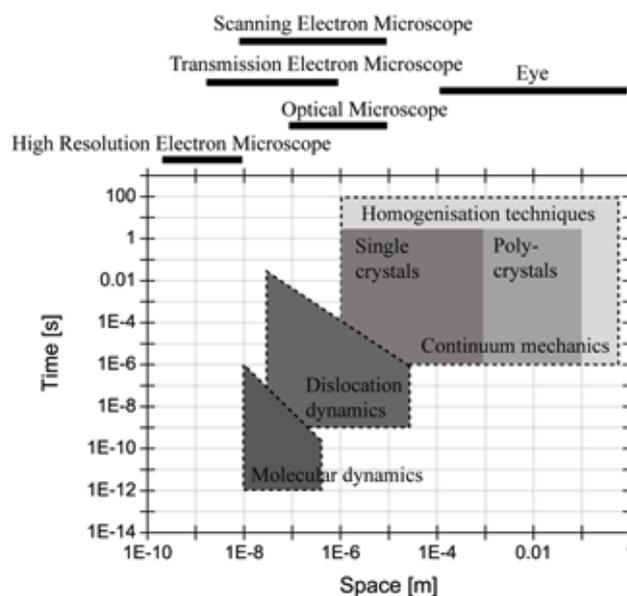
Figure 10 - Typical volume size and time covered by three models devoted to crystal plasticity [FIV04].

3.2). Each model has its own characteristic length and time scale.

Figure (10) shows such ranges of length and time scales for each method. As the performance of each numerical method is improved, the volume and the physical time which can be simulated increases (top and right domain limits of each method in figure 10). Recently the length and time scales of the different methods have begun to overlap. Ideally, continuum mechanics should use a set of constitutive equations that accurately take into account the processes that take place at length scale at which DD simulations are carried out. This gives a great impetus to exchange information between the different models in order to build up a unified description of crystal plasticity, which would ideally be able to predict the behaviour of a material from the fundamental properties of the atoms or dislocations.

In this thesis, the transition from the microscopic mechanisms to a macroscopic material model passes through the following length scales[1]

* The microscale corresponds to the scale of the crystal lattice, where considering of single dislocations is reasonable ($\sim$ 1 nm).

* The mesoscale denotes a scale where the continuous description of dislocations and their densities starts to make sense[2] ($\sim$ 1 μm).

* The macroscale represents the mm-level or above, but will also be used in the context of the continuum mechanics description of samples which are even smaller[3] ($\sim$ 1 mm$-$m).

1.2.2 The concept of dislocations

1.2.2.1 The Burgers vector

A dislocation is geometrically characterised by its so-called Burgers vector, which is defined by means of a Burgers circuit around the dislocation. According to the definition given by Frank [FRA51], a Burgers circuit is any closed atom-to-atom path in the real crystal. Taking the same path in a dislocation-free lattice, the circuit does not close if the crystal contains a dislocation. The vector required to close the circuit in the perfect crystal is called the Burgers vector. The Burgers circuit is taken in the sense of a right-hand rule looking in the direction of the dislocation line (e.g. within the 2-dimensional cut through the dislocation line in figure 11, the dislocation line points paper-inward on the right-hand side $\perp$ and paper-outward on the left-hand side $\top$). If dislocations with the same line sense but opposite Burgers vector are brought together they annihilate and restore a perfect lattice. The Burgers vector $\boldsymbol{b}$ and its length $b = |\boldsymbol{b}|$ in the fcc single crystal is given by $\boldsymbol{b} = \frac{1}{2}\langle 110\rangle$ and $b = \frac{a}{\sqrt{2}}$, where a is the lattice parameter.
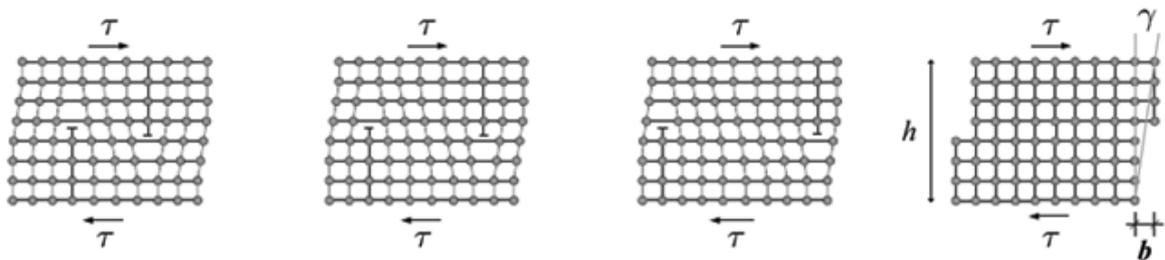
Figure 11 - Glide of an infinitely long straight edge dislocation $\perp$ under an applied shear stress τ [HIR82].

---

[1]This classification is the same as given in the Introduction.

[2]See sections 2, 2.4, and 3.1 for examples of two kinds of models (through a discrete and a continuous approaches) at this mesoscale.

[3]See section 3.2 for a representative model at the macroscale.

1.2.2.2   Edge, screw and mixed dislocations

Dislocations develop during crystallisation from the melt and with ongoing plastic deformation. Generally they form a 3-dimensional dislocation network of edge, screw and mixed dislocation segments. Edge dislocations are characterised by the fact that the Burgers vector $\boldsymbol{b}$ is perpendicular to their line direction $\boldsymbol{l}_\perp$ (figure 12 a). These two directions define a unique slip plane (shaded area in figure 12). In turn, screw dislocations are characterised by the fact that the Burgers vector $\boldsymbol{b}$ is parallel to their line direction $\boldsymbol{l}_\odot$ (figure 12 b). Thus $\boldsymbol{b}$ and $\boldsymbol{l}_\odot$ do not define a unique slip plane and consequently screw dislocations are not bounded to a specific slip plane. The mixed dislocation M is a mixing of pure edge and pure screw dislocations (figure 12 c).

(a)   (b)   (c)
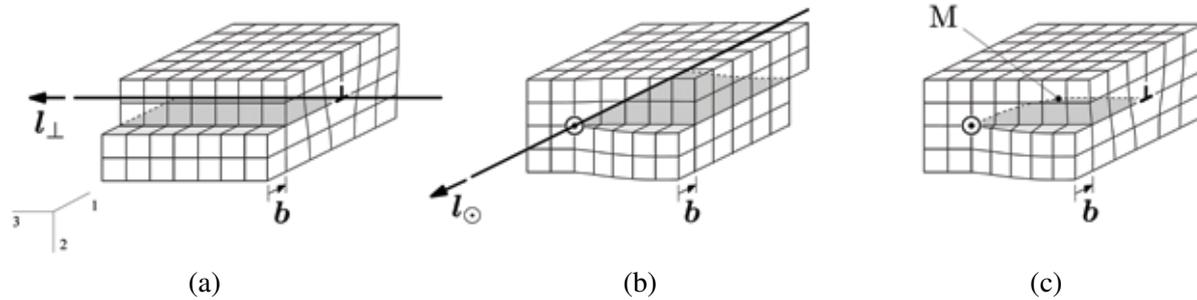
Figure 12 - Geometry of (a) pure edge, (b) pure screw and (c) at M, mixed dislocation segments. The dislocation line represents the boundary between slipped and unslipped crystal parts. A dislocation loop contains all 3 kinds of dislocation segments.

1.2.2.3   Dislocation glide

In a real crystal, a dislocation represents permanent deviations of atoms from the original position in the crystal lattice. These deviations are the result of an elementary plastic shear which takes place through consecutive displacement of neighbouring atoms and not through shearing off a complete atom layers. When the dislocation reaches the crystal boundary, a slip step of one Burgers vector length $\boldsymbol{b}$ is produced. This is visualised for a 2-dimensional cut through a cubic lattice in figure (11).

1.2.2.4   Dislocation-controlled yield

The slip plane is normally the plane with the highest density of atoms and the direction of slip is the direction in the slip plane in which the atoms are most closely spaced. Thus, in fcc metals slip often occurs on $\{111\}$ planes in $\langle 110 \rangle$ directions. A slip plane and a slip direction in the plane constitute a slip system. Fcc crystals have four $\{111\}$ planes with three $\langle 110 \rangle$ directions in each, and therefore have twelve $\{111\}\langle 110 \rangle$ slip systems. The slip systems of a fcc crystal can be classified, following the Schmid and Boas notation [SCH35], by the normal slip plane $\mathbf{n}^g$ and the slip direction $\mathbf{m}^g$ of the slip system g (see table 13 a). Assuming the small-strain framework, both quantities are constant in space and time.
The main source of plastic deformation is the expansion of dislocation loops, where a characteristic shear stress is required for slip. Consider the crystal in figure (13 b) which is being deformed in tension by an applied force F along the axis of the cylindrical crystal. On the cross-sectional area is A the tensile stress component parallel to F is $\sigma = \frac{F}{A}$. The force has a component $F\cos\lambda^g$ in the slip direction $\mathbf{m}^g$, where λ^g is the angle between F and the slip direction. This force acts over the slip surface which has an area $\frac{A}{\cos\phi^g}$, where ϕ^g is the angle between F and the normal $\mathbf{n}^g$ to the slip. Thus, the dislocation motion on the glide planes is driven by the Resolved Shear Stress[4] (RSS) τ^g acting on system g, i.e. on the slip

---

[4]The symbol τ will be used to denote the resolved shear stress in this way throughout this thesis.

No.	S-B	$\mathbf{n}^g$	$\mathbf{m}^g$
1	A2	$(\bar{1}11)$	$[0\bar{1}1]$
2	A3	↑	$[101]$
3	A6	↑	$[110]$
4	B2	$(\bar{1}1\bar{1})$	$[0\bar{1}1]$
5	B4	↑	$[\bar{1}01]$
6	B5	↑	$[\bar{1}10]$
7	C1	$(11\bar{1})$	$[011]$
8	C3	↑	$[101]$
9	C5	↑	$[\bar{1}10]$
10	D1	$(1\bar{1}1)$	$[011]$
11	D4	↑	$[\bar{1}01]$
12	D6	↑	$[110]$

(a)   (b)   (c)
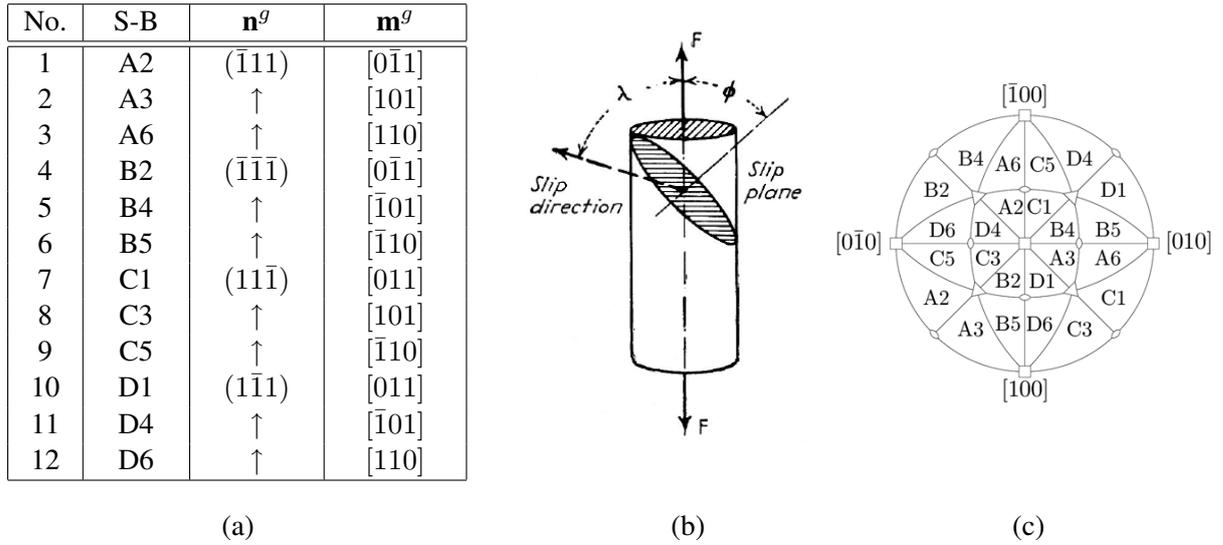
Figure 13 - (a) The 12 slip systems of a fcc crystals and their Schmid-Boas notation (S-B). (b) Resolved shear stress in an uniaxial tension test [JIL50]. (c) Standard stereographic projection showing the respective slip systems most favourably oriented in a tension test.

plane $\mathbf{n}^g$ in the slip direction $\mathbf{m}^g$, given by

$$\tau^g = \mathbf{m}^g.\boldsymbol{\sigma}.\mathbf{n}^g = \frac{F}{A}\cos\phi^g\,\cos\lambda^g \tag{1.7}$$

If $\hat{F}$ is the tensile force required to start slip, plastic yield is defined with the slip resistance $\hat{\tau}^g$:

$$\tau^g = \hat{\tau}^g \tag{1.8}$$

The specific form of equation (1.8) at the initial yield point $\hat{\tau}_0^g$ is usually referred to as Schmid's law and analogously the RSS τ^g to as Schmid stress. However, the $\hat{\tau}^g$ change significantly, especially for fcc crystals, with ongoing plastic deformation leading generally to a hardening response (see section 1.2.4.2).

According to equations (1.7) and (1.8), slip will start on the slip system(s) with the highest Schmid factor(s), i.e. $S^g = \cos\phi^g\cos\lambda^g \leqslant 0.5$. If, during a tension test, the stereographic projection of the tensile axis lies within one of the designated stereographic triangles in figure (13 c), the indicated slip system will be activated first since the RSS will have the highest value there. In the most complicated case, the [001] orientation, 4 slip planes with 2 slip directions in each are equally favoured. For bulk fcc crystals, this results in multislip and consequently in a strong interaction between the dislocations on the various systems leading to high work hardening rates.

1.2.3 Plasticity in dislocated crystals

1.2.3.1 The theory of elasticity with eigenstrains

"Eigenstrain"[5] is a generic name given to strains that would arise from thermal expansion, phase transformation, initial strains or plastic strain, if they would be unconstrained by a surrounding medium. The eigenstrain concept offers an approach for solving elasticity problems for a continuum with internal heterogeneities such as dislocations. A singularity in the displacement field along the dislocation line may be represented by an eigenstrain (i.e. a plastic strain) ε_{ij}^p which causes internal stresses in solids. Here the field equations for elasticity theory are recalled with particular reference to solving eigenstrain

---

[5]Sometimes also called "stress-free strain".

problems. These problems consist of finding displacement u_i, strain ε_{ij}, and stress σ_{ij} at an arbitrary point $\boldsymbol{x}$ (x_i) caused by the distribution of eigenstrains. For infinitesimal deformations the total strain ε_{ij} is regarded as the sum of elastic ε_{ij}^e and plastic strain ε_{ij}^p:

$$\varepsilon_{ij} = \varepsilon_{ij}^e + \varepsilon_{ij}^p \tag{1.9}$$

The total strain must be compatible, i.e.

$$\varepsilon_{ij} = \frac{1}{2}\left(u_{i,j} + u_{j,i}\right) \tag{1.10}$$

where the displacement gradient $u_{i,j} = \frac{\partial u_i}{\partial x_j}$, and the elastic strain is related to stress σ_{ij} by Hooke's law

$$\sigma_{ij} = C_{ijkl}\varepsilon_{kl}^e = C_{ijkl}\left(\varepsilon_{kl} - \varepsilon_{kl}^p\right) \tag{1.11}$$

with C_{ijkl} the fourth-order tensor of elasticity, and repeated indices are summed implicitly.

1.2.3.2 Lattice dislocation density tensor

According to Kröner [KRO58], the displacement $u_{i,j}$ (e.g. total distortion β_{ji}) is assumed to consist of elastic distortion β_{ji}^e and plastic distortion β_{ji}^p:

$$u_{i,j} = \beta_{ji} = \beta_{ji}^e + \beta_{ji}^p \tag{1.12}$$

The elastic strain ε_{ij}^e, and the eigenstrain ε_{ij}^p defined in equation (1.9) are given by

$$\varepsilon_{ij}^e = \frac{1}{2}\left(\beta_{ij}^e + \beta_{ji}^e\right) \tag{1.13}$$

$$\varepsilon_{ij}^p = \frac{1}{2}\left(\beta_{ij}^p + \beta_{ji}^p\right) \tag{1.14}$$

In the case of dislocations, because the plastic distortion β_{ji}^p is caused by the slip b_i (component i of $\mathbf{b}$) of plane $\boldsymbol{S}$ normal to the vector $\mathbf{n}$ (with components n_j), the plastic distortion is defined by [MUR87]

$$\beta_{ji}^p\left(\boldsymbol{x}\right) = -b_i n_j \delta\left(\boldsymbol{S} - \boldsymbol{x}\right) \tag{1.15}$$

where $\delta\left(\boldsymbol{S} - \boldsymbol{x}\right)$ is one-dimensional Dirac delta function in the normal direction of $\boldsymbol{S}$, being unbounded when $\boldsymbol{x}$ is on $\boldsymbol{S}$ and zero otherwise.
Note that Volterra considered two types of defects: one is translational and the other one is rotational [VOL07]. The translational defect is the dislocation defined above and the rotational defect is called disclination[6].
Using properties of Green's functions and equation (1.12) the dislocation density tensor α_{si} is introduced

$$\alpha_{si} = -\epsilon_{saj}\beta_{ji,a}^p \tag{1.16}$$

where ϵ_{saj} is the (Levi-Civita) permutation tensor[7]. The tensor α_{si} is called Nye's dislocation density tensor [NYE53], and equation (1.16) states that the dislocation density can be represented in terms of the plastic distortion β_{ji}^p expressed by equation (1.15).
The pure straight edge dislocation in figure (12 a), where the plastic strain ε_{21}^p is caused by the relative

---

[6]Disclinations have not been taken into account in this thesis.
[7]By definition, $\epsilon_{saj} = e_s.\left(e_a \times e_j\right)$.

$\boldsymbol{b}\,(b_1, b_2, b_3) = (b_1, 0, 0)$ on the half plane $(x_2 = 0,\, x_1 < 0)$ in the x_1-direction, is prescribed by

$$\varepsilon_{21}^p\,(\boldsymbol{x}) = \frac{1}{2}b_1\delta(x_2)H(-x_1) \tag{1.17}$$

where $H(x_1)$ is the Heaviside step function

$$H\,(x_1) = \begin{cases} 1 & \text{if } x_1 > 0 \\ 0 & \text{if } x_1 < 0 \end{cases} \tag{1.18}$$

and $\delta(x_2)$ is Dirac's delta function[8]. Other components of $\varepsilon_{ij}^p\,(\boldsymbol{x})$ are zero. An isolated dislocation line is a special case when the dislocation density tensor takes form of Dirac's delta function, and the same edge dislocation line is expressed (through the equation 1.16) by

$$\beta_{21}^p = b_1\delta(x_2)H(-x_1) \tag{1.19}$$
$$\alpha_{31} = b_1\delta(x_1)\delta(x_2) \tag{1.20}$$

The expression of the dislocation density tensor α_{si} is expressed here for an individual single dislocation. It can also be written for the case of continuously distributed dislocations where β_{ji}^p and α_{si} are spatial functions. This point will be discussed in section 3.1.2.3.

It can be worth noting that the transition from the real microscopic mechanisms of deformation to a macroscopic material model for plastic behaviour generally poses a problem. A quantification of dislocation density through equation (1.16) becomes overwhelming given the densities involved in plastic deformation processes, with $\rho \approx 10^{16}$ m^{-2}. That is why most models that are currently used to describe the plastic behaviour are phenomenological and averaged by nature.

For application to bulk materials, for instance metal forming processes, several phenomenological continuum models have been successful for many years. Other examples include the modelling of complex material behaviours such as creep [MAC01] [PRE09] or shape memory effects [HEL03]. The next section introduces two different types of these models.

1.2.4 Classical modelling of plasticity

1.2.4.1 Continuum framework for plastic strain due to dislocation glide

The constitutive equation of the material is an essential ingredient of any structural calculation. It provides the indispensable relation between the strains and the stresses, which is a linear relation in the case of elastic analyses and much more complex nonlinear relation in inelastic analyses, involving time and additional internal variables.

In this section, only the conventional continuum approach is considered, i.e. that the Representative Volume Element (RVE) of material is considered as subject to a uniform macroscopic stress. This continuum assumption is equivalent to neglecting the local heterogeneity of the stresses and strains within the RVE, working with averaged quantities, as the effects of the heterogeneities act only indirectly through a certain number of internal variables. Moreover, the local state assumption of continuum thermomechanics considers that the state of a material point is independent of that of the neighbouring material point. Therefore the stress or strain gradients do not enter into the constitutive equations.

The general context of modelling the inelastic behaviour in rate-independent plasticity or in viscoplasticity is supposed to be known, as being sufficiently standard. The interested reader should refer to more complete specialised works [LEM85] [FRA91] [KHA95] [KRA96].

The relationship between the rate of plastic distortion $\dot{\beta}^p$ and dislocation glide involves an averaging procedure over a material volume in which a large number of dislocations are moving as shown by Rice [RIC70]. In the case of pure glide in crystals, the rate of plastic deformation $\dot{\varepsilon}^p$ and plastic distortion $\dot{\beta}^p$

---

[8]By definition, $\delta(x_2) = +\infty$ if $x = 0$ and $\delta(x_2) = 0$ otherwise.

can be written in the form:

$$\dot{\boldsymbol{\varepsilon}}^p = \frac{1}{2} \sum_g \left(\mathbf{n}^g \otimes \mathbf{m}^g + \mathbf{m}^g \otimes \mathbf{n}^g \right) \dot{\gamma}^g \tag{1.21}$$

$$\dot{\boldsymbol{\beta}}^p = \sum_g \left(\mathbf{n}^g \otimes \mathbf{m}^g \right) \dot{\gamma}^g \tag{1.22}$$

where $\dot{\gamma}^g = \frac{\partial \gamma^g}{\partial t}$ is the rate of plastic slip on the slip plane g, $\otimes$ represents the dyadic product of two vectors[9], and $\frac{1}{2} \left(\mathbf{n}^g \otimes \mathbf{m}^g + \mathbf{m}^g \otimes \mathbf{n}^g \right)$ is known as the symmetric Schmid tensor.

The plastic flow rate is related directly to dislocation velocity, which can be visualised by considering a section of material of height h as shown in figure (11). According to the simple visualisation of a pure edge dislocation in figure (11), when the dislocation reaches the crystal boundary, its glide produces a shear strain γ given by

$$\gamma = \frac{b}{h} \tag{1.23}$$

When the dislocation line of length l moves a distance $\mathrm{d}x$ in a direction normal to the line direction, it sweeps an area $l\mathrm{d}x$ and produces a shear strain

$$\mathrm{d}\gamma = \frac{b\,l}{V} \mathrm{d}x \tag{1.24}$$

The value l can be replaced by the quantity $(n\,l)$, where n is the number of mobile dislocation in the volume of the crystal V. Expression (1.24) can then be rewritten as

$$\mathrm{d}\gamma = \frac{b\,n\,l}{V} \mathrm{d}\bar{x} \tag{1.25}$$

where $\bar{x}$ is the average propagation distance. By differentiation with respect to time, the shear strain rate $\dot{\gamma}$ is then obtained by the Orowan relation

$$\dot{\gamma} = b\rho_m \bar{v} \tag{1.26}$$

with $\rho_m = \frac{n\,l}{V}$ the mobile dislocation density, and $\bar{v} = \dot{\bar{x}}$ the average dislocation velocity.

1.2.4.2 Dislocation density-based models

The classical continuum slip theory of crystals is based on physical concepts. The plastic flow arises from the movement of dislocations on crystallographic planes [TEO70] [TEO75] [ASA83]. The presence of dislocations is not modelled in an explicit manner, but their combined action enters the model phenomenologically through the constitutive equations that govern the evolution of crystallographic slip and the slip resistance.

The present dislocation density-based approach for modelling the viscoplastic bahavior of crystalline materials, which goes back to Kocks and Mecking [KOC75] [KOC76], has proved capable of providing a description of the mechanical response of metallic materials to unidirectional loading, and beyond that, to ensure a very good predictive capability of the constitutive equations [KUB08].

In this section, a crystal plasticity model for which the dislocation densities on the different slip systems are the internal variables is presented. Three equations (i.e. equations 1.29, 1.31, and 1.33) are needed to relate the stress to the plastic strain, where each relation is derived from physical considerations of dislocation motion.

---

[9]By definition, $(a \otimes b)_{ij} = a_i b_j$.

Plastic slip rate

Assuming that lattice friction is low and that the dislocation motion is governed by the interactions with obstacles (as usually admitted for fcc crystals), these dislocation interactions can be classified into two categories: interaction with (i) obstacles with long-range stresses $\hat{\tau}$ like for example other dislocations, and (ii) obstacles inducing a short-range stress field, written as τ^*, like impurities. Note that $\hat{\tau}$ does not depend on temperature whereas τ^* is thermally activated [TEO75].

When considering only isotropic hardening, the athermal stress $\hat{\tau}$ fluctuates around zero with a large average wavelength. When a dislocation meets a short-range obstacle a few atomic distances away, it needs an additional stress τ^* to pass it. For each slip system g, the RSS needed for the dislocation motion is then $\tau^g = \hat{\tau}^g + \tau^{*\,g}$.

When the average time for the movement of a dislocation between obstacles is negligible in comparison to the waiting time in front of the obstacle, the following expression for the dislocation velocity v can be written as [TEO75]

$$v = b v_D \exp\left(\frac{\Delta G_0}{kT}\right) 2\sinh\left(\frac{\tau^* \Delta V^*}{kT}\right) \tag{1.27}$$

where v_D is the Debye frequency, ΔG_0 and ΔV^* are the activation energy and activation volume, respectively.

Averaging the velocities separately for each slip system g is achieved using the Orowan equation (1.26):

$$\dot{\gamma}^g = b \rho_m^g \bar{v}^g \tag{1.28}$$

which is considered to be key link between discrete dislocation mechanics and the continuum slip theory of crystal plasticity.

When τ^* is moderate (less than 70% of its value at 0 K [TEO75]), the $\sinh$ in equation (1.27) is replaced by its negative exponential part. Replacing $\tau^{*\,g}$ by $\hat{\tau}^g - \tau^g$, the first order approximation in terms of $\frac{\tau^{*\,g}}{\hat{\tau}^g}$ finally gives [RAU93]

$$\dot{\gamma}^g = \rho_m^g b^2 v_D \exp\left(\frac{-\Delta G_0}{kT}\right) \left(\frac{\tau^g}{\hat{\tau}^g}\right)^{\frac{\hat{\tau}^g \Delta V^*}{kT}} = \dot{\gamma}_0^g \left(\frac{|\tau^g|}{\hat{\tau}^g}\right)^{\frac{1}{m}} \operatorname{sign}(\tau^g) \tag{1.29}$$

Equation (1.29) is the flow law written in the classic form of a power relationship between strain rate and normalised stress[10] [HUT76] [PIE82]. Here $\dot{\gamma}_0$ and m are material parameters representing a reference plastic strain rate and the rate sensitivity exponent, respectively. They have been established from an average performed over all the mobile dislocations within a given slip system so that the three macroscopic variables $\tau^{*\,g}$, ΔG_0, and ΔV^* are physically justified.

The dislocation motion on the glide planes is driven by the respective RSS given by equation (1.7), since the internal variable $\hat{\tau}^g$ can be regarded as the slip resistance on system g.

Work hardening

Any obstacle which hinders consecutive dislocation movement will block further plastic deformation unless the RSS is increased. This process, by which the strength of the metal increases as it deforms, is referred to as work hardening. The following considerations will be restricted to dislocation hardening, where the obstacles which impede the motion of a dislocation are provided by other dislocations piercing the active slip plane, the forest dislocations.

The earliest work hardening theory based on the idea that the strengthening results from mutual dislocation interactions was introduced in the form of the Taylor relation [TAY34]. The Taylor relation implies

---

[10]Here, equation (1.29) does not mention the notion of kinematic hardening or back-stress/long-range internal stresses induced by polarised dislocation density distributions.

	A2	A3	A6	B2	B4	B5	C1	C3	C5	D1	D4	D6
A2	a_0	a_1	a_1	a_3	a_4	a_4	a_2	a_4	a_5	a_2	a_5	a_4
A3		a_0	a_1	a_4	a_2	a_5	a_4	a_3	a_4	a_5	a_2	a_4
A6			a_0	a_4	a_5	a_2	a_5	a_4	a_2	a_4	a_4	a_3
B2				a_0	a_1	a_1	a_2	a_5	a_4	a_2	a_4	a_5
B4					a_0	a_1	a_5	a_2	a_4	a_4	a_3	a_4
B5						a_0	a_4	a_4	a_3	a_5	a_4	a_2
C1							a_0	a_1	a_1	a_3	a_4	a_4
C3			symmetric					a_0	a_1	a_4	a_2	a_5
C5									a_0	a_4	a_5	a_2
D1										a_0	a_1	a_1
D4											a_0	a_1
D6												a_0

Table 1.2: Latent hardening in single crystals: specification of the interaction matrix a^{gr} in terms of the self interaction coefficient a_0 and the strength coefficients $a_1 \mapsto a_5$ for fcc crystals with Schmid type behaviour.

that the resolved flow stress $\hat{\tau}$ is proportional to the square root of a dislocation density ρ, which is assimilated to either the total density or the density of forest dislocations:

$$\hat{\tau} = \alpha \mu b \sqrt{\rho} \qquad (1.30)$$

In equation (1.30), $\alpha = 0.35 \pm 0.15$ in fcc metals [GIL93a] [MAD02]. To account for the anisotropy of interactions between slip systems, equation (1.30) is commonly expanded in the form [FRA80]

$$\hat{\tau}^g = \mu b \sqrt{\sum_r a^{gr} \rho^r} \qquad (1.31)$$

where $\hat{\tau}^g$ is now the critical stress for the activation of slip system g, and is determined by dislocation densities in all slip systems r including g itself. This means that the scalar constant α is now replaced by a matrix of coefficients a^{gr} such that $\sqrt{a^{gr}}$ represents the interaction strength between the two slip systems g and r.

In a fcc crystal, the interaction matrix a^{gr} has $12 \times 12 = 144$ coefficients (see table 1.2). The number of distinct coefficients is divided by two due the diagonal symmetry of the matrix (i.e. $a^{gr} = a^{rg}$) and the occurrence of four $\langle 111 \rangle$ axes with ternary symmetry further divides it by twelve. Hence, there are six independent coefficients, which are associated with six types of interactions. There are two non-contact interactions for dislocations gliding in parallel slip planes with the same or different Burgers vectors, the self-interaction (a_0) and the coplanar interaction (a_1). Three other coefficients account for forest interactions between non-coplanar slip systems, resulting in the formation of junctions or locks, namely the Hirth lock (a_2), glissile junction (a_4), and the Lomer-Cottrell lock (a_5). The last interaction, the collinear interaction (a_3), produces annihilations. It occurs between dislocations gliding in two slip planes that are cross-slip planes with respect to each other.

The values of interaction coefficients were recently determined using DD simulations for fcc [DEV06] and bcc crystals [MAD05] [QUE09b]. They incorporate the strengthening effect of both long- and short-range interactions between dislocations. Such coefficients are density-dependent and for instance in a fcc crystal at a reference dislocation density of 10^{12} m^{-2}:

$$a_2 = 0.06 \ < \ a_4 \approx a_0 = a_1 = a_5 = 0.12 \ < \ a_3 = 0.62 \qquad (1.32)$$

One may notice that four interaction strengths exhibit similar values, those for self, coplanar, glissile and Lomer interactions, while the Hirth type of interaction is slightly weaker and the collinear interaction substantially stronger.

Storage and recovery

For determining strain hardening, the key quantity is the rate at which the critical stress evolves with strain or, equivalently, the rate at which dislocations accumulate under strain. For this purpose, it is useful to define a dislocation mean free path L, which is the average distance traveled by a dislocation segment of length l immobilised by interaction with the microstructure. When the line moves a distance $\mathrm{d}x$ in a direction normal to the line direction, it produces a shear strain $\mathrm{d}\gamma = \frac{bl}{V}\mathrm{d}x$ (see equation 1.24). The stored density has then statistically increased by $\mathrm{d}\rho = \frac{l}{LV}\mathrm{d}x$, and the incremental storage rate is then given by $\frac{\mathrm{d}\rho}{\mathrm{d}\gamma} = \frac{1}{bL}$. This definition is only valid in differential form, because the dislocation line increases its line length (dislocation multiplication). Thus following the works of Kocks and Mecking [KOC76], and Teodosiu *et al.* [TEO93], the net stored rate in each slip system g results from dislocation storage and recovery and is written as

$$\dot{\rho}^g = \frac{1}{b}\left(\frac{1}{L^g} - y_c\rho^g\right)|\dot{\gamma}^g| = \frac{1}{b}\left(\underbrace{\frac{\sqrt{\sum_r a^{gr}\rho^r}}{K}}_{\text{Storage}} - \underbrace{y_c\rho^g}_{\text{Recovery}}\right)|\dot{\gamma}^g| \tag{1.33}$$

The last term at the right-hand side of equation (1.33), where y_c is proportional to the critical annihilation distance for screw dislocations, describes the effect of a mechanism called dynamic recovery [ESS79]. The mean free path L^g depends on dislocation interactions, stress, and specimen orientation [KUB09].

In summary, for each slip system g, the storage-recovery framework includes two major dislocation density-based equations: (i) a Taylor-like equation that relates the critical RSS on a slip system to the stored densities in all slip systems (see equation 1.31), and (ii) an equation for the net storage rate of dislocations per slip system (see equation 1.33), which is the sum of a positive storage rate governed by a dislocation mean free path and a negative term accounting for dynamic recovery. The set of equations is closed by a flow rule (see equation 1.29), which accounts for the strain rate sensitivity of the material. Note that these constitutive equations are only valid for monotonic loading since they do not account for any kinematic hardening. Several authors [HAR98] [DEP04] use the same framework with additional kinematic hardening variables to obtain a Bauschinger effect. These variables on each system are more or less phenomenological. For instance, Harder [HAR98] used a classical formulation of kinematic hardening proposed initially by Méric and Cailletaud [MER92].

This classical storage-recovery framework incorporating an additional internal length through the dislocation density tensor in equation (1.33) will be used to predict the mechanical properties of γ/γ' superalloys in section 3.1.

1.2.4.3 Viscoplastic constitutive theories

This section deals with phenomenological viscoplastic theories. The formalism used is that of the thermodynamics of irreversible processes, guided by the phenomenological constitutive laws with isotropic and kinematic hardening for small strains.

The main equations are given by the formulation of ε^p in a viscoplastic form and the yield function f expressed for isothermal conditions as

$$\dot{\varepsilon}^p = \frac{\partial\Omega}{\partial\boldsymbol{\sigma}} \tag{1.34}$$

$$f = \|\boldsymbol{\sigma} - \mathbf{X}\|_H - k - R \leqslant 0 \tag{1.35}$$

Here Ω represents the viscoplastic potential and the parameter k is the initial size of yield surface. Moreover, strain hardening is described by the combination of isotropic hardening and kinematic hardening. The increase of the size of the yield surface R is referred to isotropic hardening, and the back-stress $\mathbf{X}$ is the thermodynamic force associated to kinematic hardening. Figure (14) illustrates, in the deviatoric stress plane and in the particular case of uniaxial tension-compression, the transformation of the elastic domain and yield surface by the two particular cases of pure linear isotropic hardening (figure 14 a) and pure linear kinematic hardening (figure 14 b).

(a) (b)
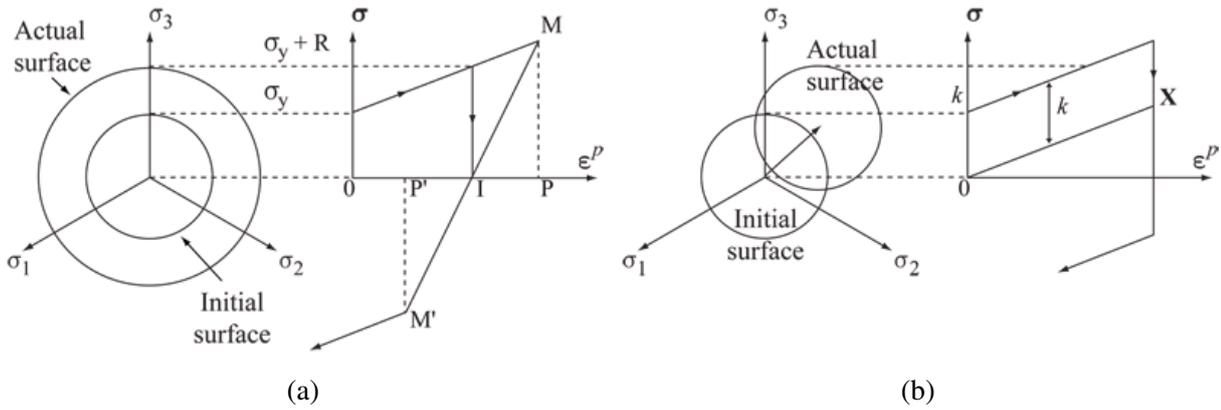
Figure 14 - (a) Isotropic hardening in the deviatoric plane, and the associated stress-strain response. (b) Linear kinematic hardening in the deviatoric plane, and the associated stress-strain response.

In what follows the associated framework is assumed and the normality law (1.34) expresses the consequence of the maximum dissipation principle. For rate-independent plasticity, the use of an elastic domain is needed, i.e. $f \leqslant 0$, as given by equation (1.35). The yield surface $f = 0$ is defined with Hill's criterion, using a fourth rank tensor $\overline{\overline{\mathbf{H}}}$ with a quadratic norm, defined as

$$\|\boldsymbol{\sigma}\|_H = \sqrt{\boldsymbol{\sigma} : \overline{\overline{\mathbf{H}}} : \boldsymbol{\sigma}} \qquad (1.36)$$

where the symbol ":" designates a double contraction. In case of a viscoplastic behaviour (or rate dependency), this is generalised by using a viscoplastic potential $\Omega(f)$. A form often used for the viscoplastic potential Ω is

$$\Omega = \frac{V}{n+1} \left\langle \frac{f}{V} \right\rangle^{n+1} \qquad (1.37)$$

with V and n two parameters characterizing the viscous state of material, and depending on the temperature. The relation between the viscous stress and the viscoplastic strain rate norm defined by $\dot{p} = \|\dot{\boldsymbol{\varepsilon}}^p\|_{H^{-1}}$ with p the length of the plastic strain path then becomes

$$\dot{p} = \left\langle \frac{f}{V} \right\rangle^{n} \qquad (1.38)$$

The Mac Cauley brackets[11] $\langle\ \rangle$ are used to ensure that when $f < 0$, i.e. inside the elastic domain, $\dot{p}$ cancels out continuously. This expression (1.38) corresponds to Norton's law where the exponent n and the parameter of drag stress V depends on the material, on the strain rate domain considered, and on the temperature. Usually $3 \leqslant n \leqslant 30$.

When the expression for the norm of the strain rate (1.38) is considered, by replacing f with equation

---

[11]By definition, $\langle x \rangle = x$ if $x \geqslant 0$ and $\langle x \rangle = 0$ otherwise.

(1.35), it is found:

$$\dot{p} = \left\langle \frac{\|\boldsymbol{\sigma} - \mathbf{X}\|_H - k - R}{V} \right\rangle^n \tag{1.39}$$

Isotropic hardening describes generally the expansion of the yield surface with respect to the cumulative plastic flow, for instance by a law of type:

$$\dot{R}(p) = b\left(Q - R\right)\dot{p} \tag{1.40}$$

with b and Q two coefficients depending on the material and on the temperature. The integration of (1.40) for uniaxial loading leads to $R\left(p\right) = Q\left(1 - \exp^{-bp}\right)$.

The simplest model of kinematic hardening is Prager's linear kinematic hardening [PRA49] in which the evolution of the kinematic variable $\mathbf{X}$ (called back-stress) is collinear with the evolution of the plastic strain. A better description is given by Armstong *et al.* [ARM66] introducing a recall term, called dynamic recovery:

$$\dot{\mathbf{X}} = C\dot{\boldsymbol{\varepsilon}}^{\mathrm{p}} - D\mathbf{X}\dot{p} \tag{1.41}$$

where C and D are two material parameters.

Both expressions (1.40) and (1.41) can also be written at the level of each slip system g. The non-linear evolution rule for isotropic hardening involves an interaction matrix[12] h^{gr} which represents self-hardening (diagonal terms) and latent hardening (non diagonal terms):

$$R^g = R_0^g + Q^g \sum_r h^{gr} \left(1 - \exp^{-qp^r}\right) \tag{1.42}$$

where R_0^g denotes the initial value of R^g and q is an isotropic hardening parameter. In addition, the scalar non-linear kinematic hardening rule is given by

$$\dot{X}^g = C\dot{\gamma}^g - DX^g|\dot{\gamma}^g| \tag{1.43}$$

The model is completely defined by the knowledge of plastic deformation defined by equation (1.21):

$$\dot{\gamma}^g = \left\langle \frac{|\tau^g - X^g| - R^g}{V} \right\rangle^n \mathrm{sign}\left(\tau^s - X^g\right) \tag{1.44}$$

Finally, the parameters to be determined for a given material and a given temperature are V and n for the viscosity, R_0, Q, q and the interaction matrix h^{gr} for the isotropic hardening, and C and D for the kinematic hardening. Application to superalloys can be found in [CAI87] [HAN91] [MER92] [MAR06].

Both models introduced in sections 1.2.4.2 and 1.2.4.3 have been successfully applied to the describe complex deformation curves in copper [TAB97] [DEV08] or stress-strain behaviour during cyclic loading in superalloys [CAI87] [HAN91]. Currently, one challenge is to link and justify the parameters of the phenomenological model with physical quantities of the dislocation density-based model. Some of the links between these models, based on an initial work of Chaboche, is illustrated in Appendix A.

It must be noted that initiation and progression of slip may be influenced by many factors such as crystal orientation, grain size, or precipitates. Dislocation structures and other dislocation distributions prior to mechanical deformation affect the response significantly and exhibit size effects. Unfortunately, due to their length scale-independent framework, the above models cannot capture these effects. In order to reproduce size effects, current approaches of crystal plasticity need to include a so-called characteristic length. Two approaches exist: the first group corresponds to discrete theories, which are capable of re-

---

[12]This matrix is playing an analogous role to the matrix interaction defined in table (1.2).

producing the deformation mechanisms introduced in section 1.1.2. In contrast, for the second group, i.e. the continuum approaches, where these mechanisms are the main statements of the modelling.

1.2.5 Small-scale crystal plasticity

1.2.5.1 Discrete theories of plasticity

The term "discrete theories" is used here as a generic term for all the models describing individual dislocations or even atoms and their mutual interactions.

Atomistic simulations

Atomistic simulations can provide an understanding of the elementary dislocation properties and dislocation core structures. Currently, atomistic simulations are restricted to about 10^8 atoms, depending on the numerical approximations chosen for the atomic interactions. The biggest problem is the constraint that the time step for the integration of the equation of motion is $\Delta t \backsim 10^{-15}$ s, thus requiring 10^6 time steps for the simulation of 1 ns. Hence, plastic deformation problems cannot be directly addressed with such a numerical approach. Nevertheless, they are critically needed in many material problems where dislocation core properties are poorly known.

Discrete dislocation dynamics

Based on the elastic theory of dislocations, numerical DD methods have been developed first in 2D. The orientation of the reference plane used in 2D simulations is either (i) parallel or (ii) perpendicular to the dislocation lines. In case (i), the plane of the simulations is parallel to the glide plane of dislocation lines, thus neither cross-slip nor climb of dislocations are allowed. Initially this configuration has been applied to study line tension problems and the shape of a dislocation under stress [BRO64] [FOR67] (see figure 15 a and b). In case (ii), dislocations are perpendicular to the simulation plane, that is, dislocations are infinitely long, straight and parallel with the same character. This geometry allows simulating the multiplication, annihilation, cross-slip and climb of dislocations. It is, however, difficult to include the effect explicitly. This kind of simulations has been mostly used to simulate spontaneous microstructure formation [LEP87].

To incorporate line tension, junction formation and multiplication or nucleation mechanisms in 2D DD simulations, Gómez-García *et al*. [GOM00] and later Benzerga *et al*. [BEN04], proposed an extension to the constitutive rules of Van der Giessen and Needleman [VAN95]. This so-called 2.5DD model intends to capture 3D effects in a 2D framework [GOM06]. This model is still largely under development and applied to several studies [LEF06] [GUR08].

The first simulation in 3D is proposed by Kubin and Canova [KUB90a] [CAN91]. Since then, the proposed method has been further developed and applied to investigate the collective motion of dislocations under various conditions. The motivation of a 3D DD has been to include the tridimensional nature of the dislocation behaviour (interactions, cross-slip, junction formation. . .). Due to the development of simulation methods and the increased computing power, these simulation methods have strengthened their positions in the field of crystal plasticity. The study of strain hardening and pattern formation in this framework was pioneered by Kubin *et al*. [KUB90]. More recent examples are the Bauschinger effect in dispersion-strengthened materials [SHI06] [QUE09a] (see figure 15 c), or the effect of grain size of ultrafine-grained polycrystals [DeS10]. Typical simulations are based on roughly 10^4 dislocation segments.

In the last decade, the 3D DD simulations have been coupled with the FE method in order to compute boundary value problems [FIV99] [LEM01]. Such hybrid models will be introduced in section 2.

In view of the computational complexity of DD simulations, repeated attempts have been made to ar-

(a)   (b)   (c)
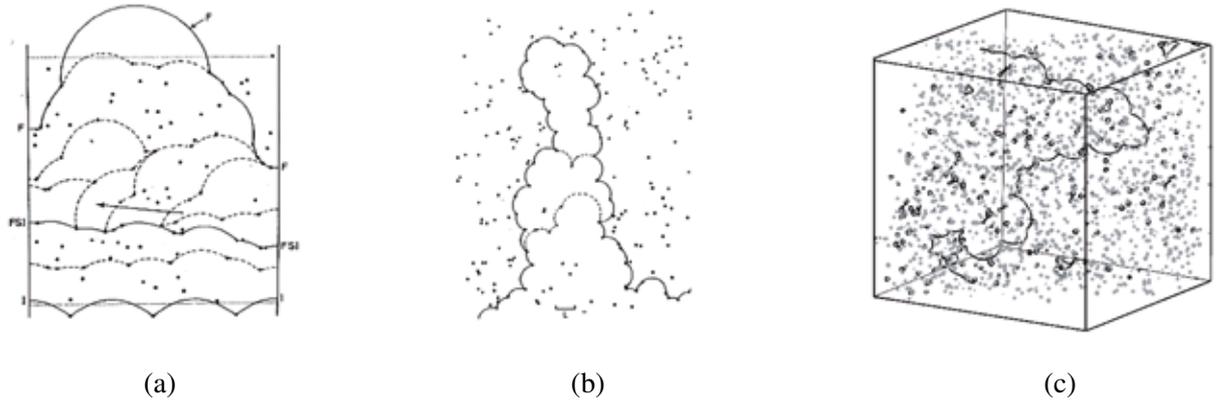
Figure 15 - 2D simulations of dislocations moving through a random array of point obstacles: effects of (a) weak and (b) hard obstacles' strength [FOR67]. (c) 3D simulations of dislocations moving through a random array of impenetrable spherical particles with periodic boundary conditions. Snapshot of a thin foil region of 1.5 μm in the [321] direction [QUE09a].

rive at some kind of coarse-grained description of dislocation dynamics in an average sense. This is the subject of the next section.

1.2.5.2   Continuum theories with internal length

The length scales mentioned previously are physically defined in the sense that they have been introduced by nature (grain size, dislocation spacing . . .). On the continuum level, conventional theories of plasticity do not contain any intrinsic length, which means that predictions of the mechanical stress-strain response of specimens whose dimensions only differ by a constant factor would coincide. This is however not consistent with experimental results observed for specimens with dimensions at the micron scale, such as for the nano-indenter load of ductile metals [LIM99], the shear test of a polycrystal [FLE94], or the precipitate size effects on the mechanical behaviour for γ/γ' superalloys [DUH87]. Hence, modelling plastic deformation at small-scale requires the introduction of a length scale within the continuum models.

Generalised continua

Generalised continua, also called continua with microstructure, are characterised by having more degrees of freedom than the classical continuum. These additional degrees of freedom can be employed to describe the microstructure of a material. The most familiar among the generalised continua are the micromorphic medium of Mindlin and Eringen [MIN64] [ERI64] and the Cosserat medium, developed by the Cosserat brothers almost 100 years ago [COS09]. The latter extends the classical continuum by additional rotational degrees of freedom Φ_k. The Cosserat microrotation R_{ij} relates the current state of a triad of orthonormal directors attached to each material point to the initial one:

$$R_{ij} = \delta_{ij} - \epsilon_{ijk}\Phi_k \tag{1.45}$$

where δ_{ij} is Kronecker's symbol[13]. The deformation measures of the Cosserat theory are the relative deformation tensor ε_{ij} and the torsion-curvature tensor κ_{ij}:

$$\varepsilon_{ij} = u_{i,j} + \epsilon_{ijk}\Phi_k \tag{1.46}$$

$$\kappa_{ij} = \Phi_{i,j} \tag{1.47}$$

---

[13] $\delta_{ij} = 1$ if $i = j$, and zero otherwise.

The resolution of a boundary value problem requires constitutive relations which include the deformation and torsion-curvature tensors. Recently it has been revisited by several authors to model special material classes, for example liquid crystals, granular media, cellular solids or dislocated crystals [FOR01] [FLO04].

Cosserat media account for the influence of the dislocation density tensor defined by $\alpha_{ij} = \kappa_{ij} - \kappa_{mm}\delta_{ij}$ for the hardening behaviour of metals, which provides an efficient way to model size effects in crystals [FOR00] [FOR03]. Unfortunately, a quantitative correspondence between the values of the characteristic lengths in generalised continuum models and the actual material state is difficult to establish [FOR03]. A review of generalised continuum crystal plasticity models can be found in [FOR06].

Strain-gradient models

The geometrically necessary dislocations, which will be introduced in detail in section 3.1.2.2, are the result of gradients of the plastic shear [NYE53] through the following expression[14]:

$$\alpha_{si} = -\epsilon_{saj}\beta_{ji,a}^{p} = -\epsilon_{saj}\sum_{g}\gamma_{,a}^{g}n_{j}^{g}m_{i}^{g} \tag{1.48}$$

One possible way to bring size effects into the constitutive laws is therefore to postulate that the hardening depends on both plastic strain and plastic strain-gradient. These models are designed to account for the size effects arising from gradients of plastic strain. This is the foundation of the so-called strain-gradient or second gradient models [MIN68]. Various models exist and they differ strongly in origin and mathematical structure. The material length scale that enters these models determines the impact made by geometrically necessary dislocations: the smaller the length scale, the more important the strain-gradient effects become [AIF87] [ACH00] [GUR00].

A strain gradient theory based on classical plasticity theories was formulated and generalised by Aifantis [AIF87] [AIF99]. The derivation of this model is not directly related to the dislocation density tensor or to the concept of geometrically necessary dislocations, but is rather based on a model of reaction-diffusion type for the dislocation evolution. The form of the strain gradient plasticity theory involves only one extra coefficient incorporating the effect of the Laplacian of the effective shear strain into the constitutive expression for the flow stress.

Most of the current theories rely on the fundamental work of Fleck *et al.* [FLE01] who developed a strain-gradient-based constitutive law including the plastic strain gradient. This approach can also be categorised in the group of generalised continua [FOR06].

Strain-gradient models can for instance successfully describe size effects, the finite width of shear bands and also crack-tip plasticity. An open problem of these models is the choice of internal length scales and of higher order boundary conditions, which currently lack physical justification. Rather, those quantities are used as fitting parameters to achieve a good representation of experimental results.

Mesoscale Field Dislocation Mechanics

Acharya [ACH01] proposed a field dislocation model for the elastic-plastic response of mesoscopic single crystals based on the continuum mechanics of continuously distributed dislocations. The model, which has been further developed and generalised for finite deformations [ACH04], incorporates the elastic theory of dislocations through the fundamental transport law of excess dislocation density α_{si} and internal stress explicitly:

$$\dot{\alpha}_{si} = -\epsilon_{saj}\dot{\beta}_{ji,a}^{p} \tag{1.49}$$

---

[14]This expression of the dislocation density tensor α_{si} is similar to equation (1.16), but written for the case of a continuous distribution of dislocation. Here, α_{si} is not a dirac-delta function but a spatial gradient of plastic deformation.

Dislocations are not described as lines or inherently considered by some evolution law for plastic slip, but rather, the dislocation density is defined as field variable constitutively specified by equation:

$$\dot{\beta}_{ij}^p = \epsilon_{jkl}\alpha_{ik} \times V_l + L_{ij}^p \tag{1.50}$$

In the latter equation, the field V_l stands for the average velocity of dislocations and L_{ij}^p is the distortion rate usually used in conventional crystal plasticity (defined for instance by equation 1.22). The relation (1.50) is interpreted as a tensorial Orowan relation.

A system of partial differential equations is therefore established which characterises the mechanical balance between the elastic stress field related to the presence of dislocations and the stress field due to the boundary conditions imposed on the considered body.

The mathematical structure of this kind of models allows for a FE implementation of the model, which has been realised recently [ROY05] [VAR07]. The stress field driving the nucleation and motion of dislocations derives in the first place from the tractions and displacements imposed on the sample boundaries. The objective assigned to field dislocation theories is to account for the emergence of inhomogeneous dislocation distributions at some mesoscopic (intermediate) length scale, as well as their consequences on the mechanical response. Field dislocation theories have successfully been applied to investigate the effects of sample size (e.g. torsion of single crystals of ice [TAU07a]) or the intermittency of plasticity in single crystals [TAU07b] [FRE09].

Statistical theories

Inspired by the statistical approach to DD originally developed by Kröner [KRO58], a number of statistically based descriptions of dislocation fields have been proposed recently. Within such approaches the RSS τ is replaced by $\tau - \tau_b$, where τ_b is a back-stress that is related to the gradient of the geometrically necessary dislocation density. As a simple extension of equation (1.29), a gradient-enhanced model is rewritten in single slip form as[15]

$$\dot{\gamma} = \dot{\gamma}_0 \left(\frac{|\tau - \tau_b|}{\hat{\tau}}\right)^{\frac{1}{m}} \text{sign}\left(\tau - \tau_b\right) \tag{1.51}$$

Equation (1.51) is very simple and may be useful for understanding fundamental effects of the introduction of scale dependency into conventional theories.

Using averaging procedures adopted from the statistical mechanics of interacting many-particle systems, Groma *et al.* [GRO97] [GRO03] developed a statistical continuum description of the collective behaviour of discrete straight parallel edge dislocations. The dislocations are restricted to their slip planes, and pierce perpendicularly to the simulation plane. Since their trace is only a point, they can be treated as point-like particles by applying the concepts of statistical mechanics. Starting from the equation of motion for a single dislocation, the continuum model is derived by means of statistical averaging, and is finally given in terms of dislocation correlation functions. This approach represents a continuous counterpart to the two-dimensional discrete DD simulations. In addition, it involves a set of coupled transport equations for the total dislocation density ρ and for the geometrically necessary dislocation density ρ_{GND}. The back-stress τ_b^{Groma} is then given by equation (1.52) with a drag coefficient D:

$$\tau_b^{\text{Groma}} = \frac{\mu b D}{2\pi(1-\nu)\rho}\nabla\rho_{\text{GND}} \tag{1.52}$$

The evaluation of the constant D was motivated by application of statistical averaging techniques to discrete DD simulations. A future task is to generalise the model to multiple slip arrangements, and the

---

[15]Models based on the difference $\tau - \tau_b$ have been used by Groma *et al* [GRO03], Kratochvíl *et al.* [KRA07], Zaiser and Hochrainer [ZAI06] and Sedláček [SED03]. However, the relation for $\dot{\gamma}$ adopted in these studies are different from each other, and are also different from equation (1.51).

first steps in this direction were already presented by Kratochvíl *et al.* [KRA07].

Recently, Zaiser *et al.* [ZAI06] [HOC06] considered a back-stress, in a similar form, for the general case of curved dislocations described in the configuration space of positions $\mathbf{x}$ and possible dislocation orientations θ. The gradient is evaluated in the direction $\boldsymbol{\nu}$ perpendicular to the dislocation line, denoted $\nabla_{\boldsymbol{\nu}}$, and the expression for the back-stress is:

$$\tau_b^{\text{Zaiser}} = \frac{\mu b D}{\rho} \int \nabla_{\boldsymbol{\nu}} \rho(\mathbf{x}, \theta) \mathrm{d}\theta \tag{1.53}$$

Based on a rigorous mathematical framework, the continuum dislocation-based model of Sedláček [SED03] introduced the line tension of dislocations and defined the back-stress as

$$\tau_b^{\text{Sedlacek}} = \frac{\mu b D}{2\pi(1-\nu)\rho} \nabla_{\boldsymbol{\nu}} \rho \tag{1.54}$$

The latter back-stress corresponds to equation (1.52), provided the current dislocation density ρ is chosen as the geometrically dislocation density ρ_{GND}. Up to now, it has been mostly applied to problems that can be formulated in one dimension.

These models aim at being both closer to physics than other phenomenological models. However, applying statistical methods turns out to be far more challenging for systems of curved dislocations.

El-Azab [AZA00] presented one of the first concepts for the description of general curved dislocations based on the methods of statistical mechanics. For each slip system a statistical measure is introduced, namely a distribution function ϕ in the phase space consisting of the actual location of the each dislocation segment, its velocity, and its orientation. However, the problems that go along with the fact that one has to consider connected dislocation lines rather than a system of unconnected dislocation segments have not been yet addressed, so that his approach did not yield results of practical interest so far.

1.2.6 Homogenisation methods based on mean-field approaches

All above theories, whether discrete (section 1.2.5.1) or continuous (section 1.2.5.2), are usually solved by using the FE method. For instance, atomistic [WAG03] or dislocation dynamics [LEM01] simulations are coupled with continuum mechanics in form of a FE code to provide boundary condition on the discrete simulations. In addition, continuum theories based on the Cosserat/Gradient-strain/Mesoscale Field Dislocation frameworks have been implemented in FE codes for two- or three-dimensional mechanical problems of a periodic cell [FOR00] [ROY05] [SCH07] [GUR07]. FE analysis of such theories is now a routine exercise that can be easily handled at the level of the RVE. However, in the context of structural analysis, the same approaches are not really feasable because of their computational cost, even though some numerical multiscale methods with two-level recursive FE, such as FE^2 have been applied in some particular situations [FEY00]. This is the reason why homogenisation methods based on mean-field approaches have been developed to be suitable for structural analysis.

Homogenisation methods have been available for a long time for non-linear materials. There are many different methods and tools that can be used to deliver the macroscopic constitutive response of heterogeneous materials from a local description of the microstructural behaviour. Here a framework called Transformation Field Analysis (TFA) is presented. Initially proposed by Dvorak [DVO92], TFA is based on the idea of a purely elastic redistribution of the macroscopic stress and strain, and the use of uniform local eigenstrains (i.e. plastic strains here). It can be used either with a low number of subdomains (subvolumes or subcells), typically one subdomain per actual phase, then recovering the context of Eshelby-type of approaches, or with a large number of subdomains, corresponding to some simplifications (or averagings) of the FE method.

Let us consider a representative volume V of a heterogeneous material, sufficiently large compared to the size of the inhomogeneities. V may be subdivided into several subdomains, such that each consists of a monophase material. The local constitutive relation in each subdomain K is written in the following

form:

$$\boldsymbol{\sigma}(\mathbf{x}) = \mathbf{C}_K : \left(\varepsilon(\mathbf{x}) - \varepsilon_K^p \right) \tag{1.55}$$

The plastic strain ε_K^p is uniform over the subdomain K, but other eigenstrains can obviously be added, and $\mathbf{C}_K$ is the elastic stiffness of the phase K (also assumed to be uniform in each subdomain). The macroscopic stress $\boldsymbol{\Sigma}$ and the macroscopic strain $\mathbf{E}$ are defined as the volume average of the local stress and strain fields:

$$\boldsymbol{\Sigma} = \langle \boldsymbol{\sigma} \rangle_V = \frac{1}{V} \int_V \boldsymbol{\sigma}(\mathbf{x}) \ \mathrm{d}V \tag{1.56}$$

$$\mathbf{E} = \langle \varepsilon \rangle_V = \frac{1}{V} \int_V \varepsilon(\mathbf{x}) \ \mathrm{d}V \tag{1.57}$$

and the averages for each subdomain K of volume V_K are:

$$\boldsymbol{\sigma}_K \equiv \langle \boldsymbol{\sigma} \rangle_{V_K} = \frac{1}{V_K} \int_{V_K} \boldsymbol{\sigma}(\mathbf{x}) \ \mathrm{d}V \tag{1.58}$$

$$\varepsilon_K \equiv \langle \varepsilon \rangle_{V_K} = \frac{1}{V_K} \int_{V_K} \varepsilon(\mathbf{x}) \ \mathrm{d}V \tag{1.59}$$

For non-zero eigenstrains, in which uniform eigenstrains are assumed, the relation between the local quantities and the overall stress, and strains are expressed as

$$\langle \boldsymbol{\sigma} \rangle_{V_K} = \mathbf{B}_K : \boldsymbol{\Sigma} - \sum_J \mathbf{F}_{KJ} : \mathbf{C}_K : \varepsilon_K^p \tag{1.60}$$

$$\langle \varepsilon \rangle_{V_K} = \mathbf{A}_K : \mathbf{E} + \sum_J \mathbf{D}_{KJ} : \varepsilon_K^p \tag{1.61}$$

where $\mathbf{A}_K$ and $\mathbf{B}_K$ are the elastic strain localisation tensor, and the stress concentration tensor respectively and, $\mathbf{D}_{KJ}$ and $\mathbf{F}_{KJ}$ are called transformation influence tensors.

The local and the overall eigenstress and eigenstrain fields are connected by the Mandel-Levin formula [MAN65]. For instance, the overall plastic strain is given by

$$\mathbf{E}^p = \langle \mathbf{B}^T : \varepsilon^p \rangle = \frac{1}{V} \int_V \mathbf{B}^T(\mathbf{x}) : \varepsilon^p(\mathbf{x}) = \sum_K f_K \ \mathbf{B}_K^T : \varepsilon_K^p \tag{1.62}$$

where $f_K = \frac{V_K}{V}$ is the volume fraction of the subdomain K. Consistently, the overall constitutive equation is written as

$$\boldsymbol{\Sigma} = \mathbf{C} : (\mathbf{E} - \mathbf{E}^p) \tag{1.63}$$

with the overall stiffness:

$$\mathbf{C} = \frac{1}{V} \int_V \mathbf{C}(\mathbf{x}) : \mathbf{A}(\mathbf{x}) \ \mathrm{d}V = \sum_K f_K \ \mathbf{C}_K : \mathbf{A}_K \tag{1.64}$$

In the TFA procedure, the tensors $\mathbf{A}_K, \mathbf{B}_K, \mathbf{D}_{KJ}$ and $\mathbf{F}_{KJ}$ depend on the local and overall elastic moduli and on the shape and volume fraction of the phases. In the case of a periodic microstructure, the TFA corresponds to the periodic homogenisation, provided that each phase is subdivided into a large number of subcells.

The framework of periodic homogenisation will be applied to the representative γ/γ' unit cell where $\mathbf{A}_K$ and $\mathbf{B}_K$ will be simplified (see section 3.2).

1.3 Open questions for modelling the γ/γ' superalloys

1.3.1 Motivation

Two open questions[16] concerning the modelling of plasticity in γ/γ' single crystal superalloys are discussed here:

* There is a considerable body of experimental evidence that shows that the mechanical response is size dependent at length scales of the order of microns and smaller. The models introduced in the previous sections may therefore be able to predict the size effects in superalloys.

* Continuum modelling of the orientation dependence of the plastic deformation in γ/γ' superalloys assumes the activation of six $\{100\}\langle 110\rangle$ cube slip systems. Nevertheless, even though observed macroscopically, they are not experimentally justified on the microscopic level. This question is linked to the strain-hardening anisotropy in the mechanical behaviour of superalloys.

1.3.2 Size effect

The size of many technical components is becoming smaller and smaller. This is continuously reviving the research on the strength of materials at a small scale and on associated models. The description of very small components is closely related to the description of materials with microstructure which have attracted a wealth of interest in recent years, because their mechanical properties drastically differ from the bulk materials [PRO04]. A well-known example is probably the case for fine grained fcc polycrystals with a grain size d^{grain} between 50 nm and a few μm. Experiments on copper polycrystal show that the grain size dependence of the yield stress $\tau_y^{\mathrm{Hall-Petch}}$ follows (at the macroscale) a Hall-Petch law:

$$\tau_y^{\mathrm{Hall-Petch}} = \sigma_0 + \frac{k}{\sqrt{d^{\mathrm{grain}}}} \tag{1.65}$$

where σ_0 and k are considered as two material constants [HAL51]. In the relation (1.65), the strength of the polycrystal $\tau_y^{\mathrm{Hall-Petch}}$ increases with decreasing grain size d^{grain}. The Hall-Petch grain size effect is generated by the compatibility stresses between grains, and may be generalised for size-dependent plasticity in many geometrically confined systems such as γ/γ' superalloys.

Size effects in the γ/γ' superalloys are observed, since the distances between precipitates at the μm-scale play a crucial role. According to the Orowan relation (1.6) the stress level τ^{Orowan} required to bow out a dislocation is related to the width of the channel. Such an effect is clearly observed in figure (8), which shows measures made by Beardmore *et al.* [SHA84] on the steady-state flow stress at different volume fractions of γ' phase for NiAlCr alloys.

Modelling such properties can be accounted for phenomenologically at the macroscale if the models include a characteristic material length scale. For instance, the dislocation density-based model of section 1.2.4.2 has been enriched by Busso *et al.* [BUS00] to account for the additional strengthening mechanism associated with the strain gradients due to the presence of dispersed precipitates. At the same time, Forest *et al.* [FOR00] proposed to enrich the classical framework of section 1.2.4.3 by incorporating internal variables associated to Cosserat plasticity.

Section 1.2.5 has given an overview of the most common modelling approaches accounting for size effects in the plasticity on the μm-scale, where explanations for these effects have to be requested on the dislocation level. Further on, in section 2.4.3, DD-based simulations will be carried out to investigate size effects in γ/γ' superalloys. In addition, in section 3.1.3, simulations through a slip-gradient based plasticity model using the concept of geometrically necessary dislocations densities will be presented.

---

[16]Of course without being exhaustive...

1.3.3 Orientation dependence

Even though the growth direction of single crystals blades is always along $\langle 001 \rangle$, a complete analysis of the orientation dependence of mechanical properties is needed because (i) the alignment of crystallographic and specimen orientation is never perfect (deviations up to $10°$ can be accepted) and (ii) the blades have to endure complex stress states. Hence, another open question concerns the orientation dependence of the mechanical properties observed in single crystal superalloys [MIN86] [SAS98].

Macroscopic slip steps corresponding to cube planes were observed at the surface of [111] crystals deformed at 650°C and 750°C [BET99]. That is why, in addition to the twelve octahedral slip systems, six cube slip systems are potentially activated for modelling the orientation-dependence of the mechanical response in superalloys.

Nevertheless, simply including cube slip has important consequences for the models: it is needed to correctly simulate the experimentally observed response of the material when it is loaded in the {111} direction, for which the yield stress is much lower than for the {001} orientation. However, as shown in figure (16), including or not the cube slip play a considerable role on the yield surface of the Schmid's law (see equation 1.7). Figure (16 a) illustrates the theoretical Schmid factor, i.e. $S^g = \cos\phi^g\cos\lambda^g$ for octahedral slip systems only as function of orientation, with a maximum value in grey ($S^g = 0.41$) near the $\langle 001 \rangle$ orientations and a minimum value in black ($S^g = 0.28$) near $\langle 111 \rangle$. Figure (16 b) shows the theoretical Schmid factor surface for octahedral and cubic slip systems as function of orientation, with a maximum value in grey ($S^g = 0.48$) near $\langle 111 \rangle$.

However, there is much debate whether cube slip physically really occurs in the matrix phase of the material. At the microscopic level, the sequential cross-slip of screw dislocations on two sets of octahedral systems, resulting in zig-zag slip on a macroscopic effective cube plane, has been observed extensively in the matrix phase of several superalloys [SAS97] [SAS98] [BET99]. The debates concerning the orientation dependence for γ/γ' superalloys might be discussed through discrete models of crystal plasticity. This is the subject of section 2.4.4, where DD-based simulations have been performed to understand the physical mechanisms responsible for the orientation dependence at the dislocation-scale.

(a)   (b)
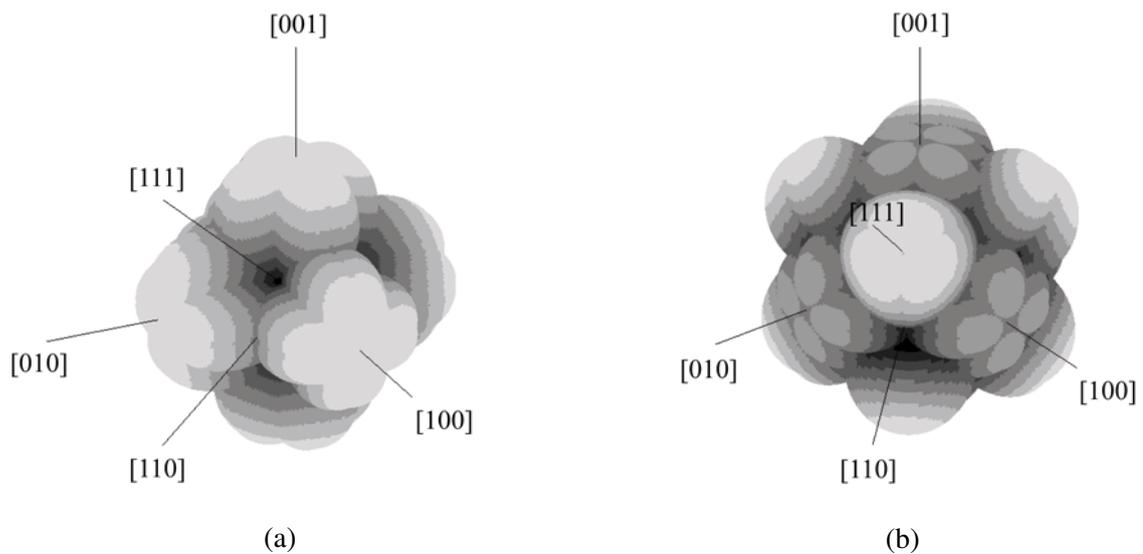
Figure 16 - Theoretical yield surface of the microscopic criterion (i.e. the Schmid law) where the Schmid factors are plotted as function of orientation for (a) octahedral slip only and, (b) octahedral and cubic slip. Maximum values are given in light grey and minimum values in black.

Résumé

Avec le développement accru des superalliages monocristallins à base nickel, les industries aéronautiques ont mené (et mènent) des études, en étroite relation avec de nombreux laboratoires de recherche, afin d'approfondir les connaissances dans les domaines reliant la composition à la microstructure et au comportement en service des aubes monocristallines. En premier lieu, la chimie des superalliages à base de nickel a évolué de manière significative depuis le développement des alliages à grains colonnaires [CAR99]. Par ailleurs, la structure biphasée que possède ce monocristal lui confère des différences de comportement notables en comparaison avec des matériaux comme le cuivre ou le nickel pur. A ces descriptions quantifiées de la microstructure des superalliages monocristallins s'est édifiée en parallèle une interprétation très affinée des mécanismes de déformation sur la base d'observations microscopiques: modes des mécanismes de déformation des dislocations en fonction de la température, énergies mises en jeu lors de la déformation etc... Par exemple, ces travaux ont permis d'enrichir les modèles antérieurs de durcissement gouvernant les propriétés mécaniques de Ni_3Al proposés par Kear dans les années 1960.

Du point de vue de la modélisation et de la simulation, l'avènement des puissants moyens de calcul a stimulé le développement d'outils de simulation sophistiqués dédiés à la prédiction du comportement mécanique des matériaux. Les simulations 3D de dynamique des dislocations en sont une illustration. Dictée par la théorie élastique des dislocations, ces simulations discrètes ont par exemple permis de vérifier l'effet Hall-Petch lié à la taille du grain dans le polycristal. En parallèle, aux échelles supérieures, le plus souvent dictées par la mécanique des milieux continus, les lois de comportement laissent peu à peu place à des relations déduites des mécanismes physiques à l'origine de la déformation plastique. Par ailleurs, afin de reproduire des effets de taille couramment observés en métallurgie physique, l'approche classique des milieux continus s'est étendue/généralisée/enrichie en incorporant dans la modélisation une longueur caractéristique du matériau. En somme, la prédiction du comportement mécanique des matériaux hétérogènes à partir de leur microstructure constitue aujourd'hui un problème complexe qui nécessite des investigations à la fois physiques (approches discrètes) et mécaniques (approches continues).

A cet effet, un modèle hybride entre un code de dynamique des dislocations et d'éléments finis a été développé à l'ONERA sous l'appellation de Modèle Discret-Continu. Les récents développements de ce modèle ont permis dans le cadre de cette thèse d'étudier le comportement du monocristal et de le confronter à deux problèmes aujourd'hui ouverts, à savoir les effets de taille et de l'anisotropie de l'orientation du chargement. Ces deux problèmes sont d'une importance capitale en terme de modélisation.

The Discrete-Continuous Model

Contents

Introduction

Le second chapitre intitulé "Le Modèle Discret-Continu" (MDC) se découpe en quatre parties. La première partie 2.1 présente les fondements des simulations de dynamique des dislocations, et en particulier l'effort constant mené pour décrire de façon toujours plus fidèle les propriétés élémentaires des dislocations. Ces simulations ont pour principale vocation d'assurer le passage des propriétés individuelles des dislocations au comportement collectif et de comprendre l'influence de ces microstructures sur le comportement mécanique macroscopique. De ce point de vue, le passage à une description tridimensionnelle de la dynamique des dislocations au début des années 1990 constitue probablement le plus grand progrès. Cependant, il est aujourd'hui reconnu que ces simulations dites conventionnelles présentent des limitations. Cette partie les évoque et c'est dans l'optique de les corriger que le MDC a été développé à partir 1999 à l'ONERA à travers maintenant trois thèses, celle de Lemarchand [LEM99], de Groh [GRO03a], et cette présente thèse.

Une seconde partie 2.2 présente le MDC ainsi que ses récents développements. Ce modèle exprime l'idée originale qu'ont eu ces dernières années plusieurs laboratoires, à savoir de coupler les simulations par dynamique des dislocations avec une méthode classique des éléments finis. La première, physique, connaît des faiblesses dans son traitement des conditions aux limites. La seconde, mécanique, souffre quant à elle de justifications physiques dans les lois de comportement qu'elle intègre. La simulation hybride ainsi réalisée combine les avantages des approches discrètes (description physique de la plasticité) et continue (traitement des conditions aux limites). Cette méthodologie située au carrefour entre les approches du physicien métallurgiste et celle du mécanicien a été améliorée et est détaillée dans cette partie.

Une troisième partie 2.3 est dédiée à la validation du nouveau code MDC avec ses améliorations à travers plusieurs configurations modèles de dislocations pour lesquelles une solution de la théorie élastique des dislocations existe. Plusieurs calculs ont permis de valider cette nouvelle version du MDC. Par exemple, des calculs ont montré l'aptitude du modèle à reproduire avec une grande précision le champ de contrainte interne d'une boucle dipolaire, le calcul de la contrainte d'activation d'une source de Frank-Read (calcul quasi-stastique), ou les interactions à courtes distances des dislocations par la formation d'une jonction (calcul de contact).

La quatrième et dernière partie 2.4 illustre deux applications du MDC consacrées à la plasticité des superalliages monocristallins. Dans un premier temps, le mécanisme de déformation produit par cisaillement des précipités γ' de dislocations appariées a été implémenté. Après une étude d'influence sur le calcul de la contrainte d'écoulement de paramètres physico-chimiques (contrainte de friction, énergie d'antiphase) ou microstructuraux (largeur des couloirs de matrice, fraction volumique), le MDC a été utilisé pour simuler les effets de la largeur des couloirs de matrice et de l'orientation du chargement sur le comportement mécanique. Cette partie montre la force du MDC lorsqu'il est appliqué à des problèmes traitant la plasticité confinée.

2.1 Principles of 3D dislocation dynamics simulations

2.1.1 Introduction

The idea of simulating the dynamics and interactions of dislocation lines in an elastic continuum in order to study the plasticity of crystals is now 40 years old. In the early times, simulation methods have been applied to simple situations, for instance the motion of a single dislocation line through a random distribution of point obstacles representing either forest dislocations or small precipitates (see figures 15 a and b). In the last 10 years, a substantial improvement of the range and realism of such simulations has been made possible by the increase in computing power. Thus, today, one can compute the collective properties of large numbers of dislocations (e.g. several hundreds of lines) in sufficiently large model crystals, with typical linear dimension of about 15 μm. This allows direct comparisons between real and "in silico" experiments. The concept of 3D DD simulations was initiated by Kubin and Canova in the early 1990s [KUB90a] [CAN91]. These simulations are now reasonably mature, and are currently the most advanced 3D technique for the modelling of collective dislocation behaviour [KUB92] [VER98] [ZBI98] [SCH99] [GHO99].

2.1.2 Discretisation of the dislocation lines in fcc crystals

The original code microMégas (mM) [MicroMégas] is a simple model in which dislocation lines of a fcc single crystal are subdivided into sets of discrete dislocation segments embedded in a continuum. In DD simulations both space and time are discretised. The discretisation of time is performed just like in conventional molecular dynamics simulations, whereas the discretisation of space is an original feature of the code.

Within the elastic continuum, a crystallographic lattice is defined with the same symmetry elements as the crystal of interest but with larger lattice parameters, in the nanometer range for mesoscopic simulations. The dislocation lines are then decomposed into chains of successive segments lying on this lattice. As a consequence, the dislocation segments can only have a finite number of characters and line directions. For example, a curved dislocation line can be represented as a connected set of discrete dislocation segments of pure edge and pure screw type. This is why the initial version of the mM code is called the "edge-screw" model.

Recently, a new topological line model was introduced by adding mixed line directions (e.g. $\pm 60°$ characters in the fcc crystal symmetry) [MAD01]. This model, the so-called "pure-mixed" model (see figure 17 a), aims at a more accurate description of a curved dislocation line with a minimum number of segments [DEV01].

(a)   (b)
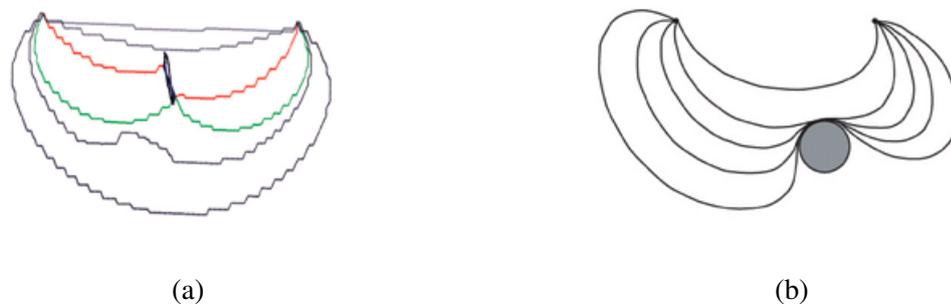
Figure 17 - Successive snapshots of (a) a lattice-based simulation ("pure-mixed" model, mM code) of a dislocation-dislocation interaction [MicroMégas], and (b) a nodal simulation of a dislocation-precipitate interaction [Douin].

"Nodal" models (see figure 17 b) may seem to be more attractive [GHO00] [WEY01]. However, such nodal model are much more complex in dealing with topological aspects of segments, because it involves more degrees of freedom in segment types as compared to the edge-(mixed)-screw model.

The line model used in the following work is the pure-mixed model. The time integration of the dislocation dynamics in mM proceeds in three main steps. Firstly, the forces acting on all segments are evaluated within linear elasticity theory. Then, the velocity of segments is determined, and the position of each segment is then updated, taking into account obstacles and contact reactions on the way.

2.1.3 Computation of dislocation driving force

The velocity of each segment is governed by the effective RSS τ_{eff} acting on the segment. This stress includes four contributions:

* The applied stress $\boldsymbol{\sigma}_{\mathrm{app}}$.

* The internal stress field $\boldsymbol{\sigma}_{\mathrm{int}}$ due to all other dislocation segments.

* The lattice friction τ_F, assumed to be homogeneous in dislocation glide planes.

* The line tension Γ, which tends to straighten dislocation lines.

The contributions of atomistic-level interactions, such as dragging forces by solute atoms or jogs, are not treated explicitly but can be included by modifying the effective stress or the equation of motion (see section 2.4.2).

Applied stresses

External stresses are applied in two ways, depending on the boundary conditions involved. In the first case (conventional DD simulations), the simulation volume represents a small element in a large crystal, and the external stress field is assumed to be uniform throughout the simulation volume. The external stress tensor is then directly applied to each segment in the volume and the magnitude of its components are updated at each step of the simulation.

In the second case (hybrid simulations), the simulation volume potentially includes heterogeneous stress fields (for instance, a volume with internal interfaces or free surfaces). This point will be discussed in section 2.2.

Internal stresses

To compute the internal stress at the centre of a segment, the expression of the stress field of a single finite straight segment is required. This problem has been addressed by Li [LI64]. According to Li, the stress field of an angular dislocation, consisting of two semi-infinite dislocations joined together at one point, is the sum of the stress fields of each dislocation arm, i.e. each semi-infinite dislocation. Although the stress field of each semi-infinite dislocation does not obey the equations of equilibrium, the sum of both does. Hence, the stress field σ_{ij} at a point $\mathbf{r}(x, y, z)$ due to a dislocation segment AB lying on the z axis running from z_B to z_A with Burgers vector $\mathbf{b}(b_x, b_y, b_z)$ is obtained by

$$\sigma_{ij}(\mathbf{r}) = \sigma_{ij}(\mathbf{r} - \mathbf{r}_A) - \sigma_{ij}(\mathbf{r} - \mathbf{r}_B) \tag{2.1}$$

Moreover, if a semi-infinite dislocation lies on the positive z axis running from the origin, O, the stress field produced at a point $\mathbf{r}(x, y, z)$ has the following components [LI64]:

$$\sigma_{xx}(\mathbf{r}) = \frac{-b_x y - b_y x}{r(r-z)} - \frac{x^2(b_x y - b_y x)(2r-z)}{r^3(r-z)^2}$$

$$\sigma_{yy}(\mathbf{r}) = \frac{b_x y + b_y x}{r(r-z)} - \frac{y^2(b_x y - b_y x)(2r-z)}{r^3(r-z)^2}$$

$$\sigma_{zz}(\mathbf{r}) = \frac{z(b_x y - b_y x)}{r^3} - \frac{2\nu(b_x y - b_y x)}{r(r-z)} \tag{2.2}$$

$$\sigma_{yz}(\mathbf{r}) = \frac{y(b_x y - b_y x)}{r^3} - \frac{\nu b_x}{r} + \frac{(1-\nu)b_z x}{r(r-z)}$$

$$\sigma_{zx}(\mathbf{r}) = \frac{x(b_x y - b_y x)}{r^3} - \frac{\nu b_y}{r} + \frac{(1-\nu)b_z y}{r(r-z)}$$

$$\sigma_{xy}(\mathbf{r}) = \frac{b_x x - b_y y}{r(r-z)} - \frac{xy(b_x y - b_y x)(2r-z)}{r^3(r-z)^2}$$

In equations (2.2), the stress components are given in units of $\frac{\mu}{4\pi(1-\nu)}$ with μ and ν the shear modulus and the Poisson ratio, respectively. The stress field of a dislocation segment AB is then obtained by substituting $\mathbf{r} - \mathbf{r}_A$ and $\mathbf{r} - \mathbf{r}_B$ respectively into equations (2.2), and using equation (2.1).

On the other hand, the compact formulae of de Wit [DEW67] are given with respect to an arbitrary Cartesian coordinate system. Devincre [DEV95] derived a final from where the stress field associated with a straight segment between two points A and B is calculated by

$$\sigma_{ij}^{\mathrm{AB}}(\mathbf{r}) = \frac{\mu}{\pi \mathbf{Y}^2} \left[[\mathbf{bYt}]_{ij} - \frac{1}{1-\nu}[\mathbf{btY}]_{ij} - \frac{(\mathbf{b}, \mathbf{Y}, \mathbf{t})}{2(1-\nu)} (\delta_{ij} + t_i t_j + \phi_{ij}) \right]_A^B \tag{2.3}$$

where

$$\phi_{ij} = \frac{2}{Y^2} \left(\rho_i Y_j + \rho_j Y_i + \frac{L}{R} Y_i Y_j \right)$$

$$L = \mathbf{R}.\mathbf{t}$$

$$\boldsymbol{\rho} = \mathbf{R} - L\mathbf{t} \tag{2.4}$$

$$\mathbf{Y} = \mathbf{R} + R\mathbf{t}$$

$$[\mathbf{bYt}]_{ij} = \frac{1}{2} \left[(\mathbf{b} \otimes \mathbf{Y})_i \, t_j + (\mathbf{b} \times \mathbf{Y})_j \, t_i \right]$$

with $(\mathbf{b}, \mathbf{Y}, \mathbf{t})$ the scalar triple product, δ_{ij} the Kronecker symbol, $\mathbf{t}$ the unit vector along the line direction of the segment, and $\mathbf{R}$ the vector from the point A or B of the segment to the point $\mathbf{r}$.

According to equations (2.2) and (2.4), figure (18) shows the computation of the stress fields in a normal plan cutting the centre of an edge (figure 18 a) and a screw segment (figure 18 b) of length 0.5 μm.

Lattice friction

The lattice friction refers to the critical RSS required to start a dislocation glide in a perfect crystal. This arises as a direct consequence of the periodic structure of the crystal lattice and acts as a friction to dislocation motion. In the DD simulations, which do not treat atomistic effects explicitly, the lattice friction is phenomenologically taken into account as a back stress τ_F opposing the motion of each segment (see equation 2.9) [MON06].

(a) (b)
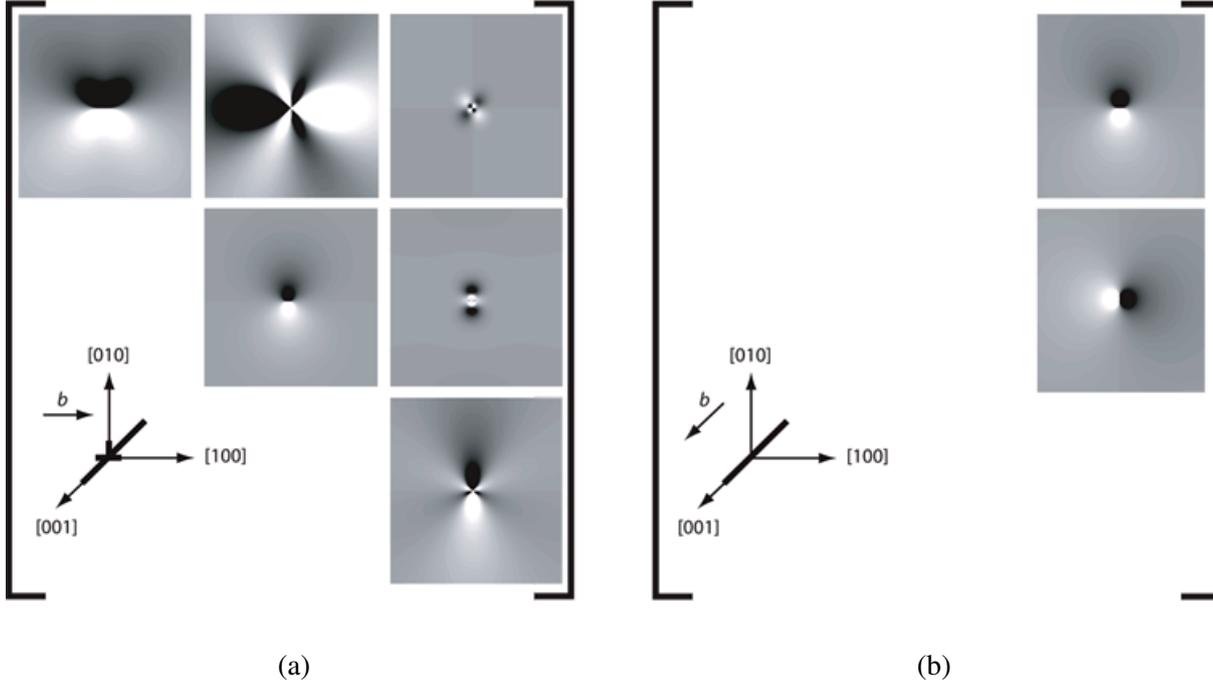
Figure 18 - Computation of the stresses σ_{ij} of a dislocation segment on the plane normal to the line direction. The stress profiles show a minimum value in black (-20 MPa for all components on the main diagonal of σ_{ij} and -5 MPa for the off-diagonal terms) and a maximum value in white (20 MPa for all components on the main diagonal of σ_{ij} and 5 MPa for the off-diagonal terms) for (a) an edge and (b) a screw dislocation segment.

Line tension

In DD simulations, as a result of the line discretisation with straight segments, the continuous curvature of dislocations is locally replaced by straight line sections, and so a force correction (i.e. the line tension) is needed to account for the exact elastic energy of the continuous curved line. The line tension $T(\theta)$ creates a force $\Gamma = \frac{T(\theta)}{bR}$ along the centre of a dislocation arc with a radius of curvature R. $T(\theta)$ is given by the energy $E(\theta)$ of the dislocation arc with θ the angle between the Burgers vector and the dislocation line direction:

$$T(\theta) = E(\theta) + \frac{d^2 E(\theta)}{d\theta^2} \tag{2.5}$$

The simplest form of the line tension would be obtained by assuming that edge, screw and mixed segments would have the same energy per unit length, i.e. $E = \alpha\mu b^2$ with α a numerical constant. The line tension of an arc of dislocation then becomes $\Gamma = \frac{\alpha\mu b}{R}$ from equation (2.5).

However, the energy of a dislocation is dependent on the character: for instance, a screw dislocation has lower energy than an edge dislocation. To include this variation of the energy with character of the segment i, different analytical equations exist. In this thesis, the line tension equation suggested by Foreman [FOR67] is used:

$$\Gamma^i(\theta^i) = \frac{\mu b^i}{4\pi(1-\nu)R^i}(1 - 2\nu + 3\nu\cos^2\theta^i)\left[\ln\left(\frac{L^i}{2b^i} - \nu\cos(2\theta^i)\right)\right] \tag{2.6}$$

where R^i is the radius of a circle defined by three adjoining centre points of segments (segments $i-1$, i and $i+1$ in figure 19). L^i is the length of the segment i and θ^i is the angle between the Burgers vector $\mathbf{b}^i$ and the dislocation line vector $\mathbf{t}^i$ at the midpoint of the segment i.
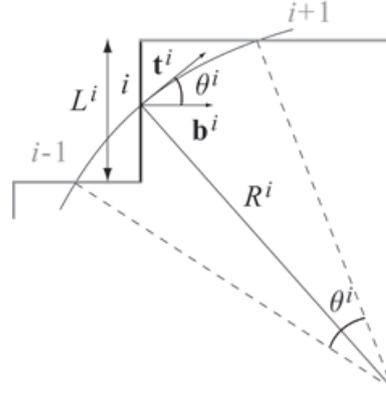
Figure 19 - Geometry of the line tension calculation.

Effective stresses

After the applied stresses $\boldsymbol{\sigma}_{\mathrm{app}}$ and the internal $\boldsymbol{\sigma}_{\mathrm{int}}$ are computed, the effective stress applied on each dislocation is evaluated at the midpoint of each of its segments. This induces a force per unit length given by the Peach-Köhler (PK) equation:

$$\mathbf{F}^{\mathrm{PK},\,i} = \boldsymbol{\tau}^{\mathrm{PK},\,i}\,|b^i| = \left[(\boldsymbol{\sigma}_{\mathrm{int}} + \boldsymbol{\sigma}_{\mathrm{app}}) \,.\mathbf{b}^i \right] \times \mathbf{t}^i = \left[\left(\sum_{j=1, j \neq i}^{N} \boldsymbol{\sigma}_{\mathrm{int}}^j + \boldsymbol{\sigma}_{\mathrm{app}} \right) .\mathbf{b}^i \right] \times \mathbf{t}^i \qquad (2.7)$$

where N is the total number of segments, and $\boldsymbol{\sigma}_{\mathrm{int}}^j$ the stress tensor due to a remote segment j. In DD simulations, most of the CPU time is devoted to evaluating equation (2.7) because this implies O(N^2) computations of the internal stress tensors, and the number of segments N generally increases with time. Thus, many efforts have been carried out in optimising the calculation of the internal stresses. For instance, these optimisations can be improved by using parallel calculations which are now a common option in most DD codes [SHI06], and a fast multipole decomposition leading to O(N) operations [WAN04].

The effective stress τ_{eff}^i is then computed by summing $\tau^{\mathrm{PK},\,i}$ and the line tension of segment i as

$$\tau_{eff}^i = \tau^{\mathrm{PK},\,i} + \Gamma^i \qquad (2.8)$$

2.1.4 Dislocation motion

Dislocation mobility depends on the applied shear stress and temperature. It varies with the crystal purity and the dislocation type. There are a number of relations between glide velocity and the effective stress, including power law forms and expressions with an activation term in an exponential function to represent the temperature-dependency [KOC75]. Here, a simple power law form $v \propto (\tau_{eff})^m$ is used to compute the dislocation velocity. A linear form of the equation, $m = 1$, is commonly adopted where the magnitude of the velocity $v^i = \|\mathbf{v}^i\|$ of a segment i is given by

$$v^i = \begin{cases} 0 & \text{if } \tau_F \geqslant \tau_{eff}^i \\ \dfrac{\left[\tau_{eff}^i - \tau_F \, \mathrm{sign}\,(\tau_{eff}^i) \right] b^i}{B} & \text{if } \tau_F < \tau_{eff}^i \end{cases} \qquad (2.9)$$

with the constant lattice friction stress τ_F, the phonon drag coefficient B, and the effective stress τ_{eff}^i on the segment i defined by equation (2.8).

Using the velocity of a segment defined by the equation (2.9), the next position of the segment $\mathbf{x}^i\,(t_{\mathrm{n}} + \Delta t_{\mathrm{n}})$

is obtained by neglecting inertial effects:

$$\mathbf{x}^i\left(t_{\mathrm{n}} + \Delta t_{\mathrm{n}}\right) = \mathbf{x}^i\left(t_{\mathrm{n}}\right) + \mathbf{v}^i \Delta t_{\mathrm{n}} \tag{2.10}$$

where $\mathbf{x}^i\left(t_{\mathrm{n}}\right)$ is the position at time t_{n} and $\Delta t_{\mathrm{n}} = t_{\mathrm{n+1}} - t_{\mathrm{n}}$ is the time increment.

2.1.5   Plastic strain due to dislocation glide

The plastic strain in a simulated volume is determined by summing up the slipped area of each slip system g. The slip increment $\Delta\gamma^g$ is computed as[1]

$$\Delta\gamma^g = \frac{|\mathbf{b}|\Delta A^g}{V} \tag{2.11}$$

with V a reference volume, which is the total simulation cell in conventional DD simulations, and ΔA^g the area swept by all mobile dislocations of the slip system g during a time increment Δt_{n}. ΔA^g is then defined as

$$\Delta A^g = \sum_{i=1}^{N} L^i v^i \Delta t_{\mathrm{n}} \tag{2.12}$$

where the summation is done over all the segments of the system g and $L^i v^i \Delta t_{\mathrm{n}}$ is the area of glide of a segment i with length L^i and velocity v^i. The components of the plastic strain tensor are given by equation (1.21), i.e.

$$\Delta\varepsilon_{ij}^p = \sum_{g=1}^{12} \frac{1}{2}\left(n_i^g b_j^g + n_j^g b_i^g\right)\Delta\gamma^g \tag{2.13}$$

with n_i^g and b_i^g the component i of the slip plane normal and of the Burgers vector of the slip system g, respectively.

2.1.6   Dislocation-dislocation reactions

During dislocation glide, a segment can encounter and react with other segments and obstacles. An important task of the simulation is then to search any possible reaction with other segments and obstacles within the virtual glide area of the gliding segment, which is defined by the length of the segment L^i and the free flight distance $v^i \Delta t_{\mathrm{n}}$. The type of reaction is determined by local rules accounting for different possible reactions between dislocation lines. The dislocation-dislocation reactions are categorised as either coplanar reactions in which two segments glide on the same plane, or non-coplanar reactions in which two dislocation segments glide on different planes.

For the coplanar cases, those reactions of two segments with the same Burgers but opposite line direction end up with the annihilation reaction. In that case the two line sections in contact are deleted and the links of the remaining segments are rebuilt. In case of the same sign, no additional special rule is required because the interaction is elastically repulsive.

As introduced in table (1.2) where junctions formed between slip systems were tabulated by a_i, five contact reactions between two segments of Burgers vectors $\mathbf{b}^1$ and $\mathbf{b}^2$ are considered here:

1. The interaction between two coplanar segments (a_1) for which $\mathbf{b}^1 \neq \mathbf{b}^2$.

2. The Hirth lock (a_2) between two segments gliding on non-coplanar planes for which $\mathbf{b}^1 \perp \mathbf{b}^2$.

---

[1]Compare equation (2.11) with (1.24).

3. The collinear interaction (a_3) of a segment with a segment on its cross-slip system for which $\mathbf{b}^1 = \mathbf{b}^2$.

4. The glissile junction (a_4) for which $\mathbf{b}^1 + \mathbf{b}^2$ is glissile on either planes.

5. The Lomer-Cottrell lock (a_5) for which $\mathbf{b}^1 + \mathbf{b}^2$ is sessile on either planes.

In DD simulations the simple energy criterion defined by Frank's rules is not required. Instead, the dislocation dynamics is explicitly solved, and junction formation is a dynamical process controlled by junction zipping and unzipping. This more general approach is critically needed in 3D calculations, as illustrated by the comparison between the predictions of molecular dynamics and DD simulations [BUL98].

2.1.7 Cross-slip of screw segments

The cross-slip of a screw segment is initiated in a stochastic manner, accounting for its thermally activated character. A cross-slip probability P^i over each time step Δt_n is computed using the equation

$$P^i = \beta \frac{l_\mathrm{screw}^i}{l_0} \frac{\Delta t_\mathrm{n}}{\Delta t_0} \exp\left(V^\mathrm{cs} \frac{|\tau^{\mathrm{PK},\,i}| - \tau_\mathrm{III}}{k_B T}\right) \tag{2.14}$$

where β is a normalisation coefficient, l_screw^i is the length of the particular screw segment i, $l_0 = 1\ \mu$m, $\Delta t_0 = 10^{-9}$ s, V^cs is the cross-slip activation volume, $\tau^{\mathrm{PK},\,i}$ is the RSS in the cross-slipped system of the segment i and τ_III is a threshold stress. Details on the modelling of cross-slip process in the mM code can be found in [DeS07].

2.1.8 Boundary conditions

In order to compare simulations to experiments, it is desirable to build a simulation volume representative of a small element taken out from a large crystal, possibly including internal interfaces due to grains or precipitates. For this reason two kinds of boundary conditions are used in DD simulations, and this section is dealing with Periodic Boundary Conditions (PBC) and internal interfaces.

Periodic boundary conditions

For the so-called massive simulations (i.e. with high dislocation density), PBC are needed in order to ensure that dislocation fluxes are balanced at the boundaries of the simulation cell to avoid undesirable size effects due to finite dimensions and artificial dislocation losses. Madec *et al.* [MAD04] have reported that portions of dislocation loops self-annihilate with replicas having emerged after a certain number of boundary crossings. This self-annihilation (of which an example is shown in figure 20) reduces the mean free path of dislocations and consequently affects the density of mobile dislocations, their storage rates and, hence, both microstructure arrangements and strain hardening properties. The artefact of self-annihilation can be controlled by using an orthorhombic simulation volume [MAD03] [MAD04].

Internal interfaces

In polycrystals, grain boundaries act as obstacles to dislocation motion, leading to dislocation pile-ups or absorption of these dislocations by the grain boundary. In DD simulations, simple geometrical barriers to dislocation motion blocking all segments under a critical stress at the internal interfaces are one way to account for their presence. When applied to dislocation-precipitate interactions, this can be considered as a first-order approximation in the sense that elastic interactions between dislocations and interfaces are not taken into account.
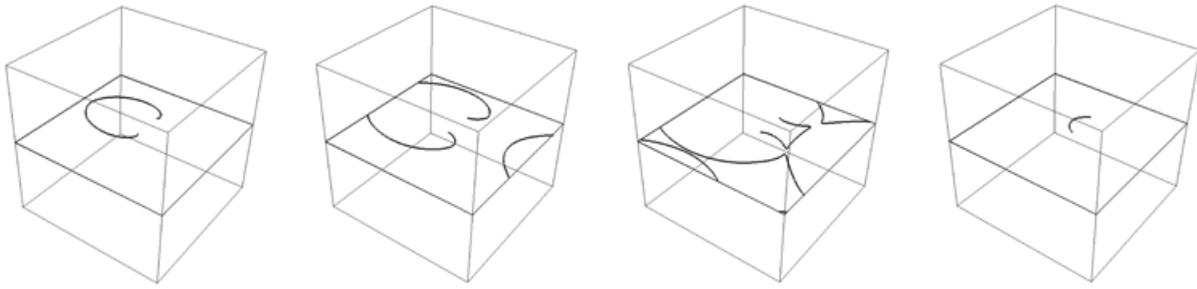
Figure 20 - Direct self-annihilation of a Frank-Read source in a cubic crystal with periodic boundary conditions.

2.1.9   Limitations

The fact that the boundary conditions of real crystals may be complex, especially when internal interfaces are to be accounted for, is one limitation of conventional DD simulations. In the following, several of these limitations are listed, and effort is needed to overcome them.

Uniform applied stress

It is generally assumed that the loading conditions create uniform stresses inside the computational cell. Strong approximations have to be adopted to account for the conditions of mechanical equilibrium at boundaries. The simplest possible approximation is (for instance, for the case of free surfaces) the "image force" approximation, based on a modification of the dislocation energy, when a dislocation line intersects a boundary [DEV96].

Internal state of stress

A second level of approximation consists of solving the boundary value problem in a purely elastic manner and then running the DD simulation with the assumption that this solution is not modified much by the presence of dislocations. Such an approach might apply reasonably well when the plastic strain is a small fraction of the total strain [CHI02].

Long-range stress

Long-range interactions are governed by the stress generated by the dislocations themselves, which is obtained by solving the elastic boundary value problem of the domain containing the dislocations. Numerically efficient formulations for the stress fields of straight dislocation segments are only available for the case of an isotropic and infinite medium. As a consequence, the boundary conditions used in most published works are not exact, and the long-range nature of the dislocation stress field is not rigorously taken into account [DEN08].

More rigorous boundary conditions need to be implemented to treat more general cases, such as a crystal with free surfaces, a crystal containing particles of a second phase or a polycrystal containing grain boundaries. To tackle these difficulties, several methods have been proposed.

2.2 A solution for boundary value problems in DD simulations

2.2.1 Introduction

Over the years, different methods have been developed to calculate the state of mechanical equilibrium in a dislocated finite body. These methods are based on the superposition principle, the eigenstrain formalism, or recently the XFEM approach.

The superposition principle

One class of DD methods is based on the superposition of analytic solutions for the mechanical fields generated by a dislocation in an infinite medium and an elastic solution of a modified boundary condition problem in the finite body without dislocations. Van der Giessen and Needleman [VAN95] modified this approach in order to take into account elastic inclusions (not presented here).
For the determination of these fields, the basic idea is to exploit the known singular solutions in an infinite continuum, and to use superposition to correct for boundary conditions, as illustrated in figure (21). The displacement, strain and stress fields are decomposed as

$$
\begin{aligned}
u_i &= \tilde{u}_i + \hat{u}_i \\
\varepsilon_{ij} &= \tilde{\varepsilon}_{ij} + \hat{\varepsilon}_{ij} \\
\sigma_{ij} &= \tilde{\sigma}_{ij} + \hat{\sigma}_{ij}
\end{aligned}
\tag{2.15}
$$

The (˜) fields are the superposition of the singular fields of the individual dislocations in their current configuration, but in an infinite continuum. Writing $\tilde{\sigma}_{ij}^k$ for the stress associated to dislocation k, the stress field due to all dislocations is obtained as $\tilde{\sigma}_{ij} = \sum_k \tilde{\sigma}_{ij}^k$. The actual boundary conditions, in terms of prescribed displacements u_i^0 or tractions $T_i^0 = \sigma_{ij} n_j$, are imposed through the (ˆ) fields, in such a way that the sum of the (˜) and the (ˆ) fields in equations (2.15) gives the solution satisfying all boundary conditions. In addition, the (ˆ) fields, often called image fields, may be solved using a FE method [VAN95] [FIV99].
The basic objective is to enable an accurate description of the dislocation-dislocation interaction. An issue addressed by Weygand *et al.* [WEY01] is that the classical linear elastic solution of dislocation fields is singular along the dislocation lines, which poses a numerical difficulty on the boundary in a FE
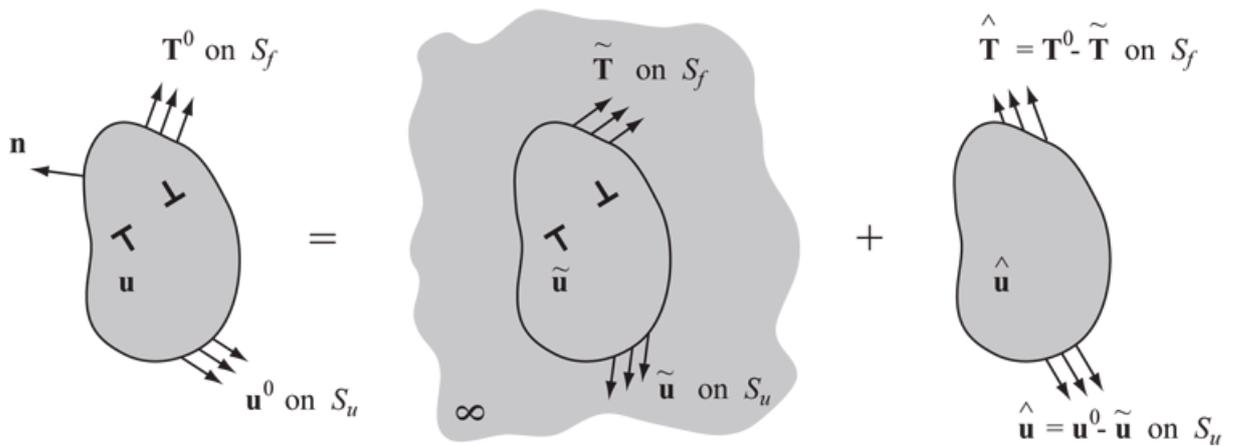
Figure 21 - The superposition principle. The problem is decomposed into the problem of interacting dislocations in the infinite continuum (˜ fields) and the complementary problem for the finite body without dislocations (ˆ or image fields).

problem. Tang *et al.* [TAN06] presented a boundary value problem formulation for the image field, in which the singular part of the traction of the image field is treated analytically while the rest of the image field is computed by applying a non-singular correction using the FE method.

The eigenstrain formalism

Another method, which considers a dislocation loop as a thin plate-like inclusion causing eigenstress in an elastic medium, has been first used in DD simulations by Lemarchand *et al.* [LEM99a] [LEM99b] [LEM00] [LEM01] and subsequently by Groh *et al.* [GRO03a] [GRO03b] [GRO04]. This hybrid DD−EF model is based on a coupling between a FE code where the usual constitutive law is replaced by a mesoscopic DD simulation. It aims at computing equilibrium conditions both inside the volume and at its external or internal interfaces. The plastic strain increments calculated by DD simulations are imposed at the Integration Points (IP) of each plastic domain of the FE model through a regularisation procedure [LEM01] [DEV03]. This procedure stands at the core of the connection between the two codes, because the regularisation of the elementary shears induced by the motion of individual dislocations constitutes the basic information transmitted from the DD simulation to the FE simulation. This hybrid model, called the Discrete-Continuous Model (DCM) is explained in detail in section 2.2.2.
Comparable solutions using an eigenstrain description of the dislocation are used in other simulation techniques. In the phase field method, the eigenstrain formalism of plastic deformation has already been used in the modelling of phase transformations [ROD01] [WAN01] [ROD03].
Other methods are the level set method in which the dislocation lines are represented in 3D by the intersection of two level set functions [XIA03]. Both models (i.e. phase field and the level set methods) are resolved with fast Fourier transforms, though in principle they can be solved with standard FE.

The XFEM approach

Recently a new FE method has been developed for the modelling of dislocations [BEL07] [GRA07] [GRA08]. The method falls in the class of eXtended FE Methods (XFEM), where the local features of the solution are added to the standard FE approximations. It is straight-forward to apply it to problems with internal boundaries and material interfaces. In this method, the dislocation is modeled by a line or surface of discontinuity, and the PK force is directly computed from the FE stress field, with a higher degree of accuracy when compared to classical FE solutions. Nevertheless, a current limitation of this method seems to lie in the interactions between dislocations at short distances.

In the present thesis, the eigenstrain formalism has been used for DD simulations via the DCM. This hybrid model has already been used to study plastic relaxation in heteroepitaxial thin films [GRO03b], plastic deformation in metal matrix composites [GRO04], and compression tests in a micro-pillar of copper [LIU09]. The method will now be enriched for plastic deformation in the γ/γ' superalloys, as will be shown later on in section 2.4.

2.2.2   Eigenstrain formalism of the boundary value problem

In the eigenstrain approach, material defects are modeled using equivalent incompatible stress-free strain distributions called the eigenstrains [MUR87]. Applied to dislocations, the idea stems from the fact that dislocation loops can be described as a set of thin plate-like coherent inclusions, as first pointed out by Nabarro [NAB51]. The eigenstrain tensor ε_{ij}^{00} has the form of a dyadic product of the components i of
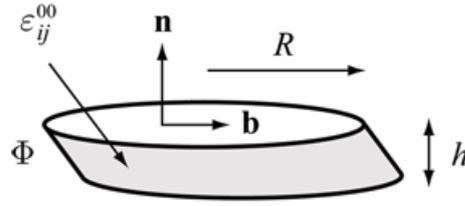
Figure 22 - A dislocation loop of radius R represented by a thin coherent inclusion with the stress-free strain given by equation (2.16). **n** is the normal to the habit plane of the inclusion, coinciding with the slip plane normal, **b** is the Burgers vector of the dislocation loop, and h is the thickness of the inclusion. For a crystal dislocation, the distance h is equal to the interplanar distance.

Burgers vector **b** and the components j of the unit vector **n** normal to the slip plane:

$$\varepsilon_{ij}^{00} = \frac{b_i n_j}{h} \tag{2.16}$$

where the proportionality coefficient h is the interplanar distance, corresponding to the height of the eigenstrain plate. Figure (22) schematically shows a plate-like coherent inclusion Φ representing a dislocation loop of radius R. The habit plane is parallel to the slip plane. Any dislocation loop can be modeled as a platelet inclusion, bordered by the dislocation loop with a stress-free strain expressed by equation (2.16). This is formally equivalent to replacing one dislocation by a continuum distribution of parallel infinitesimal dislocations. Outside the sheared volume, such distributions well reproduce the elastic fields of real dislocations [KHA83] [KRO94].

In DD simulations, the general eigenstrain problem in a dislocated finite crystal is stated as follows: find the displacement, the elastic strain and the stress fields compatible with an arbitrary eigenstrain distribution. Under the external traction and displacement boundary conditions, **T** and **U** respectively, the boundaries of the eigenstrains, i.e. the dislocation lines, move to minimise the total energy.

Consider, as in figure (23), a polycrystalline volume Ω which may contain several phases Ω^k such that $\Omega = \bigcup \Omega^k$. Here $\mathbf{n}_\Omega$ denotes the unit outward normal vector on the boundary of Ω.
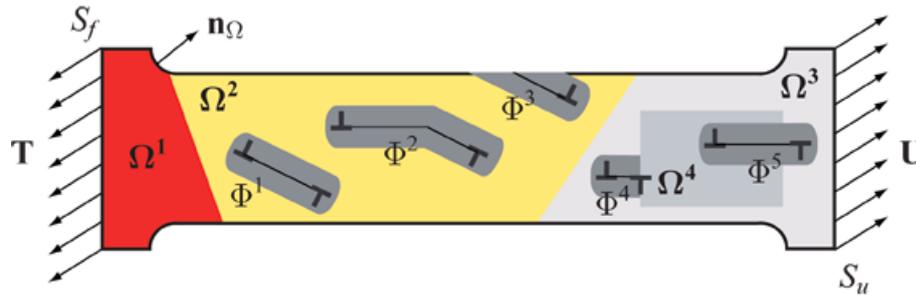
Figure 23 - Statement of the mechanical problem of a dislocated polycrystal. A description of all quantities can be found in the text. At mechanical equilibrium, all fields must satisfy equation (2.17).

In this example, each phase Ω^k represents a different case with respect to the eigenstrain distribution:

* A dislocation-free phase Ω^1.

* A dislocated phase Ω^2 where each dislocation i is represented by a coherent platelet inclusion Φ^i. Within Φ^i (of constant thickness h as in figure 22) an eigenstrain field exists. Outside the inclusions Φ^i and at their boundaries $\partial\Phi^i$, the eigenstrain is by definition equal to zero. This is illustrated for instance by the dislocation loop Φ^1.

Cross-slip (see Φ^2) requires precautions for the associated procedure of the localisation of the eigenstrain in the FE mesh. Moreover, the phase Ω^2 may contain dislocation loops Φ^3 which reach an external free surface.

* Phase Ω^3 contains another source of eigenstrain such as the precipitate Ω^4. In some cases, Ω^4 is considered as an elastic inclusion with the dislocation loop Φ^4 blocked at the internal interface $\partial\Phi^4$. In other cases, Ω^4 might also be plastically deformed. In that case, the interface is penetrable and the dislocation loop Φ^5 enters and glides from the phase Ω^3 into Ω^4.

The domain Ω can be subjected to tractions **T** prescribed at the boundary S_f, and displacements **U** at the boundary S_u. Locally, the boundaries may also include a plastic displacement $\mathbf{u}^P$ induced by dislocations that moved out the volume Ω^k in an earlier deformation stage. In addition, when a volume Ω^k is sheared by several dislocations j, the associated eigenstrain is denoted by $\varepsilon^p = \sum_j \varepsilon_j^p$.

In the limit of infinitesimal deformations considered in the present work, the total strain ε_{ij} is regarded as the sum of elastic strain ε_{ij}^e and eigenstrain ε_{ij}^p (see equation 1.9). The equilibrium state of the total volume is described by the mechanical fields that must satisfy equations (2.17) in every region of the simulated continuum $\Omega \setminus \bigcup \Phi^i$:

$$
\begin{aligned}
\varepsilon_{ij} &= \frac{1}{2}\big(u_{i,j} + u_{j,i}\big) \\
\sigma_{ij} &= C_{ijkl}\,\varepsilon_{ij}^e = C_{ijkl}\big(\varepsilon_{ij} - \varepsilon_{ij}^p\big) \\
\sigma_{ij,j} &= 0 \\
\sigma_{ij}n_{\Omega\,j} &= T_i \quad \text{at} \quad S_f \\
u_i &= U_i \quad \text{at} \quad S_u
\end{aligned}
\tag{2.17}
$$

The first equation of (2.17) gives the strain-displacement relationship. The elastic strain is related to stress σ_{ij} by Hooke's law, expressed by the second equation. The third equation of (2.17) gives the equations of stress equilibrium completed by specification of the boundary conditions for external tractions T_i and/or displacements U_i on the boundary of Ω.

Equations (2.17) are resolved by the FE code with the eigenstrain ε_{ij}^p computed by the DD code. The latter results directly from the movement of dislocations, driven by the stress equilibrated by the FE code. The numerical coupling between both codes is described in the following sections.

2.2.3 Computational methodology

The DD code accounts for the dislocation dynamics. It also computes the plastic strain generated by dislocation glide and the associated stress increment, just as any other classical constitutive law. Following the computational scheme presented in the previous section, the plastic strain is attributed to a coherent platelet of volume Φ^i.

The FE code computes the displacement and stress fields, solution of the boundary value problem, using the plastic eigenstrain distribution given by the DD simulation. For those domains that remain elastic, for instance Ω^1 in figure (23), the FE code can proceed without DD inputs. For multiphase structures, the local rules for the dislocation dynamics is different for each phase Ω^k. For instance different velocity laws are used in Ω^3 and Ω^4 in figure (23).

The coupling procedure involves two important steps. First, the stresses calculated at the IP of the FE mesh are interpolated to those positions on the segments where the PK force is computed. Next, the displacement jumps produced by the resulting motion of the segments are transformed into eigenstrains and transferred to the FE mesh. The first operation is an interpolation procedure essential to the calculation of the PK force, whereas the second one is a regularisation procedure (see figure 24).

Numerically, the FE part of the DCM works in a conventional manner except that, at the simulation step t_n, the increments of total deformation $\Delta\varepsilon_{ij}(t_n)$ are simultaneously predicted for all the IP instead of sequentially. Similarly, at the end of the time increment, the increment of plastic strain $\Delta\varepsilon_{ij}^p(t_n)$ and
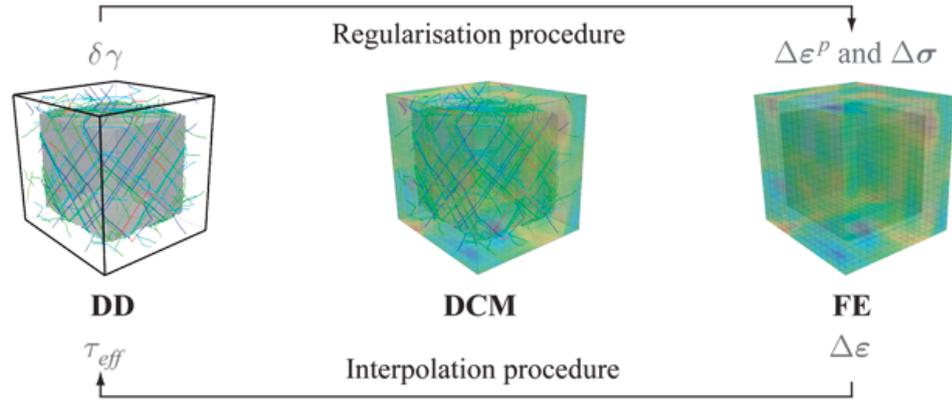
Figure 24 - The coupling between DD and FE consists on (i) an interpolation (FE⟼DD defines the stress on dislocation lines) and (ii) a regularisation (DD⟼FE defines the plastic strain field in the solid) procedures.

the reactions $\sigma_{ij}(t_{n+1})$ are obtained simultaneously from the DD code. In the DCM scheme the stress state has to be defined at all IP of the FE mesh at the beginning of each time step, because $\sigma_{ij}(t_n)$ serves as input for solving the DD part of the model and all dislocation segments move at the same time. The stresses at the IP of the FE mesh must be interpolated to the segment points where the PK force is defined in DD simulations. This is discussed in section 2.2.6. Once the forces on all the dislocation segments are known, a time step is performed by the DD code, which generates an increment of the plastic strain field $\Delta\varepsilon^p_{ij}(t_n)$. From $\Delta\varepsilon^p_{ij}(t_n)$ generated during the time increment Δt_n, the stresses at step $t_{n+1} = t_n + \Delta t_n$ are defined at the IP of the FE mesh:

$$\sigma_{ij}(t_{n+1}) = \sigma_{ij}(t_n) + \Delta\sigma_{ij}(t_n) \; , \qquad \text{and} \qquad (2.18)$$

$$\Delta\sigma_{ij}(t_n) = C_{ijkl}\Big[\underbrace{\Delta\varepsilon_{ij}(t_n)}_{\text{imposed by FE}} - \underbrace{\Delta\varepsilon^p_{ij}(t_n)}_{\text{imposed by DD}} \Big] \qquad (2.19)$$

Note that it is also possible to divide the time increment Δt_n imposed by the FE code into K smaller ones of duration δt_n for the DD code according to $\delta t_n = \frac{\Delta t_n}{K}$. In that case, the total strain increment $\Delta\varepsilon_{ij}(t_n)$ is written as $\Delta\varepsilon_{ij}(t_n) = K\delta\varepsilon_{ij}(t_n)$ and the stress is updated at the start of each DD increment k (with $k = 1 \ldots K$) according to

$$\sigma_{ij}(t_n + k\delta t_n) = \sigma_{ij}(t_n + (k-1)\delta t_n) + \delta\sigma^k_{ij}(t_n) \; , \qquad \text{and} \qquad (2.20)$$

$$\delta\sigma^k_{ij}(t_n) = C_{ijkl}\Big[\delta\varepsilon_{ij}(t_n) - \delta\varepsilon^p_{ij}(t_n + (k-1)\delta t_n) \Big] \qquad (2.21)$$

The way this increment of the eigenstrain field is regularised and associated to the IP of the FE mesh plays a key role in the DCM. This is discussed in the next section.

2.2.4 Regularisation of the slip

In the DCM scheme, the displacement jump associated to the dislocation loop propagates with the dislocation line on a specific crystallographic plane direction. It is then distributed over a slab of thickness h, as shown in figure (22). The small core region of a real dislocation is also included in the slab, and thus excluded from the elastic continuum, because linear elasticity is not valid there anymore [VAN95]. Here, this corresponds to a tube of radius $\frac{h}{2}$ around the dislocation line. In other words, the displacement jump associated to the Burgers vector is spread out over the region represented by the coherent inclusion Φ^i of the dislocation i.
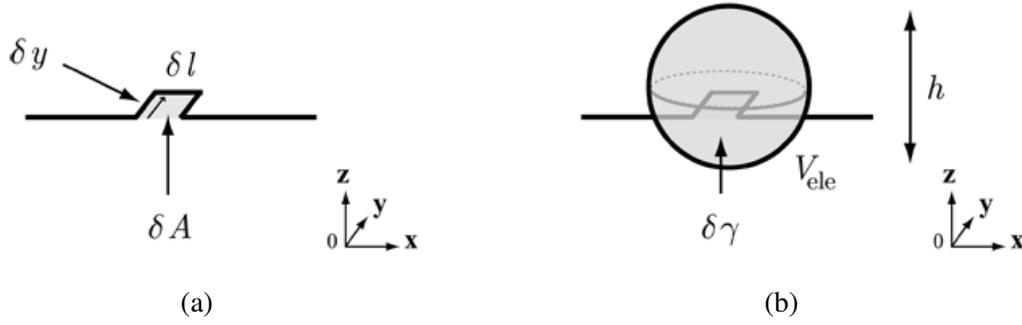
Figure 25 - (a) Area δA swept by an elementary segment of length δl, and (b) its corresponding homogeneous elementary shear strain $\delta \gamma$ induced by the displacement δy within an elementary volume V_{ele}.

In the following, the movement of a straight segment[2] of length L over a distance $v\delta t$ is split into smaller constituents. As illustrated in figure (25 a) this corresponds to a small distance δy that a segment of length δl can move in DD simulations. The total segment length L is thus written as $L = n\delta l$ and the distance $v\delta t = m\delta y$, with n and m integers. The length δl and the distance δy depend both on the direction of the movement and on the orientation of the segment. The segment of length δl is called elementary segment. Consider, as illustrated in figure (25 a) the elementary segment of length δl in the coordinate system specified by the Cartesian frame $\Re = (\mathbf{x}, \mathbf{y}, \mathbf{z}, \mathrm{O})$. Moving a distance δy, it sweeps an area $\delta A = \delta l \, \delta y$. Moreover, the movement of δl along δy generates an elementary shear $\delta \gamma$ (i.e. elementary eigenstrain). The elementary eigenstrain $\delta \gamma$ is calculated with respect to an elementary volume V_{ele} (see figure 25 b), which is a sphere of radius $\frac{h}{2}$ centered on the origin of the new elementary segment position. This incremental shear strain $\delta \gamma$ is obtained by (see equation 1.24):

$$\delta \gamma = \frac{b \, \delta A}{V_{\text{ele}}} = \frac{b \, \delta l \, \delta y}{V_{\text{ele}}} = \frac{6b \, \delta A}{\pi \, h^3} \qquad (2.22)$$

The incremental shear strain $\delta \gamma$ in equation (2.22) is then homogeneously distributed to the material points in the elementary spherical volume V_{ele} (see the grey area in figure 25 b). In a FE mesh the positions of the material points correspond to the position of each IP. This implies that h must be at least of the order of the size of the element [LEM99] [LEM01]. This is because if the element size is much larger than h, it becomes quite probable that V_{ele} does not contain any IP. Note that for these values of h, V_{ele} automatically includes the core region as well.

Next, the objective is to distribute each elementary eigenstrain generated by the movement of segment i to the FE mesh by using a sucession of elementary volumes V_{ele}, which together represent the complete inclusion Φ generated by the slip of a large segment. Formally, this numerical procedure is equivalent to the regularisation procedure recently proposed by Cai *et al.* [CAI06].

The recent developments made in the DCM during this thesis in order to optimise this computationally demanding procedure and to ensure a numerically efficient model are now presented. This is accomplished by adopting several approximations in the calculation of $\delta \gamma$ in equation (2.22). For that, the following geometrical entities, associated to a segment AB of length L (see figure 26 a), are introduced:

* The elementary volume V_{ele} (with its boundary drawn with solid grey circle), initially located at the origin A of the segment AB, after its displacement by δy.

* The domain $\mathcal{D}$, whose boundary is drawn in dashed grey lines, which is the union of all volumes occupied by V_{ele} if it would move continuously from A to B along the segment.

---

[2]For sake of clarity in this section, only one segment is here considered, so that the index i of the segment has been removed, i.e. $L^i = L$ and $v^i = v$.

(a)   (b)
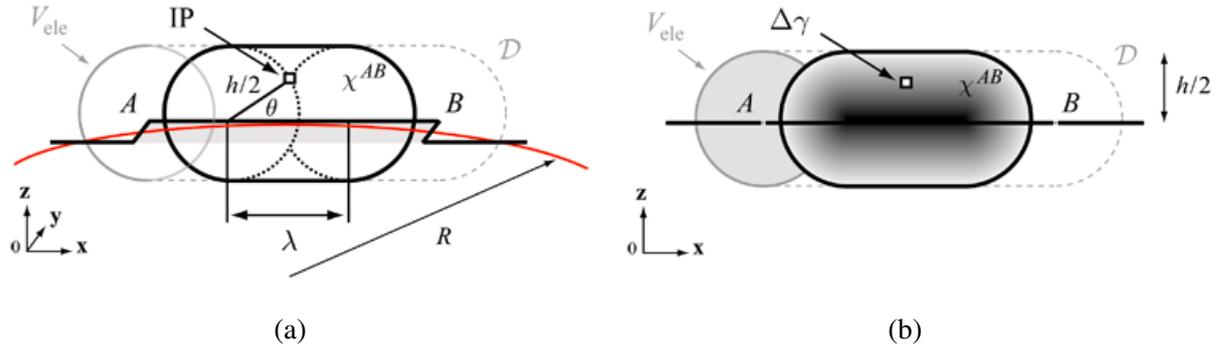
Figure 26 - Eigenstrain associated to a segment AB of a dislocation line (drawn in red). (a) View of an Integration Point (IP) inside the sheared domain $\mathcal{D}$. This domain corresponds to the volume occupied by V_{ele} if it would be moved from A to B along the complete segment AB. One volume χ^{AB} is associated to each IP through an internal length λ as defined in the text. (b) The corresponding heterogeneous distribution of eigenstrain within χ^{AB} where $\Delta\gamma$ is affected to the IP.

* The IP drawn with an open square, located by local cylindrical coordinates at $\left(\frac{h}{2},\ \theta\right)$.

* The volume χ^{AB} associated to one IP, whose plastic shear $\Delta\gamma$ is incremented in steps of amplitude $\delta\gamma$ because of the contributions of several elementary volumes V_{ele} along the segment AB.

Each IP within $\mathcal{D}$ receives elementary eigenstrains $\delta\gamma$ from those elementary volumes V_{ele} containing it. The total eigenstrain obtained in this way is denoted by $\Delta\gamma$. The number of elementary volumes containing a particular IP (and thus the $\Delta\gamma$ that gets attributed to it) depends on its position within $\mathcal{D}$. As a result, the distribution of $\Delta\gamma$ at all IP within $\mathcal{D}$ is heterogeneous[3]. For instance, with respect to its distance to the segment AB, the IP near the line get the maximum values of the plastic shear (shown in black in figure 26 b) and the IP near the boundary of χ^{AB} get the minimum values (shown in light grey). Now the plastic shear at all IP within $\mathcal{D}$ associated to the displacement δy of the segment AB is calculated. In order to evaluate it, an internal length λ is defined. This length is particular to each IP in $\mathcal{D}$ and represents, when expressed in units of δl, the number of elementary volumes that contribute $\delta\gamma$ to the IP (see figure 26 a). It is equal to $(h\cos\theta)$, and the associated incremental value of the plastic shear $\Delta\gamma$ of the IP is then given by

$$\Delta\gamma = \frac{b\,\lambda\,\delta y}{V_{\text{ele}}} = \frac{b\,(h\cos\theta)\,\delta y}{V_{\text{ele}}} \tag{2.23}$$

Computing this quantity for each IP inside $\mathcal{D}$ is an extensive calculation because it may contain many IP, the more so for long segments. For this reason, a simplification of the evaluation of $\Delta\gamma$ is proposed. The aim is to avoid calculating $\Delta\gamma$ for each IP in $\mathcal{D}$, but to affect an average $\langle\Delta\gamma\rangle$ to each IP instead. As a consequence, the approximation consists of replacing λ in equation (2.23) by an average distance $\langle\lambda\rangle$. As illustrated by two extreme cases, λ varies between 0 and h. The two extreme IP locations correspond to the case where one IP is on the segment AB of the dislocation line and the other at the boundary of $\mathcal{D}$. If the IP is exactly located on the segment, the associated length λ is maximum and its value is h (figure 27 a, with $\theta = 0$). The associated plastic shear is then maximum, i.e. $\Delta\gamma = \Delta\gamma_{\text{max}}$. When the IP is on the boundaries of $\mathcal{D}$, λ is minimum and the value is zero (figure 27 b, with $\theta = \frac{\pi}{2}$). Hence $\langle\lambda\rangle$ is given by the following integral calculation:

$$\langle\lambda\rangle = \frac{2}{h}\int_0^{\frac{h}{2}} \lambda\,\mathrm{d}z = \frac{1}{h}\int_0^{\frac{\pi}{2}} h^2\cos^2\theta\,\mathrm{d}\theta = \frac{h\pi}{4} \tag{2.24}$$

---

[3]For sake of clarity in figure (26 b), the heterogeneous distribution is only drawn within χ^{AB} but is similar for all $\mathcal{D}$, except near the extremities of the segment.
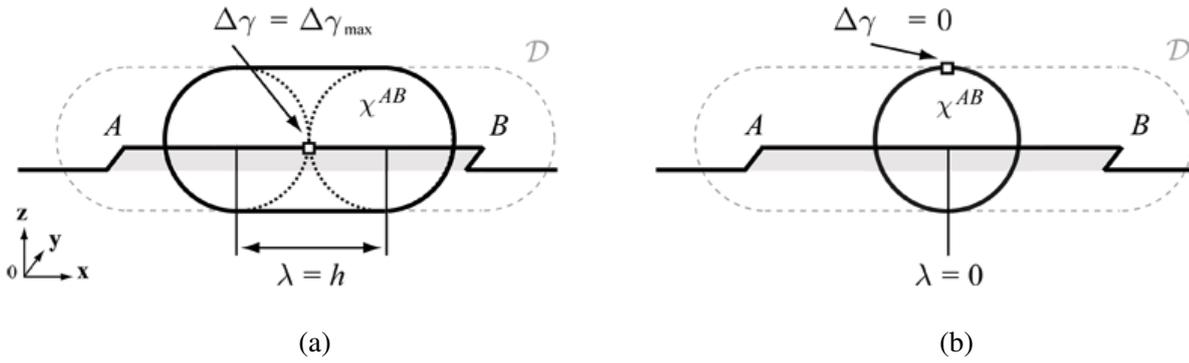
Figure 27 - Evaluation of $\Delta\gamma$ for two extreme cases. (a) The IP is located on the dislocation segment AB, and (b) on the boundary of $\mathcal{D}$.

with $dz = \frac{h}{2}\cos\theta\, d\theta$. According to equation (2.23), $\langle\Delta\gamma\rangle$ is related to $\langle\lambda\rangle$ by

$$\langle\Delta\gamma\rangle = \frac{b\langle\lambda\rangle\delta y}{V_{\text{ele}}} = \frac{3}{2}\frac{b\,\delta y}{h^2} \tag{2.25}$$

The expression (2.25) is an average quantity of equation (2.23) which is calculated once for each segment, and affected to all IP within $\mathcal{D}$. In comparison with the procedure where $\Delta\gamma$ is calculated by the passing of V_{ele} for each IP within $\mathcal{D}$, this regularisation procedure offers a considerable gain in terms of CPU time.

However, the extremities of segment AB need a special treatment. As illustrated in figure (28 a), at each instant a segment i (i.e. segment AB) is joined to two immobile segments $i-1$ and $i+1$, i.e. immobile at least during the calculation of $\langle\Delta\gamma\rangle$. By definition, an immobile dislocation segment does not generate plastic shear. Nevertheless, one can see in figure (28 a) that V_{ele} at both extremities affect the immobile segments $i-1$ and $i+1$. Thus, precautions must be taken in these regions where the approximation $\langle\lambda\rangle$ is not justified.

Consider V_{ele}^A and V_{ele}^B as V_{ele} at points A and B, respectively. Both volumes are drawn in grey in figure (28). The position of each point A and B is given in the frame $\Re$ by their respective vectors $\mathbf{c}^A$ and $\mathbf{c}^B$. With $\boldsymbol{\zeta}$ the unit line vector of the segment, $\mathbf{c}^B = \mathbf{c}^A + L\boldsymbol{\zeta}$. In addition, the position of the IP is given in the frame $\Re$ by $\mathbf{c}^{\text{IP}}$. For sake of clarity, consider only the treatment of V_{ele}^A associated to the point A. A compatible function is introduced, i.e. compatible in the sense that the plastic shear is continuous between V_{ele}^A and $\mathcal{D}\backslash V_{\text{ele}}^A$. A first order approximation is to use an additional linear regularisation function inside V_{ele}^A. Equation (2.25) is then modulated by a linear function Γ_A varying between 0 if IP is located
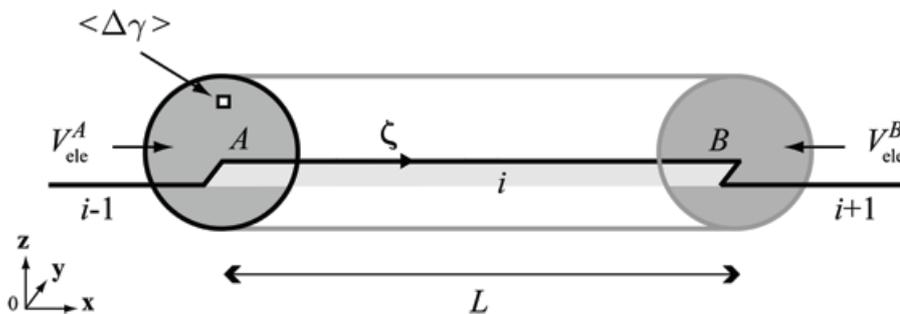
Figure 28 - The regularised and compatible function for one segment at its extremities.

at $\mathbf{c}^{\mathrm{IP}} = \mathbf{c}^A - \frac{h}{2}\zeta$, and 1 if IP is located at $\mathbf{c}^{\mathrm{IP}} = \mathbf{c}^A + \frac{h}{2}\zeta$. The same treatment is applied for V_{ele}^B with Γ_B, and the final formulation of equation (2.25) including the treatment of the extremities of a segment is then defined by

$$\langle \Delta\gamma \rangle = \frac{b\langle\lambda\rangle\delta y}{V_{\mathrm{ele}}}\,\Gamma_A\,\Gamma_B = \frac{3}{2}\frac{b\,\delta y}{h^2}\,\Gamma_A\,\Gamma_B \tag{2.26}$$

where

$$\Gamma_A = \left\{ \begin{array}{ccc} \frac{1}{h}\,\min\Big(L,\big[\mathbf{c}^{\mathrm{IP}} - (\mathbf{c}^A - \frac{h}{2}\,\zeta)\big]\cdot\zeta\Big) & \mathrm{if} & \mathrm{IP} \in V_{\mathrm{ele}}^A \\ 1 & \mathrm{if} & \mathrm{not} \end{array} \right. \tag{2.27}$$

and

$$\Gamma_B = \left\{ \begin{array}{ccc} \frac{1}{h}\,\min\Big(L,\big[(\mathbf{c}^B + \frac{h}{2}\,\zeta) - \mathbf{c}^{\mathrm{IP}}\big]\cdot\zeta\Big) & \mathrm{if} & \mathrm{IP} \in V_{\mathrm{ele}}^B \\ 1 & \mathrm{if} & \mathrm{not} \end{array} \right. \tag{2.28}$$

The function $\min(L, x)$ is introduced in equations (2.27) and (2.28) for the particular case of segments of length $L < \frac{h}{2}$. The plastic distortion increment affected to the IP in $\mathcal{D}$ due to the movement along δy of the segment then becomes

$$\Delta\beta_{ij}^p = b_i n_j \langle \Delta\gamma \rangle \tag{2.29}$$

and the corresponding increment of plastic strain $\Delta\varepsilon_{ij}^p$ is given by the symmetric part of $\Delta\beta_{ij}^p$ as

$$\Delta\varepsilon_{ij}^p = \frac{1}{2}\left(\Delta\beta_{ij}^p + \Delta\beta_{ji}^p\right) \tag{2.30}$$

Each mobile segment in the computational cell is treated in this manner. This treatment is then repeated for the remaining displacements $(m-1)\delta y$ of the segment. Generally, m can be set very small, so that no optimisation need to be carried out there. The regularisation procedure defined here works well in handling crystals of any types of symmetry, as will be shown in sections 2.3 and 2.4. Nevertheless, equation (2.26) must be modified to account for interfaces and surfaces, as will be discussed in the next section.

2.2.5   Dislocation eigenstrain in the vicinity of interfaces and surfaces

In section 2.2.4, dislocations were considered inside a homogeneous material phase. This is now extended to dislocations in heterogeneous materials with interfaces and free surfaces (for instance Φ^4 and Φ^5 in figure 23) or external free surfaces (Φ^3 in figure 23). Two different cases must be considered, as shown in figure (29 a and b).

In the case of a penetrable interface, dislocations can cross the interface separating two phases Ω^1 and Ω^2. In our case, where no residual Burgers vector is left at the interfaces, the eigenstrain must pass continuously from phase Ω^1 to Ω^2 (see figure 29 a). A penetration condition has to be fulfiled in the DD code according to a local constitutive rule which fixes the physical properties of the interface, but otherwise no special treatment is required and the regularisation procedure defined in section 2.2.4 applies here as well. The geometry of the interface must be defined in a coherent way in the DD and FE codes. Note that due to the spherical shape of V_{ele} (drawn in the grey dotted circle in figure 29 a) the plastic shear remains homogeneous during the glide of the dislocation. In comparison with a rectangular elementary volume, as used in earlier versions of the DCM [LEM99] [LEM01], the spherical volume does not create artefacts such as overlap of plastic shear or voids, specially at the interface Ω^1/Ω^2. Furthermore, these artefacts appear when the slip plane changes orientation, for instance when passing an interface between two grains, or in cross-slip.

(a)   (b)
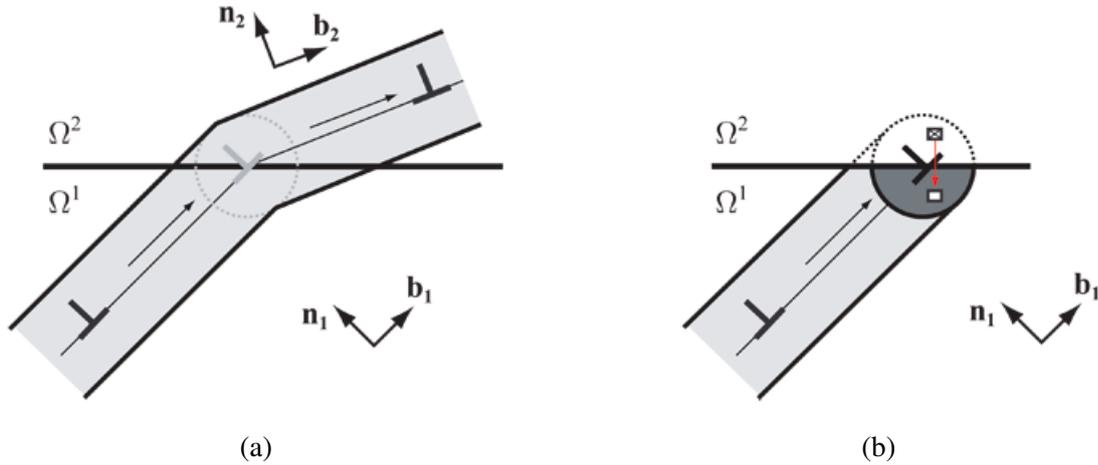
Figure 29 - Eigenstrain problem in the DCM in the vicinity of phase boundaries. (a) Interaction between dislocations and penetrable interfaces where $\mathbf{b}_1$, $\mathbf{n}_1$ and $\mathbf{b}_2$, $\mathbf{n}_2$ denote the Burgers vectors and the normal slip planes of Ω^1 and Ω^2, respectively. (b) Interaction between dislocations and free surfaces or impenetrable internal surfaces.

The cases of free surfaces and non-penetrable interfaces require a modified calculation of the eigenstrain. As illustrated in figure (29 b), the eigenstrain must be cut off at the interface, because no plastic deformation exists in Ω^2 on the other side of the interface. For both cases, the same treatment is performed, in which the interface is thought of as a mirror. When an IP within Ω^2 (the marked square in figure 29 b) would be attributed an incremental plastic strain from the regularisation procedure, this plastic strain is instead associated to its mirror image with respect to the interface (open square). The localisation of the plate-like inclusion and its corresponding eigenstrain are conserved inside the crystal without affecting any plastic strain to Ω^2 and the eigenstrain remains homogeneous in Ω^1. This mirror correction can be accounted for numerically in an efficient manner by tabulating all IP within Ω^1 at a distance $\frac{h}{2}$ from the interface and multiplying by two their corresponding eigenstrains.

To conclude this section, the numerical method described above provides a solution for crystals of finite dimensions. The DCM scheme allows to treat interface problems naturally without introducing computational costs to account for dislocation interactions with internal and external free surfaces (for instance micro-crack problems), and dislocation interactions with rigid particles (for instance γ/γ' problems, see section 2.4).

2.2.6   Calculation of the stress field

Once equation (2.30) is calculated at every IP of the FE mesh, the stress fields can be obtained as part of the global solution of the mechanical problem expressed by equations (2.17). From the increment of the plastic strain field $\Delta\varepsilon_{ij}^p(t_\mathrm{n})$ obtained by equation (2.30) at the previous DD step, the incremental stress field $\Delta\sigma_{ij}^\mathrm{IP}(t_\mathrm{n})$ is calculated at every IP using the explicit scheme of equation (2.19). This stress is then interpolated to the point of the dislocation segment where the PK force must be calculated. This interpolation procedure is split into three sub-steps.

The first step is an extrapolation of σ_{ij}^IP to the nodes of the FE mesh (see figure 30 a). Each node n of the mesh receives contributions from the elements to which it is attached. The value of σ_{ij}^IP at a given IP, at position $\mathbf{x}$ and at corresponding parametric coordinates Ψ_e inside the element e, is expressed in terms of the M interpolation functions $N^m(\Psi_e)$ for the M nodes attached to the element, and the M (unknown)

nodal values $\sigma_{ij}^{\text{N}m}$ according to

$$\sigma_{ij}^{\text{IP}} = \sum_{m=1}^{M} N^m(\Psi_e)\sigma_{ij}^{\text{N}m} \tag{2.31}$$

Here m corresponds to the local numerotation of the nodes attached to the element. By inversing the equation (2.31), the unknown nodal values can readily be determined from the solution of the inverse problem. Thus, for each phase Ω^k the stresses defined at the IP are transformed into nodal stresses by using the inverse shape functions of the element.

(a)   (b)
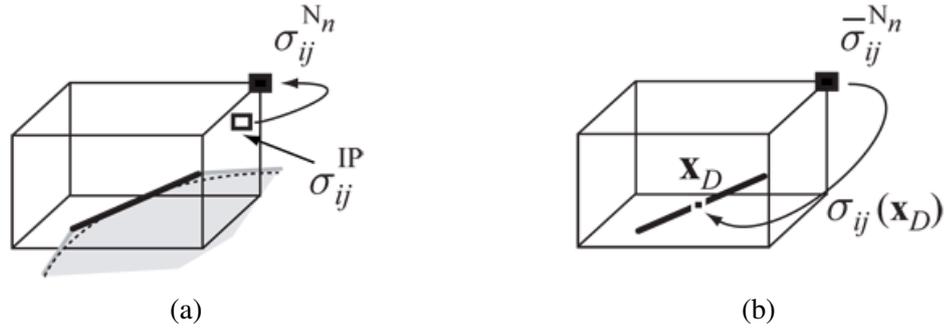
Figure 30 - Extrapolation and interpolation (see figure 24) in the DCM scheme where a dislocation segment (black segment) of a dislocation line (dotted line), sweeps an area (grey area) located in an element of the FE mesh. (a) Extrapolation of the stresses calculated at the IP σ_{ij}^{IP} to the value $\sigma_{ij}^{\text{N}n}$ at node n. (b) Interpolation of the average stress value $\bar{\sigma}_{ij}^{\text{N}n}$ calculated at the node n to the midpoint $\mathbf{x}_D$ of the dislocation segment.

In a second step, an additional calculation on nodal stress values common to its attached elements, must be exercised. This is because the shape function used in the first step interpolation does not impose continuity of the stress field between elements, i.e. the values $\sigma_{ij}^{\text{N}n}$ calculated separately for each element to which the node belongs are not necessarily the same. The existence of such a discontinuity in conventional FE simulation cannot be accepted in the DCM. The DD simulation requires a continuous description of the stress field in the solid to integrate a continuous motion of dislocations. Hence, to avoid numerical discontinuities at the boundaries between elements, the second step consists of a calculation of the average stress value $\bar{\sigma}_{ij}^{\text{N}n}$ at each node n.

The third step consists of interpolating the stress $\bar{\sigma}_{ij}^{\text{N}n}$ in the usual manner to the points $\mathbf{x}_D$ where the PK force on each dislocation segment is calculated. The stress $\sigma_{ij}(\mathbf{x}_D)$ is then calculated by

$$\sigma_{ij}(\mathbf{x}_D) = \sum_{m=1}^{M} N^m(\Psi_e)\bar{\sigma}_{ij}^{\text{N}m} \tag{2.32}$$

The quality of this interpolation is directly related to the shape functions of the elements used in the FE simulation. For this reason, the DCM scheme uses quadratic FE elements of 20 nodes and 27 integration points.

However, it was shown by Groh *et al.* [GRO04] that for massive simulations involving many dislocations, this procedure is numerically insufficient. The element size is often larger than the mean distance between dislocations, and the shape function used to interpolate the stress then becomes inadequate to capture the variations of the stress between interacting dislocations. This is the major limitation of the model: in some cases with many dislocations, it is not possible to account for the short-distance reactions between dislocations (see for instance [GRO03b]).

A simple solution was proposed to overcome this limitation. In the DD code, the analytical self-stress field $\sigma_{ij}^{\text{local}}$, given by equations (2.3) and (2.4), is superimposed to the stress prediction yielded by the FE code (equation 2.32) when dislocation segments are at close range. This procedure only includes segments located in a volume limited to the regularised core region of radius $\frac{h}{2}$ around the dislocation line. This correction is essential if one wishes to realistically model dislocation interactions and reactions at short distances (see for instance section 2.3.3). This part of the DCM calculation is easy to implement but it significantly increases the computational burden.

To summarise this section, two contributions to the stress field are considered in the DCM calculations: (i) the long-distance contribution is computed numerically by a FE method supported by the theory of eigenstrains. In addition, (ii) the analytical expressions for the elastic field of the segments are used within the regularised eigenstrain volume to take into account the short-distance interactions.

2.2.7 Numerical procedures

The two codes, microMégas and ZéBuLoN, are coupled into a unified system as summarised in figure (31) to form the Discrete-Continuous Model.
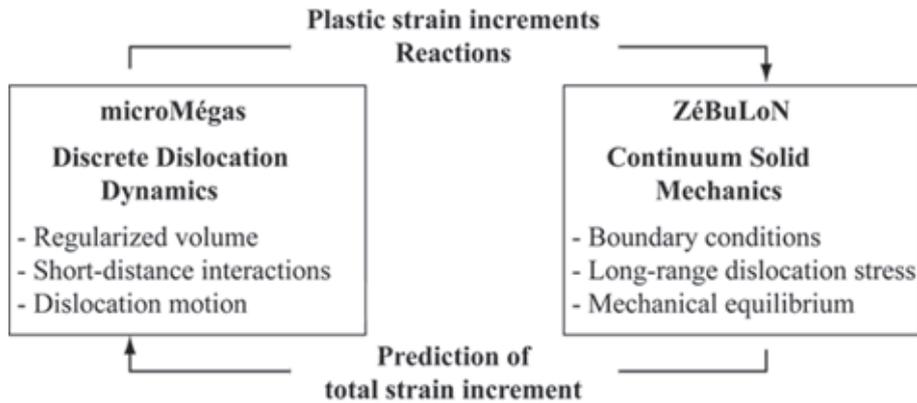
Figure 31 - Summary of the Discrete-Continuous Model.

Both codes run independently, but wait for some input provided by the other one at certain steps of the computations (see Appendix B for information on the acquisition and the basic handling of the hybrid code). They are strongly coupled by a quasi-Newton algorithm, i.e. convergence is verified at every coupled time increment, and the tangent matrix is approximated by the local tensor of elasticity. In principle, the DCM deals with all possible boundaries, interfaces and dislocations in heterogeneous materials, which has the following features: (i) at time t_n, all fields $\boldsymbol{\sigma}$, $\boldsymbol{\varepsilon}$, ε^p and $\mathbf{u}$ are supposed to be known to fulfil equation (2.17). Then, the displacements $\mathbf{u}(t_{n+1})$ in the crystal under some boundary conditions is predicted by the FE code. Then $\Delta\varepsilon(t_{n+1})$, calculated from the prediction $\mathbf{u}(t_{n+1})$, is passed to the DD code. There (ii), the stress is determined with equations (2.18) and (2.19), from which the PK forces for all segments can be calculated to drive the dislocation dynamics. By solving equation (2.10) and taking into account all possible dislocation reactions and obstacles, the new positions $\mathbf{x}^i(t_{n+1})$ of all dislocation segments i are known. Finally (iii) the plastic shear increments (i.e. the eigenstrains) $\Delta\gamma^i$ are distributed to the IP and the plastic strain increment $\Delta\varepsilon^p(t_n)$ during Δt_n can be expressed. The localised plastic quantities are used to calculate the reaction $\boldsymbol{\sigma}(t_{n+1})$ which is then passed back to the FE code, along with $\Delta\varepsilon^p(t_n)$. If this stress verifies the mechanical equilibrium, the next increment Δt_{n+1} is started, if not, a new Newton-Raphson iteration is started. In practice, due to the fact that the coupled time step is very small (e.g. $10^{-10} - 10^{-12}$ s for the present simulations), convergence is reached after only one coupled iteration.

2.3 Simple test cases and validation of the DCM

2.3.1 Initial dislocation configurations and boundary conditions

As mentioned above, all dislocations in the DCM are considered as plate-like inclusions causing eigen-strains. This implies that the initial state of dislocation in the simulated volume must consist of closed dislocation loops. Dipolar loops, i.e. four connected edge segments with the same Burgers vector, are placed at random positions in each phase, and left to expand. On subsequent loading, the dislocation lines emitted from the dipolar loops can act as dislocation sources. Figure (32 a) shows a square dipolar dislocation loop, defined as four $\{001\}$ edge segments in a (001) slip plane, located in the middle of a parallelepipedic volume of dimension $L^3 = 0.48 \times 0.50 \times 0.52$ μm^3. In this example, a simple cubic crystal lattice is considered for reason of simplicity. The FE mesh consists of $16 \times 16 \times 16$ quadratic elements to which PBC are applied. All segments are initially 0.25 μm long, and the solid is elastically isotropic with $\mu = 51$ GPa, and $\nu = 0.37$. Figure (32 a) shows the displacement $\mathbf{u}^P$ caused by the dipolar loop (the greyscale goes from white for $+\|\mathbf{u}^P\|$ to black for $-\|\mathbf{u}^P\|$).

(a) (b)
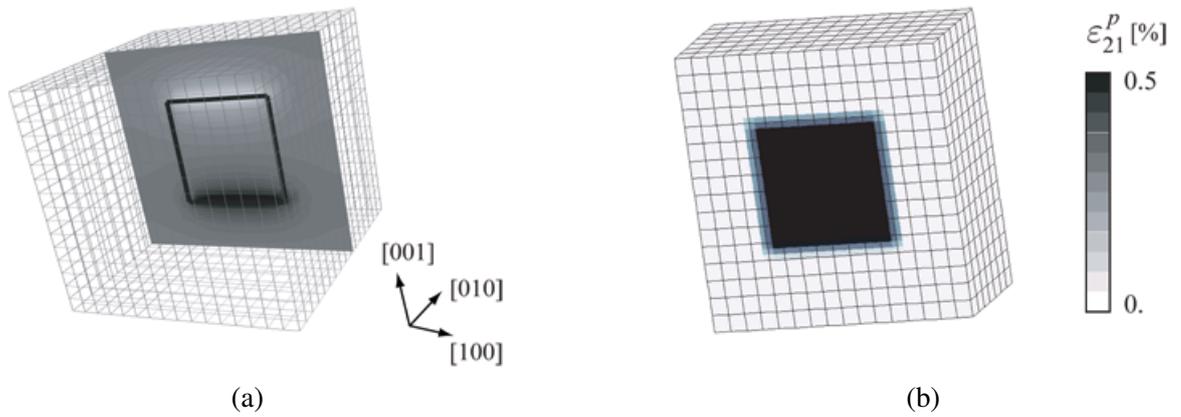
Figure 32 - (a) Initial dipolar dislocation loop in a (001) slip plane at the centre of the simulated volume, discretised by $16 \times 16 \times 16$ quadratic brick elements. The Burgers vector of the loop is $\mathbf{b} = b\,\mathbf{z} = b\,[001]$. Illustration in greyscale of the displacement (the scale goes from white $+\|\mathbf{u}^P\|$ to black $-\|\mathbf{u}^P\|$) due to the presence of the dislocation segments. (b) Eigenstrain associated to the dislocation loop at the integration points in the finite element mesh. The regularisation of the eigenstrain discussed in section 2.2.4 delivers a uniform plastic shear field inside the loop.

The initial dipolar loop is created with a Volterra-like process: two edge segments of the same initial length and with the same Burgers vector but opposite line direction are placed at the same initial position. Instead of annihilating, one of the segments is held at its original position, whereas the other is moved a previously specified distance along its slip direction. The displacement jump created in this manner is distributed to the IP of the FE mesh as an eigenstrain by the process described previously. Figure (32 b) shows the eigenstrain ε_{21}^p associated to the plate-like inclusion simulated via this process. To validate the interpolation procedure of equation (2.32), a stress component calculated with the DCM is compared to the exact analytical solution (see figure 33 a) for the elastic stress field of the same dislo-cation configuration. This comparison is performed for the stress component σ_{31} of two edge dislocation segments of the dipolar loop. Figure (32) shows σ_{31} in a cross-section of normal [100] centered on the dipolar loop inside a periodic volume. The results obtained with the interpolation procedure defined above are plotted in figure (33 b). Figure (33 c) shows the relative error η between the analytical and numerical calculation of σ_{31}. As illustrated in figure (33 c), at distances larger than h (the eigenstrain regularisation dimension), $\eta < 4\%$. This shows the accuracy of the interpolation procedure described in
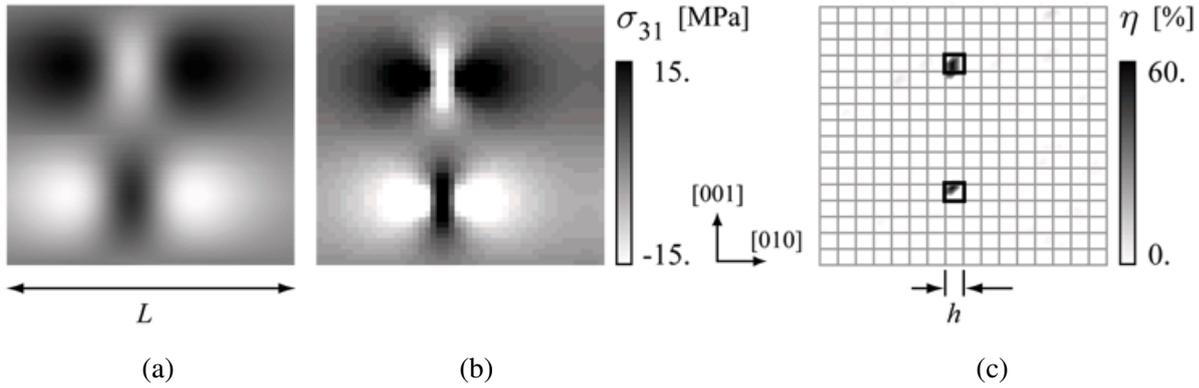
Figure 33 - Validation of the calculation of the stress field due to the dipolar loop shown in figure (32 a). (a) Stress component σ_{31} given by the theoretical solution and (b) the corresponding component computed by the DCM. The magnitude of the stress is represented at the same scale. (c) Relative error η between both stress components: it shows the areas (marked by thick squares) where the interpolation procedure fails to yield the correct value. It corresponds to the size of the volume of the regularisation procedure, here approximatively the size of one element of the finite element mesh.

section 2.2.6. The component σ_{31} obtained by the DCM fully agrees with the complex solution given by the elastic theory of dislocations. Nevertheless, in conformity with the discussion of the regularisation procedure in section 2.2.6, the elastic singularity at the dislocation line is smeared out by the regularisation procedure. Thus, at distances smaller than h, the interpolation procedure fails to yield the correct stress value, and η is of the order of 60%. This result justifies the short-distance stress field correction discussed in section 2.2.6. Its benefits at short distances will be illustrated in section 2.3.3.

2.3.2   Frank-Read source

The second test case is the Frank-Read (FR) source mechanism. This simple mechanism illustrates a way of introducing dislocation sources in the simulations and validates the stress calculation by carrying out a classical model calculation of the critical stress required to activate the FR source.

One way of creating a FR source in the DCM is to use a dipolar loop, such as the one described in the previous section (see figure 32), and artificially immobilise three of the four segments. Under loading the remaining mobile segment will act as a FR source. The critical shear stress for bowing out a dislocation
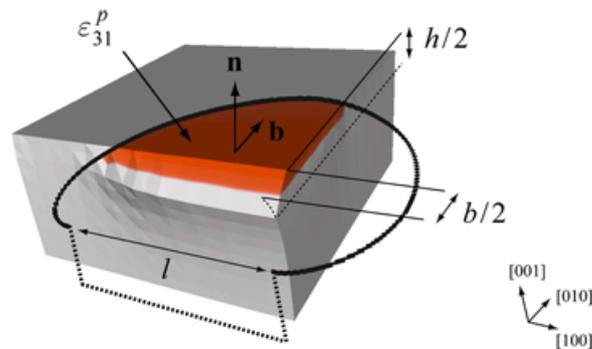
Figure 34 - The critical shape of an edge Frank-Read source as obtained by the DCM. The eigenstrain slab ε_{31}^{p} of thinkness h used in the DCM computation is illustrated (in red): **n** is the glide plane normal and **b** is the Burgers vector. Due to the presence of the eigenstrain, it shows the displacement jump of value b. Triangular visible facets at some surfaces do not represent the finite element mesh, but are due to the visualisation software Paraview.

segment or operating a FR source is a classical benchtest of conventional DD simulations [SCH96] [GOM99]. Here the critical stress of a FR source of initial length 0.1 μm is calculated with the DCM. The DCM yields $\tau^{FR} = 116$ MPa, whereas the classical DD simulation yields $\tau^{FR} = 113$ MPa. The benchtest shows the accuracy of the hybrid method, and the agreement between both simulations is a confirmation that the DCM correctly reproduces the stress field of dislocations.

Figure (35) shows snapshots of the FR source operating in a cubic plane in a periodic cell. The snapshots were taken at increasing time steps. An uniform eigenstrain ε_{21}^{p} is present inside the dislocation loop. At each passage of a novel dislocation, the magnitude of the displacement caused by the eigenstrain increases by one Burgers vector. This test shows the capability of the DCM to describe the uniform eigenstrain distribution due to each moving dislocation.
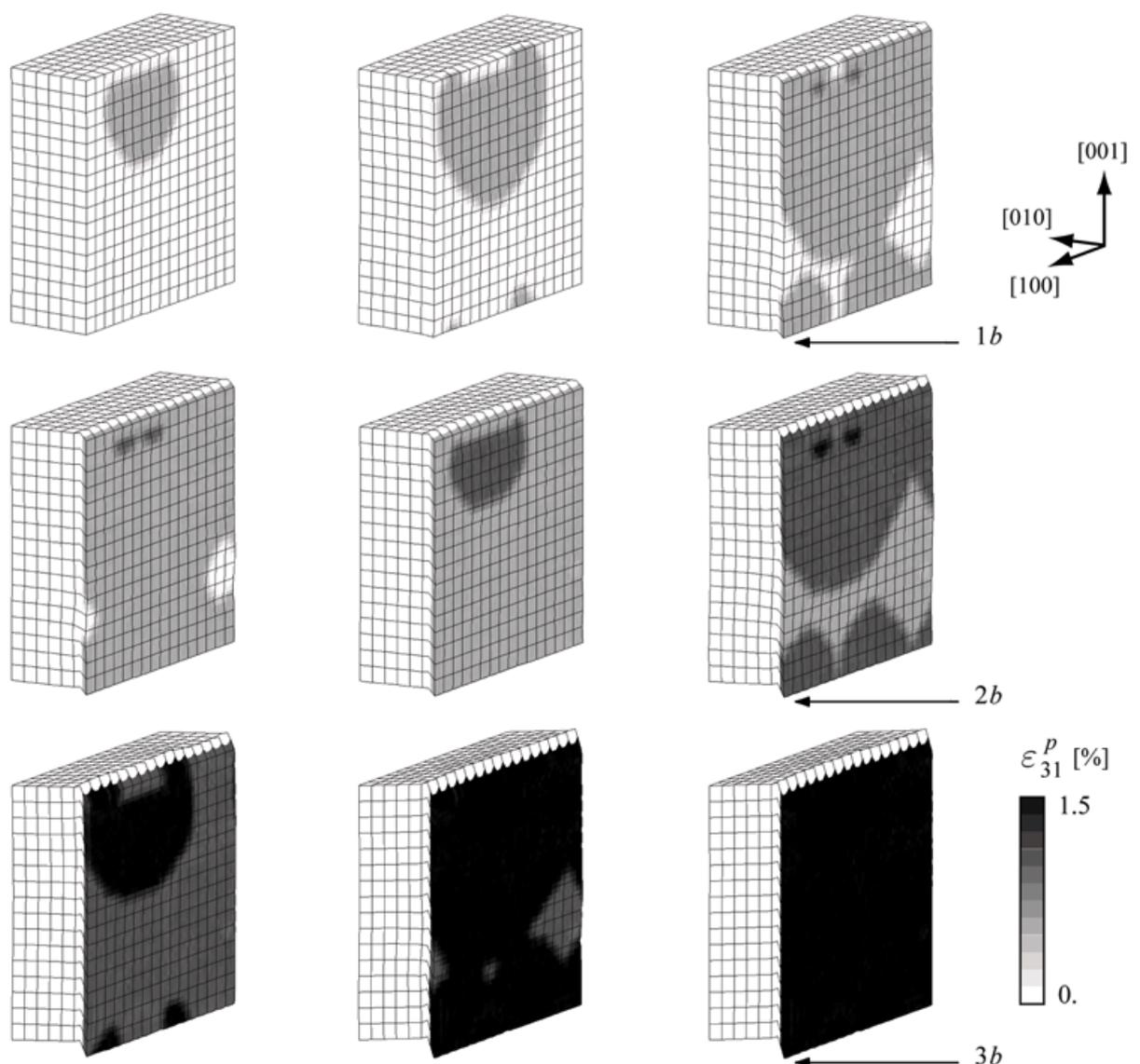
Figure 35 - 3D simulation of Frank-Read source under periodic boundary conditions on a cubic plane: successive snapshots of the cross sections of the operating slip plane (in which the source segment bows out) show the evolution of the Frank-Read source. At each passage of a dislocation (represented in greyscale) the shear displacement caused by each dislocation is increased by b. The displacements are magnified by a factor of 100 for better visualisation.

2.3.3   Dislocation reactions

This section shows the importance of the contribution of the additional stress $\sigma_{ij}^{\text{local}}$ to the DCM, as explained in section 2.2.6. The aim is to show that the DCM can treat junction formation with accuracy. A simulation of Lomer junction zipping is carried out. This benchtest is important because short-distance interactions control many properties of plastic flow such as dislocation patterning and work hardening in fcc crystals.

Figure (36 a) presents the simulation of two attracting segments with Burgers vectors $[\bar{1}10]$ and $[10\bar{1}]$ respectively, on intersecting octahedral slip planes. Three simulations have been performed with PBC, using the standard DD simulation (figure 36 b), the DCM with the short-distance correction $\sigma_{ij}^{\text{local}}$ (figure 36 c), and the DCM without this local correction (figure 36 d). The results of these simulations are shown at two instants t_1 and t_{eq}, with $t_{\text{eq}} > t_1$. The latter corresponds to the equilibrium (reference) state of the junction in each simulation. This figure shows that the two attractive segments approach each other rapidly and that at contact they form a junction segment of type $[01\bar{1}]$. On the one hand, figure (36 d) shows that no junction has been formed during the simulation. This is due to the local stress field given by the FE code, which is not in agreement with dislocation theory close to the dislocation line. On the other hand, as illustrated in figure (36 b and c) the zipping length of the junction for both standard DD and DCM with the local correction are similar.

In summary, when the short-distance stress field correction discussed in section 2.2.6 is taken into account, the contact interactions between dislocations are well reproduced. Tests have been carried out to verify that this is the case for dislocation-dislocation interaction, junction formation, dipole formation, as well as coplanar dislocation annihilation and cross-slip induced annihilations.

(a)   (b)   (c)   (d)
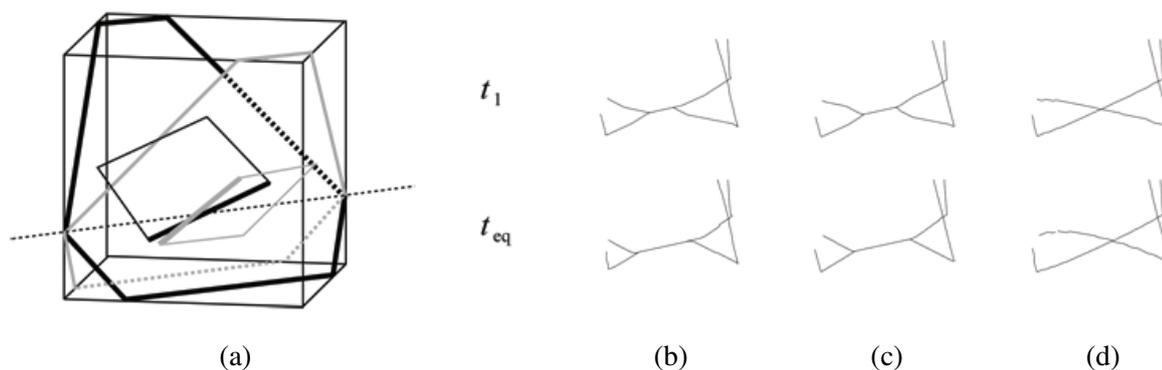
Figure 36 - (a) Geometry involved in the dislocation-dislocation interaction in simulation of a junction of two attracting dislocation segments. The results of simulations are shown at two instants, t_1 and t_{eq} ($t_{\text{eq}} > t_1$) for (b) the standard DD simulation, (c) the DCM with the short-distance correction, and (d) without this local correction.

2.4   DCM studies of plastic deformation in γ/γ' superalloys

2.4.1   Motivation

This section presents DCM simulations of various (micro)plasticity phenomena in γ/γ' superalloys. First, the mechanism of γ' precipitate cutting by superdislocations, described in section 1.1.3.5, has been implemented. This is needed to calculate the flow stress of nickel-based γ/γ' superalloys containing up to 73 vol.-% of precipitates by DD simulations of a dislocation pair gliding on {111} planes, for temperatures up to 850°C. It is calculated for different composition-related parameters (friction stress and APB energy), as well as for different microstructural parameters (channel width, precipitate volume fraction

and the geometry of the intersection of the $\{111\}$ glide plane with the precipitate). The aim is to set the simulation parameters in order to reproduce the mechanical behaviour of an industrial superalloy with high precipitate volume fraction in massive calculations, and to predict the dependence of the Critical RSS (CRSS) as a function of temperature.

Then, two massive simulations have been carried out at high temperature. The channel width dependence of the flow stress and of the stored dislocation density are investigated at 850°C. The size effect is interpreted at meso- and macroscale to highlight precipitate strengthening and the Orowan mechanism.

Finally, the anisotropic mechanical response is analysed with the DCM. At 850°C, two tensile loading cases are simulated: one with the [001] axis oriented along the tensile direction, and another with the [111] axis. The resulting stress-strain curves, stress distributions, interfacial dislocation structures and basic dislocation reactions underlying the mechanical response are analysed, and the simulated results are compared with experimental data from the literature.

Even though the sensitive effects of temperature and strain rate on mechanical properties of superalloys are well-known in the literature, a thermally activated mobility law of dislocations has not been used in the DCM. Several reasons explain the choice. First, a physically realistic relation between dislocation velocity and applied stress is difficult to establish due to the lack of knowledge of the thermally activated mechanisms controlling by dislocation glide, cross-slip or climb in superalloys. Molecular dynamics may give guidelines to define and adjust such a relationship, but such simulations have not been performed yet. Secondly, the thesis has not been focused on the simulation of the mechanical behaviour of a crystal nickel-based superalloy over a wide strain rate and temperature, but the interest here is the dislocation-precipitate interactions at only one temperature (for instance, the stress distributions or interfacial dislocation structures within the γ/γ' microstructure). All the above simulations have been carried out at 850°C, where precipitates are assumed to be elastically deformed. That is why a simple linear dislocation mobility law is used (see equation 2.9), and the strain rates applied for simulations are larger than the rates performed in laboratory tests.

2.4.2 Dislocations − γ' precipitates interactions

2.4.2.1 Motivation

The interaction between dislocations and precipitates is a classical case where the determination of plastic flow cannot always be evaluated by simple superposition rules. This problem appears to be critical when investigating hardening in γ/γ' superalloys. Recently, Mohles *et al.* [MOH99] [MOH01] [MOH04] have performed numerous two-dimensional DD simulations in which one or a few dislocations glide in a plane intersected by many coherent precipitates, but at a low volume fraction. Rao *et al.* [RAO04] [RAO06] have carried out DD simulations on γ/γ' superalloys with up to 40 vol.-% of coherent precipitates. In the later work, special attention was paid to the low-temperature yield stress in the cutting regime of small precipitates. In order to extend the work of Rao *et al.* [RAO04], DD investigations are carried out here for predicting the CRSS in the range of high volume fractions, between 40% and 70%. Their purpose is twofold. In the first place, ingredients for future massive DCM simulations of γ/γ' superalloys are set up and evaluated. Moreover, valuable design guidelines for the development of superalloys and for determining the influence of the microstructural parameters on the mechanical properties can be obtained by these simple computer experiments.

2.4.2.2 Strengthening mechanisms

The strength of the γ phase

Plastic yield in superalloys is controlled by the motion of dislocations in the γ matrix channels and their interactions with γ' precipitates and other dislocations. In precipitation-hardened alloys, dislocation-precipitate interactions include Orowan looping (see figure 7 a) and precipitate cutting (see figure 7 b).

In nickel-based superalloys with high precipitate volume fraction, both mechanisms are observed under different deformations or microstructural conditions. From the classical review paper of Pollock and Argon [POL92], the initial microstructure contains dislocations in the matrix, whereas the precipitates are free of dislocations. Upon mechanical loading, dislocations first move through the channels, thereby pressing segments of dislocations against the γ/γ' interfaces.

In the channels, dislocation motion is hindered by the interactions with solute atoms. As mentioned in section 1.1.3.2, the corresponding chemical force has been calculated and estimated by the corresponding friction stress at 107 MPa. In the DD simulations here, this solid-solution friction stress is taken into account through a stress τ_{SS} opposing the dislocation motion, and this is considered as the elementary mechanism controlling the CRSS of the γ phase.

The strength of the γ' phase

The cutting of coherent intermetallic γ' precipitates is controlled by glide of $\langle 110 \rangle$ superdislocations (see section 1.1.3.5). Such superdislocations are pairs of $\frac{1}{2}\langle 110 \rangle$ dislocations (a leading dislocation $D1$ and a trailing dislocation $D2$) with a Burgers vector of magnitude $b = 0.25$ nm. Dislocations $D1$ and $D2$ delimit an APB several nanometers wide [NAB97]. As mentioned in section (1.1.3.5), when the leading $\frac{1}{2}\langle 110 \rangle$ dislocation glides through the γ' phase, it destroys the L1$_2$ order in the glide plane, thus creating an APB [POP84]. The subsequent trailing dislocation moving on the same glide plane restores the initial L1$_2$ structure according to reaction (1.2). The APB of energy density γ^{APB} created behind the first dislocation $D1$ exerts a drag stress $\tau_{\text{APB}} = -\frac{\gamma^{\text{APB}}}{b}$ on it. This is sufficiently strong to stop it from penetrating any further into the coherent precipitate. The opposite is true for a second trailing dislocation $D2$, with $\tau_{\text{APB}} = +\frac{\gamma^{\text{APB}}}{b}$, i.e. it can enter into the precipitate at lower applied stress.

2.4.2.3   Computer simulations

The L1$_2$ alloys exhibit an anomalous temperature dependence on the flow stress (see figure 8 b). Takeuchi and Kuramoto [TAK71] [TAK73] first proposed that such a yield stress anomaly, observed experimentally for Ni$_3$Ga, could result from cross-slip from octahedral {111} glide planes onto the cubic {010} planes of screw character dislocations, the KW locking [KEA62] [THO70]. Subsequently, their model was revised by Paidar *et al.* [PAI84] for Ni$_3$Al. Currently, a variety of microstructural models is available for the positive temperature dependence of the flow stress anomaly in L1$_2$ alloys [NAB97]. KW locking is often assumed to take place in the superalloy precipitates, even though this is still the subject of some debates. Recently, Demura *et al.* [DEM07] revisited this problem and proposed a simple formulation accounting for the dynamics of dislocation multiplication and immobilisation by KW locks. In the latter process, the entire segment cross-slips in one thermal activation event, and thus the activation enthalpy for the KW locking event is a function of the screw segment length. This model provides a simple way to reproduce the positive temperature dependence of the flow stress and is therefore adopted in the present work.

Demura et al. model of the yield stress anomaly in Ni$_3$Al

Following previous studies of Hirsh [HIR92] and Vessyière *et al.* (see the review [VEY98]), in the recent model proposed by Demura *et al.*, the yield stress is assumed to be governed by the expansion of the superkink lying between the long KW locks. Figure (37) is a schematic illustration of superkink motion in the model [DEM07]. The superkink AB expands as shown by the arrows $1 \longmapsto 3$, and the screw segment is locked by the KW mechanism at the position 4, where two superkinks AC and DE are produced. If the newly produced superkinks can expand, plastic deformation can continue. Based on the

Figure 37 - Superkink expansion and KW locking [DEM07].

analogy of the FR dislocation source, the stress necessary for superkink expansion is given by

$$\tau = \frac{2E}{hb} \tag{2.33}$$

where h is the height of the superkink, and E the line energy of dislocation per unit length. Here E is approximated by $E = \frac{1}{2}\mu b^2$. By substituting E into the equation (2.33), the mean height of the superkink is approximated by

$$h = \frac{\mu b}{\tau} \tag{2.34}$$

From equation (2.34), a superkink with a height larger than h can expand under a given stress τ. In figure (37) the height h of the superkink AC is equal to the travel distance of the screw segment until the KW locking occurs. That is, h is given by the product of the velocity of the screw segment v_{screw} and an interval between the KW locking events

$$h = \frac{v_{screw}}{f} \tag{2.35}$$

where f is the KW locking frequency per unit time, equal to the inverse of the interval between the KW locking events. In addition, v_{screw} is here assumed to be similar to the expression (2.9)

$$v_{screw} = \frac{\tau b}{B} \tag{2.36}$$

with B a drag constant. From equations (2.35) and (2.36), the height of the superkink AC is obtained as follows

$$h = \frac{b}{fB}\tau \tag{2.37}$$

The height of the superkink AC should be larger than the height given by the expansion condition for continuous plastic deformation, which gives a critical condition in the Demura *et al.* model. That is, the critical stress for continuous plastic deformation, τ_{KW} and the critical height h_c of superkink during the deformation are obtained from equations (2.34) and (2.37) as follows

$$\tau_{KW} = \sqrt{\mu B f} \tag{2.38}$$

and by substituting equation (2.38) into (2.34), h_c is obtained as

$$h_c = \sqrt{\frac{\mu}{Bf}} b \tag{2.39}$$

Constant parameter	Symbol	Value	Unit
Magnitude of Burgers vector	b	2.5×10^{-10}	m
Shear modulus	μ	51	GPa
Boltzmann constant	k	8.67	eV.K^{-1}
Debye frequency	f_D	1×10^{13}	s^{-1}

Fitting parameter	Symbol	Value	Unit
Damping constant	B	1×10^{-4}	Pa.s
Driving force for KW locking	E_D	127	mJ.m^{-2}
Energy barrier for KW locking	H	0.32	ev

Table 2.1: Constants and fitting parameters used in the Demura *et al.* model.

In addition, the KW locking frequency f is given by

$$f = f_0 \exp\left(-\frac{\Delta H_0}{kT}\right) \tag{2.40}$$

where f_0 is a reference frequency, k the Boltzmann constant, T the temperature and ΔH_0 the activation enthalpy. The latter activation enthalpy is given by

$$\Delta H_0 = H - b^2 E_D \tag{2.41}$$

where H is the energy barrier for cube cross-slip which corresponds to the Peierls potential for the cube-slip system. E_D is a driving force for cube-slip per unit area, which is a critical parameter for the yield stress anomaly [YOO86]. f_0 depends on the thermally activated process, e.g. the length of the dislocation l_s which is thermally activated, and is given by

$$f_0 = \frac{b}{l_s} f_D \tag{2.42}$$

with f_D a Debye frequency factor. As shown in figure (37), the screw segment length l_s depends on the curvature of the expansion dislocation arc. Demura *et al.* express the screw segment length as a function of the critical stress τ_{KW} as follows

$$l_s = \frac{2b}{3}\sqrt{\frac{6\mu}{\tau_{KW}} - 1} \tag{2.43}$$

Moreover, by substituting equations (2.40) and (2.42) into equation (2.38), the temperature dependence of the critical yield stress τ_{KW} is given by (see for details [DEV97] [DEV99] [DEM07])

$$\tau_{KW} = \sqrt{\mu B f_D \frac{b}{l_s} \exp\left(-\frac{\Delta H_0}{2kT}\right)} \tag{2.44}$$

The equation (2.44) clearly shows the positive temperature dependence of the yield stress. The free parameters B, E_D and H of equations (2.41) and (2.44) have been identified using experiment measurements of the RSS of Ni$_3$Al[4]. All constants and fitting parameters are summarised in table (2.1). The model gives the superkink height for sustainable plastic deformation h_c by equation (2.39). Figure (38) shows the temperature dependence of h_c calculated from the obtained parameters in table (2.1) according to equations (2.39) and (2.40). The superkink height decreases from 0.28 μm at 297 K to 0.03 μm at 1120 K with increasing temperature because the KW locking frequency increases with temperature.

---

[4]Unpublished data: internal research report.
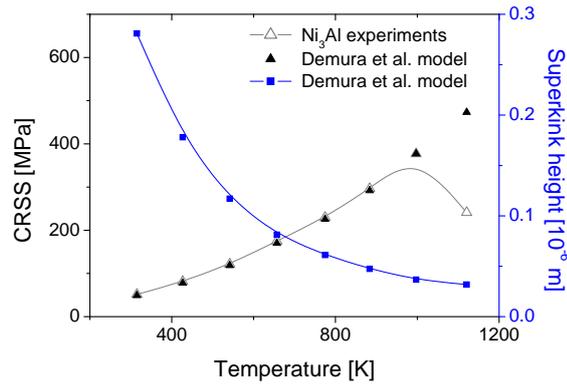
Figure 38 - Calculated and experimental CRSS versus temperature. In addition, superkink height calculated from the fitting parameters listed in table (2.1) according to equations (2.39) and (2.40).

Such superkink heights are consistent with TEM studies [JUM94].
According to equation (2.44), the CRSS can be evaluated as a function of temperature (see figure 38) using the parameters listed in table (2.1). Note that the calculated values are in fairly good agreement with the experimental values below the peak temperature.

Dislocation dynamics simulations

The local simulation rules employed in the simulation to account for the formation and destruction of KW locks are duplicated from previous work on Ni$_3$Al plasticity by Devincre *et al.* [DEV97] [DEV99]. Only the expression (2.44) for the KW unlocking stress τ_{KW} has been changed in order to be consistent with the Demura *et al.* model.
The movement of each dislocation segment is controlled through an effective shear stress τ_{eff} which originates from several different contributions:

* An applied resolved applied stress τ_{app} accounting for the mechanical loading.

* A solid-solution friction stress τ_{SS} (γ phase only).

* A KW unlocking stress τ_{KW} (γ' phase only).

* A configuration stress τ_{APB} accounting for APB creation or recovery (γ' phase only).

* An internal stress τ_{int} accounting for the elastic dislocation-dislocation interactions.

* A line tension term Γ imposed by the discretisation of the line curvature.

For each dislocation segment, its free glide velocity v during one simulation step is determined by equation (2.9), i.e.

$$v = \begin{cases} 0 & \text{if } \tau_F \geqslant \tau_{eff} \\ \dfrac{\left[\tau_{eff} - \tau_F \, \text{sign}\,(\tau_{eff})\right]b}{B} & \text{if } \tau_F < \tau_{eff} \end{cases} \tag{2.45}$$

where B is set to 1.10^{-4} Pa.s and τ_F is a constant friction stress defined by $\tau_F = \tau_{SS}$ in the γ phase, and $\tau_F = \tau_{KW}$ in the γ' phase. The effective stress given by equation (2.8) is thus rewritten as

$$\tau_{eff} = \tau_{app} + \tau_{int} + \tau_{APB} + \Gamma \tag{2.46}$$

w (μm)	l (μm)	$w+l$ (μm)	f (%)	CRSS (MPa)
0.065	0.580	0.645	73	326
0.065	0.330	0.395	58	266
0.065	0.200	0.265	42	211
0.115	1.050	1.165	73	282
0.115	0.580	0.695	58	225
0.115	0.350	0.465	42	173
0.170	1.550	1.720	73	219
0.170	0.850	1.020	58	167
0.170	0.510	0.680	42	121

Table 2.2: Geometrical characteristics as defined in figure (39) for the different simulated volumes, and the resulting CRSS for $\gamma^{\text{APB}} = 320$ mJ.m^{-2} and $\tau_{SS} = 107$ MPa.
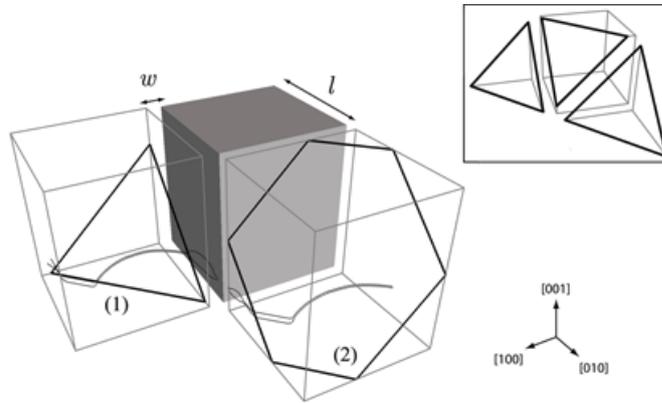
Figure 39 - Drawing of the cubic simulation cell with one γ' precipitate (dark grey) and two replicas illustrating the symmetries imposed by periodic boundary conditions: w is the width of the γ channels, l is the cube edge length of precipitates, and $w + l$ is the edge length of the simulated cell. The two types of (111) slip planes considered in section 2.4.2.4 are shown, respectively an equilateral triangular intersecting plane (1), and a hexagonal intersecting plane (2). A pair of dislocations is also show on plane (1). As shown in the inset, neighbouring triangular intersections alternatively point up or down.

where Γ is the line tension term [FOR67] given by equation (2.6). Note that $\tau_{SS} = 0$ inside the precipitate and $\tau_{KW} = \tau_{\text{APB}} = 0$ in the matrix channels.

The periodic simulated volume is shown in figure (39). It contains one γ' cubic precipitate of edge length l surrounded by thin γ channels of width w. The edge length of the simulated volume equals $w + l$ and the volume fraction of precipitate is denoted f. The different geometries of the simulated volumes used in this study are listed in table (2.2). In addition, the following simplifying hypotheses are adopted in both phases: the elasticity is isotropic with shear modulus $\mu = 51$ GPa and Poisson ratio $\nu = 0.37$. Also, only simple glide is considered without cross-slip or climb. All simulations were carried out at room temperature, except those presented in section 2.4.2.4 where the temperature dependence of the flow stress is specifically investigated. All simulations have been performed in a quasi-static regime in which dislocations are pushed slowly against the γ' precipitate. Dislocation lines are discretised into segments with a maximum discretisation length of $\frac{w}{5}$.

Lastly, the DD simulations use PBC to mimic the behaviour of a bulk material sample. Such conditions satisfy mechanical equilibrium and provide useful solutions to the problem of dislocation flux balance and line continuity at the boundaries of the simulated volume [DEV01]. In figure (39), it can be observed that with such boundary conditions, gliding dislocations can shear the precipitate microstructure either in

planes containing a regular periodic pattern of two equilateral triangular sections (which are alternatively pointing up and down as shown in the inset of figure 39) or in planes containing a regular periodic pattern of hexagonal sections.

A novel localisation procedure was introduced in the simulations to determine which dislocation segments are candidates for entering pairwise into the precipitate, and whether they are a leading or of a trailing dislocation of superdislocation. This is determined by a test on the internal stress τ_{int} at the location of segments entering into the precipitate. With only the sign and the amplitude of τ_{int}, one can differentiate the cases of leading and trailing dislocations. Details on this procedure, implemented in the DD code, is provided in Appendix C.

2.4.2.4   Simulation results of the flow stress temperature dependence

In this section, for reason of simplicity, γ' precipitates are supposed to be perfectly cubic and the γ/γ' interface is considered as perfectly coherent. The only glide system considered is $\langle 110 \rangle \{111\}$. Hence, the intersections between a precipitate and the glide plane of dislocations are triangles or irregular hexagons. At the start of a simulation, one pair of dislocations of either screw or mixed character is placed on a glide plane of one channel. Dislocations of mixed type are oriented at an angle of $60°$ with respect to **b**. Due to the PBC, these dislocations are infinitely long and cut an infinite periodic array of precipitates.

For each temperature and for each γ' volume fraction, it was first established that a single dislocation of screw or mixed character could not shear the precipitate array. A single dislocation can only move around the precipitates, through the channels. In this process, the dislocation line is strongly bowed out in the matrix channels, causing a very high Orowan critical stress, which is inversely proportional to the channel width.

Snapshots of a simulation of a $60°$ dislocation pair cutting through the precipitates are shown in figure (40). In figure (40), the stress-strain curve shows a stress drop, which is characteristic of a bowing-assisted cutting process. Such a process can be decomposed into four stages. In *stage* (1), the pair of dislocations $D1$ and $D2$ glide into the channels. $D1$ is pushed by $D2$ and enters the precipitate at its
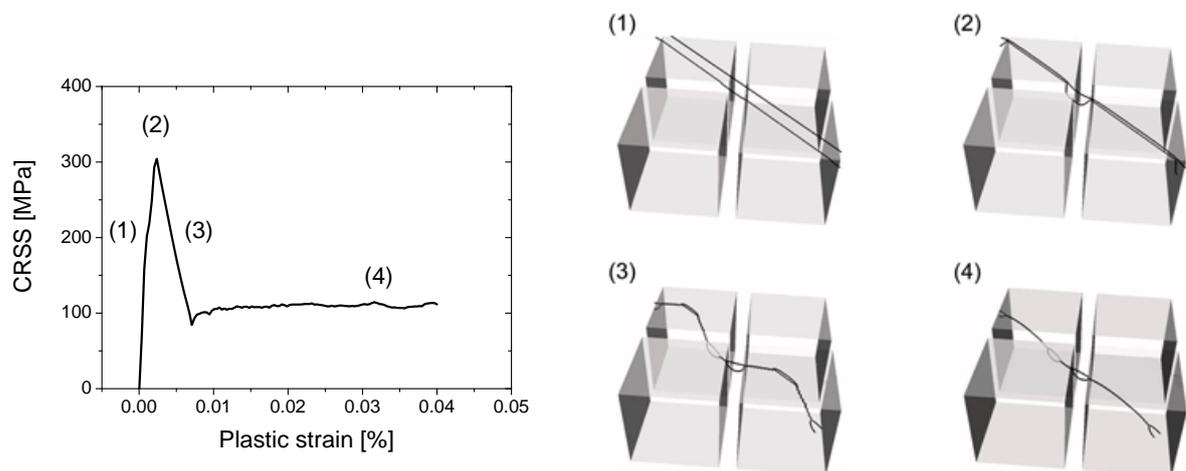
Figure 40 - The four stages of the bowing-assisted cutting process of precipitates. These stages are identified on the simulated stress-plastic strain curve and with the help of snapshots taken from the simulations. In *stage* (1), plastic deformation only occurs in the matrix channels. In *stage* (2), the superdislocation starts entering the precipitate. During *stage* (3), the superdislocation shears the precipitate but sections of the lines remain in the initial channels. *Stage* (4) corresponds to complete shearing of both channel and precipitate with a fully formed superdislocation in the latter.

corners but is then stopped by the process of APB formation. Without trailing dislocation, $D1$ can only enter the precipitate at corners as a result of the strong locally imposed line tension. In *stage* (2), assisted by the short-range mutual interaction between $D1$ and $D2$, the RSS reaches a critical value where the superdislocation is formed and starts entering the precipitates. Sections of $D1$ start to be strongly bowed-out in the matrix channels. From this point on, the progression of the superdislocation in the precipitate is mostly controlled by τ_{KW}. In *stage* (3), the superdislocation progressively enters the precipitate, but some sections of $D2$ are still anchored at the interface. Finally, in *stage* (4), the bowing of $D1$ and $D2$ into the matrix channel drags the superdislocation along, thereby cutting through the whole precipitate. In this process, strengthening depends on two kinds of parameters. Some parameters are related to the material composition (the APB energy γ^{APB} and the solid-solution friction stress τ_{SS}), the other parameters are related to the material microstructure (the channel width w and the precipitate volume fraction f). In the following sections, the influence of each of these parameters is determined by means of many DD simulations.

Influence of the APB energy

Figure (41) shows the CRSS needed by the $60°$ dislocation pair to overcome the precipitates as a function of γ^{APB}, the APB energy, for a constant channel width $w = 65$ nm and for three different precipitate volume fractions $f = 0.42$, 0.58 and 0.73. Based on literature data, the APB energy is assumed to lie between 100 and 350 mJ.m^{-2} [SAA04].

In all simulations, the dislocations overcome the precipitate by bowing-assisted cutting in a strongly coupled regime. For each tested APB energy ($\gamma^{\mathrm{APB}} = 100$, 170, 230 and 320 mJ.m^{-2}), precipitates were cut by the formation of a superdislocation and its subsequent dragging by the dislocations bowing out in the matrix channels. Figure (41) shows a roughly square root dependence on the APB energy for all three volume fractions. This result is in good agreement with the predictions of Reppich [REP93]. In the strongly coupled regime, the stress required to cut precipitates increases with the square root of APB energy (as in the present case), whereas in the weakly coupled regime, i.e. when precipitates are cut with one dislocation, the dependence of the cutting stress on APB energy is linear. The present results are also in agreement with Rao *et al.* [RAO04] in the case of their largest precipitate size (see [RAO04] figure 2 and the 400 nm precipitate edge length).
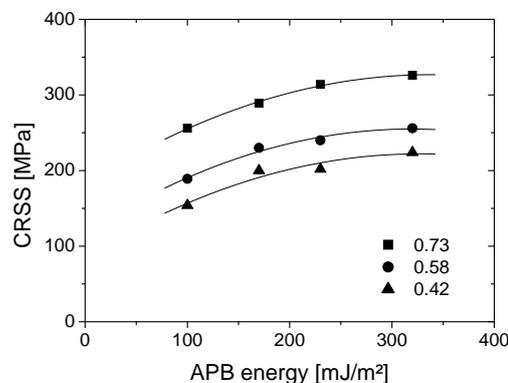
Figure 41 - Simulated (symbols) CRSS for a $60°$ $\frac{1}{2}\langle 110 \rangle$ dislocation pair as a function of APB energy in a superalloy with channel width $w = 65$ nm and with three different volume fractions of precipitates ($f = 0.42$, 0.58, 0.73). The lines fit a square root dependence on APB energy.

Influence of the width of the γ channels

Figure (42) gives the critical stress required to shear the precipitates as a function of the channel width $w = 65, 115$ or 170 nm, for a pair of $60°$ dislocations, a volume fraction $f = 0.73$ and $\gamma^{\mathrm{APB}} = 100, 170,$ 230 and 320 mJ.m^{-2}. Here, the size of the simulated (111) octahedral plane depends on the width w of the channel, with larger simulation cells for larger channel widths. As before, bowing-assisted cutting of the precipitates is observed in all simulations. From figure (42) it can be observed that the CRSS is sensitive to the channel width over the whole range of APB energies. The CRSS required to shear the precipitate is always monotonically decreasing with increasing channel width. Thus, for precipitation hardening in high γ' volume fraction superalloys, a size effect appears in the process of bowing-assisted cutting, but in the simulations this effect is found to be related linearly rather than inversely proportional to w, as theoretically predicted [REP93] [NEM00].
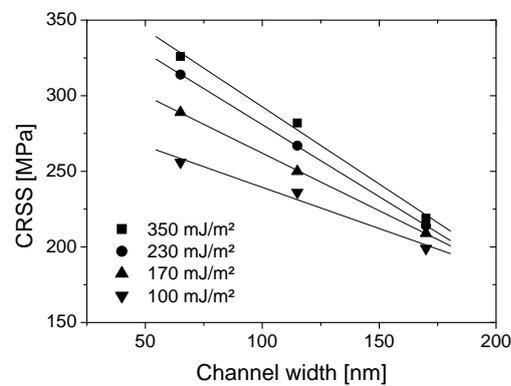
Figure 42 - Effect of the width w of the γ channel on the CRSS to move a $60°$ $\frac{1}{2}\langle 110 \rangle$ dislocation pair through a γ/γ' superalloy at different APB energies, and fixed volume fraction $f = 0.73$. The lines represent a fit of a linear size dependence.

Influence of the volume fraction of the γ' precipitate

Figure (43) gives the critical stress required to overcome precipitates as a function of the volume fraction f, for a pair of $60°$ dislocations. The channel width w was kept constant at 65 nm. As before, the APB energy is increased from 100 to 320 mJ.m^{-2} and the volume fraction f of the precipitates was varied from 0.42 to 0.73. Figure (43) shows that the CRSS increases strongly with increasing volume fraction f when the mean precipitate spacing w is kept constant.

In all simulated cases it is observed that the precipitates are cut in the strongly correlated regime. A superdislocation is first formed at the corners of the precipitates and is pulled by the connected pair of dislocations bowing out in the matrix channels. Hence, a higher volume fraction of precipitates at constant channel width is equivalent to increasing the mechanical work to be done by the pulling dislocations in the channels. As illustrated in figure (43), the CRSS increases linearly with f. This is because a constant length of dislocation in the channels pulls an increasing length of superdislocation in the precipitates. Again, the present result is in good agreement with the calculations of Rao *et al.* [RAO04] at smaller volume fractions of the precipitate, i.e. both lines in figure (43) have the same slope. The difference in vertical offset is thought to be caused by the different treatment of the coherency strain: in the present work this is not taken into account, whereas Rao *et al.* [RAO04] carried out their simulations with a 0.3% coherency strain.
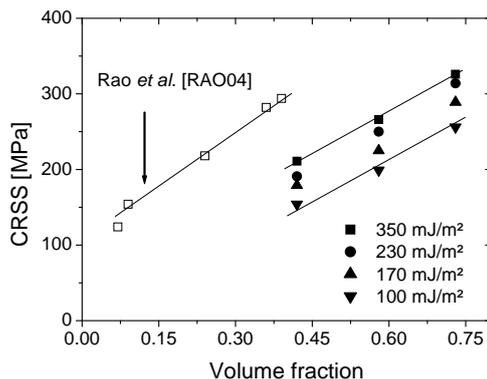
Figure 43 - Effect of the precipitate volume fraction f on the CRSS for different APB energies. In these computations the matrix channel width $w = 65$ nm and the cutting dislocations form a $60°$ $\frac{1}{2}\langle 110\rangle$ dislocation pair. For comparison, the results of Rao *et al.* [RAO04] are also shown. Their simulations were carried out at lower volume fractions and with a 0.3% coherency strain. Linear fits are plotted as a visual guide.

Influence of the geometry of the planes cutting the γ' precipitates

Octahedral slip planes can intersect cuboïdal precipitates in two different ways. As illustrated in figure (39), the intersections are either equilateral triangles or irregular hexagons. Figure (44) compares the critical stress required to cut a cubic precipitate as a function of the channel width w and for the two different types of intersections. Here the volume fraction $f = 0.73$ and the APB energy $\gamma^{\mathrm{APB}} = 320$ mJ.m^{-2}. For a direct comparison between the two types of intersections, the glide plane in the γ channels is chosen in such a way that the initial segment length in contact with the precipitates is the same in all the simulations.

Figure (44) shows that in the bowing-assisted cutting regime, the mixed-character dislocation pair requires a higher CRSS for cutting the precipitate than the screw dislocations. This non-intuitive result has already been discussed by Mohles [MOH04] and is explained as follows. The superdislocations needed to cut precipitates are the most easily formed with a pair of screw dislocations: as a result of elastic interactions at a given stress amplitude, the spacing between two repulsive dislocations pushed against
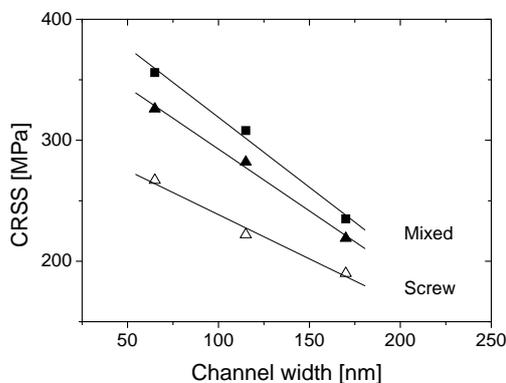
Figure 44 - CRSS as a function of channel width w for a $\frac{1}{2}\langle 110\rangle$ screw dislocation pair (open symbols) and a $60°$ mixed dislocation pair (full symbols). In the mixed dislocation case two different precipitate-glide plane intersections are tested. The triangles and squares denote respectively the triangular and irregular hexagonal intersections. The precipitate volume fraction $f = 0.73$.

an obstacle attains a minimum for screw dislocations. This explains why for screw dislocations, the formation of superdislocations inside precipitates occurs at a lower applied stress.

For all cases, the CRSS decreases linearly with the channel width w. In addition, it is shown in figure (44) that the CRSS obtained with triangular intersections are significantly lower than the corresponding ones calculated with the irregular hexagonal intersections. This difference is simply explained with geometrical arguments. In the hexagonal case, the angle between channels around each corner of the precipitates is 120°, whereas in the triangular case it is 60°. In the latter case, the dislocation pressed against the edges of a precipitate adopts a strong local curvature which intensifies the line tension and elastic self-interactions. The hexagonal and triangular intersections are the two limiting cases which can be calculated with a fixed length of dislocation pressed against a precipitate. The error bars plotted in figure (46) account for this geometrical dispersion.

Influence of the solid-solution friction stress in the γ matrix

In the simulations described so far, the friction stress in the γ matrix τ_{SS} was 107 MPa [SAA04], accounting for the solid-solution hardening there. Figure (45) shows the influence of this mechanism on the CRSS of the γ/γ' superalloy, for a channel width $w = 65$ nm, a volume fraction $f = 0.73$, and and APB energy $\gamma^{APB} = 320$ mJ.m^{-2}. The increment of the CRSS is found to be approximately the same as the increment of the friction stress: the CRSS increases linearly with increasing frictional stress. Hence, a reduction of dislocation mobility in the channels directly affects the mechanical response. This indicates that solid-solution hardening of the matrix is a potent strengthener of γ/γ' superalloys. In the following section, more attention will be paid to the role of τ_{SS} and its consequences on the overall mechanical response.
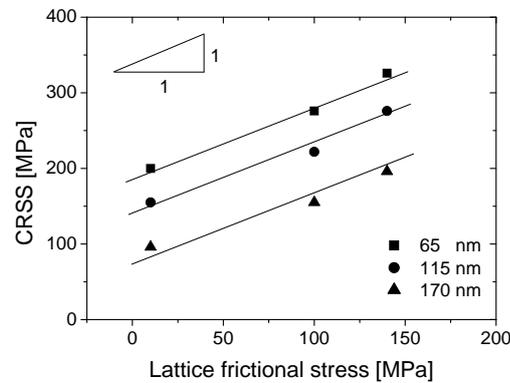
Figure 45 - Effect of solid-solution friction in the γ matrix on the CRSS required to move a 60° $\frac{1}{2}\langle 110 \rangle$ dislocation pair at different channel widths w. The lines represent a linear fit of its dependence on the lattice friction.

Temperature dependence of the CRSS

The aim of this subsection is to set the simulation parameters in order to reproduce the mechanical behaviour of an industrial superalloy with high precipitate volume fraction, and to predict the dependence of the CRSS as a function of temperature. In the following a temperature dependence of elastic constants is taken which is based on experimental measurements[5]. According to Parthasarathy *et al.* [PAR04], the γ^{APB} depends on temperature approximately as $\gamma^{APB} = 320 \exp\left(-\frac{T-297}{2000}\right)$ where $\gamma^{APB} = 320$ mJ.m^{-2} at 297 K [NAB97]. Moreover, a temperature dependence of τ_{SS} was also taken into account. This

---

[5]Unpublished data: internal research report.
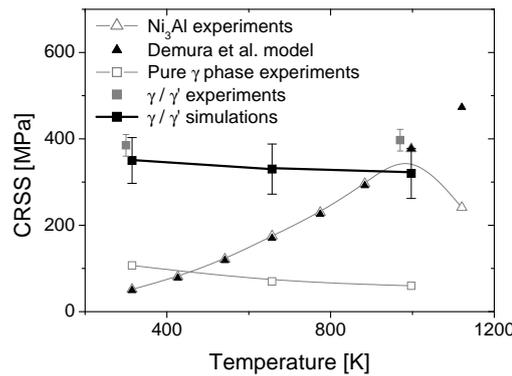
Figure 46 - Simulations of the CRSS for a γ/γ' superalloy as function of temperature (filled black squares) and comparison with experiments [CAR87] (filled grey squares). For comparison the CRSS for Ni$_3$Al (open triangles for experiments [MIU98] and filled triangles for the Demura *et al.* model [DEM07]) and Ni solid-solution [CLE96] are reproduced. For these simulations $f = 0.73$, $w = 65$ nm, and γ^{APB} as explained in the text.

dependence is fitted from the experimental data summarised by Clement *et al.* [CLE96]. As reproduced in figure (46), τ_{SS} decreases with increasing temperature from about 100 MPa at room temperature to 60 MPa at 1000 K.

In figure (46), the simulated CRSS of a γ/γ' superalloy with a precipitate volume fraction $f = 0.73$ and a channel width $w = 65$ nm is plotted. The simulation results are shown for temperatures up to 1000 K together with the corresponding CRSS of the two constituent phases. The error bars on the simulation results account for the statistical dispersion observed during the calculations. This dispersion is entirely associated to the geometry of the intersection between the glide plane and the precipitate and to the character of the dislocations pairs, as discussed in "Influence of the geometry of the planes cutting the γ' precipitates".

In good agreement with experiments, it is found that the CRSS of the simulated γ/γ' superalloy depends only weakly on temperature up to the maximum tested temperature. As expected, the CRSS reproduced at low temperature is much higher than the corresponding CRSS for each constitutive phase. Moreover, the simulation results are in good quantitative agreement with the response of the industrial single crystal nickel-based superalloy CMSX-2 with $f \approx 0.70$ [CAR87].

2.4.2.5   Discussion and concluding remarks

DD simulations have been carried out in order to study the plastic deformation of γ/γ' superalloys with a high volume fraction of γ' precipitates. These simulations account for the most important mechanisms controlling dislocation glide in the two constitutive phases. From a large number of simulations for volume fractions between 0.42 and 0.73, it is observed that:

* At γ' volume fraction $f = 0.73$ and channel width $w = 65$ nm, the CRSS of γ/γ' superalloy shows a square-root dependence on the APB energy of the γ' phase.

* At γ' volume fraction $f = 0.73$, the CRSS increases linearly with decreasing channel width w, in the range from 65 to 170 nm.

* At channel width $w = 65$ nm, the CRSS increases rapidly with increasing volume fraction of the precipitates. This is consistent with previous simulations carried out at lower volume fractions [RAO04].

∗ A dislocation pair on a glide plane cutting a precipitate with an irregular hexagonal shape requires a 20% higher RSS to shear the precipitate than on the alternative triangular intersection, for the same segment length in contact with the precipitate initially.

∗ Dislocations initially having a 60° character require a 25% higher RSS for penetrating into a cuboïdal precipitate than dislocations with an initial screw orientation.

∗ Increasing the friction stress τ_{SS} associated to solid-solution elements in the matrix affects directly the CRSS because it decreases the mobility of the dislocations which are bowing out into the channels and which are pulling the superdislocations through the precipitates.

In all the simulated conditions, it can be observed that a pair of dislocations, possibly emitted from the same source, can progress through the microstructure by shearing the precipitates. A strong gliding correlation between pairs of dislocations is observed in the channels. This correlation facilitates the formation of superdislocations and the subsequent process of precipitate cutting. The latter phenomenon is assisted by the dislocations bowing out in the channels. As a result of this mechanism, the CRSS measured in the simulations are strongly dependent on the density of solute elements in the γ phase and on the width of the channels. Moreover, the simulated CRSS is found to be weakly dependent on the value of the APB energy in the γ' phase (when considering realistic values larger than 100 mJ.m^{-2}). The latter parameter is nevertheless an essential quantity because it controls the formation of superdislocations when entering precipitates. Incidentally, and in agreement with previous studies carried out at lower precipitate volume fractions, it can be observed that the CRSS required for cutting the precipitates depends on the dislocation character: it is lowest for a pair of screw dislocations because such a dislocation can enter precipitates more easily than other orientations.

In this thesis, the general problem of one pair of infinite dislocations cutting through a periodic microstructure of precipitates is considered as a critical benchmark test. Such calculations are needed to validate the simulation and to provide a first estimation of the temperature dependence of the CRSS of superalloys with volume fractions larger than 50%. More complex computations are of course needed to account for strain hardening and the orientation dependence of the CRSS on the tensile axis, as observed experimentally. This problem will be discussed in the two following sections accounting for more realistic 3D dislocation microstructures. These multislip simulations will be performed to investigate in detail the mechanisms explaining the formation of dislocation pairs, the dislocation-dislocation forest hardening in the channels and the storage of dislocations at γ/γ' interfaces. The latter feature, as well as the temperature dependence of the misfit stresses in the microstructure of superalloys cannot be simply captured by classical DD simulations. This is why for these applications the DCM introduced in section 2 is used, and applied for a first set of calculations, to investigate the effect of channel width on the mechanical behaviour.

2.4.3 Size effects

2.4.3.1 Motivation

A substantial increase of the macroscopic flow stress of the single crystal can be achieved by decreasing the precipitate size while keeping the volume fraction constant [DUH87]. Duhl measured experimentally the change of the $\langle 001 \rangle$ steady-state flow stress at different precipitate sizes for PWA1480 at 760°C, a representative SC alloy.

These precipitate size effects cannot be predicted by classical continuum theories. The failure of conventional continuum theory is caused by the lack of a characteristic length-scale dependence. As introduced in section 1.2.5.2, several more sophisticated theories have been developed which, in various ways, include a length-scale dependence [AIF84] [ACH00] [GUR00]. Some of these theories attempt to incorporate an internal length through the concept of geometrically necessary dislocations introduced by Nye [NYE53]. For instance, non-local continuum plasticity theories such as [FOR00] [SED00] or strain-

gradient based plasticity using the evolution of geometrically necessary dislocations densities have already been applied to the simulation of the flow behaviour of single crystal superalloys [BUS00] [MEI01] [CHO05] [TIN08].

DD simulation appears to be the most appropriate tool to address such microstructural issues and the origin of the size effect. For instance, DD simulations were carried out on a composite material subjected to simple shear by [CLE97] [CLE98] or on a constrained strip [SHU01]. Both DD simulation studies have been carried out with 2D simulation. In this case, the main feature controlling plastic properties is the formation of dislocation pile-ups. For the single crystal γ/γ' superalloys, such pile-ups are not observed experimentally and this underlines that the size effects reproduced by 2D simulations are not applicable to this case, and this is why one needs fully 3D simulations here.

In this section, the effect of the channel width (with a constant volume fraction of precipitates) on the tensile plastic deformation of γ/γ' superalloys is investigated using the DCM. Emphasis is put on the elementary mechanisms governing the yield stress in multislip conditions.

The simulation volumes are subject to tensile stress at fixed applied strain rate. The results indicates that, at the micron scale, polarised (or geometrically necessary) dislocations located at the γ/γ' interfaces play an important role in setting the flow stress.

2.4.3.2   Problem formulation

The discrete-continuous model

The simulated volume contains only one cuboïdal precipitate surrounded by six channels, and is discretised by $16 \times 16 \times 16 = 4096$ quadratic FE and 56361 degrees of freedom, and PBC are applied. Calculations were performed on three different unit cells scaled up with the same mesh discretisation. Two cases are shown in figure (53). In all simulations, the precipitate volume fraction was maintained constant at 0.61, yielding a ratio r between the channel width w and precipitate size l of $r = \frac{w}{l} = 0.16$, while varying the channel width $w = 0.08$, 0.16, and 0.24 μm. In order to avoid PBC artifacts due to self-annihilation of dislocation loops [MAD04], the ideal periodic arrangement of cubic precipitates is modified by considering precipitates with orthorhombic dimensions ($0.48x \times 0.50x \times 0.52x$ μm^3, with x a scaling parameter to assess the effect of precipitate size, $x = 1$, 2, and 3) for the three morphologies. Isotropic elasticity is assumed everywhere with shear modulus $\mu = 51$ GPa and Poisson ratio $\nu = 0.37$. In the DD code, the lattice parameter $a = 0.36$ nm is assumed identical in both phases. This implies a Burgers vector of length $b \approx 0.25$ nm.

As discussed in section 2.4.2, shearing of the precipitates has been incorporated into the DCM and it correctly reproduces the anomalous temperature dependence [WES67] of the bowing-assisted cutting process (see figure 46). In the γ' phase the main parameter controlling the dynamics of precipitate shearing is the configuration stress τ_{APB}, which accounts for an APB creation or recovery through the APB energy γ^{APB}. In all simulations of this section, $\gamma^{\text{APB}} = 350$ mJ.m^{-2} [NAB97] and at 850°C the precipitates are bypassed by the Orowan mechanism, i.e. the precipitates are only deformed elastically. This is consistent with experimental observations at small plastic deformations [CAR77] [FRE87] [POL92], where the dislocation loops move through the channels, bowing out between the precipitates when a critical shear stress, the Orowan threshold stress $\tau^{\text{Orowan}} \approx \frac{\mu b}{w}$, is reached. Moreover, in the γ phase, relation (2.45) is applied for the velocity of the dislocation segments.

Initial dislocation configurations

Initial conditions in DCM simulations should be as close as possible to the experimental conditions in terms of dislocation density, dislocation source distribution and dislocation entanglement. As explained in section 2.3.1 the initial configuration in a DCM simulation is generated with a Volterra shearing procedure [DEV03]. This procedure is needed to set up an eigenstrain distribution [MUR87] in the FE mesh that is mechanically compatible with the initial dislocation microstructure.

σ_{Mises} (MPa)

110.

0.

[001]

[010]   [100]

(a)   (b)
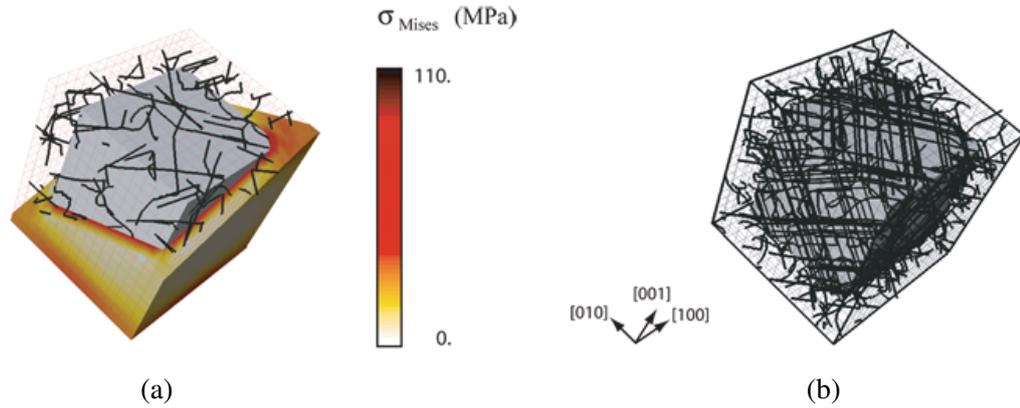
Figure 47 - (a) An initial dislocation configuration after relaxation, as explained in the text. The persistence of coherency stress is illustrated by the von Mises stress σ_{mises} at the surface of a diagonal cut through the channels. This can be compared to the large network of dislocations found at the γ/γ' interfaces in (b), after 0.2% plastic strain for tensile loading along the [001] axis.

For reason of simplicity and in order to avoid significant annihilation of dislocations in the first steps of the simulations, the initial dislocation distribution consists only of dipolar loops, i.e. four connected edge segments with the same Burgers vector (see figure 32). In this manner, dislocation segments act as Frank-Read sources and build up an interconnected dislocation network free of pending lines (see figure 34). A total dislocation density is homogeneously assigned to the 12 octahedral slip systems in the form of 24 dipolar loops. Cube slip systems are excluded on purpose.

Consider the microstructure with cubic precipitates with dimensions $0.48 \times 0.50 \times 0.52 \ \mu\text{m}^3$, i.e. $x = 1$ (figure 47). For this microstructure, the initial length of the edge segments is $0.12 \ \mu\text{m}$, longer than the channel width $w = 0.08 \ \mu\text{m}$. This precaution is needed in order to prevent artifacts due to a source activation stress operating within the channel which may be superior to the Orowan threshold stress. Considering a smaller initial dislocation source length than the channel width would generate an unrealistic macroscopic mechanical behaviour with an initial overstress of several hundred MPa. According to section 2.3.2, the dislocation segments bow out and multiply at a simulated critical RSS of 116 MPa, which is lower than the theoretical Orowan stress of 163 MPa for this channel width. In order to assure the condition that each initial segment has a length of $0.12 \ \mu\text{m}$, the starting dipolar loops cannot lie exclusively in the channel: parts of the loops are located in the channel and other parts in the precipitate. The latter segments create an APB, so they are energetically unfavorable and the dislocation distribution must be relaxed before applying mechanical loading.

An additional strengthening mechanism is due to the lattice mismatch between the two phases (see section 1.1.3.3). The difference in lattice parameter between the γ and the γ' phases creates a coherency stress field, which is not well-known experimentally at high temperatures [POL92] [ROY95]. In the DCM simulations, it can be computed by means of a preliminary thermo-elastic FE calculation, by artificially heating the γ/γ' microstructure from an initial state without misfit at room temperature. This requires two thermal expansion coefficients, a^γ and $a^{\gamma'}$, respectively associated to the γ matrix and γ' precipitate, and the appropriate heating interval ΔT. The misfit strain δ is then given by $(a^{\gamma'} - a^\gamma)\Delta T$, here equal to -3% at $850°\text{C}$. Figure (47 a) shows the von Mises equivalent stress σ_{Mises} of the coherency stress field in the matrix, before any mechanical loading. The matrix is in tension and the equivalent stress attains a minimum in the middle of the channels, and a maximum along the interfaces. In the precipitate, the misfit generates an uniform von Mises stress of about 30 MPa.

During the initial relaxation, the APB energy and the coherency stress drive the dislocations towards the interfaces. At this stage, the DD simulation time step is 5×10^{-11} s and the FE time step is ten times as long. The dislocation configuration is supposed to be relaxed when there are no more dislocations inside the precipitate. Complete relaxation takes about 3000 DD steps. After the process, the total dislocation

Parameter	Symbol	Value	Unit
Magnitude of Burgers vector	b	2.5×10^{-10}	m
Shear modulus	μ	51	GPa
Poisson ratio	ν	0.37	-
Damping constant	B	1×10^{-4}	Pa.s
Lattice friction	τ_F	107	MPa
APB energy	γ^{APB}	350	mJ.m^{-2}
Initial dislocation density	ρ_0	6.2×10^{13}	m^{-2}
Misfit strain	δ	-3	%
Imposed strain rate	$\dot{\gamma}$	20	s^{-1}

Table 2.3: Parameters used in the DCM simulations.

density on the 12 octahedral slip systems is 6.2×10^{13} m^{-2}. As shown in figure (47 a), the dislocations have moved to the interfaces where they locally reduce the coherency stress.

It was observed that the relaxed configuration is modified even when a very small load is applied during the relaxation. For that reason, the configurations subsequently used for mechanical loading were obtained by already imposing a tiny fraction ($\approx 10^{-7}$) of the mechanical loading that will be applied later on. This simple trick helps to eliminate possible transitory plastic deformation at the beginning of the simulation of the tensile test. It was verified that this modification does not change the mechanical response beyond this initial transitory stage.

Finally, not all initial configurations need the same time to eliminate their dislocation segments from the precipitate and to form the dislocation network at the interfaces. Those initial configurations which happen to have only a small fraction of segments inside the precipitate probably would need less time to relax than other initial configurations with almost all segments there. Therefore, in order to minimise the relaxation time, the dipolar loops are positioned in such a way that the fraction of their segments inside the precipitate is as low as possible. If the main concern of the present work would have been the relaxation process itself, this procedure would of course not be justified, but here the interest is the dislocation dynamics and the dislocation-precipitate interactions during the subsequent mechanical loading. Figure (47 a) shows a relaxed dislocation network and the remaining coherency stress field just before mechanical loading. By comparison, figure (47 b) shows the dense interfacial network after 0.2% plastic strain in the [001] case.

Loading conditions

During the simulations, the relaxed dislocation configurations for the three microstructures are subjected to a pure tensile loading along the [001] crystallographic axis. In order to run calculations within a reasonable time, a high resolved strain rate of $\dot{\gamma} = 20$ s^{-1} is imposed. Note that the convention is adopted throughout this section that all macroscopic stresses or strains are resolved on the slip system(s) with the highest Schmid factor(s), unless specifically indicated otherwise. This strain rate is larger than the macroscopic strain rates applied in laboratory tests, but reducing it would not affect the conclusions of this work. Processes controlled by diffusion such as dislocation climb are not taken into account. The remaining simulation parameters are the same as during the plastic relaxation. However, contrarily to the relaxation phase, no dislocation glides in the precipitates. At high temperatures plastic deformation takes place only through dislocation glide in the channels, and the interfaces are effectively impenetrable [CAR77] [POL92]. Therefore, only a small fraction of the simulated volume is deformed plastically and a significant strain incompatibility is expected. To summarise, all parameters are listed in table (2.3).

Scaling factor x	Channel width w (μm)	τ^{Orowan} (MPa)	$\tau_{f,0.1\%}$ (MPa)	$\tau_{f,0.2\%}$ (MPa)	θ/μ
1	0.08	164	243	320	0.149
2	0.16	83	155	212	0.142
3	0.24	55	108	152	0.134

Table 2.4: Characteristics of the hardening response of the three morphologies of a γ/γ' single crystal superalloy. The symbols τ^{Orowan}, $\tau_{f,0.1\%}$, $\tau_{f,0.2\%}$ and θ refer to the Orowan yield stress at 0.01% plastic strain, the flow stresses at 0.1% and 0.2% plastic strain and the rate of hardening, respectively.

2.4.3.3 Simulation results

Mechanical responses

Figure (48) shows the simulated stress-strain curves for the three specimens. Two different stages can be distinguished. A first stage corresponds to a transient regime from zero to 0.01% plastic strain, during which plastic deformation mainly results from the motion of the dislocations initially present inside the channels toward the γ/γ' interfaces. A second stage corresponds to the irreversible plastic deformation from 0.01% plastic strain to the end of simulations. During this second stage, the strain hardening rate is constant and plastic deformation arises from dislocations by-passing impenetrable precipitates. Irrespective of the strain value, the flow stress increases significantly with decreasing channel width.
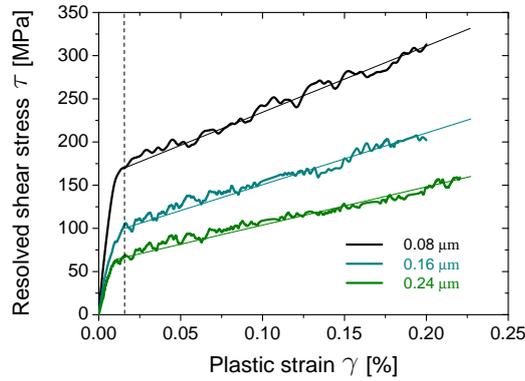
Figure 48 - Effect of morphologies on the simulated stress-strain curves. The solid straight lines represent linear fits, and the dotted vertical line indicates the boundary between the first and second stages (see text).

Flow stress and work-hardening

To quantify the size effect, the values of the 0.01% yield stress (called Orowan stress here) τ^{Orowan}, the values of the flow stresses at 0.1% and 0.2% plastic strain, $\tau_{f,0.1\%}$ and $\tau_{f,0.2\%}$ respectively, and the rate of hardening θ are reported in table (2.4). The precise definition of the parameters listed in the table is given in figure (49 a). The instantaneous work-hardening rate is defined as $\theta = \frac{\Delta\tau}{\Delta\gamma}$, where τ and γ refer to the shear strain and the flow stress, resolved on the most active octahedral slip system. The flow stress τ_f increases with decreasing specimen size. To quantitatively assess this size effect, the flow stress is plotted in figure (49 b) at 0.01%, 0.1% and 0.2% plastic strain as a function of $\frac{1}{w}$. This plot shows that the simulation results correspond to a $\frac{1}{w}$ scaling law. In particular, the value of the 0.01% yield strength

(a)　　　　　　　　　　　　　　　　　　　　(b)
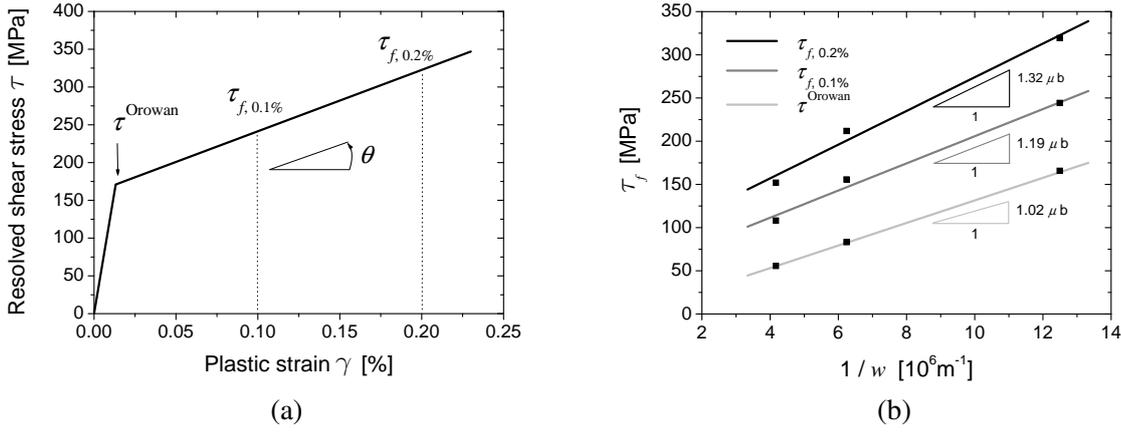
Figure 49 - (a) Sketch of a typical simulated stress-strain response of a single crystal superalloy showing the definition of the strength and hardening quantities listed in table (2.4). (b) Plastic flow stress τ_f, versus the inverse of the width w of the γ channel. The value of the scaling $1.02\,\mu b$, $1.19\,\mu b$ and $1.32\,\mu b$ correspond to 0.01%, 0.1% and 0.2% plastic strain, respectively. The straight lines represent a linear fit of the dependence on the inverse of the width w. The work hardening rate increases steadily with decreasing specimen width w of the γ channel (values are listed in table 2.4).

corresponds quantitatively to the critical macroscopic Orowan stress expressed here as

$$\tau^{\text{Orowan}} = 1.02\,\frac{\mu b}{w} \tag{2.47}$$

In addition, figure (49 b) depicts the values of the flow stress τ_f at 0.1% and 0.2% plastic strain, as a function of $\frac{1}{w}$. The Orowan-like law, inversely proportional to w, fits well to the data in figure (49 b) at all plastic strain levels and the flow stress may be given as

$$\tau_f = k\frac{\mu b}{w} \tag{2.48}$$

with k constant and positive. The values of k are given in figure (49 b) and identified to be $k = 1.19$ at 0.1% plastic strain, and $k = 1.32$ at 0.2% plastic strain. Equation (2.48) means that the flow stress is strongly dependent on the channel width w.

The effect of specimen size on hardening is quantified in table (2.4) by the values of θ/μ. The work-hardening rate θ increases with decreasing specimen size. These values can be related to dislocation storage at the γ/γ' interfaces, i.e. the size dependence of θ is related to the dislocation density deposited at the γ/γ' interfaces. The dislocation density is now analysed.

Dislocation densities

Figure (50) shows the evolution of the dislocation density ρ with plastic strain. At the same γ' volume fraction, the dislocation density increases linearly with strain, and faster for smaller channel widths. Figure (51 a) illustrates the dislocation density rate $\frac{\partial \rho}{\partial \gamma}$ as a function of plastic strain. The rate is constant during the second stage, and the figure (51 b) illustrates the saturated density rate as a function of $\frac{1}{bw}$. According to figure (51 b), a relation which correlates the saturated dislocation density rate with the inverse of the channel width w is given by

$$\frac{\mathrm{d}\rho}{\mathrm{d}\gamma} = 2.17\frac{1}{bw} \tag{2.49}$$
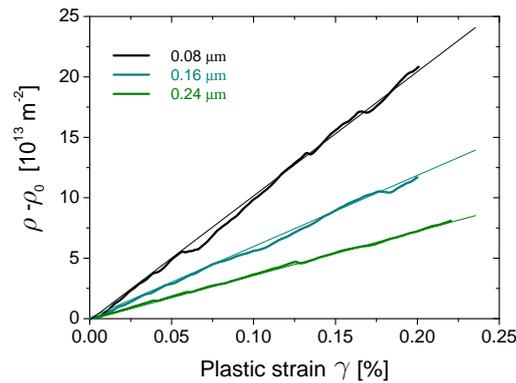
Figure 50 - Evolution of dislocation density with plastic strain corresponding the stress-strain responses of figure (48) for all specimen sizes.
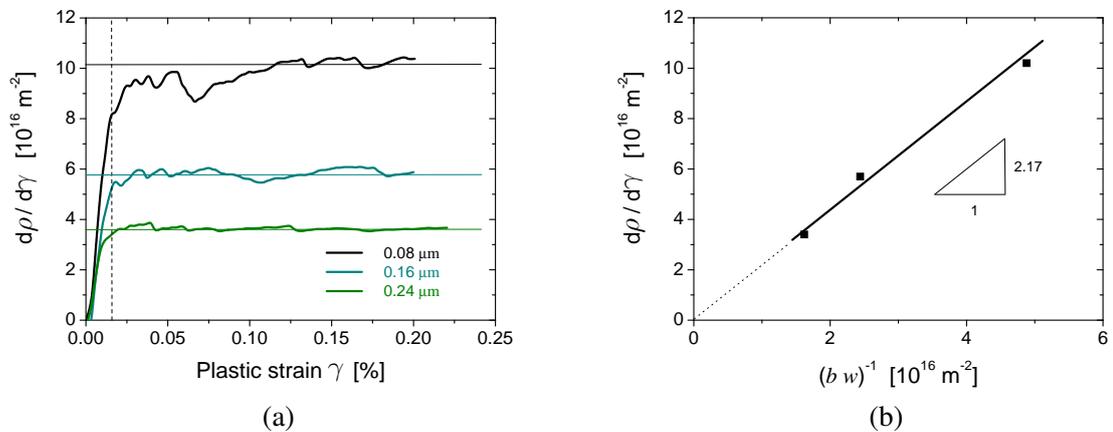
Figure 51 - (a) Rate of the total dislocation density with plastic strain for the three simulated specimens. Horizontal lines represent the constant rate during the second stage. (b) Saturation rate of the dislocation density evolution as a function of $\frac{1}{b\,w}$. The line represents a linear fit.

The relation (2.49) can be viewed as expressing a macroscopic storage rate, which, as expected from a classical storage-recovery model (see section 1.2.4.2), is governed by a dislocation mean free path [EMB71] [KOC76] [KOC03]. This means that the dislocation mean free path is mainly controlled by the microstructure of the material, and not by the spacing between forest dislocations. It will be shown in the following sections that there is a noticeable decrease in the junction production rate after some straining (see figure 56 b). Even if all junctions would contribute to forest hardening, the size-dependence of the flow stress does not correlate to the spacing between forest dislocations. This is why the plastic behaviour (given by equation 2.49) is highly dependent on the channel width, which represents for dislocations their average obstacle distance.

Distribution of dislocation density

The question addressed now is that of what relationship there is, if any, between flow stress and local dislocation density. In order to quantify the local dislocation density variation, averages of density were calculated over strips of thickness $h = 8$ nm, running parallel to the interfaces.

Two densities are considered: the total dislocation density, and the polarised (positive and negative) dislocation density obtained by the Nye tensor [NYE53]. The Nye tensor α gives the closure mismatch

(a)   (b)
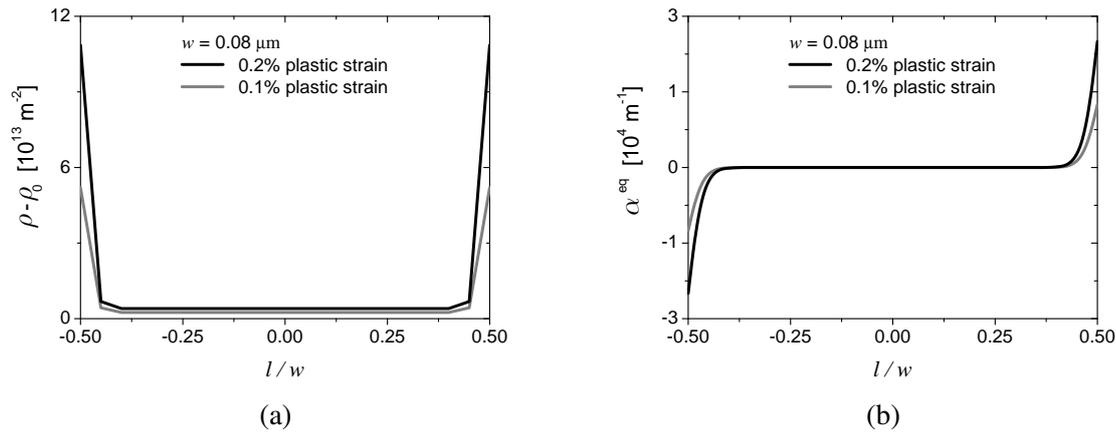
Figure 52 - (a) Total dislocation density distributions across the channel width for the selected specimen $w = 0.08$ μm at 0.1% and 0.2% plastic strain. (b) Averaged polarised dislocation density α^{eq} calculated by equation (2.50). Both densities are calculated over strips of equal thickness $h = 8$ nm within the channels.

of a linear path traced on a three dimensional surface S enclosing a volume V containing an arbitrary dislocation microstructure. In the discrete sense, this tensor is computed by adding up the contributions of every dislocation segment[6] according to

$$\alpha_{ij} = \frac{1}{V} \sum_{1}^{N} l^k b_i^k t_j^k \tag{2.50}$$

where N is the total number of segments in the volume V, l^k is the length, b^k is the Burgers vector associated with the segment k, and t^k is the unit vector aligned with the segment of the segment k. Only a local polarised dislocation density produces a net, non-vanishing Nye's tensor.

As shown in figure (52 a), the total dislocation density is higher at the interfaces than within the channel, and the density of these stored dislocations continues to increase with ongoing deformation. In addition, no pile-ups against precipitate interfaces are observed, contradicting DD simulations carried out in 2D. The averaged polarised dislocation density profiles defined by $\alpha^{\mathrm{eq}} = \mathrm{sign}(\alpha_{11})\sqrt{\alpha_{ij}\alpha_{ij}}$ and obtained at a 0.1% and 0.2% plastic strain for the microstructure with a channel width $w = 0.08$ μm are shown in figure (52 b). It shows that the dislocation densities located at the two interfaces are polarised. The presence of these polarised (positive or negative) interfacial dislocations affect strongly the local flow stress when imposing a [001] tensile loading, as will be shown in section 2.4.4. It is assumed that the polarised dislocations induce internal stresses opposite to the applied stress and therefore reduce the mobility of dislocation in the channels.

2.4.3.4   Discussion

Critical threshold

As discussed in the previous section, when the threshold of the Orowan critical shear stress is reached, the dislocation are sufficiently curved to glide in a narrow channel. The channel width for γ/γ' super-alloys plays a important role in the critical threshold which in the simulated results is assumed to be at 0.01% plastic strain. The microplastic phase (i.e. from zero to 0.01%) corresponds to the displacement of preexisting dislocations towards the interfaces. For larger channel width w, the dislocations can glide

---

[6]See section 3.1.2.3 (for instance, equation 3.8).

a longer distance before being blocked by interfaces. The critical threshold corresponds to the theoretical Orowan stress where dislocations begin to bow out between the precipitates and glide within a channel. This stress is dependent of the channel width according to $1.02 \frac{\mu b}{w}$ (see equation 2.47), where the critical stress increases with the decreasing channel width. The theoretical value of this stress is also verified through collective effects and multi-slip conditions in 3D DD simulations.

When the critical Orowan stress is reached, a dislocation loop expands on a glide plane within the channel and deposits dislocation segments at the interfaces. These segments have a screw or $\pm 60°$ mixed character, and give rise to a polarised dislocation density at the interfaces (see figure 52 b). Their accumulation between the soft precipitate and hard matrix give rise to internal stresses, and therefore contribute strongly to the high work-hardening for $\langle 001 \rangle$-oriented specimens in γ/γ' superalloys. This point will be discussed in section 3.1.4.

Interfacial dislocation

The dislocation density increases almost linearly with plastic strain, and at the same γ' volume fraction the rate of increase is larger for smaller channel widths (see figure 50). Moreover, the dislocation density rate $\frac{\partial \rho}{\partial \gamma}$ increases with decreasing channel width. Strengthening is due to an increase in stress in the channel when the specimen size is reduced. This increase is associated with the emergence of a dislocation density which is polarised at the interfaces. A network of interfacial dislocations is formed and these dislocations are necessary at the γ/γ' interfaces to accommodate the strain strain gradient between both phases (see figure 53), with no pile-up formation.

Figure (53 b) shows the dense interfacial network after 0.2% plastic strain for two specimens. In case of a singular surface, i.e. if the distortion is discontinuous across a surface with normal vector $\hat{n}$, the dislocation density α_{hi} has a surface density given by

$$\alpha_{hi} = -\epsilon_{hlj} [\![\beta_{ji}^p]\!] \hat{n}_l \tag{2.51}$$

where $[\![\beta_{ji}^p]\!]$ is the jump of the plastic distortion across the interfaces [MUR63] [MUR87] [FED99] [FED02]. This will be analysed in full detail in section 3.1.

(a)   (b)
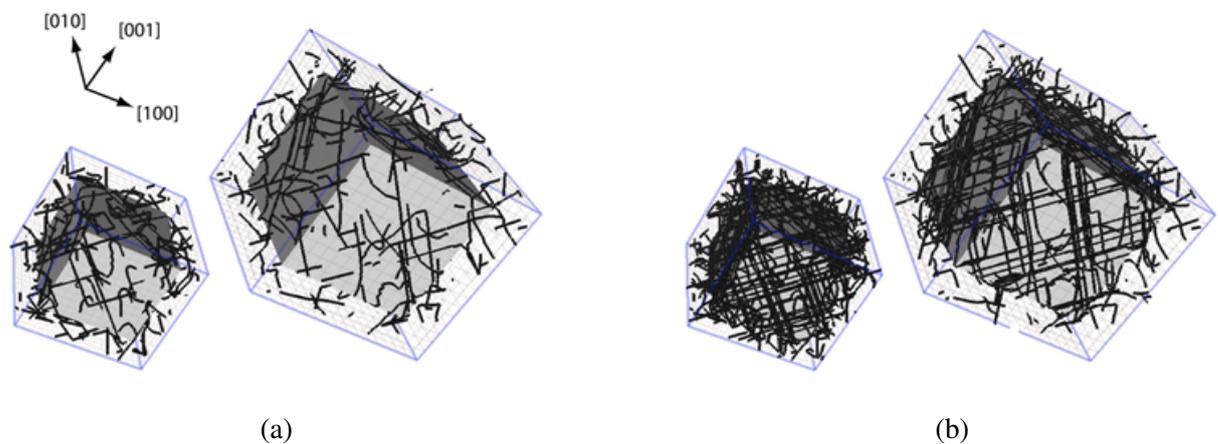
Figure 53 - Illustration of two simulated volumes with associated channel width and precipitate size assuming the same precipitate volume fraction of 0.61. (a) Initial dislocation configuration before the mechanical loading. (b) Dislocation microstructures at 0.2% plastic strain. Note that dislocations are strongly located at γ/γ' interfaces.

Work hardening

In physical theories of crystal plasticity, the dislocation density is commonly used as the structural parameter for macroscopic descriptions of plastic flow, with the flow stress governed by Taylor-like hardening (see section 1.2.4.2). Hence, the flow stress is defined by equation (1.30) as

$$\tau = \alpha \mu b \sqrt{\rho} \tag{2.52}$$

where α is a constant[7] in the range $0.3-0.5$ when the athermal component of τ is retained [GIL93b]. Figure (54) shows the evolution of τ with strain for the three specimens, with the flow stress given in units of $\mu b \sqrt{\rho}$ to explore the validity of equation (2.52). This plot clearly shows that the increase in dislocation density with decreasing specimen size (see figure 50) does not explain the corresponding increase of the flow stress (see figure 48). At fixed specimen size, there is no deformation regime where the bulk scaling law (2.52) holds with values of the pre-factor α within the range $0.3-0.5$. Indeed, a deviation from this behaviour is observed for all specimens because the pre-factor α is much higher, within a range $1.3-1.8$ (see figure 54). The behaviour in figure (48) indicates that at the microscale the dislocation density does not suffice to set the flow stress, and the latter point breaks down the classical storage-recovery theory in equation (2.52).
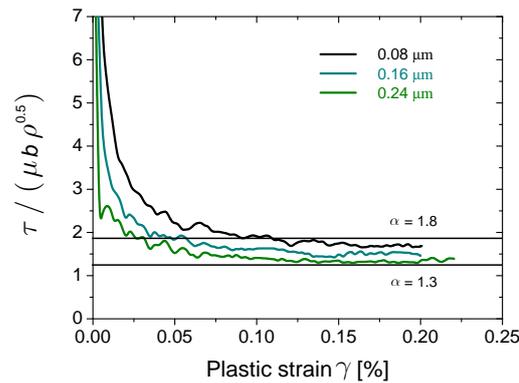
Figure 54 - Macroscopic flow stress τ, in units of $\mu b \sqrt{\rho}$ versus plastic strain. The specimen realisations correspond to those in figures (48) and (50) for the stress-strain and density-strain curves, respectively.

In addition, equation (2.49) for the storage rate confirms this point. It predicts a storage rate as function of the channel width, not the inverse of $\sqrt{\rho}$ as predicted by the classical storage-recovery model for dislocation-dislocation interactions (equation 2.52). This shows that the mean free path of dislocation is proportional to the microstructural length w of the material, associated to the dislocation-precipitate interactions, and is not correlated to the forest interaction through the $\frac{1}{\sqrt{\rho}}$ storage term expressed in equation (1.33).

2.4.3.5 Concluding remarks

In this section, simulations have been carried out containing an intrinsic length scale, which is the length of the Burgers vector. By means of the DCM framework, plastic flow is directly simulated by dynamics and interactions of dislocations. Moreover the simulations provide a physically justified manner for including dislocation nucleation from dislocation sources, dislocation glide, dislocation annihilation and dislocation interactions with the γ' precipitates. This section focused on investigating the effect of the channel width on the macroscopic flow stress at 850°C, while maintaining a constant precipitate volume

---

[7]Not related to Nye's tensor.

fraction. By assuming that the precipitate interface is impenetrable for dislocations at that temperature, the main role of interfaces in the dependence of the flow stress on the channel width is investigated, and the results are summarised in the following:

∗ The size effect is significant for both the flow stress and the work-hardening rate. In particular, the initial reversible plastic regime is controlled by the Orowan critical stress, below which dislocations cannot curve and glide within channels. The stress is strongly dependent on the channel width w, and the size effect is inversely proportional to w (equation 2.47).

∗ Because in superalloys w can be very small, the mean free path of glide distance of dislocation is proportional to the microstructural length w, and not $\frac{1}{\sqrt{\rho}}$ as predicted by the classical storage-recovery model for dislocation-dislocation interactions (equation 2.49). The spatial distribution of polarised dislocations around the γ' precipitates affect the flow stress by creating an internal stress field, which is not taken into account in the classical work-hardening framework.

∗ No pile-ups were observed in the simulations, so the mean free path was not reduced by dislocations gliding within the channels. The dislocations are located at the interfaces, and the interfacial dislocation density increases by glide of mobile dislocations within the channel which deposit immobile segments at the interfaces.

These calculations demonstrate that Taylor-like hardening is insufficient for modelling of superalloys, because it does not take into account the internal stress induced by a polarised dislocation density distribution. This finding raises fundamental questions regarding the formulation of extended plasticity theories for modelling work hardening included the long-range internal stress generated by these polarised dislocation density. Many such theories are based on the understanding that plastic flow processes are inherently size-independent in the absence of strain gradients at the scale of the elementary volume. The scale-dependence of strength and hardening beyond yielding poses a challenge to modelling of plasticity at the micro-scale (see section 1.3.2).

2.4.4 Orientation dependence of plastic deformation

2.4.4.1 Motivation

Another problem concerning the anisotropic mechanical response is now investigated with the DCM.
In uniaxial tension or compression tests, the yield strength depends strongly on loading direction [SHA83] [MIN86] [HAN91] [SAS97] [SAS98] [SIE99] [BET99] [WAN09]. As shown in the previous calculations at 850°C and at low tensile stress, plasticity is mainly concentrated within the channels on $\frac{1}{2}\langle 110\rangle\{111\}$ planes [CAR77] [POL92]: the precipitates are not plastically deformed, because of the anomalous yield behaviour of the Ni_3Al phase. Also, in the $\langle 001\rangle$ loading cases (i.e. for crystals with one of the $\langle 001\rangle$ axes oriented along the loading direction), the 0.2% yield stress and the strain hardening are considerably higher than for other orientations. Understanding such plastic behaviour is essential because the crystallographic alignment during blade solidification can deviate from the strongest $\langle 001\rangle$ orientation, and blades can be subjected locally to complex stress states.
The question has been raised whether cube slip occurs in crystals oriented away from the $\langle 001\rangle$ directions [SAS97] [SAS98] [BET99]. In the $\langle 111\rangle$ loading cases, i.e. for crystals oriented with one of the $\langle 111\rangle$ axes along the loading direction, $\{100\}$ slip traces have been observed within the channels. Activation of cube slip systems has important consequences for the models of the orientation-dependence of the mechanical response [CAI87] [NOU95] [OST00] [FED02] [LEV06] [PRE08]. Adopting cube slip is a convenient scheme to account for the softer plastic response of non-$\langle 001\rangle$ oriented specimens. Microscopically, dislocations would then glide on the cubic planes in the matrix channels. The boundaries of those channels are parallel to the glide planes, so they cannot block these dislocations which could then glide freely over large distances.

However, at higher magnifications no dislocations were found to glide on cube planes [SHA83] [MIN86] [WAN09]. Recent TEM analyses [VOL94] [BET99] [WAN09] showed that the {100} traces previously observed with optical microscopy consist of repeated slip occurring on different {111} planes within the γ channels, appearing visually as zig-zag configurations. According to Bettge and Österle [BET99] [SAS97] [SAS98], this is a result of successive cross-slip between the {111} slip planes. The cubic slip systems in the crystallographic viscoplastic models dedicated to single crystal superalloys can then be thought of as phenomenologically representing the "pseudo-cubic" slip traces caused by the zig-zag slip on octahedral planes.

This section seeks to clarify some of these issues by using the DCM. Uniaxial tensile tests of a single crystal nickel-based superalloy are simulated at 850°C, for a [001] and for a [111] loading case. Calculations are compared with experimental results from the literature. The simulated dislocation microstructures and the internal stress distributions are analysed in detail, providing original information on the mechanisms controlling plastic deformation in these tests. The simulations are shown to deliver a qualitative and quantitative description of plastic strain localisation, consistent with experimental observations.

2.4.4.2 Problem formulation

As in the problem formulation of the size effects presented in section 2.4.3, the simulated volume is periodic and contains only one γ' cuboïdal precipitate surrounded by six γ channels with a volume discretised by 4096 quadratic FE and 56361 degrees of freedom. PBC are applied and the dimensions of the periodic arrangement of the cubic precipitates are $0.48 \times 0.50 \times 0.52 \ \mu m^3$. The channel width is $w = 0.08 \ \mu m$, which corresponds to a precipitate volume fraction, $f = 0.61$. Figure (55 a) shows the simulated volume and some of its periodic replicas. For better visibility of the dislocation lines, not all of the precipitates are shown.

Isotropic elasticity is again assumed with shear modulus $\mu = 51$ GPa and Poisson ratio $\nu = 0.37$ at 850°C, and the magnitude of the Burgers vector is $b = 0.25$ nm. The APB energy γ^{APB} is equal to 350 mJ.m^{-2}, the viscous drag constant $B = 1.0 \times 10^{-4}$ Pa.s, and the lattice friction $\tau_F = 107$ MPa. Moreover, δ was fixed at -3%, and the initial dislocation density is 6.2×10^{13} m^{-2}, assigned to the 12

(a)   (b)
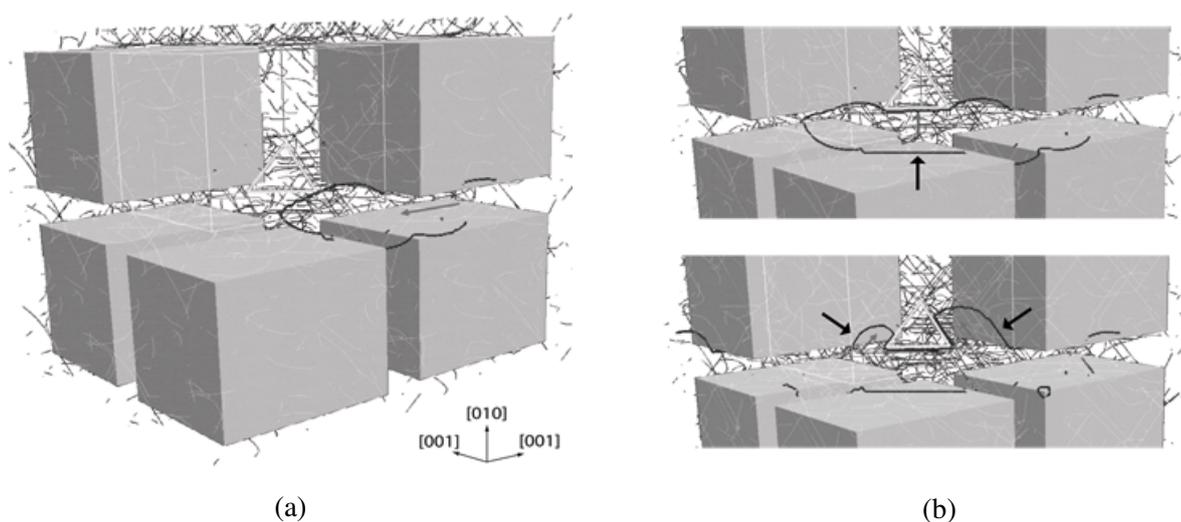
Figure 55 - (a) The simulated γ/γ' microstructure and some of its periodic replicas. The three possible types of dislocation character (screw and $\pm 60°$ character) arrested by {100} precipitate/matrix interfaces during the Orowan bypassing process are illustrated in (b): the vertical black arrow shows the screw segment deposited at the horizontal interface, whereas the two diagonally oriented arrows shows the $\pm 60°$ character segments deposited at the vertical interfaces.

octahedral slip systems (see figure 47 b). Cube slip systems are excluded on purpose.

As mentioned in section 2.1.2, in microMegas the dislocation lines are discretised into segments of screw, edge and two mixed characters ($\pm 60°$ character in the $\langle 110 \rangle$ directions). This discretisation is numerically very efficient for the specific case of the γ/γ' superalloy, because dislocation-dislocation junctions between octahedral slip planes and dislocation segments arrested by the $\{100\}$ precipitate/matrix interfaces are all along $\langle 110 \rangle$ directions. This last point is illustrated in figure (55). Figure (55 a) shows a dislocation (highlighted by a somewhat thicker line) gliding through the matrix channels on a $\frac{1}{2}\langle 110 \rangle \{\bar{1}11\}$ plane. The dislocation leaves behind dislocation segments pressed against the interfaces which have either a screw character in the horizontal channel (indicated by the vertical black arrow in figure 55 b), or a mixed character in the vertical channels, with a Burgers vector at $\pm 60°$ with respect to the line direction (indicated by the black arrows oriented diagonally in figure 55 b). During the simulations, the relaxed dislocation configurations are subjected to a pure tensile loading in the [001] or [111] directions with an imposed resolved strain rate of $\dot{\gamma} = 20$ s^{-1}. Processes controlled by diffusion such as dislocation climb are not taken into account. Furthermore, cross-slip is not considered initially, but in a second set of computations an easy cross-slip process is taken into account for comparison with the pure glide results.

2.4.4.3 Simulation results

Macroscopic mechanical response

Figure (56 a) shows the simulated stress-strain curves for both [001] and [111] cases. The two curves are in good agreement with experiments and are characteristic of plastic deformation of γ/γ' superalloys at high temperature [SAS98] [OST00] [WAN09]. Two distinct stages can be observed. During the first transient stage, from zero to 0.015% plastic strain, the flow stress is identical for both cases. The dislocations initially present in the channels start moving towards the interfaces. Due to the small channel width, the plastic deformation at 0.015% is mainly controlled by the line tension. The initial yield point correlates well with the Orowan stress prediction $\tau^{\text{Orowan}} = 1.02\frac{\mu b}{h} = 166$ MPa (see equation 2.47) [BRO71]. The prefactor 1.02 accounts for the mean character of the dislocation lines involved.

During the second stage (from 0.015% onwards), the relative influences of forest interactions or disloca-

(a)   (b)
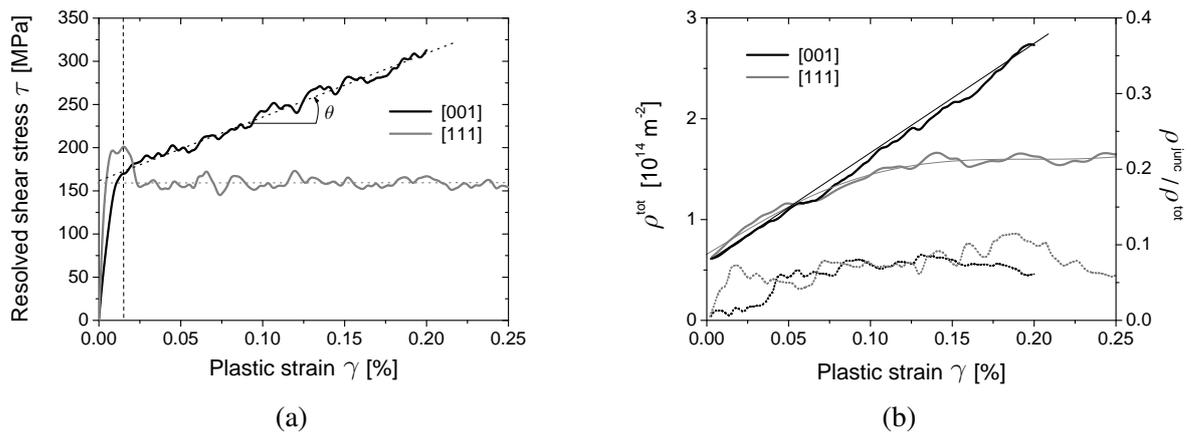
Figure 56 - (a) Simulated stress-strain curves at 850°C, in black for the [001] case and in grey for the [111] case. The dotted lines represent linear fits, except the vertical one which indicates the boundary between the first and second stages (see text). (b) Evolution of dislocation densities with plastic strain, in black for the [001] case and in grey for the [111] case. Solid lines: total dislocation density ρ^{tot} averaged over the whole simulated volume. Dotted lines: the ratio $\frac{\rho^{\text{junc}}}{\rho^{\text{tot}}}$ of junction density to total dislocation density.

tion storage at the interfaces can potentially increase. In accordance with experiments, the two loading cases respond completely differently. The [001] case hardens linearly with slope $\theta = \frac{\Delta\tau}{\Delta\gamma} = 0.149\mu$ (see table 2.4). The [111] case first shows a stress drop of about 50 MPa without any strain hardening afterwards. The form of this curve is typical: the experimental curves reported by Bettge and Österle [OST00] also show a stress drop of the same magnitude after an upper yield point, followed by a low-hardening domain. Moreover, the resolved flow stress calculated for both cases differ by approximately 130 MPa at 0.20% plastic strain. Again, this is in good agreement with experiments [SHA84] [OST99] [OST00]: for instance Österle *et al.* [OST00] obtained a difference of 113 MPa at 750°C and 129 MPa at 850°C for SC16 after 0.2% plastic strain at a strain rate of 10^{-3} s^{-1}.

In both loading cases, dislocation segments accumulate at the interfaces. Each dislocation gliding through a channel deposits long straight segments of opposite sign at the two opposite interfaces bounding the channel. At low effective stress, the deposited segments re-arrange themselves on the interfaces in order to minimise the elastic energy. This creates the characteristic networks which have been observed many times in TEM studies [FEL89].

Figure (56 b) shows the evolution of the dislocation density ρ^{tot} with plastic strain. In conformity with the previous observations on strain hardening, the net dislocation storage rate $\frac{\partial\rho}{\partial\gamma}$ is largest in the [001] case. Inversely, the absence of hardening for the [111] case manifests itself as a much lower dislocation storage. This results from plastic strain localisation, and this will be explained in later sections.

The difference between the two cases is not caused by forest hardening. This is demonstrated in the same figure, where the ratio of junction density ρ^{junc} (which is a signature of forest hardening [DEV06] [KUB08], i.e. the average length per volume of the stored junction segment formed by a reaction between dislocations) to total dislocation density is plotted as a function of plastic strain. For both cases, ρ^{junc} is much smaller than in usual fcc metals, and both ratios are quantitatively the same. Also, the rate of both ratios decreases after some straining. Even if all junctions would contribute to forest hardening, they do not contribute much to the flow stress in both loading cases.

Interfacial dislocation microstructures

Deformation incompatibilities between two phases can be accommodated by geometrically necessary dislocations accumulated at the interfaces [ASH70]. These interfacial dislocations induce a long-range internal stress that contributes, with the applied stress and the coherency stress, to the total stress distri-

(a)   (b)
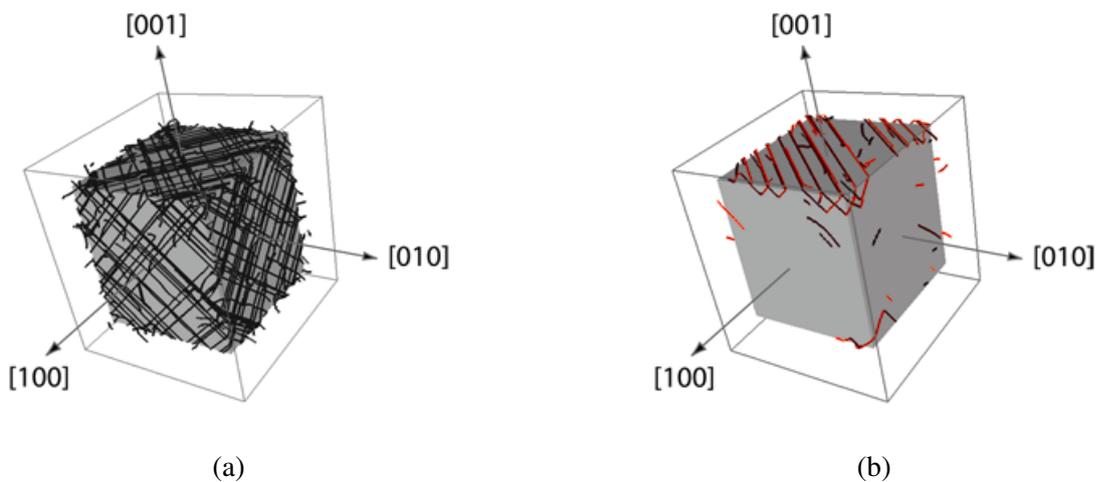
Figure 57 - Dislocation networks formed at the γ/γ' interfaces after deformation to 0.2% plastic strain. Only dislocations within a distance of 0.015 μm from the interfaces are shown for (a) the [001] case, and (b) the [111] case.

bution in the microstructure. In the DCM simulations these contributions are calculated simultaneously, and a relation between mechanical strengthening and the dislocations stored at the interfaces is expected. Figure (57) shows the dislocations deposited at the interfaces. Only those dislocations close to the interfaces (i.e. at distances smaller than 0.015 μm) are shown. For the [001] case in figure (57 a), a dense network of straight dislocations is rapidly formed at all surfaces of the precipitate. This network consists of dislocations with four different Burgers vectors, homogeneously distributed between the three {100} interfaces. In the channel direction parallel to the loading axis, the line character of the interfacial dislocations is exclusively of $\pm 60°$ type. In the two channel directions normal to the loading axis it can be either screw or $\pm 60°$ type. This results from the direction of the Burgers vector of the activated slip systems.

In the [111] case (figure 57 b), a completely different configuration is found. The dislocation network is restricted to only one interface. It consists of long parallel screw segments, all with the same Burgers vector ([110] in the figure). This configuration is one reason for the absence of hardening that was observed previously. Dislocations multiply in one single crystallographic direction and are confined to the channel containing this direction. The periodic arrangement of precipitates does not block the dislocation motion, and so it does not cause strain hardening either.

In figure (57 b), positive dislocations gliding on A6 are indicated in black and negative dislocations gliding on D6 in red. The relative equilibrium and the homogeneous distribution of red and black colors at the interfaces indicate that the interfacial dislocations do not induce a long-range stress. This will be discussed further in "Strain hardening mechanism" in section 2.4.4.4.

The strong differences between these interfacial dislocation microstructures suggest a correlation with the hardening anisotropy. In order to clarify exactly what mechanisms affect the strain hardening, a more detailed analysis is presented in the next section.

Analysis of slip systems and deformation bands

Figure (58) shows the plastic shear on each of the twelve octahedral slip systems. In accordance with the Schmid law, eight slip systems are found active in the [001] case (see figure 58 a). However, their contributions to the total plastic deformation are not distributed evenly. Several simulations were run in order to establish that this results from heterogeneities in the initial dislocation configuration. Activation of all eight slip systems is coherent with strong hardening and the dense dislocation microstructure found at the interfaces.

(a) (b)
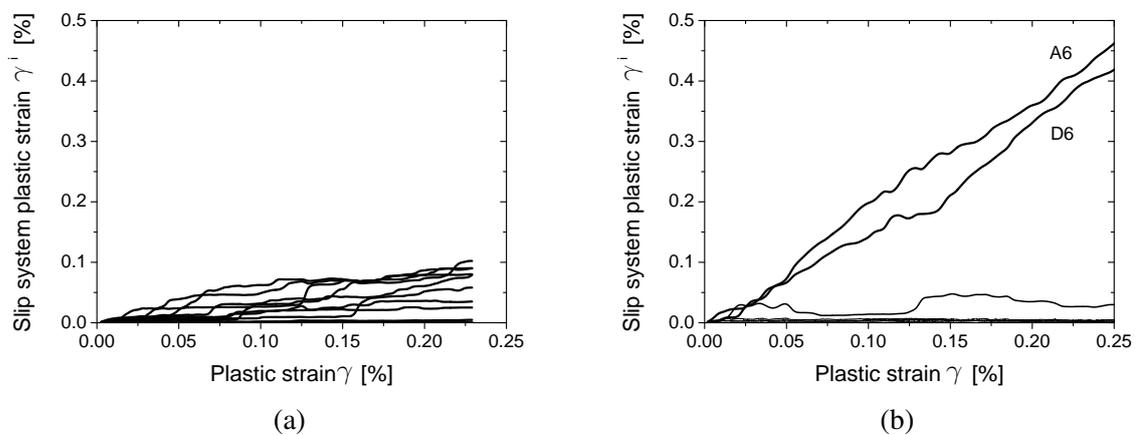
Figure 58 - Plastic strain γ^i on individual slip systems i. (a) In the [001] case, eight slip systems are activated more or less equally, in accordance with the Schmid law. (b) In the [111] case, only two slip systems are activated whereas six slip systems have the same non-zero Schmid factor.
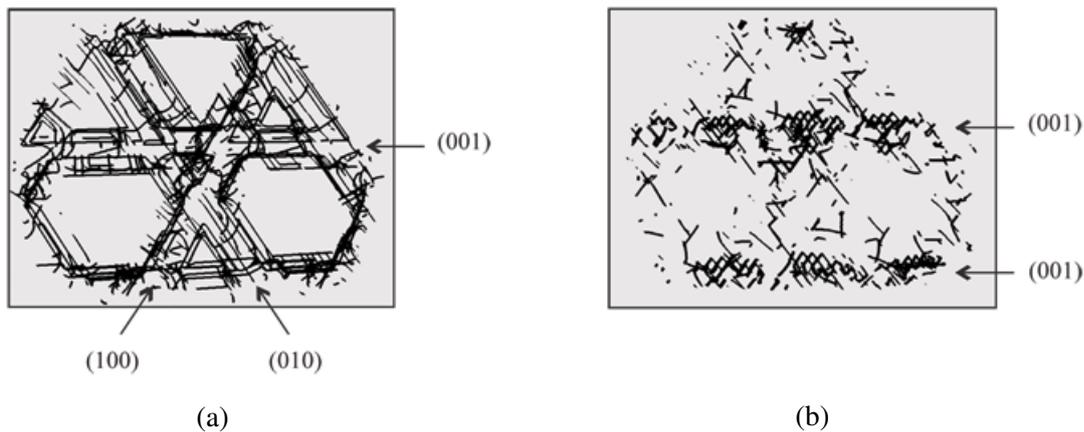
Figure 59 - Thin foils in the {111} direction are shown in order to illustrate the relation between slip system activity and dislocation microstructure for (a) the [001] case and (b) the [111] case.

In the [111] case, six slip systems have identical non-zero Schmid factor. Surprisingly, only two slip systems accommodate the imposed strain rate. For instance, in figure (58 b) the two active slip systems are A6 and its collinear system D6. Similar duplex collinear slip is observed for four other initial dislocation microstructures. In each simulation the total plastic strain is accommodated by only two slip systems: one primary system (not necessarily the same for each initial microstructure) and its collinear slip system. These two particular slip systems are correlated because they always have the same Burgers vector. Duplex collinear slip has been referenced as the strongest existing forest interaction [MAD03] [DEV05], so it should cause very high strengthening. However, the opposite is observed here. Clearly, the manner in which duplex collinear slip influences the mechanical response needs to be clarified in this particular case.

At high temperature, octahedral slip traces are very short because plastic deformation is confined to the channels, and deformation bands are observed parallel to the $\langle 100 \rangle$ directions. The deformation bands can be visualised by showing the dislocation lines stored in a thin slice of the channels. In figure (59) deformation bands are shown in slices of 0.15 μm thickness, with [111] normal and at 0.20% plastic strain, extracted from the periodic simulation cell. At low magnification, plastic deformation indeed appears as slip bands parallel to {100} cube planes. However, in the [001] case (figure 59 a) plastic strain is distributed more or less evenly among the three $\langle 100 \rangle$ directions, whereas in the [111] case (figure 59 b) the plastic deformation is restricted to only one direction.

It might be argued that the localisation of the plastic deformation into one single channel in the [111] case is caused by the lattice mismatch at the γ/γ' interfaces. However, this would create the opposite effect. This can be seen as follows. Without external loading, the mismatch creates a misfit stress which is the same in each channel. Loading along a $\langle 111 \rangle$ direction would preserve this symmetry whereas loading along a $\langle 001 \rangle$ direction would not. If there would be any localisation because of the misfit stress, it would therefore be in the [001] case, and not in the [111] case. Moreover, simulations have been carried out with two other coherency stresses ($\delta = -2\%$ and -3.5%), and it was observed that the internal stresses in the calculation affect neither the macroscopic nor the microscopic behaviour (it would have affected the initial dislocation configuration if the relaxation phase would have been included, but that is not the case here). Rather, such a localisation appears to be the result of an elementary dislocation reaction promoting dislocation glide in a specific direction and confining the deformation into one specific channel. The plastic strain remains localised throughout the whole loading path, so it must also be explained how this dynamical property is related to the absence of strain hardening in the [111] case.

In summary, dislocation dynamics and dislocation storage strongly depend on the orientation of the channels relative to the tensile axis. In the [001] case, the activation of several octahedral slip systems leads to the formation of deformation bands parallel to the {100} directions. Plastic deformation in those bands

is homogeneously distributed. Alternatively, the deformation bands in the [111] case are systematically parallel to one unique cubic direction. This direction appears to be randomly selected at the early stages of deformation. The selection depends on which particular glide systems succeed first at depositing the long screw segments at the interfaces, and this depends on the random fluctuations between one initial configuration and another. Subsequent plastic deformation is then accommodated completely there. Additional work is needed to understand how such an instability is related to the duplex collinear slip observed in the [111] case. The second part of this section aims to identify dislocation reactions controlling this complex plastic behaviour.

2.4.4.4 Dislocation dynamics analysis

Pseudo-cubic slip

In one of the very few experimental studies addressing the occurrence of cube slip in γ/γ' alloys, Bettge and Österle [OST00] observed the appearance of slip bands by TEM. Single crystals oriented with the [111]-direction near the tensile axis were deformed in uniaxial tension at 923 K and 1023 K. The deformation bands appeared in two stages: at a low plastic strain of 0.20%, the first deformation bands were all parallel to one single cubic direction. Then, at a larger plastic strain of 2.55%, deformation bands were homogeneously distributed along all three {100} directions. No cubic dislocations were observed at higher magnifications, in both stages. The deformation bands contained only $\frac{1}{2}[011]\{111\}$ type dislo-

(a)

(b)
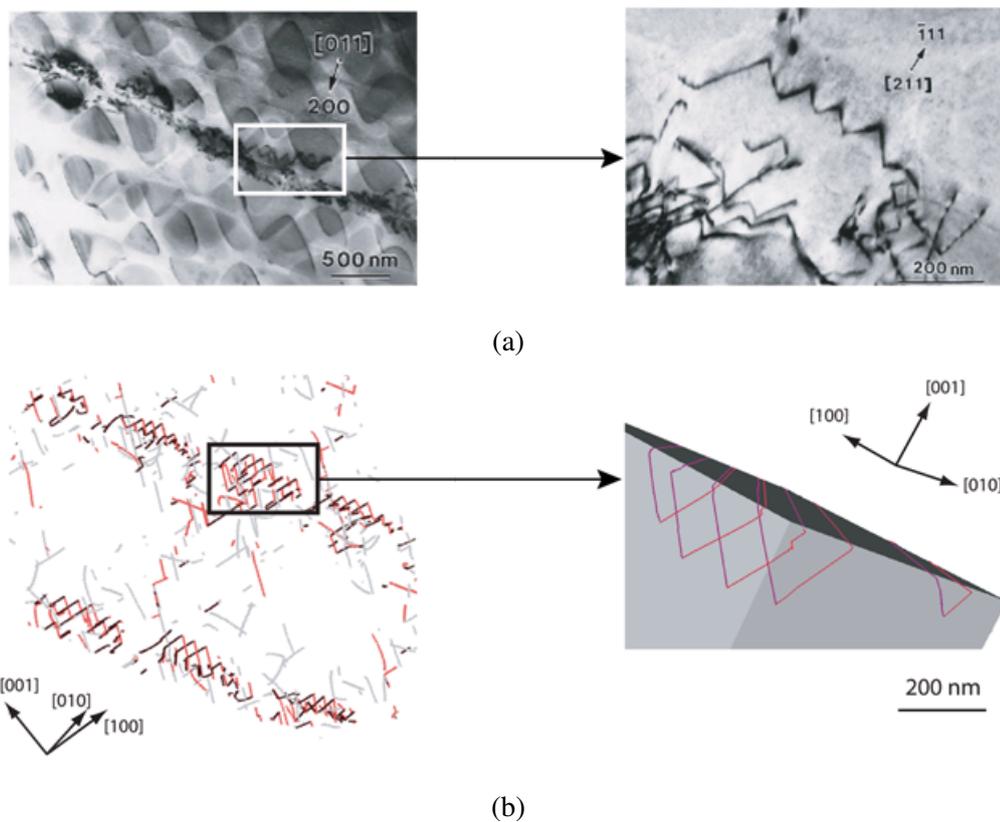
Figure 60 - Comparison between (a) experimentally-observed (after [OST00]) and (b) simulated dislocation microstructure in a matrix channel for the [111] case, after 0.2% plastic strain. (a) left: TEM bright-field image with foil normal (111) of a (100) slip band at 923 K. Right (enlarged view of the rectangular area in the image on the left): zig-zag dislocation configurations, (b) simulated dislocation microstructure at 850°C with the same foil characteristics.

cations of mixed 60° character, forming zig-zag configurations in the channels (figure 60 a). The angle between zig and zag direction was approximately 60°. Note that the results from the DCM simulations correspond to these observations for the first stage (see figure 60 a), albeit at a somewhat higher temperature.

According to Sass *et al.* [SAS97] [SAS98] and Bettge and Österle [OST00], repeated double cross-slip events might explain the formation of the zig-zag configuration and the pseudo-cubic slip traces. Their explanation is as follows: a $\frac{1}{2}[011]$ screw segment gliding in a channel on a $(1\bar{1}1)$ plane will eventually be blocked by a (100) interface. As a result of some high local stress it cross-slips onto a $(11\bar{1})$ plane. After crossing the channel on this new plane, the segment is blocked again by the interface at the other side of the channel. There it cross-slips back onto a $(1\bar{1}1)$ plane. If this double cross-slip process occurs repeatedly, the initial screw segment generates two trailing zig-zag-shaped dislocations, tracing its path. Subsequently, the two trailing dislocations glide in the $[011]$ direction, thereby shearing the material with a net cubic ("pseudo-cubic") slip.

In order to test this mechanism, two distinct sets of DD simulations have been carried out. In the first set, the cross-slip mechanism was suppressed artificially, whereas in the second set it was not. Unfortunately, the way in which cross-slip actually occurs in γ/γ' superalloys is not known. Therefore, another constitutive rule for cross-slip had to be used, similar to the one used in pure fcc metals [KUB92].

In both sets of simulations, exactly the same zig-zag configurations were obtained as in figure (60 b). Therefore, the formation of the zig-zag configuration is not necessarily associated to cross-slip, but rather must be the outcome of contact reactions during dislocation glide. In the next section, it is demonstrated that the simulated zig-zag configurations are the result of collinear annihilation between dislocations with the same Burgers vector gliding in different slip planes [DEV07].

Elementary mechanisms

The $[111]$ case is analysed first. Only two slip systems with the same Burgers vector accommodate the imposed deformation. A simple analysis of dislocation-dislocation reactions shows that dislocations are either elastically repulsive or strongly attractive and can annihilate at contact with the collinear reaction [KUB03]. In single phase materials, this reaction can annihilate very long sections of dislocation line. Therefore it has a significant impact on strain hardening and dislocation patterning [DEV07] [DEV08]. In the specific case treated here, the contribution of the collinear reaction appears to be very different as a result of the confinement of the dislocation dynamics in the narrow channels. Consequently, the following points need clarification: (i) how the zig-zag configurations are formed, (ii) how collinear reactions cause the localisation of the plastic deformation into a single cubic direction and (iii) why the $[111]$ and the $[001]$ cases are so different.

Figure (61) shows the expansion of two dislocation loops on two different slip planes, but with the same Burgers vector. The snapshots are illustrations of the most frequently occurring collinear reaction during massive simulations (i.e. simulations where loops are present on all slip systems and with realistic dislocation densities). Because of line tension anisotropy, dislocation loops expand preferentially in those channels in which their edge segments can move large distances (in the figure this corresponds to the horizontal channel). Screw dislocation segments are deposited at the precipitate surfaces bounding these channels. Other screw segments cross the vertical channels but do not bow out there much because they are held back by the higher line tension in those directions. As illustrated in figure (61) at t_4 and t_5, if the intersection of the two slip planes does not lie too far into the vertical channel, the screw line sections of both dislocations are annihilated there. This leaves behind "V"-shaped dislocation debris of 60° character against the two precipitate surfaces which bound the vertical channel. The accumulation of such "V"-shaped debris during plastic deformation is the explanation of the zig-zag configurations observed in the simulations (see figure 60).

As argued above, dislocations of a given Burgers vector preferentially glide in a specific channel because of the line tension anisotropy. Consequently, within the plastically active channels there is a high probability of collinear interactions, and a large diversity of reactions is indeed observed there. Figure (62)
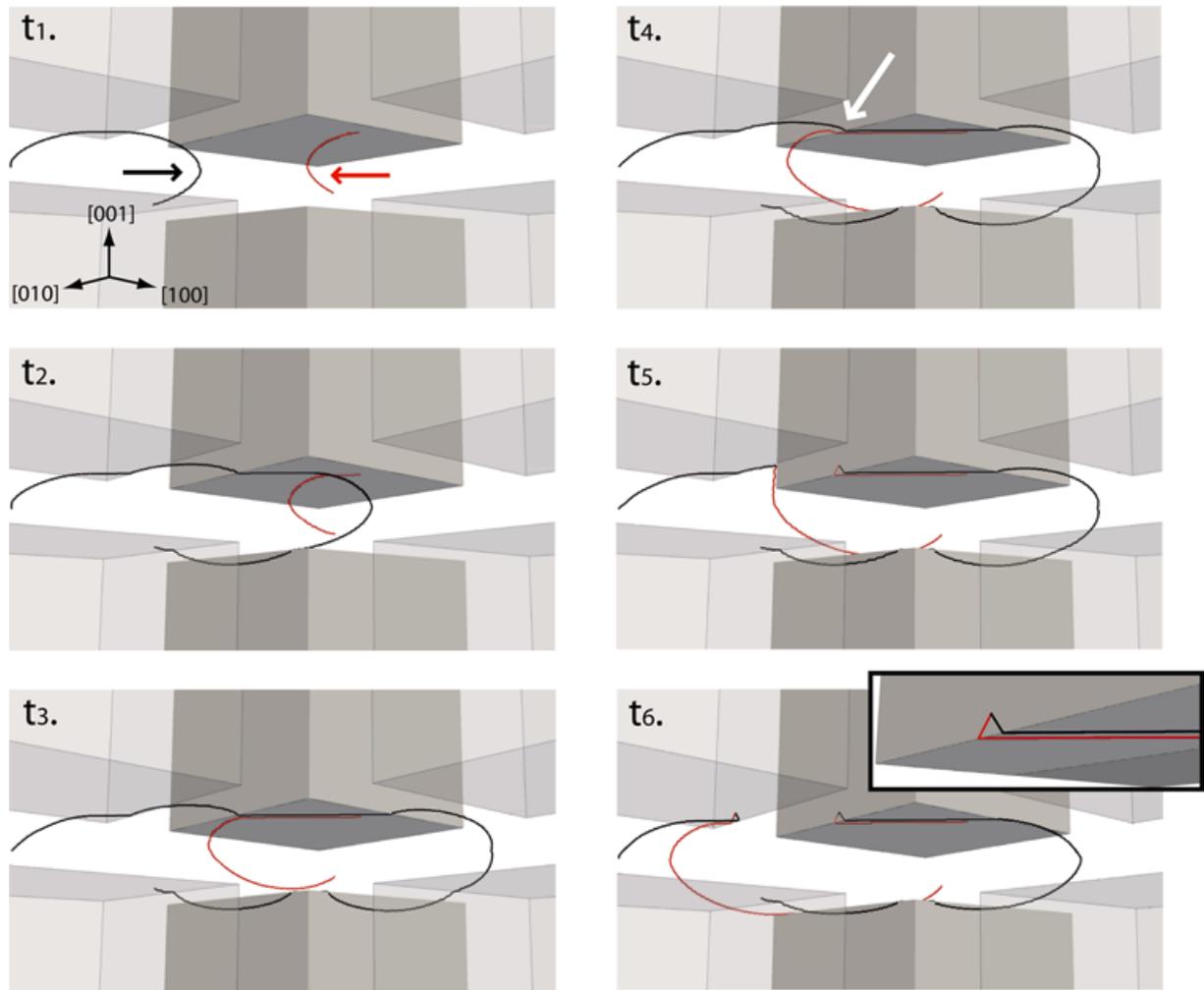
Figure 61 - Successive snapshots $t_1 - t_6$ of the creation of "V"-shaped debris, the elementary pieces of the zig-zag dislocation configuration.

shows three representative examples.

Figure (62 a) shows the simplest one. Two attractive dislocations bow out on intersecting planes, but now the planes intersect inside the active channel instead of outside, as in the previous case. The line of intersection is shown as the dotted line in figure (62 a_3). The dislocations exchange line sections ("arms") as a result of a collinear reaction, and again two "V"-shaped configurations are formed. This time however, there are no vertical interfaces to block them, and they can glide across long distances after the reaction.

Figure (62 b) shows subsequent possible reactions between "V" configurations (or even more complex dislocation configurations). For each collinear reaction, an exchange of dislocation arms is observed and the new dislocation configurations contain collinear super-jogs, forcing dislocation glide in the direction of the Burgers vector. The latter direction is parallel to the channel interfaces, so the new dislocation configuration is potentially mobile. Two cases can now be distinguished: (i) the super-jog glides in the same direction as the primary line. For the same applied stress the total force acting on the dislocation line then increases, because it is now longer than before. This facilitates cutting or bypassing obstacles, so that its mobility increases [DEV07] (see figure 62 b). (ii) The super-jog glides in the opposite direction as the primary line. Then it tends to increase its length, to bow out and sometimes act as a dislocation source (see figure 62 c).

The larger the plastic deformation, the more collinear super-jogs accumulate along the dislocations. This evolution justifies two important properties of the [111] case. First, the decoration with collinear super-
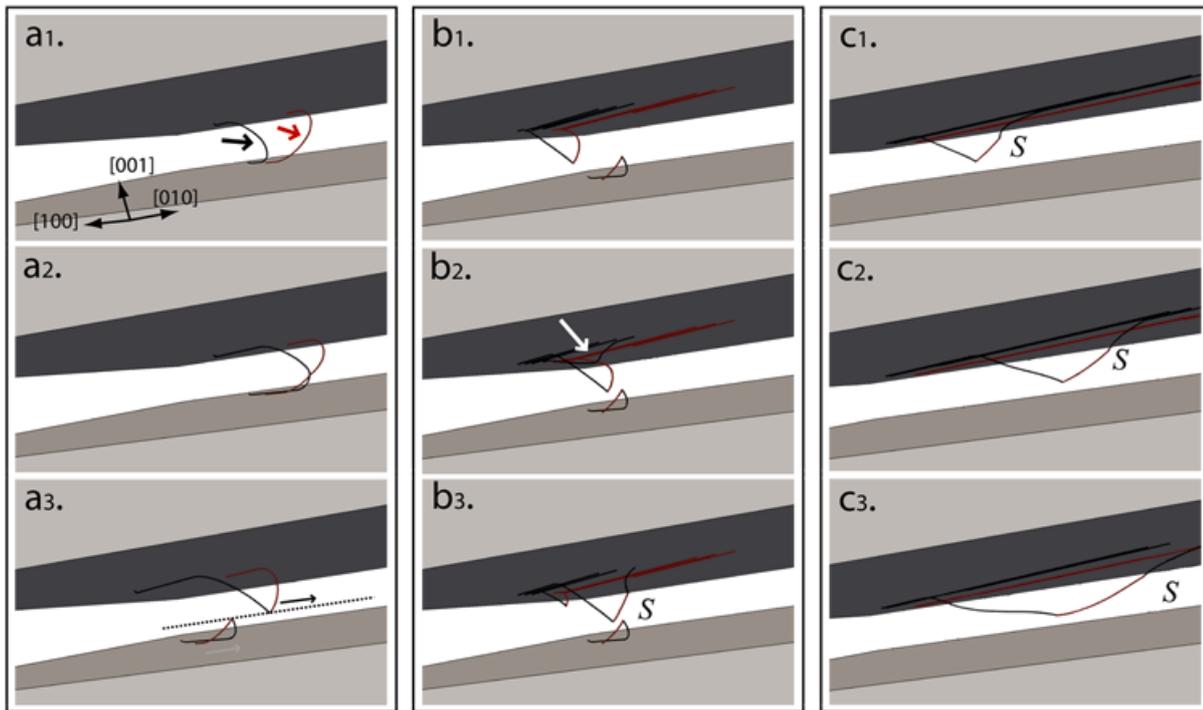
Figure 62 - (a) The collinear reaction: two curved dislocations with the same Burgers vector are gliding in a γ channel. After a collinear reaction, dislocation arms can only move in the same channel and in the same direction (illustrated by the dotted line and the black arrow at a_3). (b) Creation of a superjog S: mobile arms can react with an immobile dislocation to create a superjog (shown by the white arrow at b_2). The latter moves in the same direction as the primary lines, thereby increasing the mobility of the dislocation. (c) Creation of another superjog S: in this case it moves in the opposite direction as the primary lines, thereby increasing its line length. The newly created dislocation line can then bow out and even act as a dislocation source.

jogs enforces a localisation of dislocation motion in their initial channel because they can glide easily only in the direction of the Burgers vector. Second, super-jogs increase the mobility of some dislocations, because they increase the length of those mobile lines which can progress easily in-between the interfaces.

The plastic localisation observed in the simulations is certainly exaggerated because of the ideal arrangement of the periodic replicas of the precipitate. In reality, the precipitate arrangement is not perfectly regular and because of that the easy glide simulated here, with a very long dislocation free path, will eventually be blocked by some precipitate. At larger strains, additional slip systems must then be activated in the other channels.

Next, the [001] case is analysed. In this orientation it must be understood why the same elementary dislocation reactions do not lead to the same plastic instabilities as in the [111] case. At the start of the simulation of the [001] case, the first slip systems activated in a channel are depositing pure screw segments at the γ/γ' interfaces, as in the previous case. Hence, the argument of line tension anisotropy promoting collinear duplex slip in specific channel directions also applies here. However, this time the plastic strain does not localise into one single channel, and a very strong strain hardening is observed. The origin of this strain hardening is explained in the next section.

In agreement with other simulations on single-phase fcc crystals [DEV07], the mobility of dislocation lines decorated with collinear super-jogs is different between the two loading cases. As explained in [DEV07], in the [001] case most collinear super-jogs decorating the dislocation lines are resistive. They tend to move in the opposite direction as the main line and must be dragged along by the mobile disloca-

tions, thus increasing the flow stress somewhat. They also increase the rate of dislocation multiplication, because the long collinear super-jogs can act as dislocation sources. This contributes significantly to the high strain hardening observed in the [001] case.

Strain hardening mechanism

In the previous section it was observed that the same dislocation reactions give very different plastic responses for the two loading directions. In the [111] case, dislocation mobility is high and there is no strain hardening. This is why the localisation of plastic strain into one specific channel can hardly be stopped once it has been initiated. In the [001] case, dislocation mobility is lower, the multiplication rate is high and there is significant strain hardening. Given that forest hardening hardly contributes to the flow stress (see "Macroscopic mechanical response" in section 2.4.4.3), the internal stress in the simulated volume is now analysed in order to identify the dislocation mechanisms that govern strain hardening.

A first hypothesis is that the strain hardening in the [001] case is an incidental effect of the larger number of slip systems that can be activated. For testing this hypothesis, a model simulation containing only dislocation loops on two collinear slip systems A6 and D6 is carried out for both loading cases. The resulting stress-strain curves are very similar to the ones obtained with loops on all slip systems. In addition, the evolution of the total dislocation density in these simulations has the same tendency as in figure (56 b). For the [001] case, interfacial dislocations are accumulated around all channels. For the [111] case, only a few screw dislocations are stored at the interfaces of one channel. This demonstrates that the observed strain hardening does not depend on the number of activated slip systems. Rather, it depends on the manner in which the dislocations are stored at the interfaces. In the simulations, this orientation dependence of the dislocation density distribution and the resulting hardening is obtained when at least two collinear slip systems are activated. The importance of the simultaneous activation of collinear slip systems is justified in what follows.

Next, returning to the massive simulations, the strain hardening of both orientations can be linked to the internal stresses created by the dislocations stored at the interfaces. Figure (63) shows the internal stress τ^{int} (see section 2.1.3) in the simulated volume for both loading cases. This is calculated as the self-stress field of all dislocations resolved on one $(\bar{1}11)[110]$ active octahedral slip system in an infinite periodic microstructure. The images in figure (63) are the averages of ten cross-sections of normal [001], taken at regular intervals along the entire edge of the simulated volume.

From figure (63 a), the strain hardening in the [001] case can be correlated to the high internal stress in the channels. Analysis of the dislocation dynamics in the active slip planes shows that the PK force on gliding dislocations is systematically reduced by the stress field of the dislocations accumulated at the

(a)   (b)
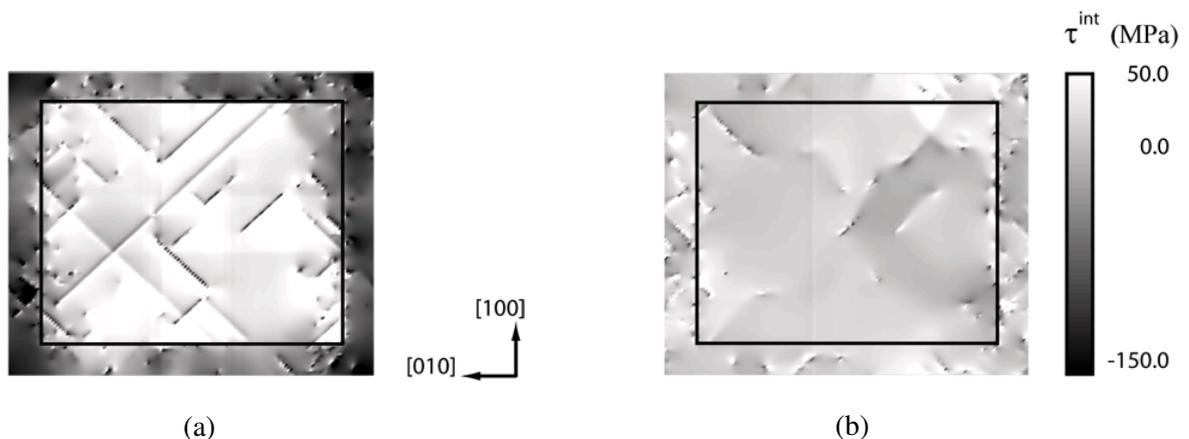
Figure 63 - The internal stress τ^{int} in the simulated γ/γ' microstructure for (a) the [001] case and for (b) the [111] case. The internal stress is calculated as explained in the text.

interfaces. The origin of this polarised internal stress is that the sign and amplitude of the Schmid factors on collinear slip systems are identical. As a consequence, the sign of the dislocations gliding in a crystal direction and the sign of the dislocations accumulated at a given interface are identical. In addition, with the elevated multiplication rate (see "Elementary mechanisms"), the repulsive back stress associated to interfacial dislocations rapidly prevails. This explains why the dislocation dynamics is rapidly distributed among the three channels. At the precipitate surfaces dislocations of screw and $\pm 60°$ character are then found.

In the same manner, absence of strain hardening in the [111] case can be explained by two observations: (i) the interfacial dislocation network is not polarised, and (ii) the dislocation density during deformation remains low. The first point occurs because the Schmid factors on collinear slip systems are of opposite sign. For a specific line direction of the long screw segments covering a specific interface, the sign of the Burgers vector is not unique. As shown in figure (63 b) this generates only a low internal stress in the microstructure which hardly contributes to the strain hardening. The second point is explained as follows: as a result of the many collinear reactions taking place inside the channel, a dislocation segment decorated with an odd number of collinear superjogs and which remains in the same channel is necessarily connected to two interfacial dislocations with identical sign (see figure 64). For such segments, the length of dislocation on different slip planes is unbalanced, so they can glide in the screw direction, with a constant total length of interfacial dislocations. These two points explain how the channels can be easily deformed plastically with hardly any increase in the dislocation density.

Lastly, it must be noted that the strain hardening is essentially kinematic in nature because it is mainly controlled by the formation of a polarised interfacial dislocation network. The internal stress in the channels created during a [001] tensile test would increase dislocation mobility in a subsequent compression test. More generally, one can conclude from the analysis of the simulated results that a strong kinematic hardening is expected in single crystal superalloy samples deformed uniaxially in a direction close to one
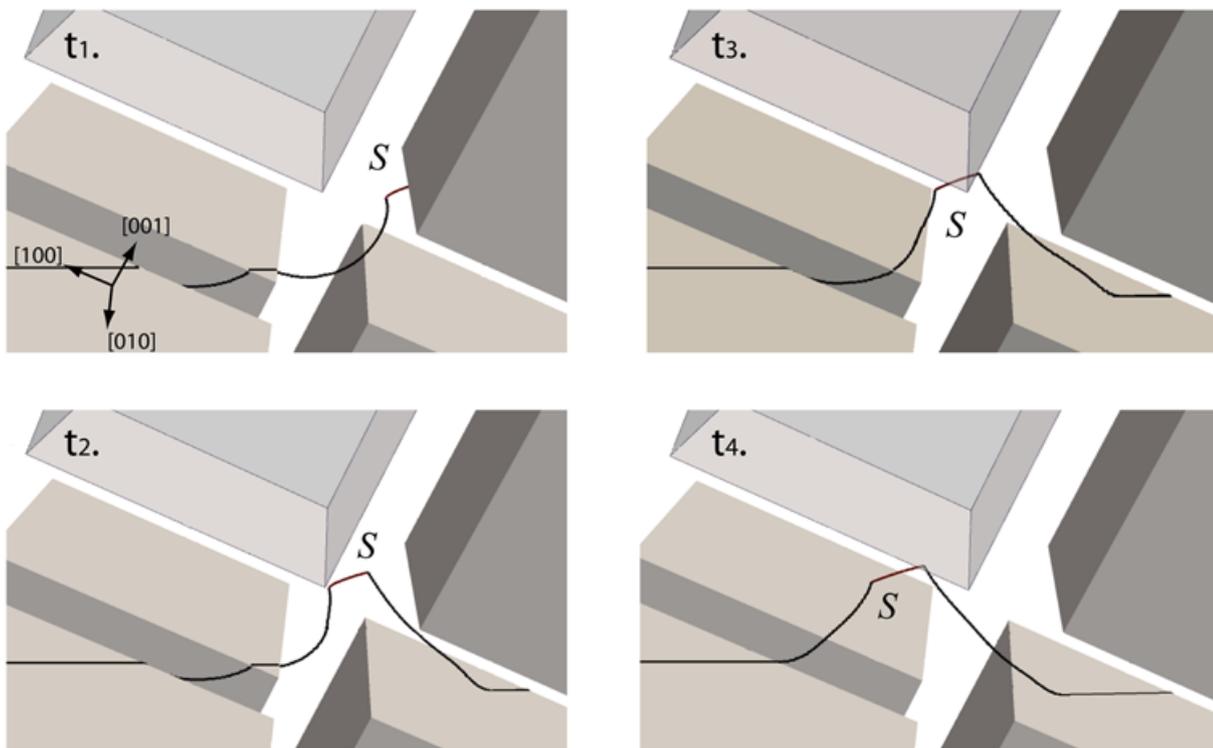
Figure 64 - Dynamics of a dislocation line decorated with a collinear superjog, moving in the screw direction. Glide of the line section in the γ channel (including the superjog S) produces plastic deformation, but without variation of the total dislocation length.

of the $\langle 001 \rangle$ directions. Also, a smaller and more isotropic hardening is expected in uniaxial tests where the Schmid factors on collinear slip systems have opposite signs, e.g. with the tensile axis close to the $\langle 111 \rangle$ or $\langle 101 \rangle$ crystal directions.

2.4.4.5 Concluding remarks

Many studies have modelled the mechanical response of single crystal γ/γ' superalloy by using the FE method. However, conventional continuum theory can predict neither the anisotropy nor the size dependence. Rather, they have to be included a priori, for instance by explicitly introducing a length scale into the constitutive descriptions, or by adding additional mechanisms to account for the anisotropy.
In this section, the objective of the DCM simulations was to reproduce the macroscopic response for the [001] and [111] cases, and to analyse the resulting dislocation structures in order to understand the differences. Precautions have been taken to obtain realistic initial dislocation microstructures, and the dislocation analyses have been compared with experiments. The main results are summarised as follows:

* In accordance with experiment, the macroscopic stress-strain curve for [001] oriented specimens exhibits a strong linear hardening, whereas the stress-strain curve for the [111] orientation shows a stress drop after an upper yield point, followed by a low hardening stage. The difference has been correlated with much less dislocation storage for the [111] case than for the [001] case. In addition, at small strains forest hardening does not significantly influence the mechanical response because it is rendered ineffective by the dislocation-precipitate interaction.

* DCM simulations have shown that all dislocations are ultimately stored at the γ/γ' interfaces. When the Orowan stress is reached, dislocation loops move through the channels, bowing out between the precipitates and depositing dislocation segments at the interfaces. For the [001] case, these discrete segments have a screw character or a mixed $60°$ character, and the interfacial dislocation network thus created is polarised (see figure 52 b). For the [111] case, only two active octahedral glide systems deposit dislocation segments at the channel walls. These long parallel screw segments all have the same Burgers vector. Due to the fact that the two active systems are always collinear, the number of possible dislocation reactions is strongly reduced.

* Dislocation structures at the interfaces differ strongly between both orientations. In an optical microscope, the dislocation structures appear as deformation bands parallel to the $\{100\}$ cube planes. In the [001] case, eight octahedral slip systems are activated and a dislocation network is formed at all six surfaces of the precipitate. This appears as deformation bands along all three cubic directions. In the [111] case, the dislocation network is formed only on two interfaces, because the dislocation dynamics takes place only within one channel. In accordance with experiment, the deformation band is located within one unique channel. This channel is deformed almost exclusively by only two slip systems.

* As previously observed experimentally by Bettge and Österle [BET99], at the fine scale, zig-zag dislocation configurations are observed. Such configurations are more easily observed in the [111] orientation because the dislocation density is lower there, but they exist whatever the loading axis. These zig-zag configurations are the product of collinear annihilation reactions between dislocations in slip systems having the same Burgers vector. Two kinds of zig-zag configurations are observed: (i) a series of immobile "V" debris located at the interfaces, and (ii) very mobile jerky dislocation lines decorated with collinear superjogs, confined within a channel. The latter are responsible for the localisation of the plastic deformation and are the main mechanism for the easy glide observed in the [111]-oriented specimens.

* During the localisation of the plastic deformation in the [111] orientation, long segments with the same Burgers vector but opposite line vectors are deposited at the interfaces. These dislocation configurations are not polarised at the interfaces and so do not create long-range internal stresses.

In addition, the high mobility of superjogs within the deformed channel increases the possibility of annihilation of these long interfacial segments, thus explaining the reduction of the dislocation storage rate during deformation. Hence, the absence of hardening in the [111]-oriented specimens is caused by the diminishing evolution of dislocation density and the absence of long-range internal stress.

2.4.5 Guidelines for improving constitutive laws

Guidelines to improve the constitutive laws for γ/γ' single crystal superalloys used in continuum modelling can be deduced from the simulations in the sections 2.4.3.3 and 2.4.4.

On the one hand, it has been observed that the work hardening rate in these materials is higher than estimated from simple theoretical models based on forest hardening. In this context, Ashby [ASH70] has introduced the term "geometrically necessary dislocations" to account for the dislocations related to the mesoscopic gradients of plastic deformation. Being deposited in the vicinity of inclusions in addition to the usual "statistically stored" ones, these dislocations are thought to increase the work hardening of the composite materials. Brown and Clarke [BRO77] have suggested three contributions to the flow stress τ_f in an analysis of the work hardening in composites: (i) the usual forest contribution τ^{forest} (similar to equation 2.52), (ii) the so-called "source-shortening" term $\tau^{\text{s-shortening}}$, and (iii) the mean internal stress τ^{Eshelby} in the matrix which can be estimated using for instance by the Mori-Tanaka or Eshelby approaches.

These phenomena are nontrivial in γ/γ' superalloys, and for sake of simplicity, the strengthening contributions are considered to be independent and additive. Thus τ_f may be written as

$$\tau_f = \tau^{\text{forest}} + \tau^{\text{s-shortening}} + \tau^{\text{Eshelby}} + \tau^{\text{Orowan}} \tag{2.53}$$

with τ^{Orowan} the critical stress for the Orowan process illustrated in section 1.1.3.4.

∗ As explained above, forest hardening is not significant with respect to Orowan strengthening. The latter corresponds to the threshold stress τ^{Orowan} inversely proportional to w. Forest hardening can thus be neglected, i.e. $\tau^{\text{forest}} \approx 0$.

∗ The source-shortening term has been explained as the effect of the Orowan loops left behind around the precipitates. The local stresses due to the Orowan loops reduce the effective inclusion spacing by causing the successive dislocations to stand off of the precipitates, thus increasing the dislocation bow-out stress. This effect is well-known in the literature [BRO77] [MOR98] as the source-shortening model. Nevertheless, due to the small microstructural dimensions and the confined plasticity in the γ channels, dislocations are forced to bow out between the particles and no pile-ups are formed in the simulations. This is why a source-shortening effect has not been observed and it does therefore not contribute to the reduction of the dislocation mean free path, so that in γ/γ' case, $\tau^{\text{s-shortening}} = 0$.

∗ Even though in the 3D simulations no pile-ups have been found, a network of interfacial dislocations pressed onto the impenetrable boundaries of γ' precipitates has nevertheless been observed at the simulated temperature of 850°C (see figure 53 b). Whereas the critical threshold is controlled by the spacing between precipitates, the work hardening seems to depend on the high volume fraction of the precipitates: the larger the volume fraction, the higher the storage of dislocations. In a first approximation, the critical threshold τ^{Orowan} is controlled by the Orowan mechanism, and the work hardening by the accumulation of dislocations at interfaces which induce internal stresses inside the microstructure (see figure 63 a). The polarised dislocation distribution at the interfaces create long-range internal stresses. These interfacial dislocations are responsible for the hardening, which is mainly controlled by the stress fields of dislocations stored at the interfaces. Macroscopically, only the long-range internal stresses generated through the Nye tensor and represented by the mean internal stress τ^{Eshelby} may be taken into account.

On the other hand, many crystal plasticity models use additional cubic slip systems in order to capture the tensile anisotropy between the [001] and the [111] case phenomenologically. At a macroscopic scale this assumption is justified by the presence of deformation bands along the cubic directions. However, at lower length scales or (presumably) for more complex loading cases this is no longer valid. Moreover such a simplification is not needed for large scale computations:

* In the [001] case, the storage of dislocations into a polarised interfacial network can be modeled by considering the polar/excess/geometrically necessary dislocation density. Most of the dislocation density is concentrated at the interfaces instead of into pile-ups. It can then be supposed to be concentrated at a singular surface and be measured by the surface dislocation density tensor defined by Nye [NYE53].

* The anisotropy of the strain hardening is essentially determined by the nature of the dislocation network at the interfaces. For the [111] case, the interfacial dislocations are not geometrically necessary, in contrast to the [001] case discussed above. In order to capture this difference, the sign of the Burgers vector of each interfacial dislocation should be taken into account explicitly. One way to do this is to split the usual 12 octahedral systems containing dislocations of both signs into 24 systems containing dislocations of only one sign. Then, depending on the sign of the Schmid factor, one specific interfacial dislocation may have (for instance) a positive sign of the Burgers vector in the [001] case, whereas the same dislocation will have a negative sign in the [111] case [KUB06]. The net effect is a different macroscopic response for the two cases.

The latter points have been taken into account in the enrichment of a dislocation-based micromechanical model initially developed by Fedelich [FED02]. This will be presented in section 3.2.

Résumé

Le but des simulations 3D de DD est de fournir un outil de compréhension permettant d'aborder la modélisation de la plasticité des cristaux de manière réaliste. Ces dernières années, la DD s'est avérée précieuse dans l'étude des interactions élémentaires entre dislocations et du durcissement de la forêt des métaux cfc sans paramètre ajustable. Néanmoins, la prédiction du comportement mécanique des matériaux hétérogènes constitue aujourd'hui un problème complexe qui nécessite, afin de dépasser le stade conceptuel du monocristal soumis à une contrainte uniforme, de pouvoir prendre en compte des situations impliquant soit des sources de contraintes internes (présence de précipités), soit des chargements complexes. En somme, il est important d'intégrer dans les simulations, les conditions aux limites réalistes de matériaux complexes couramment testés en laboratoire.

Dans ce contexte, un couplage original de la simulation de DD avec un code d'EF a été initié par Lemarchand [LEM99] [LEM01] et Groh [GRO03a] à l'Onera, sous l'appellation de Modèle Discret-Continu (MDC). Notons qu'il existe depuis quelques années d'autres approches de simulation hybride, plus ou moins proches de la solution du MDC [VAN95] [FIV99] [ROD01] [GRA07] [LIU09]. Chacune de ces méthodes présentent des avantages et inconvénients en comparaison avec le MDC (écriture aux grandes déformations, type de code DD sous-jacent, résolution des interactions à courte distance...). Le MDC consiste principalement à substituer la loi de comportement classique du code EF par une simulation de DD permettant de décrire les processus fondamentaux physiques de la déformation plastique. Dans le schéma EF, les dislocations sont décrites à travers les eigenstrains induits par le mouvement des dislocations régularisées dans un volume de "coarse graining".

Au-delà des aspects purement techniques, comme le portage des modules des deux codes (mM , Z-SeT, ainsi que le wrapper Zpvm et le greffon zMDC, voir Annexe B) vers leurs dernières versions, les développements récents effectués sur le MDC ont portés sur (i) la discrétisation des lignes de dislocation qui intègre maintenant le récent modèle "mixte" du code de DD, (ii) les conditions initiales du problème mécanique à travers des boucles dipolaires de Volterra, (iii) la réécriture sous une forme optimisée de la

procédure du calcul de la déformation plastique afin d'améliorer les performances en termes de temps CPU (pour les même temps de calcul, les performances ont été améliorées d'un facteur 10 depuis la précédente version utilisée dans la thèse de Groh), et enfin (iv) le caractère multi-domaines du MDC pouvant désormais appréhender des problèmes avec plusieurs phases plastiques et/ou plastifiables.

Dans un premier temps, après validation du MDC, les règles fondamentales introduites dans le code afin d'accéder aux mécanismes fondamentaux de la plasticité dans les superalliages monocristallins ont été détaillées. Le mécanisme de cisaillement des précipités cuboïdaux cohérents par superdislocations a été implémenté. L'objectif est de comprendre l'influence de certains paramètres physico-chimiques et morphologiques de chacune des phases sur les propriétés mécaniques du monocristal biphasé. Les résultats montrent que dans les couloirs de matrice, le rayon de courbure de la dislocation dictée par la tension de ligne contrôle principalement la contrainte critique de cisaillement. Une forte contrainte de friction de réseau dans la matrice ou une forte énergie d'antiphase dans le précipité sont deux paramètres qui contribuent à la diminution de la mobilité des dislocations. Cette étude a permis de reproduire la contrainte critique de cisaillement dans une large gamme de températures de 25 à environ 850°C.

Dans un deuxième temps, deux applications qui ont toutes deux trait au traitement des effets de taille et de l'orientation de chargement ont été réalisées à 850°C. Concernant l'effet de taille, le MDC a pu prédire la contrainte d'Orowan macroscopique, contrainte couramment observée en métallurgie. Par ailleurs, le MDC prévoit une limite d'élasticité à 0.2% de déformation plastique dépendante de la largeur du couloir. Les mécanismes de microplasticité qui sont responsables de cet effet sont dictés par une forte accumulation de dislocations aux interfaces, dont le taux de stockage de la densité de dislocation est fonction de la largeur des couloirs de matrice. C'est pour cette raison que les modèles classiques de plasticité de type stockage-restauration semblent insuffisants pour le biphasé lorsque le libre parcours moyen des dislocations est lié à la présence des interfaces du précipité.

La seconde application porte sur les effets de l'anisotropie de l'orientation du chargement en traction monotone suivant $\langle 001 \rangle$ et $\langle 111 \rangle$ à hautes températures. Bien qu'aucune modélisation par DD n'avait été effectuée auparavant, une abondante littérature expérimentale existait dans ce domaine. Les résultats numériques rendent compte de nombreuses observations obtenues expérimentalement: des similitudes entre les microstructures simulées de dislocation en zig-zag aux interfaces et observées au microscope électronique en transmission ont été montrées. Cette comparaison a permis d'accorder du crédit supplémentaire aux résultats simulés et à comprendre en détail les microstructures formées.

L'étude des densités de dislocation a permis de montrer que l'accumulation des dislocations aux interfaces est bien plus faible en $\langle 111 \rangle$, et que seuls deux systèmes actifs localisés dans un couloir du cristal accommodent la quasi-totalité de la déformation plastique. L'étude des mécanismes responsables de la formation de la localisation, faite d'enchevêtrements de supercrans mobiles dans le couloir et tapissant les interfaces de dislocations non polarisées, a conduit à l'explication de cette anisotropie d'écrouissage. Cette étude est capitale car une question sur la véritable activité des systèmes cubiques sur la matrice des superalliages se pose. De ce fait, la mise en évidence de ce nouveau mécanisme et de ses conséquences sur le comportement sera exploitée dans le prochain chapitre dans un but d'amélioration un modèle micromécanique de plasticité.

A ce stade, il est important de concevoir que l'utilisation du MDC ne doit pas seulement être perçu comme un outil prédictif mais aussi comme jalon incontournable intégré dans un schéma multi-échelles.

Continuum plasticity in dislocated γ/γ' superalloys

Contents

Introduction

Ce troisième chapitre intitulé "Plasticité continue dans les superalliages γ/γ' disloqués" est composé de deux parties. La première partie 3.1 illustre un modèle de plasticité à longueur interne faisant appel à la notion métallurgiste de densité de dislocations dites géométriquement nécessaires. Ces calculs sont justifiés à une échelle intermédiaire caractérisée par des régions riches et pauvres de dislocations. Le calcul de volume élémentaire représentatif qui décrit une distribution inhomogène de dislocations s'avère d'une importance capitale dans l'optique d'établir des directives pour la construction d'un modèle "plus macroscopique". En somme, la principale fonction de ce modèle est d'appréhender "le *macro* du physicien" pour mieux ajuster "le *micro* du mécanicien" via une transition discrète-continue de la plasticité.

La seconde partie 3.2 présente un modèle micromécanique prenant en considération les résultats obtenus aux échelles inférieures ainsi que le rôle de la microstructure du matériau hétérogène dont le comportement est de nature élastoviscoplastique. Ce modèle a initialement été développé par Fedelich [FED99] [FED02] et amélioré dans le cadre d'une étroite collaboration avec le Bundesanstalt für Materialforschung und -prüfung (BAM) à Berlin durant ce travail de thèse. Les efforts réalisés ont porté sur la justification physique du modèle continu à travers les résultats obtenus par le MDC, et plus particulièrement sur la question de l'activation des systèmes de glissement cubiques des dislocations sous un chargement autre que $\langle 001 \rangle$. Il s'agit d'un exemple de transition (micro-macro) d'échelles où les simulations discrètes ont permis d'asseoir un modèle continu aux échelles supérieures. Le comportement mécanique est déduit des mécanismes physiques à l'origine de la déformation plastique. A ce titre le modèle est physiquement justifié, identifié et validé à 850 et 950°C sur le CMSX-4 pour une large gamme d'essais sous diverses vitesses de sollicitation et d'orientations.

3.1 An intermediate dislocation-density based model on the μm-scale

3.1.1 Introduction

Numerical analysis of single crystal superalloys using classical FE method can be categorised into two basic approaches.

The first approach uses a homogenised constitutive description for the γ and γ' phases without a distinct delineation of the γ/γ' phases in the FE mesh. Each IP can be thought of as containing a RVE, which is assumed to contain the microstructural details of the γ and γ' phases in a homogenised constitutive description [NOU95] [FLE96] [FED99] [MAC01] [FED02] [PRE09]. These constitutive descriptions applied to engineering applications, such as those in actual component design. This approach is conceptually more global in representing the microstructure as a volume element. It will be used in section 3.2. The second approach is to use a periodic unit cell representation of the microstructure, where the two

phases are represented separately: a parallelepiped with the mechanical properties of the γ' precipitate, embedded inside another with those of the γ matrix. Several authors have modelled the mechanical behaviour of superalloys for an idealised microstructure using FEM [GLA89] [POL92] [NOU97] [KUT98] [BUS00] [FOR00] [MEI01] [CHO05]. Numerical modelling of idealised alloy microstructures using FE method can be used to examine the effects of precipitate-level morphology on the flow response of the overall body. In this approach one can apply separate constitutive descriptions for the γ matrix and the γ' precipitate, and investigate the local flow distributions and the macroscopic flow responses under various γ/γ' geometries.

This section 3.1 of the thesis deals with an intermediate model, proper to the second approach. As already stated in section 1.2.4, classical local plasticity theory, in which no length scale enters, disregards the influence of the microscopic material structure on the macroscopic material behaviour. Although local theories are able to interpret the material behaviour in a large number of applications, they become inadequate to model phenomena such as the experimentally observed size-dependence of plastic response of micro-sized solids. Indeed, experiments (or for instance the numerical DCM results, see figure 49) show that the real material behaviour exhibits significant size effects under certain circumstances. Typical examples of such experiments are depicted in figure (65) [FLE94].

Each of these experiments results in a plastically inhomogeneous deformation and consequently plastic strain gradients induced by one of the following underlying mechanisms:

 * For complex loading cases, a homogeneous specimen can exert deformation inhomogeneities. In the bending and torsion specimens (see figures 65 a and b) the plastic slip remains zero ($\gamma = 0$) on the neutral or the central axis and increases ($\gamma \gg 0$) towards the compressive/tensile fibre or the wire surface, respectively.

 * The local boundary conditions may induce a locally inhomogeneous deformation. In the inden-
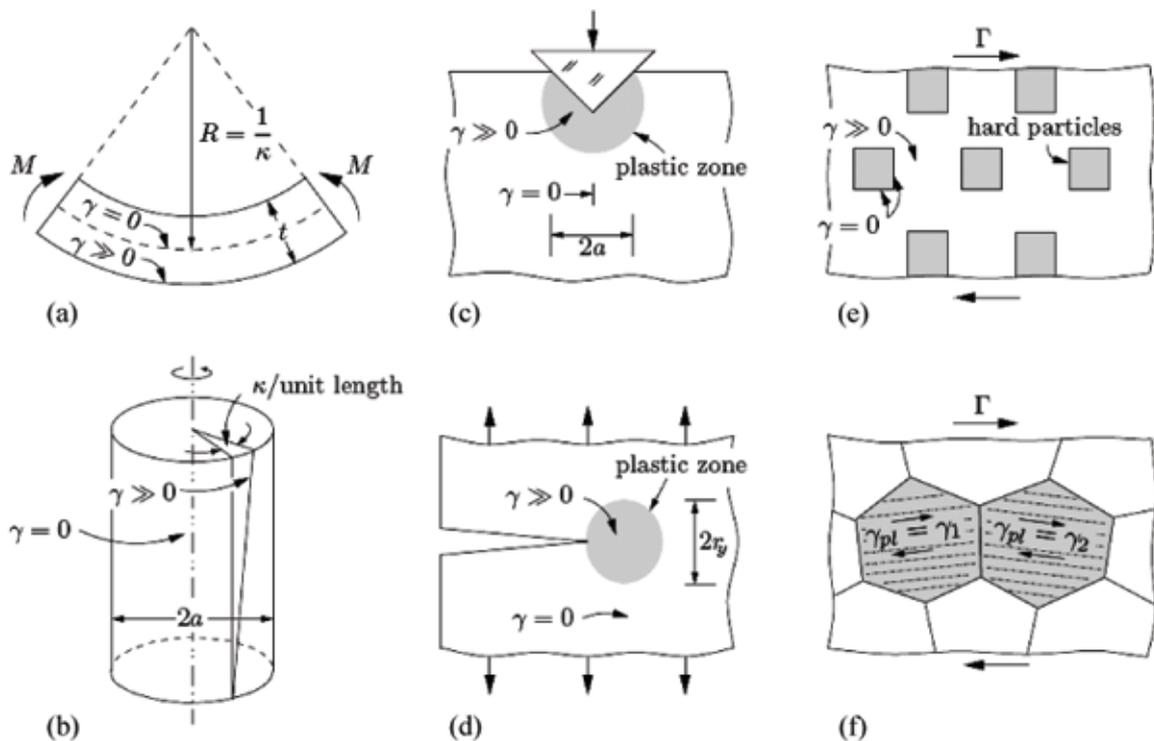
Figure 65 - Experiments inducing plastically inhomogeneous deformations and thus plastic strain gradients [FLE94]. (a) Bending and (b) torsion test of a homogeneous specimen, (c) and (d) indentation test and cracking of a specimen with a zone of concentrated plastic deformation, (e) shear test of a heterogeneous composite and (f) of a polycrystal.

tation test (see figure 65 c) and in the cracked specimen (see figure 65 d) a plastic zone with maximum plastic slip ($\gamma \gg 0$) develops beneath the indenter or at the crack tip, respectively, while the remaining part of the specimen exhibits only elastic deformations ($\gamma = 0$).

∗ The heterogeneity of the specimen results in an inhomogeneous deformation. In the shear test of a heterogeneous composite (see figure 65 e) the stiff particles deform only elastically ($\gamma = 0$) while the matrix material exhibits an inhomogeneous elastic-plastic deformation ($\gamma \gg 0$). In the shear test of a polycrystal (see figure 65 f) neighbouring grains undergo different amounts of plastic slip in varying directions resulting in a possible mismatch of slip at the grain boundaries.

In either of the three cases, the inhomogeneous deformations induce gradients of plastic slip between plastically non-deforming zones ($\gamma = 0$) and plastic zones ($\gamma \gg 0$). These gradients require the storage of dislocations for compatibility reasons. Thus, since these dislocations are necessary in order to accommodate non-uniform strains, they are denoted as Geometrically Necessary Dislocation (GND) in contrast to the redundant or Statistically Stored Dislocations (SSD) which accumulate during uniform straining of the crystal [ASH70]. Thus, at the continuum level where the concern is with distributions of large numbers of dislocations, one can adopt the following key distinction[1]. Dislocations are stored for two reasons:

∗ SSD accumulate due to random trapping and subsequent dislocation multiplication with ongoing plastic deformation, also in uniform deformations. The precise density of these dislocations is not predictable through geometric arguments and thus must be described with constitutive equations.

∗ The storage of GND is a direct consequence of the inhomogeneity of the deformation state. The arrangement of these dislocations is responsible for a remaining inhomogeneous plastic deformation upon load removal. Thus, the specific density of this dislocation population can be related to the gradients of plastic slip or the corresponding lattice curvature through geometric arguments. Accordingly, a homogeneous deformation does not induce any GND storage.

Here, a dislocation-density based constitutive model for fcc crystals is introduced and implemented into a crystal plasticity FE framework. The approach tracks the dislocation evolution on each slip system where the GND density is introduced in order to consider slip gradients on the μm-scale.
The extended model allows to reproduce the initial stages of the microplasticity and predict the mechanical behaviour at larger plastic deformation range where the discrete simulations are limited. It also serves as a scale transition in the bottom-up approach from discrete simulations to continuum mechanics in proposing the foundations for the development of a macroscopic constitutive model.

3.1.2 Representation of continuously distributed dislocation density

3.1.2.1 Kinematics

Mathematical relations for the description of crystal plasticity have been developed by Hill [HIL66] in the small strain context and consecutively in the finite strain setting by Teodosiu [TEO70] or Rice [RIC71].
A relative description for the motion of the material body is obtained by considering the nonlinear deformation map $\varphi_t : \mathbf{X} \longmapsto \mathbf{x} = \varphi_t(\mathbf{X})$, with $\mathbf{X}$ a generic point in the reference configuration B and $\mathbf{x}(\mathbf{X})$ its image in the deformed configuration S (see figure 66). The reference configuration B illustrates a reference material element along with the lattice unit vectors $\mathbf{n}$ and $\mathbf{m}$ representing the original slip plane normal and slip direction, respectively.
Generally the initial undeformed configuration B at time $t = t_0$ is chosen as reference configuration as this configuration of the material body is usually known. Only in the special case of a homogeneous

---

[1]Note that, if the concern is with a single discrete dislocation, there is no difference between SSD and GND.

(a)   (b)
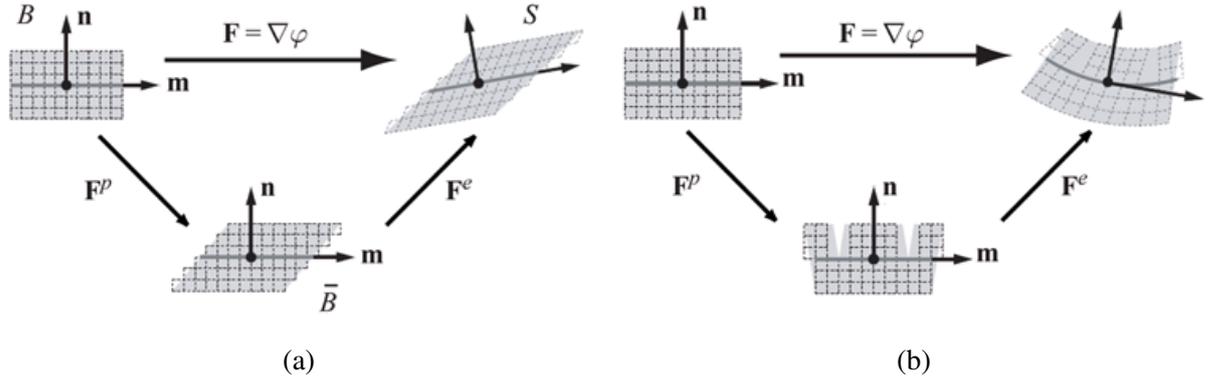
Figure 66 - Geometric setting of multiplicative crystal plasticity. The total deformation gradient $\mathbf{F}$ is split into a plastic part $\mathbf{F}^p$ representative of the dislocation movements and an elastic part $\mathbf{F}^e$ describing elastic lattice distortions and rigid rotations. (a) For a homogeneous deformation state, the corresponding intermediate configuration $\bar{B}$ is compatible. (b) For the case of an inhomogeneous plastic deformation, the corresponding intermediate configuration is characterised by incompatibilities.

deformation $\mathbf{F}^e$ and $\mathbf{F}^p$ are gradient fields. The key quantity in the description of finite strain kinematics is the deformation gradient. It is defined by the Frechet-derivative of the nonlinear deformation map φ_t with respect to the material coordinates $\mathbf{X}$:

$$\mathbf{F}(\mathbf{X}) \equiv \nabla_X \varphi_t(\mathbf{X}) \tag{3.1}$$

The total deformation of a crystal consists of a plastic part, elastic lattice distortions and rigid body rotations. The plastic part of the deformation results from the simultaneous motion of dislocations on the active slip systems. The homogenisation of these combined dislocation movements induces a continuous plastic shear deformation on the macroscopic length scale. Following Lee [LEE69], this suggests a multiplicative decomposition of the total deformation gradient:

$$\mathbf{F} = \mathbf{F}^e.\mathbf{F}^p \tag{3.2}$$

into an elastic part $\mathbf{F}^e$, which describes the elastic distortion and the rigid rotation of the lattice, and a plastic part $\mathbf{F}^p$ representative of the combined dislocation movements. By definition, the lattice rotation is fully included in $\mathbf{F}^e$, so that the plastic part $\mathbf{F}^p$ corresponds to an intermediate configuration in which the material is plastically deformed but the lattice is undeformed and unrotated. Along with the multiplicative split, the fictitious intermediate configuration $\bar{B}$ is introduced (see figure 66).

3.1.2.2 Lattice (in)compatibility

For a locally homogeneous deformation, a purely local description in terms of the elastic part $\mathbf{F}^e$ and the plastic part $\mathbf{F}^p$ of the total deformation gradient is sufficient because the corresponding intermediate configuration $\bar{B}$ is compatible (see figure 66 a). If it comes to plastically inhomogeneous deformations such as the examples considered in figure (65), a purely local description is insufficient because the corresponding intermediate configuration $\bar{B}$ would be incompatible while the total deformation state remained compatible (see figure 66 b).

From a mathematical point of view, the result that the total distortion β must derive from a displacement field (equation 1.12) can also be written as $\mathbf{curl}(\beta) = \mathbf{0}$. In the continuum theory of dislocations, one assumes the distortion to be compatible, i.e. $\mathbf{curl}(\beta) = \mathbf{0}$, but this need not hold for its elastic and plastic part when considered separately, i.e. in general $\mathbf{curl}(\beta^{e/p}) \neq \mathbf{0}$. So, $\mathbf{curl}(\beta^{e/p})$ can be interpreted as a measure for the incompatibility of the deformation.

From the physical viewpoint, an incompatible deformation is counteracted by the formation of GND. It is up to these line defects to compensate the misfit between incompatibly deformed small volume elements: the bigger the incompatibility of a deformation, the larger is the required number of dislocations in the material. These two statements motivate the second definition for the dislocation density tensor $\boldsymbol{\alpha}$:

$$\boldsymbol{\alpha} \stackrel{\text{law}}{=} \mathbf{curl}\,(\boldsymbol{\beta}^e) \tag{3.3}$$

This latter equation, also known as the first order (in)compatibility, is a fundamental field equation of the linear continuum theory of dislocations. It expresses that a continuum can be in a state of incompatible elastic distortion provided there exists a tensor field $\boldsymbol{\alpha}$ which guarantees the compatibility of the material distortion. In this sense, it becomes apparent that $\boldsymbol{\alpha}$ describes the dislocation density in the material. Moreover, according to the linear decomposition defined by equation (1.12), the first order incompatibility law can be written as

$$\boldsymbol{\alpha} \stackrel{\text{def}}{=} -\mathbf{curl}\,(\boldsymbol{\beta}^p) \tag{3.4}$$

or, with components,

$$\alpha_{hi} = -\epsilon_{hlj}\beta^p_{ji,l} \tag{3.5}$$

Note that although the expression (3.5) holds for the case of continuously distributed dislocations, it is the same expression as (1.16) obtained for a single dislocation loop.

Now, relations between incompatibilities and the concept GND density through the Nye tensor [NYE53] are discussed.

3.1.2.3   Geometrically necessary dislocations

Crystallographic interpretation

In order to define the concept of the dislocation density tensor in the context of crystal plasticity, a direct representation of the dislocation density tensor associated to crystallographic slip is now discussed.

Considering continuously distributed dislocations, Nye's tensor $\boldsymbol{\alpha}$ quantifies a special set of dislocations whose geometric properties are not canceled out by other dislocations in the crystal. Consider the volume element shown in figure (67 a), which is a section of a crystal containing two edge dislocations threading through the volume. The most rigorous manner to describe the dislocation state in the volume would be to characterise the lines by two Dirac delta distributions of strength b in space, written by equation (1.19). However, such a quantification of dislocation density becomes overwhelming given the densities involved in plastic deformation processes up to $\rho \approx 10^{16}$ m^{-2}. Allowing such point densities to become continuously distributed within a volume creates a more compact way of describing dislocations in space. A result of this process is that the spatial correlation of the individual dislocation lines within the volume is lost.

In the original formulation, Nye [NYE53] quantified the (macroscopic) net Burgers vector $\mathbf{B}$ of a continuously distributed dislocation density piercing a unit area perpendicular to the unit normal $\mathbf{n}$ through

$$\mathbf{B} = \boldsymbol{\alpha}\,\mathbf{n} \tag{3.6}$$

where the dislocation density tensor $\boldsymbol{\alpha}$ follows for a given set of dislocations from

$$\boldsymbol{\alpha} = N\mathbf{b} \otimes \mathbf{r} \tag{3.7}$$

This supposes a continuous distribution of N dislocations of unit length with a Burgers vector $\mathbf{b}$ and a corresponding common unit tangent vector $\mathbf{r}$. Furthermore, if several sets of dislocations with different values of N, $\mathbf{b}$ and $\mathbf{r}$ reside in the same unit volume, the total dislocation density tensor is obtained

(a) $\alpha_{ij} = \mathbf{0}$ (b) $\alpha_{ij} = \begin{bmatrix} 0 & 0 & 0 \\ N_{\perp}b_{y\perp} & N_{\odot}b_{y\odot} & 0 \\ 0 & 0 & 0 \end{bmatrix}$ (c) $\alpha_{ij} = \dfrac{1}{V}\sum_g \bar{l}^g b_i^g \bar{t}_j^g$
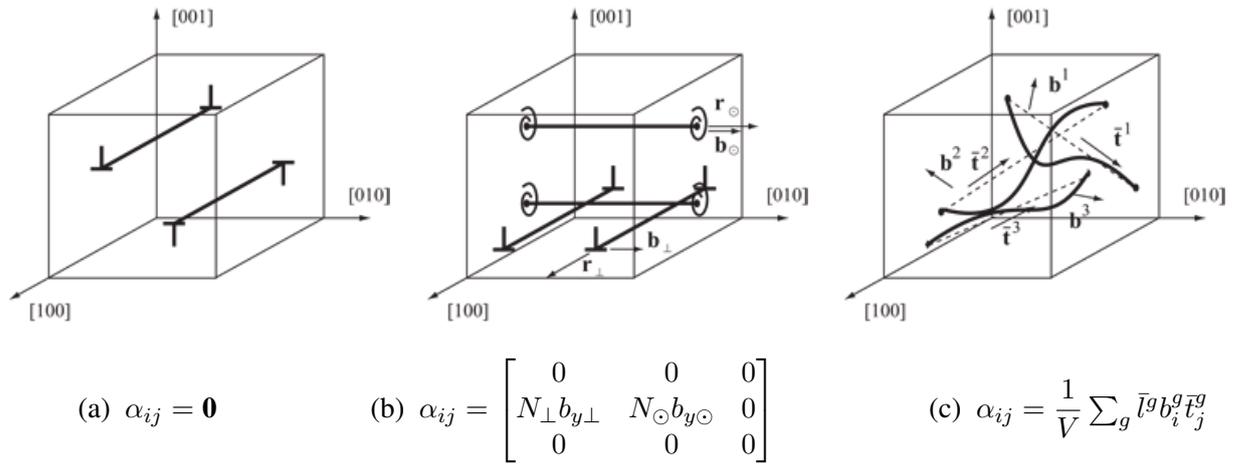
Figure 67 - Nye's dislocation tensor $\boldsymbol{\alpha}$. (a) An edge dislocation dipole give no net contribution to Nye's tensor. (b) Example distribution of $N_{\perp}$ edge and $N_{\odot}$ screw dislocations resulting in a nonvanishing $\boldsymbol{\alpha}$. (c) Extension to a discrete dislocation structure.

by summations over these contributions. Consequently, Nye's tensor quantifies only those dislocation populations which do not cancel one another within the unit volume, i.e. the GND. In turn, the dislocations which cancel each other if summed over the volume, like dislocation dipoles or self-terminating dislocation loops, make up the SSD density. In contrast to the GND density, the latter does not give any net contribution to Nye's tensor. A simple example of such a dislocation distribution with an edge dislocation dipole is visualised in figure (67 a) where the net Nye's tensor of the element is zero because the dislocation density, as drawn, consists of two dislocations with common line vector but opposite Burgers vector. In terms of Nye's tensor, an equivalent form would be to place the two dislocations on top of one another, allowing them to annihilate, leaving behind no dislocation density in the element.

Through equation (3.7), any state of dislocations resulting from an inhomogeneous plastic deformation can be constructed by combination of nine sets of dislocations of unit length with their line directions and Burgers vectors arranged parallel and perpendicular to the coordinate axis. The three terms on the main diagonal of α_{ij} represent pure screw dislocations and the six off-diagonal terms describe the six possible types of pure edge dislocations. A visualisation for the simple case of one set of screw and one set of edge dislocations within a unit volume is illustrated in figure (67 b).

In addition, as discussed by Arsenlis and Parks [ARS99], the extension to discrete dislocation arrangements is straightforward and results in the expression

$$\boldsymbol{\alpha} = \frac{1}{V}\sum_g \bar{l}^g \, \mathbf{b}^g \otimes \bar{\mathbf{t}}^g \tag{3.8}$$

where $\bar{l}^g$ is the secant length of the g-th discrete dislocation segment and $\bar{\mathbf{t}}^g$ is the corresponding average line direction vector. This expression, which closely resembles the definition of the tensor in equation (3.7), is illustrated in figure (67 c). In the procedure by which Nye described the dislocation tensor, the dislocations which constituted it were considered to be continuously distributed, and the tangent line vectors were implicitly constant. In contrast to $\mathbf{r}$ in equation (3.7), $\bar{\mathbf{t}}^g$ in equation (3.9) is no longer a unit vector but also contains the resulting path length of the dislocation segment threading the reference volume element (see figure 67 c).

Only the direct connection of the start and end point of the dislocation segment in the volume element (dashed lines in figure 67 c) results in a net contribution to Nye's tensor, while the remaining segment length has no geometric consequences and thus contributes only to the SSD density. Using the description of dislocation density as line length in a volume, the summation of geometric dislocation lengths $\bar{l}^g$ in a reference volume V can be replaced by a summation of geometric dislocation densities ρ_{GND}^g. Thus

equation (3.8) can be rewritten as

$$\boldsymbol{\alpha} = \sum_g \rho_{\text{GND}}^g \, \mathbf{b}^g \otimes \bar{\mathbf{t}}^g \tag{3.9}$$

where $\rho_{\text{GND}}^g = \frac{\bar{l}^g}{V}$. The dislocation density described in equation (3.9) is not the total dislocation density of any arbitrary dislocation line segment, but it is the portion of the total dislocation density due to dislocation g which has geometric consequences. The remaining density of the total line, which has no geometric consequence, must be considered statistical in character. The GND density constitutes a part of the total density defined by

$$\rho^g = \frac{1}{V} \int_l \mathrm{d}s^g = \rho_{\text{SSD}}^g + \rho_{\text{GND}}^g \tag{3.10}$$

With this decomposition of total dislocation density, an arbitrary line threading through a reference volume element may be separated into that portion of the total density which has geometric effects ρ_{GND}^g, and the portion ρ_{SSD}^g which does not.

In this formulation of Nye's tensor, the size of the reference volume element over which the density is averaged plays a crucial role. A volume element that is too large with respect to the geometric constraints may miss the existence of important geometrically-derived dislocations in one portion of the element that, when averaged with the other dislocations in the same element, create no net Nye's tensor. Conversely, a volume element which is too small may begin to reach length scales where dislocation density can no longer be considered continuously distributed, so that discrete dislocation mechanics must be adopted.

Slip gradient induced dislocation storage

Any storage of GND/polar/excess density, i.e. arrays of dislocations with equal signs, leads to a lattice curvature and is a direct consequence of the demand to maintain continuity in the presence of gradients of plastic slip. To understand the crystallographic consequences of this assertion, consider the schematic picture of a single crystal with one single slip system g as depicted in the figure (68 a). Here, $\mathbf{n}^g$ denotes the slip plane unit normal, $\mathbf{m}^g$ is a unit vector in the slip direction and $\mathbf{t}^g = \mathbf{m}^g \times \mathbf{n}^g$ lies in the slip plane and is perpendicular to $\mathbf{m}^g$.

Following conceptually the work of Arsenlis and Parks [ARS99], first imagine that the material is separated into three sections in figure (68 b). Each section is then deformed separately through crystallo-
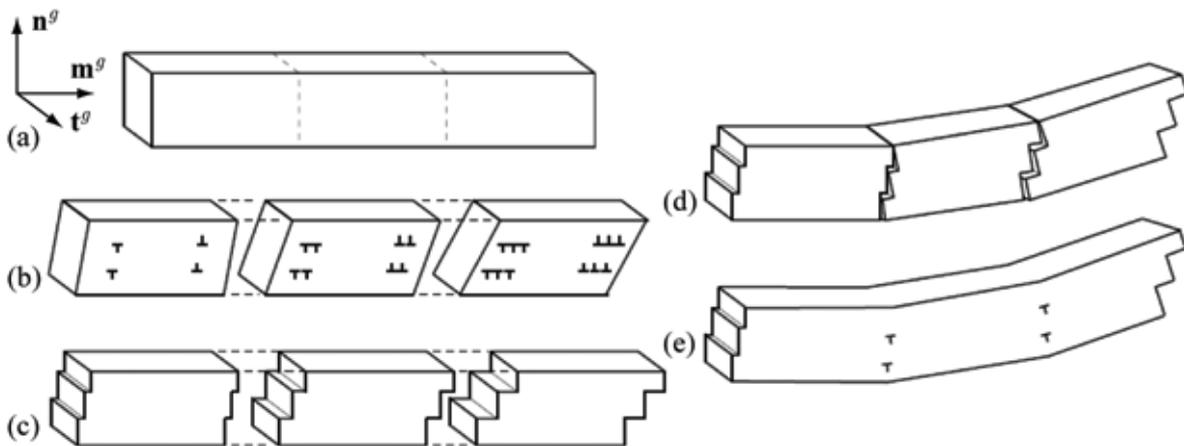
Figure 68 - Storage of geometrically necessary edge dislocations: schematic process of plastically inhomogeneous deformation with a gradient of plastic slip in the direction $\mathbf{m}^g$ [ARS99].

graphic slip. A plastically inhomogeneous deformation is assumed such that the plastic slip increases linearly in the slip direction $\mathbf{m}^g$. Consequently, in the left-most section the expansion of two dislocation loops leads to a total slip step of two Burgers vector lengths, while the right-most section experiences a total slip step of six Burgers vector lengths in figure (68 c). When the sections are now forced again together in figure (68 d), the opposite slip steps cancel out but a portion of negative edge dislocations remains at each section boundary in figure (68 e), leading to a lattice curvature.

Mathematically, the relationship between the plastic strain gradient on a slip system and the edge dislocation density (subscript $\perp$) takes the form [ARS99]

$$\rho_{\text{GND} \perp}^{g} = -\frac{1}{b} \nabla_X \gamma^g . \mathbf{m}^g \tag{3.11}$$

where $\rho_{\text{GND} \perp}^{g}$ is the geometrically necessary positive edge dislocation density.

In analogy to the previous considerations, the storage of geometrically necessary screw dislocations is established as the crystallographic consequences of a gradient of the plastic slip in the $\mathbf{t}^g$ direction. When the sections are forced back together, there are positive screw dislocations which do not annihilate, remaining in the material and causing the lattice to warp. The interested reader can refer to [ARS99]. The relationship between the plastic slip gradient on a slip system and the screw dislocation density (subscript $\odot$) takes the form

$$\rho_{\text{GND} \odot}^{g} = \frac{1}{b} \nabla_X \gamma^g . \mathbf{t}^g \tag{3.12}$$

where $\rho_{\text{GND} \odot}^{g}$ is the geometrically necessary positive screw dislocation density.

In addition, performing the **curl** operation inside the summation of the plastic distortion defined by equation (1.22) gives

$$\epsilon_{pjk} \beta_{ik,j}^{p} = \sum_g \epsilon_{pjk} \gamma_{,j}^{g} m_i^g n_k^g = \sum_g \gamma_{,j}^{g} m_i^g \left(m_j^g t_p^g - t_j^g m_p^g \right) \tag{3.13}$$

where the last step follows from the definition $\mathbf{t}^g = \mathbf{m}^g \times \mathbf{n}^g$. Using equations (3.11) and (3.12), the right-hand side of equation (3.13) can be replaced by dislocation densities

$$\epsilon_{pjk} \beta_{ik,j}^{p} = b \sum_g \left[- \rho_{\text{GND} \perp}^{g} m_i^g t_p^g - \rho_{\text{GND} \odot}^{g} m_i^g m_p^g \right] \tag{3.14}$$

Finally, using the definition (3.4), the incompatibility measure through the Nye's dislocation density tensor can finally be identified

$$\alpha_{pk} = -\epsilon_{pjk} \beta_{ik,j}^{p} = b \sum_g \left[\rho_{\text{GND} \perp}^{g} m_i^g t_p^g + \rho_{\text{GND} \odot}^{g} m_i^g m_p^g \right] \tag{3.15}$$

or

$$\boldsymbol{\alpha} = b \sum_g \left[\rho_{\text{GND} \perp}^{g} \mathbf{m}^g \otimes \mathbf{t}^g + \rho_{\text{GND} \odot}^{g} \mathbf{m}^g \otimes \mathbf{m}^g \right] \tag{3.16}$$

These developments show that gradients of plastic slip lead to the storage of dislocations. Thus a direct relation between plastic slip gradients, incompatibilities and the storage of GND densities has been obtained. Expressions similar to the right-hand side of the equation (3.16) were found by Fleck *et al.* [FLE94], Ohashi [OHA97] [OHA04], Arsenlis and Parks [ARS99], Busso *et al.* [BUS00], or Cermelli and Gurtin [CER01] in the small strain context.

3.1.2.4   Numerical implementation of the slip gradient

Implementation and validation

According to the previous section, the spatial distribution of the plastic slip γ^g is required in order to compute the slip gradients $\nabla_X \gamma^g$ and consequently the GND density $\rho_{\mathrm{GND}}(\nabla_X \gamma^g)$. There are two main approaches to compute the slip gradient.

Firstly, a fully implicit treatment consists of introducing the plastic slip as additional nodal degree of freedom besides the standard displacement degrees. Within the context of dislocation density-based strain gradient crystal plasticity, Evers *et al.* [EVE04] proposed a formulation where the GND densities are chosen as additional nodal degrees of freedom. Secondly, the problem can be treated by computing the spatial distribution of the plastic slip computed by means of interpolation algorithms.

The first formulation of crystal plasticity is rather costly since it requires up to 12 additional nodal degrees of freedom (corresponding to the 12 octahedral glide systems) in a full fcc crystal plasticity model. These drawbacks of the formulation motivate the development of a more efficient approach where the slip gradient computation is based on a smoothing procedure. The slip gradients and thus GND densities are computed in a postprocessing step. This procedure is similar to the interpolation procedure of the DCM described in section 2.2.6 (see figure 30).

First the values of $\gamma^g_{\mathrm{N}_n}$ at the nodes N_n of the FE mesh are calculated from the solutions at the local IP solutions for the plastic slip γ^g_{IP} by using the inverse of the shape functions N^{N_n}. This procedure yields n different values of plastic slips in each node from the N_n adjacent elements. That is why the average of these values $\bar{\gamma}^g_{\mathrm{N}_n}$ is calculated. Subsequently the values of the slip gradients $\nabla_X \gamma^g$ are computed based on the averaged nodal values $\bar{\gamma}^g_{\mathrm{N}_n}$ and the FE shape functions N^{N_n}:

$$\nabla_X \gamma^g = \nabla_X N^{\mathrm{N}_n}.\bar{\gamma}^g_{\mathrm{N}_n} \qquad\qquad (3.17)$$

Such an approach has already been adopted by several models of plasticity [DAI97] [BUS00] [MA06]. With the slip gradient at hand, the local material response can be determined for each IP.

Dislocation pile-up and GND

A simple illustration of (edge and screw) GND densities formed by the formation of a dislocation pile-up against a γ' precipitate into the DCM scheme is shown. The computation of the gradient operator is applied for the plastic slip generated by the motion of discrete dislocations.

The aim of this calculation is triple: this simulation allows to (i) link both discrete (given by the DD code) and continuous (given by the postprocessing step) evaluations of GND densities stored against the interfaces, (ii) assure that the FE mesh can capture the gradient generated by a physically justified spatial distribution of plastic strains given by a dislocation pile-up, and (iii) validate the appropriate average volume where the polarised dislocation densities are calculated.

As illustrated in figure (69), the finite mesh of the simulated volume is discretised by 4096 quadratic elements with dimensions $0.50 \times 0.50 \times 0.50$ $\mu\mathrm{m}^3$ and PBC are applied. The γ' precipitate is assumed cuboïdal and is discretised with a $10 \times 10 \times 10$ finite mesh. For reason of simplicity, a single cubic glide system is activated in the DCM calculation and slip occurs in the y direction. As shown in figure (69 a) the normal to the slip plane is along the z axis and the plane is located at the centre of the volume. The Burgers vector **b** of the dislocations is codirectional with the slip direction.

At the beginning of the simulation, an infinitely long dislocation of edge character is placed in a γ channel (see figure 69 a). Cross-slip or climb are not considered. In the DCM scheme, such an infinite dislocation can be obtained by the expansion of a square dislocation loop where the origins and extremities of two edge segments are superposed. In this process, the two edge segments are moved to the boundaries and can also annihilate mutually. At the end, two infinite dislocations are obtained (see image t_1 of the snapshot of figure 69 a). For the present computation, only one of the two infinite dislocations is allowed to glide. The inactive dislocation is not shown in the other snapshots. The shear modulus μ is equal to
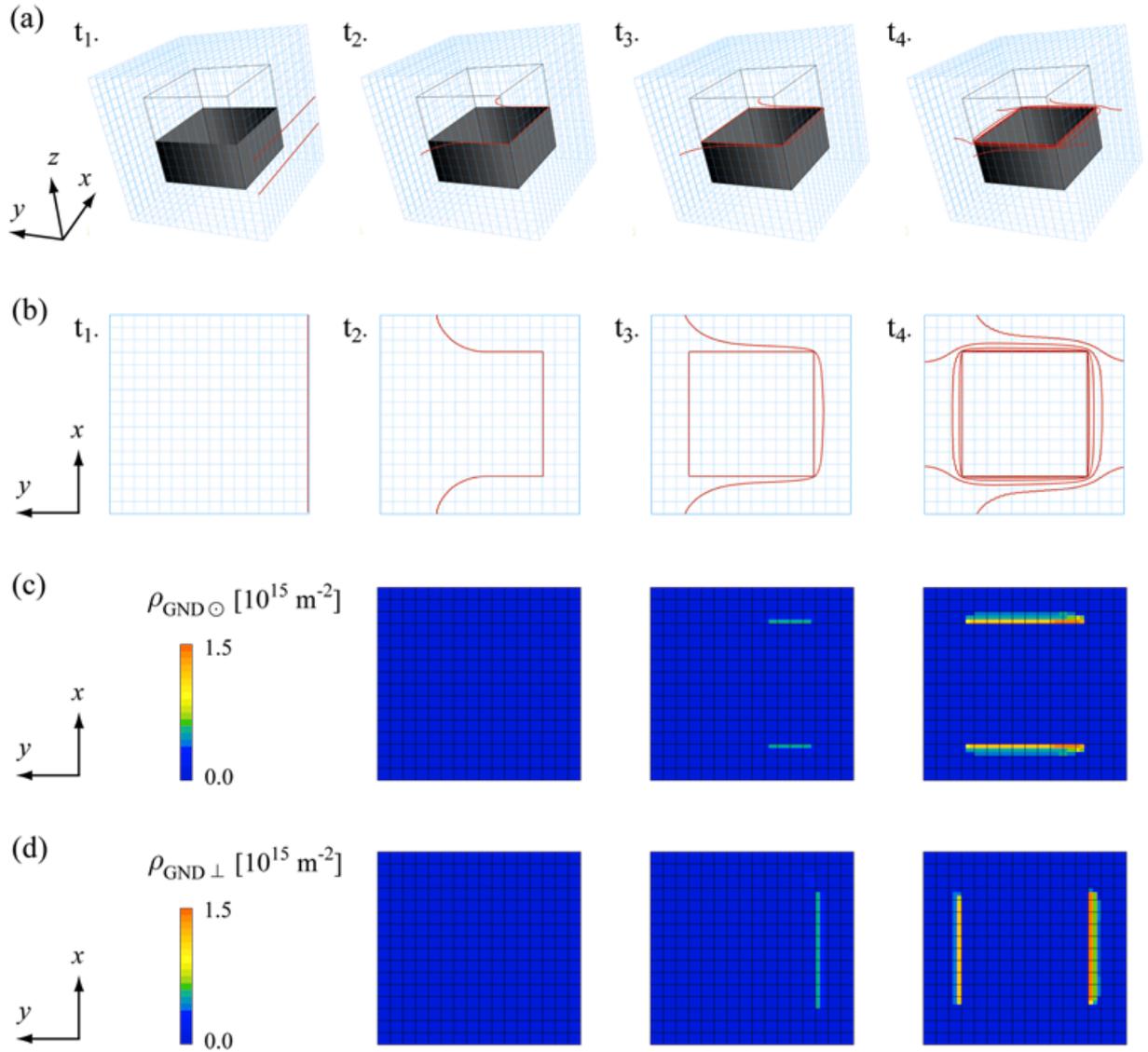
Figure 69 - (a) 3D and (b) 2D view of the dislocation pile-up simulated by the Discrete-Continuous Model. (c) Visualisation of the geometrically necessary screw dislocations $\rho^g_{\text{GND} \odot}$ lying along the y direction computed by $\frac{\partial \gamma}{\partial x}$, and (d) the edge dislocations $\rho^g_{\text{GND} \perp}$ lying along the x direction computed by the postprocessing step $\frac{\partial \gamma}{\partial y}$. Here, a minimum slip step of two Burgers vector length are shown.

51 GPa, Poisson ratio ν to 0.37, Burgers vector to $b = 0.25$ nm, and the simulation is performed in a quasi-static regime in which the dislocations are pushed slowly against the γ' precipitate. As illustrated in figure (69 a), because of the PBC, dislocations form a pile-up against the impenetrable γ/γ' interfaces. Figure (69 b) illustrates the distribution of density of geometrically necessary screw and edge dislocations given by the calculation of the gradient of plastic slip at each IP of the FE mesh during the dislocation pile-up. The associated gradient of slip computed in postprocessing is shown for a minimum slip step of two Burgers vector lengths. The figure (69 b) shows that the dislocation pile-up accumulated against a γ' precipitate generates a gradient of plastic slip localised at the γ/γ' interfaces. In particular, a gradient of slip $\frac{\partial \gamma}{\partial y}$ gives rise to a density of geometrically necessary edge dislocations $\rho^g_{\text{GND} \perp}$ lying along the x direction. Likewise, a gradient of slip $\frac{\partial \gamma}{\partial x}$ gives rise to a density of screw dislocations $\rho^g_{\text{GND} \odot}$ lying along the y direction.

To compare these continuous computations of polarised dislocation densities with the discrete density
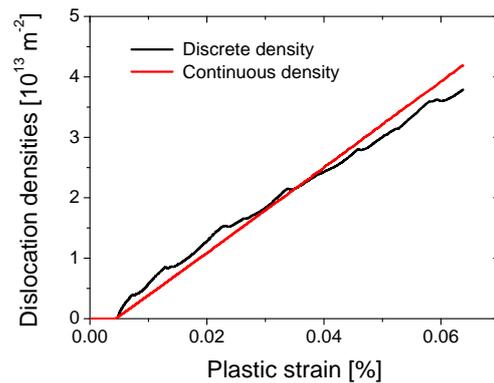
Figure 70 - Comparison between the postprocessing calculation of GND density stored in a pile-up (red line) and direct dislocation density measure obtained by the Discrete-Continuous Model (black line).

generated by the DCM, total dislocation densities averaged over the total simulation volume are calculated. Figure (70) shows the evolution of the dislocation density with plastic strain. In this particular case where all dislocations at the interfaces are GND, the continuous calculation of GND density is in good agreement with the density given by the discrete simulation, increasing linearly with strain for both approaches. These results illustrate that the computation of the gradient of plastic slip calculated by the postprocessing procedure is a good tool to evaluate the density of GND accumulated in a pile-up at the γ/γ' interfaces. In this way the pseudo slip-gradient constitutive model[2] now is introduced.

3.1.3 GND into a dislocation mean free path model

3.1.3.1 Motivation

During the past ten years, the concept of GND and its incorporation into a phenomenological continuum theory of plasticity have been actively developed. Depending on the particular theory, the measure of the density of GND is incorporated into the expression for the flow strength [SHU01], the hardening [OHA97] [GAO99] [ACH00] [MEI01], or the free energy [GUR00]. For instance, two approaches have been used to establish mesoscale plasticity theories linking GND to continuum plasticity via the Taylor model stated in section 1.2.4.2. The first is a higher-order theory which is based on the Cosserat-Koiter-Mindlin-Fleck-Hutchinson framework [GAO99], and the second consists of introducing slip gradients in the incremental stress-strain relation through the plastic work hardening [BUS00].

Figure (71) deals with the differences between both approaches in terms of boundary conditions and illustrates them in the case of one channel of superalloys constrained between two rigid and impenetrable γ/γ' interfaces:

* Some strain gradient theories involve higher-order stresses such that the order of governing equations increases and additional boundary conditions are needed. The theories which both require higher-order boundary conditions, are able to capture the boundary layers [AIF87] [GUR02] [FOR03]. Figure (71 a) illustrates schematically the latter point, where without higher-order boundary conditions at γ/γ' interfaces, the associated deformation remains uniform within the γ channel (in black in the left figure 71 a). As a consequence of the homogeneity of the deformation state, the GND are not induced (in black in the right figure 71 a). Consideration of additional boundary conditions at the interfaces in terms of deformation and GND density are shown as blue curves in figure (71 a).

---

[2]Here, the term "pseudo" is used to draw a distinction with models where the gradient is computed as additional nodal degree of freedom.

* Others (lower-order) theories are based on the notion of lattice incompatibility, as measured by Nye's [NYE53] dislocation density tensor $\boldsymbol{\alpha}$, incorporated into the continuum plastic constitutive laws only as an additional contribution to the hardening. One of the characteristics of the above theory is that it preserves the classical structure of local single-crystal plasticity, and does not involve higher-order stresses nor additional boundary conditions. However, it seems to be not possible to predict certain type of nonuniform plastic flow such as the shear of an initially homogeneous layer[3] [VAN03].

  Nevertheless, two alternatives are allowed to tackle this requirement. On the one hand, it can be assumed that there exists a subregion of thickness h across the γ/γ' interfaces where the two interfacial regions on either side of matrix or precipitate region behave in a transient regime, both in terms of plastic deformation and in terms of GND density gradients (see figure 71 b). The discontinuity of plastic slip distribution within the microstructure due to the presence of the γ' precipitates is replaced by a smooth continuous function in a strip of thickness h located at γ/γ' interfaces [PIP08]. On the other hand, such as in simulations with the DCM, initial dislocation microstructures can be initially heterogeneously distributed into the γ channel. This assumption may be taken into account by pre-deformation effects such as the lattice misfit effects. In this way, the associated deformation is not homogeneously located within the matrix channel, and the effects of the presence of a boundary can then been captured (see figure 71 c).

A pseudo slip-gradient plasticity model based on the work of Busso *et al.* [BUS00] [MEI01] and developed within this thesis is introduced in the next section. The development and improvement of such a type of model is challenging and should be collectively tackled by the whole mechanics and materials community. As a contribution to this long-term task, a comparison of the predictions of non-local plasticity with the DCM results is carried out in order to provide an assessment of the strengths and weaknesses of such continuous theories.

3.1.3.2 Incorporation of non-local effects in a constitutive framework

Fundamental equations

The kinematics adopted in this section is commonly used in the field of crystal plasticity, where the geometrically linear framework given by the set of equations (1.9), (1.10), (1.11) and (1.21) is assumed. For fcc metals, 12 octahedral systems can be characterised by the Miller indices $\{111\}\langle110\rangle$, where each system g is represented by the two time-independent orthonormal vectors $\mathbf{m}^g$ and $\mathbf{n}^g$, the slip direction and slip plane normal, respectively. Figure (13 a) shows the definition of the 12 slip systems used in the present model. In addition, the plastic rate $\dot{\gamma}^g$ is stated as the power law function according to the flow rule [HUT76] [PIE82] defined by equation (1.29)

$$\dot{\gamma}^g = \dot{\gamma}_0^g \left(\frac{|\tau^g|}{\hat{\tau}^g} \right)^{\frac{1}{m}} \text{sign}\left(\tau^g\right) \tag{3.18}$$

where $\dot{\gamma}_0^g$ and m are material parameters. The RSS τ^g is given by equation (1.7) and the deformation resistances $\hat{\tau}^g$ measure the impeding of dislocation movement by the formation of dislocation-dislocation interactions, i.e. both SSD and GND.

Dislocation interactions

In contrast to many classical crystal plasticity models, which relate the slip resistance to the history of plastic shear on all slip systems in a phenomenological fashion, here, the movement of mobile dislocations on slip system g is impeded by obstacles, the strength and density of which are determined by the

---

[3]The case of the layer may be assimilated for example to the case of the channel in superalloys.

Additional boundary conditions on γ^p

GND distribution density through $\nabla \gamma^p$

(a)

Smooth continuous distribution of γ^p

GND distribution density

(b)

Initial heterogeneous SSD density

GND distribution density

(c)
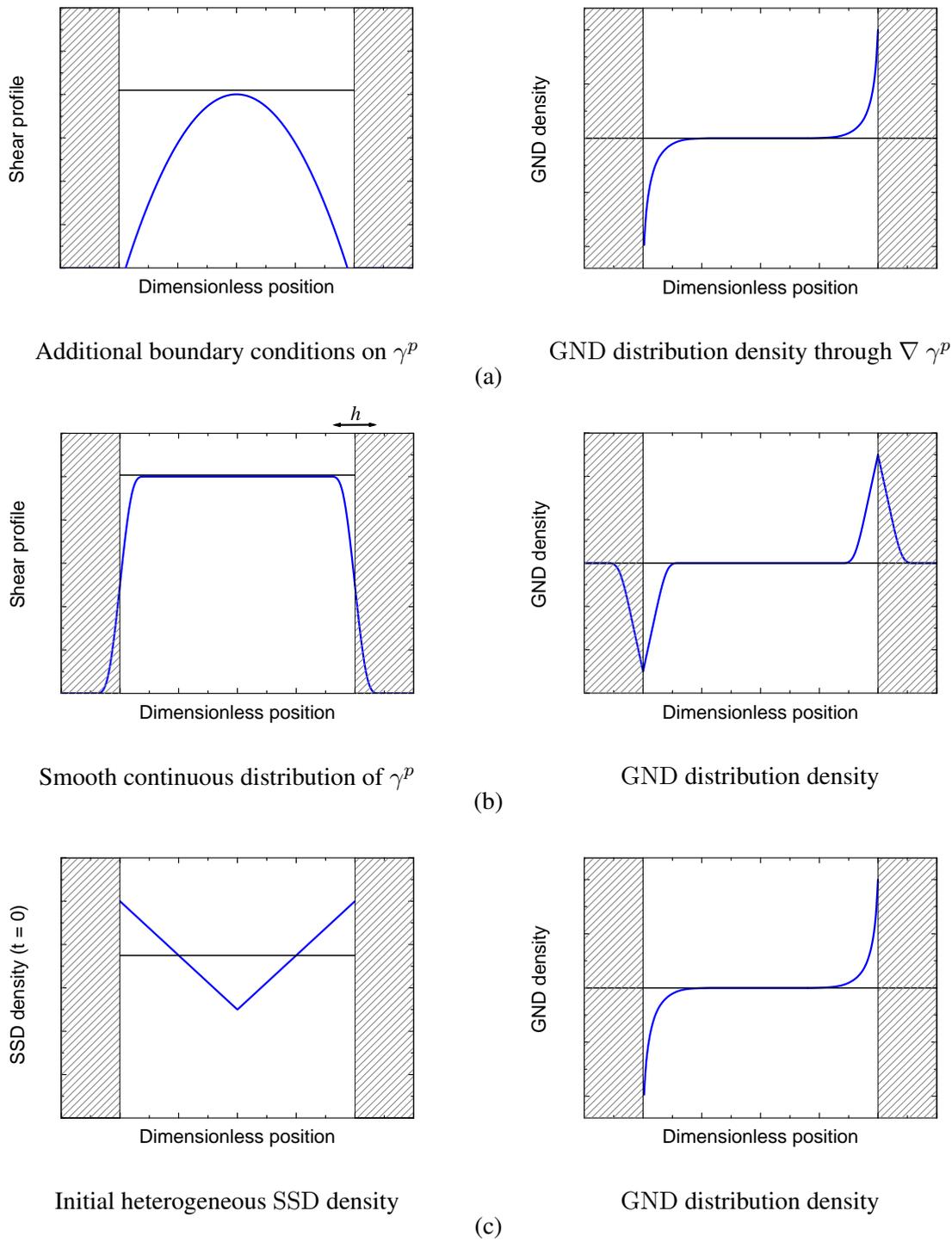
Figure 71 - Simple illustrations of shear profiles and initial distribution of dislocation density along the dimensionless matrix channel width between precipitates (in dashed) for three kinds of model in order to capture the GND densities. (a) Initially additional boundary conditions to the model applied to the γ/γ' interfaces captures the inhomogeneous plastic flow. (b) The piecewise plastic slip distribution is replaced by a continuous plastic function within a strip of thinkness h at the γ/γ' interfaces, or (c) the initial microstructure of SSD density is initially heterogeneously distributed within the γ matrix channel.

type and number of interactions that might occur between dislocations of coplanar or intersecting slip systems. The present formulation is an extension of the model described in section 1.2.4.2.

The critical stress $\hat{\tau}^g$ for the activation of slip system g as a function of the SSD and GND densities stored (i.e. temporarily or permanently immobilised) in all slip systems is considered in the gradient-based formulation. This critical stress is given by a generalised Taylor relation of the form[4]

$$\hat{\tau}^g = \mu b \sqrt{\sum_s a^{gs} \rho_{\text{SSD}}^s} + \mu b \sqrt{\sum_s c^{gs} \rho_{\text{GND}}^s} \tag{3.19}$$

In fcc crystals, the symmetric tensor a^{gs} and c^{gs} contains each six independent dimensionless coefficients, which account for the average strength of pair interactions between slip systems that result from, respectively, SSD and GND interactions. In addition, because of the poor knowledge of the interactions between GND, equation (3.19) is simplified and for simplicity only their self hardening is considered. Hence equation (3.19) is rewritten and the GND contribution in equation is weighted by a dimensionless coefficient c (in the range $0.3-0.5$ in a bulk fcc [GIL93b]) as

$$\hat{\tau}^g = \mu b \sqrt{\sum_s a^{gs} \rho_{\text{SSD}}^s} + c \mu b \sqrt{\rho_{\text{GND}}^g} \tag{3.20}$$

The first term of equation (3.20) then represents the classical dislocation-dislocation interaction and the second term represents the dislocation-precipitate interaction.

In section 2.4.4, it was demonstrated that the strength of each interaction may be strongly different, so here the strength $\hat{\tau}^g$ is chosen as the sum of the contributions of both individual strengthening mechanisms [ASH70], in spite of a quadratic sum of type $\hat{\tau}^g = c \mu b \sqrt{\rho_{\text{SSD}}^g + \rho_{\text{GND}}^g}$ used for instance by Ohashi [OHA97] [OHA04] in a similar model.

SSD **and** GND **density evolutions**

As already pointed out in the section 1.2.4.2, the evolution equation of SSD in each system g is written following the works of Kocks and Mecking [KOC76], and Teodosiu *et al.* [TEO93]

$$\dot{\rho}_{\text{SSD}}^g = \frac{1}{b} \left(\frac{1}{L^g} - y_c \rho_{\text{SSD}}^g \right) |\dot{\gamma}^g| \tag{3.21}$$

with $\rho_{\text{SSD}}^g(t=0) = \rho_{\text{SSD},\,0}^g$. Only annihilation between SSD is considered. It is assumed that the main free path L^g is proportional to the inverse of the Taylor stress, through

$$L^g = \frac{K \mu b}{\hat{\tau}^g} \tag{3.22}$$

where K is the constant dislocation mean free path parameter [TAB97].

In order to obtain a closed set of constitutive relations, the geometrically necessary (edge and screw) dislocation densities remain to be determined. The latter quantities are geometrically coupled to the gradients of the plastic slip (see section 3.1.2.3) and are computed (equations 3.11 and 3.12) as

$$\rho_{\text{GND}}^g = \rho_{\text{GND},\,0}^g + \underbrace{\left| \frac{1}{b} \nabla_X \gamma^g . \mathbf{m}^g \right|}_{|\rho_{\text{GND}\,\perp}^g|} + \underbrace{\left| \frac{1}{b} \nabla_X \gamma^g . \mathbf{t}^g \right|}_{|\rho_{\text{GND}\,\odot}^g|} \tag{3.23}$$

---

[4]The first term of equation (3.20) resembles equation (1.31), except that it is rewritten in terms of ρ_{SSD}^s and ρ_{GND}^s instead of the total density ρ^s.

The above crystallographic formulation through equations (3.18), (3.20), (3.21), and (3.23) has been implemented into the FE code ZéBuLoN [FOE97]. Non-local effects associated to the deformation gradients at each IP are incorporated through the postprocessing procedure illustrated in section 3.1.2.4.

3.1.3.3   Application to a γ/γ' unit cell

Simulations have been performed using the same microstructure and FE mesh of γ/γ' superalloys used for the DCM simulations in sections 2.4.3 and 2.4.4 (see figure 72). The width of the channel $w = 0.16\ \mu$m, and the simulated volume is about $l^3 = 0.50 \times 0.50 \times 0.50\ \mu\text{m}^3$ discretised by 4096 three-dimensional quadratic FE (thus 56361 degrees of freedom). Symmetric PBC are considered and the simulated volume contains only one γ' precipitate (in blue in figure 72) surrounded by γ channels (in red in figure 72) with a volume fraction of precipitates $f = 0.61$.

The tensile behaviour in direction [001] is investigated using $\dot{E}_{33} = 10^{-3}\ s^{-1}$ on the γ/γ' unit cell. Only octahedral slip systems are considered. Moreover, as in all DCM calculations, the same elastic properties are used in each phase, i.e. isotropic elasticity is assumed with shear modulus $\mu = 51$ GPa and Poisson ratio $\nu = 0.37$. The γ phase is described by the slip-gradient dependent crystallographic formulation specified in the previous section, and the precipitates are assumed to remain elastic. The cutting process of precipitates will be considered later on.
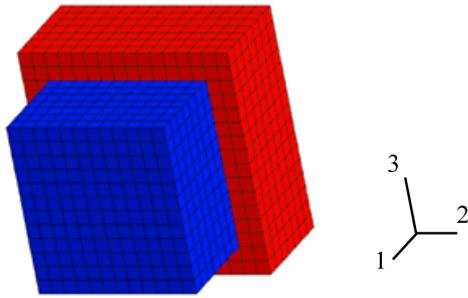
	Symbol	Value	Unit
Channel width	w	0.08	μm
Precipitate size	l	0.42	μm
Volume fraction	f	0.61	-

Figure 72 - Finite element mesh of the unit-cell model: $l = 0.42\ \mu$m and $w = 0.08\ \mu$m for a volume fraction $f = 0.61$.

Calibration of the adjustable parameters

The flow rule parameters (see equation 3.18), $\dot{\gamma}_0$, m, τ_0, are taken from Kocks *et al.* [KOC75], where the pre-exponential term $\dot{\gamma}_0$ typically equals 10^{-3} s^{-1}, and the exponent m equals 0.01. For the hardening law (see equations 3.20 and 3.21), the relevant parameters are the annihilation distance y_C and the constant mean free path of dislocation K. Here $y_C = 10^{-3}\mu$m and $K = 15$ are used. In fcc crystals, values of the symmetric tensor components a^{gs} are given by relation (1.32). The initial SSD density, $\rho_{\text{SSD, 0}}^g$ is distributed heterogeneously within the γ channels in order to account for the misfit dislocations at $t = 0$ located at the γ/γ' interfaces. The profile of the initial distribution of $\rho_{\text{SSD, 0}}^g$ is assumed linear within the channel with a maximum value of density located at the interfaces and a minimum value at the middle of channel, as illustrated in figure (71 c). The averaged initial total dislocation density specified is 6×10^{13} m^{-2}, equivalently distributed at each slip system, similarly to the initial density used in the DCM calculations. The shape of the profile of the initial SSD distribution within the γ channel is assumed to be negligible at the macroscopic level, since only the GND density contributes effectively to the hardening. It is assumed that initially the GND densities are zero. Finally, the key parameter of the present formulation is the parameter c in equation (3.20). This is why special attention has been paid to identify c with the help of the DCM results. In accordance with the DCM results of sections 2.4.3.3 and

Parameter	Symbol	Value	Unit	Used in equation
Reference plastic strain rate	$\dot{\gamma}_0$	0.001	s^{-1}	3.18
Rate sensitivity exponent	m	0.01	-	3.18
Magnitude of Burgers vector	b	2.5×10^{-10}	m	3.20
Shear modulus	μ	51	GPa	3.20
Interaction coefficient	a_0	0.12	-	3.20
$\uparrow$	a_1	0.12	-	3.20
$\uparrow$	a_2	0.06	-	3.20
$\uparrow$	a_3	0.62	-	3.20
$\uparrow$	a_4	0.11	-	3.20
$\uparrow$	a_5	0.12	-	3.20
Initial SSD density per system	$\rho_{\text{SSD, 0}}^g$	$\approx 6.0 \times 10^{13}$	m^{-2}	3.21
Critical annihilation length	y_C	10^{-3}	μm	3.21
Mean free path parameter	K	15	-	3.22
Initial GND density per system	$\rho_{\text{GND, 0}}^g$	0.0	m^{-2}	3.23
Strength parameter for GND	$\bar{c}$	0.63	-	3.24

Table 3.1: Constitutive parameters for the γ channels around the elastic γ' precipitate.

2.4.4, if it is assumed that the storage of GND density is mainly responsible for the strong hardening rate observed in γ/γ' superalloys, then the hardening law (3.20) may be reduced to $\hat{\tau}^g = c\mu b \sqrt{\rho_{\text{GND}}^g}$.
It has been illustrated in section 2.4.3.4 that macroscopically, the Taylor-like hardening equation is poorly justified in γ/γ' superalloy, because the corresponding Taylor coefficient of equation (3.20) equals 1.75 (see figure 54), which is much higher than the range of predicted values $0.3-0.5$ for forest interactions in bulk fcc [GIL93b]. Nevertheless, the development of this scaling law, i.e. $\hat{\tau}^g = 1.75\mu b \sqrt{\rho_{\text{GND}}^g}$ has a macroscopic aspect, because the corresponding GND density in this expression vanishes at the macroscale. That is why this law cannot be explicitly used in this form at the mesoscale and needs to be rewritten. The new form of the slip system strength $\hat{\tau}^g$ of equation (3.20) can also be written as

$$\hat{\tau}^g = \mu b \sqrt{\sum_s a^{gs}\rho_{\text{SSD}}^s} + \bar{c}\mu b \sqrt{\rho_{\text{GND}}^g} \tag{3.24}$$

where $\bar{c}$ is an adjustable non-dimensional parameter which determines the magnitude of the contribution of ρ_{GND} at the mesoscale. The key feature of the DCM analyses carried out in section 2.4.3.3 was used to adjust the mesoscopic coefficient $\bar{c}$ to correctly account for the strengthening GND of the new scaling law applicable at the μm-scale and larger strains than in the DCM. In comparison with stress-strain curves given by the DCM simulations the parameter $\bar{c}$ has been identified to 0.63 (< 1.75). This comparison is illustrated in figure (75).
A summary of the material constants and model parameters at 850°C, is shown in table (3.1). Furthermore, the time increment is relatively small: $\Delta t = 0.02$ s.

Simulation results

The predictive capabilities of the pseudo slip-gradient model on the simulated [001] tensile responses are discussed now. Figure (73) shows the macroscopic stress plotted against the macroscopic strain for the simulated microstructure. Since the plastic slip remains zero throughout the elastic range, no gradient effects appears in the description of the material behaviour. An arrow indicates the point at the onset of plastic slip where the channel becomes plastic.
In addition, figure (73) shows the three evolutions of densities ρ_{GND} (in full blue line), ρ_{SSD} (marked
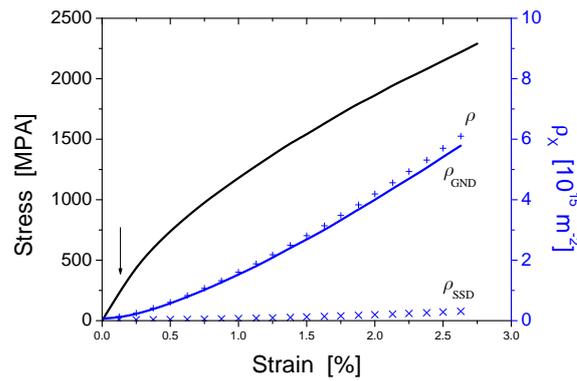
Figure 73 - Macroscopic stress-strain curve (in black), and dislocation density evolutions with strain (in blue), e.g. total dislocation density ρ, geometrically necessary dislocation density ρ_{GND}, and statistically stored dislocation density ρ_{SSD}.

with $\times$) and total dislocation density $\rho = \rho_{\text{GND}} + \rho_{\text{SSD}}$ (marked with $+$). As illustrated in figure (73), increase of SSD density is much lower that the increase of GND density. Thus, the total dislocation density is mostly controlled by the evolution of GND and a considerable strengthening effect is then induced by their presence within the channels.

The plastic slip in the microstructure is concentrated in "bands" at their interfaces. Thus, according to the previous observations, a strongly heterogeneous distribution of GND is expected. The visualisation of the local GND density distributed in the channel at $\varepsilon = 0.2\%$ and 1.0% is shown in figure (74). It can also be seen that the deformation is heterogeneous, i.e. the GND are localised near the interfaces. It can be observed that during the plastic deformation, the GND spread out through the channel. Hence, the presence of GND around the particles is indeed equivalent to having a precipitate with an apparent size larger than the actual one. Nevertheless, no such source-shortening was found in the DCM simulations (see section 2.4.3.3). As a consequence of the absence of dislocation pile-ups within the microstructure, the effective width of the channel does not change during straining. In other words the strip associated to the localisation of polarised dislocation density remains at the same thickness during the deformation. For this reason, a confrontation of local dislocation densities within the channel between the pseudo slip-gradient model and the DCM predictions is now investigated.

| (a) | (b) |
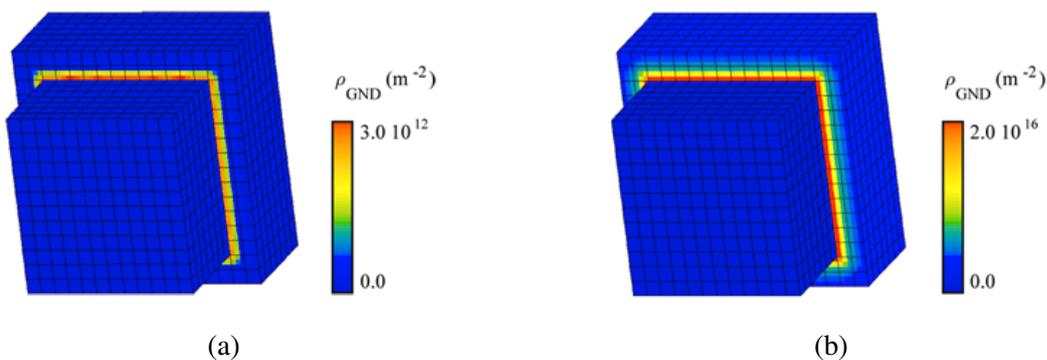
Figure 74 - Distribution of the GND density in the microstructure at (a) $\varepsilon = 0.2\%$ and (b) $\varepsilon = 1.0\%$.

Comparison with DCM results

In DD simulations, transport of dislocation densities is fully resolved by the motion of individual dislocations. As a rule of thumb, using present day computing facilities, DD codes can handle a tenfold increase of the dislocation density. Hence, the DCM simulations are still limited to a plastic strain achieved amounting here to about 0.25%, and the chances to tackle large-scale engineering problems in the future with discrete approaches are slim. Figure (75) illustrates the interest to develop a non-local model through a transition between discrete and continuum approaches of plasticity. It allows predicting the mechanical behaviour at a larger plastic deformation range that the DD simulations are limited.
Figure (75) shows the case where the continuum model extends the stress-strain and total dislocation density evolution curves predicted by the DCM. In the insets of this figure the comparison of both (macroscopic) simulated stress-strain curves (figure 75 a, which served to identify the parameter $\bar{c}$), and the corresponding evolution of dislocation densities (figure 75 b) are shown. Therefore, because the overall flow stress is associated to an increase in dislocation density, the question that will be addressed now is what relationship might exist between the local discrete dislocation density and the continuous density in both models. In particular, of interest is the way in which the dislocations are spatially distributed within the channel, and their evolution during plastic deformation.

(a)   (b)
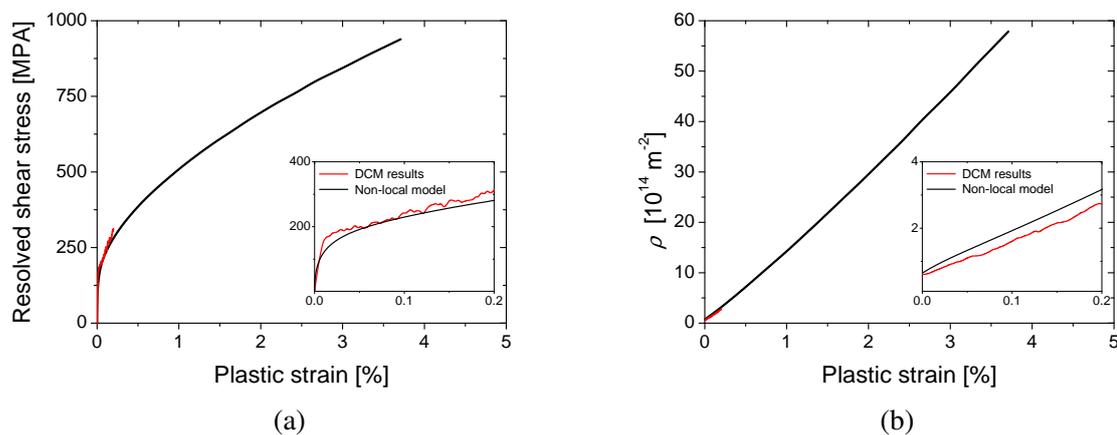
Figure 75 - Confrontation between the discrete simulations versus the pseudo slip-gradient model of (a) the stress-strain responses and (b) the global evolution of dislocation densities with plastic strain.

Figure (76) compares the distribution of total dislocation density within the channel for both approaches. Even if dislocation storage is mostly located at the interfaces in both calculations, detailed profiles within the channels show strong differences between the DCM results and the pseudo slip-gradient model. Profiles of the total dislocation density distributions within the channels are calculated over ten strips of equal thickness normal to the interfaces, at 0.1%, and 0.2% macroscopic plastic strain. Two main qualitative and quantitative differences can be noted:

* Whatever the plastic strain levels, the distribution of dislocation density with the pseudo slip-gradient crystallographic model is much smoother than the results from the DCM simulation: the profiles differ extremely because in the discrete distribution all dislocation segments are located at the interfaces.

* With increasing deformation in the pseudo slip-gradient model, the dislocation density increases as well towards the middle of the γ channel. This point is not consistent with the DCM results, where the strip associated to the storage of dislocations remains unchanged at the interfaces.
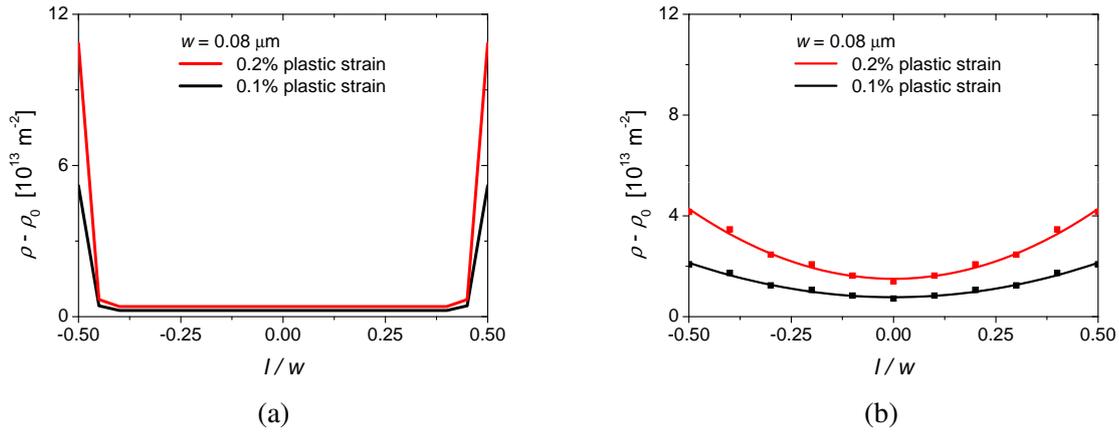
Figure 76 - Confrontation between the (a) discrete (from the DCM simulations) and (b) continuous (from the pseudo slip-gradient model) distributions of the local dislocation density along the dimensionless width of the channel.

Precipitate cutting and large strain simulations

As shown in figure (75 b), while the evolution of GND density increases linearly during the plastic deformation, there is no reason that slip resistance would stop increasing. Nevertheless, the form of the tensile curves in the $\langle 001 \rangle$ orientation for superalloys at high temperature are characterised by the existence of a stress plateau at high strain (see for instance the curves in figures 91).

A first possible solution to account for such phenomena is to consider that the internal variable ρ_{GND} can reach a saturation value $\rho_{\text{GND}}^{\text{sat}}$. A second solution is to take explicitly into account the plastic behaviour of the precipitates. This is why in the following, the γ' phase is regarded as shearable above a CRSS. At high strain, when the stress is larger than this critical value, the γ' precipitates can be sheared by superdislocations (see section 2.4.2). Hence, precipitate cutting is assumed to be the physical process controlling the saturation observed in the experimental curves. In order to achieve this goal, the classical formulation in viscoplasticity described in section 1.2.4.3 is used. It can be resumed by the following set of equations, closed by the flow rules and hardening laws:

$$\dot{\gamma}^g = \left(\frac{|\tau^g - X^g| - R^g}{V} \right)^n \text{sign} \left(\tau^g \right) \tag{3.25}$$

$$R^g = R_0^g + Q^g \sum_r h^{rg} \left(1 - \exp^{-kp^g} \right) \tag{3.26}$$

$$X^g = C\alpha^g \tag{3.27}$$

Here R_0^g describes the CRSS at which the precipitate can be plastically sheared. Moreover, $\dot{p}^g = |\dot{\gamma}^g|$, and the evolution of the kinematic hardening variable (equation 3.27) is given by $\dot{\alpha}^g = \dot{\gamma}^g - D\dot{p}^g\alpha^g$. For simplicity, only self hardening is considered, i.e. $h^{ij} = \delta_{ij}$ [ESP96]. All the material parameters are given in the table (3.2).

The form of the tensile curves (77) in the $\langle 001 \rangle$ orientation considering the shearing of γ' precipitate is characteristic for superalloys at high temperature, and it exhibits three domains. The domains correspond roughly to the elastic regime (marked by "1" in figure 77), the strong hardening due to the plastic deformation within the γ matrix channel ("2"), and the shearing of γ' precipitate ("3"). It must be noted that this study, where the precipitates are regarded as shearable for a high CRSS, gives a guideline for the micromechanical model (see section 3.2) in which this precipitate cutting process is assumed to be the reason for the stress plateau observed in the experimental curves.

Parameter	Symbol	Value	Unit	Used in equation
Viscosity	V	1100	MPa.s$^{\frac{1}{n}}$	3.25
↑	n	5	-	3.25
Critical stress	R_0	220	MPa	3.25
Isotropic hardening	h_{ij}	δ_{ij}	-	3.26
↑	Q	0	MPa	3.26
↑	k	0	-	3.26
Kinematic hardening	C	1000000	MPa	3.27
↑	D	1000000	-	3.27

Table 3.2: Constitutive parameters for γ' elasto-viscoplastic precipitates.
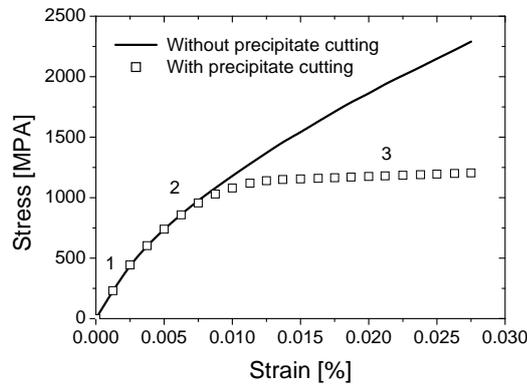
Figure 77 - Simulated stress-strain curves without (full line) and with (symbols) taking into account the cutting of γ' precipitates in simulations on the μm-scale.

3.1.3.4   Towards a simplified dislocation mean free path model

To conclude this section, a simplified framework of the previous gradient-based plasticity model is introduced. This solution was suggested by the work of Lefèbvre *et al.* [LEF06] who recently developed a simple storage-recovery formulation accounting for the Hall-Petch size effect in ultra-fine grained metals. This model, called Simplified Storage Model (SSM) here, proposes an intuitive but physically justified solution to the gradient operator for the case of γ/γ' superalloys.

In previous sections, it has been shown that gradients of plastic slip are strongly connected to the storage of GND due to the plastically heterogeneous microstructure. Mathematically, the magnitude of the plastic slip gradient at an IP inside the channel may be approximated by an internal length λ. The slip gradients $\nabla_X \gamma^g_{\text{IP 2}}$ at an IP can also be written as

$$\nabla_X \gamma^g_{\text{IP 2}} = \frac{\gamma^g_{\text{IP 2}} - \gamma^g_{\text{IP 1}}}{\lambda} \, \mathbf{l} \tag{3.28}$$

Here $\gamma^g_{\text{IP 1}}$ and $\gamma^g_{\text{IP 2}}$ represent two values of the plastic slip γ^g located at two IP in the microstructure, IP 1 and IP 2 respectively, and $\mathbf{l}$ is the unit vector between both IP. For compatibility reasons, the difference $\gamma^g_{\text{IP 2}} - \gamma^g_{\text{IP 1}}$ requires the presence of GND where the corresponding density (equation 3.23) is defined by

$$\rho^g_{\text{GND}} = \rho^g_{\text{GND, 0}} + \frac{1}{b\,\lambda} \left[\left| \left(\gamma^g_{\text{IP 2}} - \gamma^g_{\text{IP 1}} \right) \mathbf{l}.\mathbf{m}^g \right| + \left| \left(\gamma^g_{\text{IP 2}} - \gamma^g_{\text{IP 1}} \right) \mathbf{l}.\mathbf{t}^g \right| \right] \tag{3.29}$$
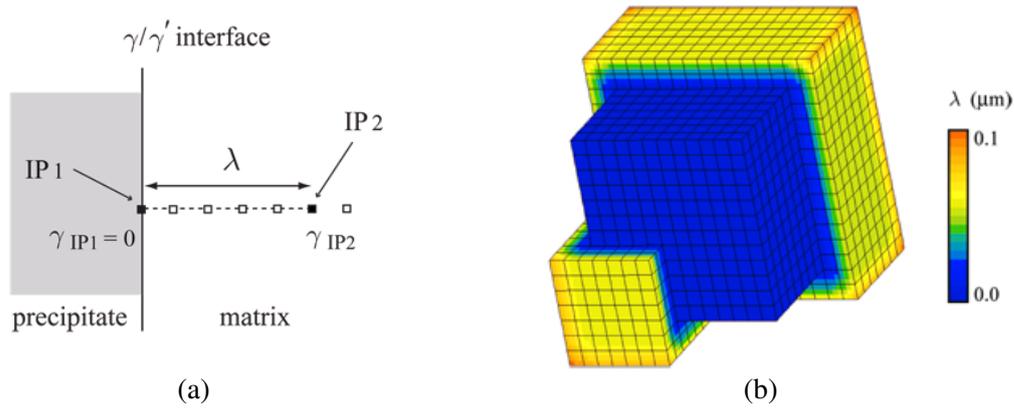
Figure 78 - (a) Illustration of the local length λ, i.e. the minimum normal distance between $\gamma_{\text{IP 2}}^{g}$ and the nearest precipitate interfaces. (b) Visualisation of computational variable λ associated to each integration point within the γ matrix phase.

Now a question may arise on the physical justification of λ at mesoscale?

Physically, it has been discussed through equation (2.49) that at the macroscale the evolution of the dislocation density could be identified as $\frac{d\rho}{d\gamma} = \frac{2.17}{b\,w}$. In this form, the characteristic length λ associated to ρ_{GND} is related to the distance w between precipitates. At the mesoscale, this relation cannot been applied because the strain γ in equation (2.49) is a macroscopic quantity. However, it has been shown that the contribution of the forest hardening to the strengthening is insignificant. In other words, at the mesoscale the mean free path of one dislocation in a channel is strongly related to its distance to the interface. Thus, the internal length λ is assumed to be the shortest distance between IP 2 and the γ/γ' interfaces where IP 1 is located (see figure 78 a). Let us consider the case where γ' precipitates behave elastically. Then $\gamma_{\text{IP 1}}^{g} = 0$, and equation (3.29) is then reduced to $\rho_{\text{GND}}^{g} = \frac{1}{b\,\lambda}\big[\,\big|\gamma_{\text{IP 2}}^{g}\,\mathbf{l.m}^{g}\big| + \big|\gamma_{\text{IP 2}}^{g}\,\mathbf{l.t}^{g}\big|\,\big]$, with $\rho_{\text{GND, 0}}^{g} = 0$.

The present model needs to know the values of λ at each IP before the mechanical loading. Thus, a pre-computation is performed in order to obtain these values, which are then stored as a parameter field. These computed lengths, i.e. the minimum distance between each IP and the nearest precipitate interface, are shown in figure (78 b). Such quantities, tabulated once (at the beginning of the computation) are later explicitly used in the constitutive laws. This point corresponds to the main difference with the pseudo slip-gradient model: whereas the latter model "computes its evolutive internal length" at the ends of each time increment of simulation, the SSM "knows *a priori* its fixed internal length".

A comparison between the pseudo slip-gradient model and the simplified model is shown in figure (79) in terms of stress-strain curves and the evolutions of GND density. Figure (79) shows that the stress-strain curve and the evolution of dislocation density are similar for both models. SSM is a very good efficient numerical solution when the precipitates behave elastically because it requires about 80% less CPU time than the non-local model for the determination of GND density in a 3D calculation. Indeed, it is the calculation of the gradient operator which is the most expensive in the pseudo slip-gradient model.

3.1.3.5   Concluding remarks

A pseudo slip-gradient crystallographic formulation, which relies on internal state variables explicitly linked to effective obstacle spacings to introduce non-local effects, has been proposed on the μm-scale and numerically implemented into the FE method. The core idea has been to incorporate the concept of GND into the constitutive laws via the Taylor hardening relation for specific slip systems. In addition to the SSD density, the GND density is introduced in order to consider slip gradients and thus render the model potentially size sensitive. These size effects (not illustrated here) have been introduced phenomenologically through the reduction of the dislocation mean free path in the presence of GND
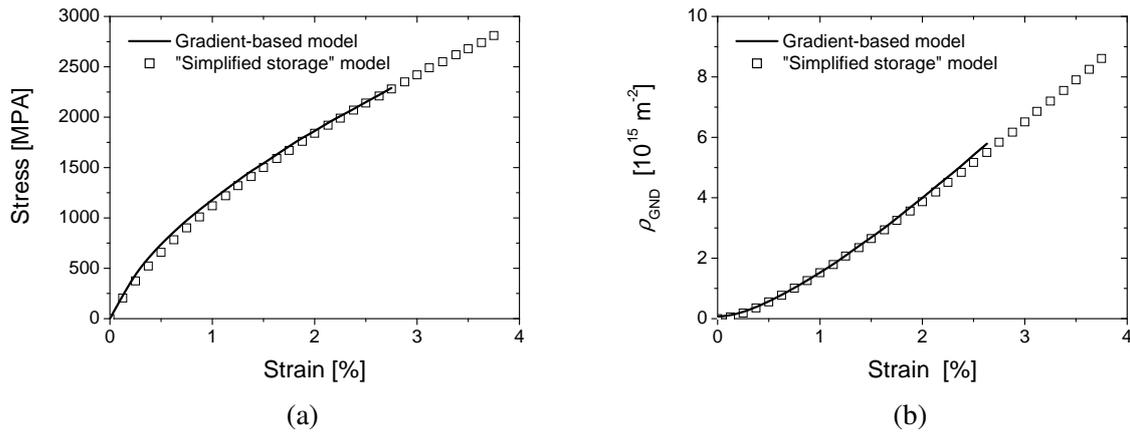
Figure 79 - Comparison between the pseudo slip-gradient plasticity model and the simplified storage model for the (a) simulated stress-strain curves and (b) evolution of dislocation densities with strain.

incorporated into the evolution of the slip resistance.

The aim of the pseudo slip-gradient model was to (i) incorporate (in a continuous sense) the micromechanisms of deformation simulated with the DCM, (ii) simulate larger strain deformations than can be achieved by the DCM, (iii) estimate the parameters responsible for the overall composite response, (iv) compare the predictions of one specific microstructure at meso- and macro-scale with the discrete results, and (v) give guidelines for the development of a macroscopic constitutive model.

Notably, it has been shown that predictions of the effects of the generation/accumulation of GND are related to the slip gradients which develop during deformation. These dislocations generated as a result of the initial slip gradients far exceeded the density of SSD, thus enabling the stored GND to dictate the flow stress and the work-hardening rate of the single crystal γ/γ' superalloy from the onset of deformation.

However, comparison with DCM predictions raises some differences and weaknesses

* Through the pseudo slip-gradient model, the GND density around the precipitate tends to reduce the mean channel width. This point is physically associated to a source-shortening-type mechanism which is in contradiction with the DCM predictions. Indeed, no pile-ups have been observed in the discrete simulations, and all mobile dislocation loops in the channels deposit dislocation segments at the interfaces. Consequently, the qualitative and quantitative profiles of distributed dislocation density during straining within matrix channel are not in good agreement with the DCM predictions. This insufficiency might be explained (i) physically, by the inappropriate deformation mechanism described by the reduction of the mean free path of dislocation (i.e. the pile-up formation), and (ii) numerically, by a mesh dependence of the gradient computation. However, Meissonnier *et al.* [MEI01] found that the level of mesh refinement shown in figure (72) gives an acceptable converged solution, so that a mesh sensitive study has not been explored in this thesis. The aim of the present work was to compare discrete and continuous models with the same FE mesh.

* To tackle the problem of the source-shortening-type mechanism inherent to the pseudo slip-gradient model, the gradient operation of the plastic strain computed in the neighbourhood of each IP has been approximated by a physically justified internal length. The internal length is the minimum distance between the IP and the interfaces. Its justification resides in the fact that the dislocation mean free path in the channel (i.e. the local line tension) is mainly controlled by its distance to the interfaces. The main difference of the calculation of $\nabla_X \gamma^g$ and $\frac{\Delta \gamma^g}{\lambda}$ in the hardening relation lies in the fact that λ is fixed during the simulation, whereas the gradient operator computes the internal

length which evolves during straining. In terms of CPU time, the simplification of $\nabla_X \gamma^g$ by $\frac{\Delta\gamma^g}{\lambda}$ is strongly more efficient than the computation of the slip gradient given by the postprocessing step.

∗ The comparison between discrete and continuous models demonstrates that (isotropic) Taylor-like hardening breaks down at both macro- and meso-scale. This can be explained by the lack of internal stress induced by the GND density within the microstructure. One of the important consequences of this is that the theory is not capable of predicting a Bauschinger effect. Moreover, according to the results of section 2.4.4 that show that the anisotropic mechanical response of single crystal superalloys is related to the internal stress created by interfacial dislocations, the present model could not take into account this hardening feature. At this μm-scale, a recent model developed by Acharya *et al.* [ACH01] [ACH04] [FRE09] allows to take into account a kinematic type of hardening since the dislocation storage at interfaces contributes to the polarised stress.

Finally, in the pseudo slip-gradient model, the shearing of γ' precipitates has been taken into account for describing consistently the macroscopic behaviour observed experimentally at large strains. It highlights that the cutting of precipitates allows to reproduce the shape of the stress-strain curve characteristic for superalloys at high temperatures, and to capture the steady state stress level. It exhibits three domains that correspond to the elastic regime, the plastic deformation of the channels, and the precipitate cutting.

3.1.4 Meso-Macro scale transition

In a multiscale approach, developments at the μm-scale are of interest in terms of improving continuum macroscale models. The correct development of specific theoretical formulations requires care, particularly with regard to the choice of independent variables in the constitutive theory. The way in which the details of the finer scaled physical features are incorporated into the macroscopic theory is essential: the finer structure can be homogenised providing a continuum model of an effective homogeneous material, and individual physical features can be explicitly modeled.

Here, the key assumptions deduced from small-scale simulations to benefit a continuum macroscale model are the following: (i) the stored dislocation density may be defined by the surface dislocation density tensor [BUL56], (ii) the material hardening is controlled by the internal stresses associated to the stored dislocation, and (iii) the local plastic strains may be also approximated by piecewise constant fields. These three points are now discussed.

3.1.4.1 Stored dislocation assumption

It has been discussed in section 2.4.5 that when the plastic distortions are not uniform, geometrically necessary dislocations must restore the compatibility of the overall deformations. The dislocation density tensor defined by equation (3.5) describes the GND density to accommodate a smooth distribution of plastic deformations [NYE53]. However, if the plastic distortions are discontinuous across a singular surface S (here the γ/γ' interfaces) with normal vector $\hat{\mathbf{n}}$, the corresponding dislocation density tensor has a surface density given by [BUL56]:

$$\alpha_{hi} = -\epsilon_{hlj} [\![\beta^p_{ji}]\!] \hat{n}_l \tag{3.30}$$

where $[\![\beta^p_{ji}]\!]$ is the jump of the plastic distortion across the interface. Physically, these dislocations surround the γ' precipitates and therefore can be regarded as Orowan loops. Their approximate distributions in the microstructure are illustrated by the thick solid lines in figure (80 a). For comparison, the figure also shows a schematic dislocation density profile obtained by an usual slip-gradient model (dotted lines in figure 80 a).

Considering such surface dislocation distributions also allows to represent the dislocation density profile given by the DCM simulations, where most of the dislocation density is concentrated at the interface

(a)   (b)
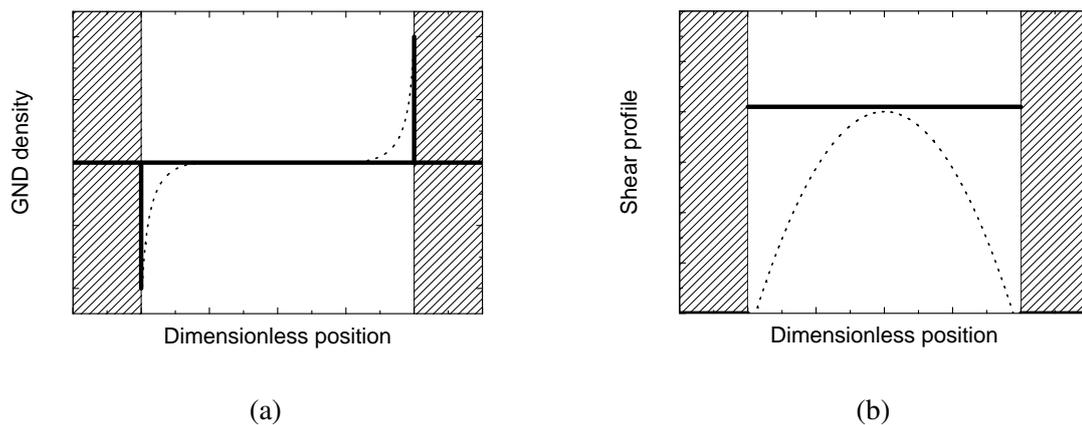
Figure 80 - Scheme of the (a) geometrically necessary dislocation densities, and (b) distribution of plastic strains in the γ/γ' microstructure. The series of thick straight solid lines are the piecewise uniform approximations of the dislocation density and of the corresponding plastic shear. The dashed curved lines represent the continuous plastic distribution that is expected with a slip-gradient model.

instead of into pile-ups. Consequently, as mentioned in section 2.4.5, the "source-shortening-type" mechanism (which is not physically justified in the present applications) inherent to the slip-gradient model is avoided.

3.1.4.2   Material hardening assumption

It has been shown in section 2.4.4 that forest hardening can be neglected. In addition, the limitation of the Taylor-like relation of section 2.4.4.3 highlights the assumption that important long-range internal stresses may be generated by the interfacial dislocations. The latter contribution must therefore be accounted for by the hardening description in the constitutive framework.

3.1.4.3   Mean field assumption

As a consequence, the real deformation distribution can be simplified by assuming uniform plastic slip caused by the Orowan loops inside the γ phase. This is illustrated in figure (80 b), where the thick solid horizontal line represents the piecewise uniform approximation of plastic slip since the expected distribution of plastic slip given by an usual gradient-based model is represented in the dotted lines.

Finally, the objective addressed in the next section concerns the incorporation of the three assumptions into a micromechanical framework suitable for analysis of engineering problems. To achieve this goal, the micromechanical model developed by Fedelich [FED99] [FED02] is adopted and extended.

3.2 Towards a physically justified micromechanical model

3.2.1 Introduction and motivation

The aim of the present work is to incorporate the insights on the "pseudo-cubic" slip discussed in section 2.4.4 into the M3RSX (Multiple Mechanisms Multiple Regions Single Crystal) model. This model proposed by Fedelich [FED99] [FED02] relies on a simplified description of the plastic strains distribution in the microstructure. The plastic strain are taken piecewise homogeneous in appropriately defined subdomains (see section 3.1.4.3). This assumption enables an efficient calculation of the local stress distribution by Fourier series and allows reducing the number of variables necessary to describe the deformation state of the microstructure. By combining the stress analysis results with the relevant dislocation mechanisms, a constitutive law with a large but still finite number of internal variables is formulated, which may be applied for structural analysis. Thereby, the model has been improved as some deficiencies of the initial version are removed and some assumptions receive a firm physical support.

3.2.2 Experimental observations of the deformation mechanisms

The deformation mechanisms of the γ/γ' alloys have been extensively studied in the past and involve a number of elementary processes. Here, the observations discussed in detail in section 1.1.3 are briefly summarised:

* Dislocation glide in γ channels: dislocations traveling through the channels are bowing out between the precipitates [POL92]. New dislocations are created at the crossings between channels (dislocation multiplication), and during plastic deformation, the trailing dislocation segments are deposited at the interfaces (dislocation storage).

* Cutting of precipitates proceed either by matrix dislocation pairs or partial dislocations, leading to complex stacking faults inside the γ' phase. Dislocation segments can be annihilated if reaction partners are present at the other side of the precipitate (dislocation recovery).

* Climbing of dislocation segments along the interfaces with partial or complete recovery of the dislocation density.

While these mechanisms in fcc crystals mostly take place on octahedral slip systems, the so-called pseudo-cubic slip systems occurs in near [111]-oriented specimens (see section 2.4.4.4). These structures have been interpreted as resulting from alternating cross-slip on two octahedral planes between the opposite γ/γ' interfaces of the screw segments trailed by mobile dislocation loops [VOL94] [BET99]. The objective of the M3RSX model is to capture these deformation mechanisms in its constitutive description. The next section presents the model.

3.2.3 Presentation of the M3RSX model

3.2.3.1 Continuum modelling of the deformation mechanisms

Figure (81) shows the three deformation processes listed in the previous section. In particular, figure (81 "1") shows how a $\frac{a}{2}[01\bar{1}](111)$ dislocation loop enters a channel and deposits two $\pm 60°$ or screw dislocation segments at γ/γ' interfaces. Figure (81 "2") shows the bowing-assisted cutting of the precipitates resulting from the coupled movement of two $\frac{a}{2}\langle 110\rangle$ dislocations forming a superdislocation in a (111) octahedral plane. Lastly, a deformation mechanism observed at much lower flow stress is illustrated in figure (81 "3"). In this process the $\frac{a}{2}\langle 110\rangle$ dislocations can pass the precipitates by individual (and unpaired) climbing along the interfaces.

Finally, the pseudo-cubic slip has been interpreted in section 2.4.4. In summary, cubic slip does not
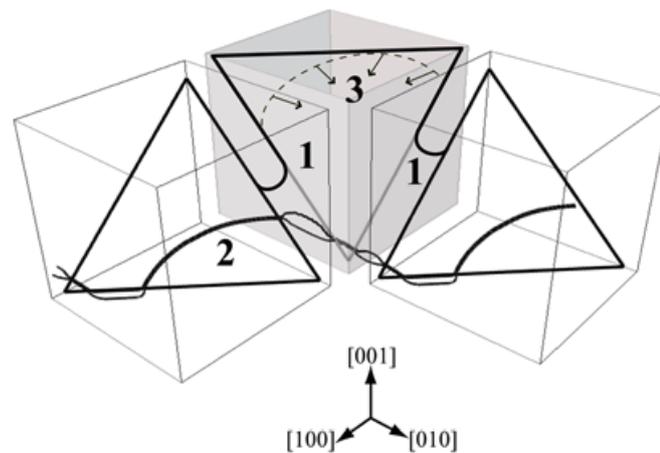
Figure 81 - Three main deformation mechanisms taken into account in the M3RSX model: "1" glide in the γ channel; "2" cutting of coherent γ' precipitates by dislocation pairs, and "3" recovery climb along the γ/γ' interfaces.

appear at the microscopic scale and at small deformation it is not physically justified deformation mechanism. Hence, the goal is to remove the cubic slip systems from the M3RSX, while still accounting for the orientation dependence of the strength at high temperature. To achieve this goal, the guidelines indicated by the DCM are the following

∗ The [001] oriented specimen exhibits a strong hardening rate, but the strength of [111] orientation is significantly reduced.

∗ Interfacial dislocation structures are strongly different for both orientations. For the [001] orientation, eight octahedral slip systems are activated and a dislocation network is formed at the six interfaces of the γ' precipitate. These discrete segments deposited at the interfaces may have a screw character or a mixed $\pm 60°$ character, as illustrated in the figure (82 a). For the [111] orientation, the DCM simulations performed in section 2.4.4 show that only two conjugated octahedral systems (per channel) are activated and together accommodate quasi totally the plastic deformation. Simulations did not include the cubic slip mechanism nor cross-slip events, but nevertheless zig-zag dislocation arrangements are formed, similar to those observed by Bettge and Österle [BET99] (see figures 60). Both activated slip systems depose long interfacial dislocation segments with exclusively screw character and with the same Burgers vector, but with opposite line vectors. It has been shown, for the combination of these depositing segments in terms of polarisation (see figure 82 c) that their long-range stresses compensate at a sufficient distance.

∗ Jerky dislocation lines decorated with collinear superjogs and confined within one channel are formed in near [111]-oriented specimens. The high mobility of these collinear superjogs is responsible for the localisation of the plastic deformation in a particular channel.

The M3RSX model assumes a periodic microstructure and the analyses are focused on a periodic cell. Figure (83 a) shows one-eighth of the periodic cell with an edge length of $2L$ and a cubic precipitate of $2c$ edge length.
Kinematics in the microstructure is controlled by the dislocation glide within the channels. A DCM simulation suggests that the expansion of a dislocation loop may be characterised by the glide of a mobile segment (overdrawn in red in figure 83 b) depositing immobile long segments at the interfaces
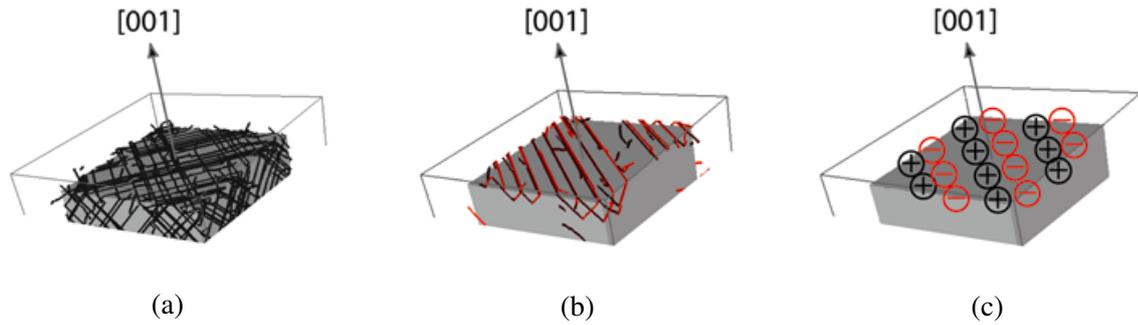
Figure 82 - View of the dislocation networks formed at the γ/γ' interfaces after deformation to 0.2% plastic strain in one channel (see figure 57) for (a) the [001] case, (b) the [111] case, and (c) the illustration of (b) in term of polarised, e.g. positive and negative, dislocations.

(drawn in black). This is why the mobile dislocation density expressed in the classical Orowan relation (equation 1.26) is related here to the kinetics of straight segments of length equal to the channel width. The next sections will introduce the kinetic equations associated to the deformation mechanisms.

3.2.3.2 Kinematics

The linear framework already applied for the DCM and the pseudo slip-gradient model, is assumed here (see equations 1.9, 1.10, 1.11 and 1.21). Because it has been shown that the polarity of the segments deposited at the interfaces plays a key role on the strength of $\langle 111 \rangle$ specimens, the present model considers a number of 24 octahedral slip systems in order to distinguish the (positive ou negative) sign of the interfacial segments (see figure 82 c). The slip systems g and their opposites $\bar{g}$ are again defined in table (3.3). In particular, the plastic flow rate (equation 1.21) and the plastic distortion rate (equation 1.22)
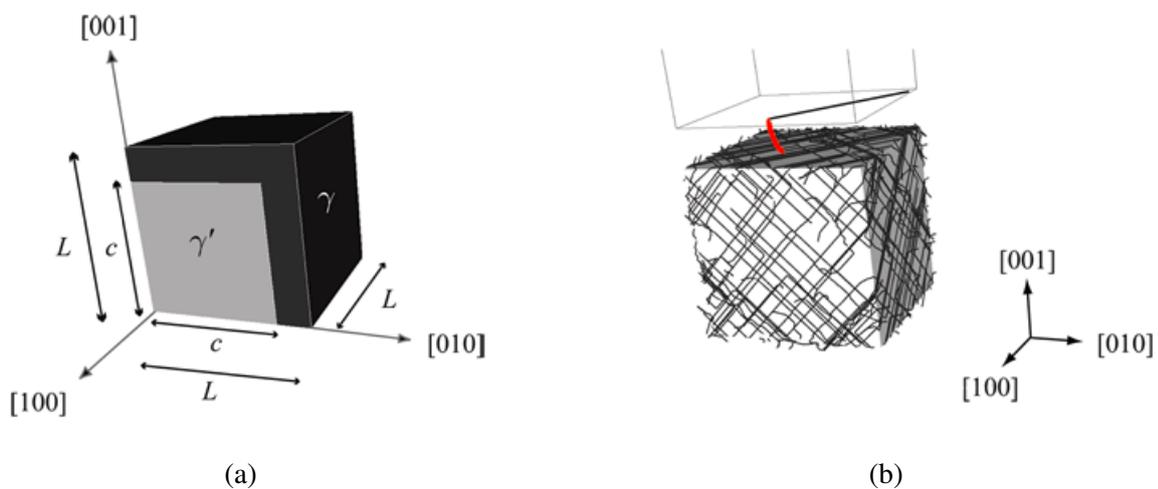
Figure 83 - (a) One-eighth of the periodic cell with associated dimensions, containing a γ' precipitate of $2c$ edge length, surrounded by narrow γ channels. (b) A DCM simulation illustrates that kinematics is mainly controlled by the glide of the mobile straight segment within the channel (red mobile segment) which deposits dislocation segments at the γ/γ' interfaces (black immobile segments).

No.	Notation	n^g	m^g	No.	Notation	n^g	m^g
1	A2	$(\bar{1}11)$	$[0\bar{1}1]$	13	$\overline{A2}$	$(\bar{1}11)$	$[01\bar{1}]$
2	A3	↑	$[101]$	14	$\overline{A3}$	↑	$[\bar{1}0\bar{1}]$
3	A6	↑	$[110]$	15	$\overline{A6}$	↑	$[\bar{1}\bar{1}0]$
4	B2	$(\bar{1}1\bar{1})$	$[0\bar{1}1]$	16	$\overline{B2}$	$(\bar{1}1\bar{1})$	$[01\bar{1}]$
5	B4	↑	$[\bar{1}01]$	17	$\overline{B4}$	↑	$[10\bar{1}]$
6	B5	↑	$[\bar{1}10]$	18	$\overline{B5}$	↑	$[1\bar{1}0]$
7	C1	$(11\bar{1})$	$[011]$	19	$\overline{C1}$	$(11\bar{1})$	$[0\bar{1}\bar{1}]$
8	C3	↑	$[101]$	20	$\overline{C3}$	↑	$[\bar{1}0\bar{1}]$
9	C5	↑	$[\bar{1}10]$	21	$\overline{C5}$	↑	$[1\bar{1}0]$
10	D1	$(1\bar{1}1)$	$[011]$	22	$\overline{D1}$	$(1\bar{1}1)$	$[0\bar{1}\bar{1}]$
11	D4	↑	$[\bar{1}01]$	23	$\overline{D4}$	↑	$[10\bar{1}]$
12	D6	↑	$[110]$	24	$\overline{D6}$	↑	$[\bar{1}\bar{1}0]$

Table 3.3: Slip systems of fcc crystals applied to the case of the single crystal superalloy.

denoted $\dot{\varepsilon}^p$ and $\dot{\beta}^p$, respectively, are also written in the form

$$\dot{\varepsilon}^p = \frac{1}{2} \sum_{g=1}^{24} \left(\mathbf{n}^g \otimes \mathbf{m}^g + \mathbf{m}^g \otimes \mathbf{n}^g \right) \dot{\gamma}^g \tag{3.31}$$

$$\dot{\beta}^p = \frac{1}{2} \sum_{g=1}^{24} \left(\mathbf{n}^g \otimes \mathbf{m}^g \right) \dot{\gamma}^g \tag{3.32}$$

except that g now runs from 1 to 24 instead of from 1 to 12. Using equation (3.32), the surface (geometrically necessary) dislocation density given by equation (3.30) is decomposed into the contributions of the slip systems

$$\boldsymbol{\alpha} = \sum_{g=1}^{24} \boldsymbol{\xi}^g \otimes \mathbf{b}^g \, \lambda^g \tag{3.33}$$

with

$$\lambda^g = \frac{1}{\|\mathbf{b}^g\|} \sin\left(\hat{\mathbf{n}}, \mathbf{n}^g \right) [\![\gamma^g]\!] \tag{3.34}$$

where $[\![\gamma^g]\!]$ is the jump of the shear across the surface with normal vector $\hat{\mathbf{n}}$, and $\boldsymbol{\xi}^g = \frac{\hat{\mathbf{n}} \times \mathbf{n}^g}{\|\hat{\mathbf{n}} \times \mathbf{n}^g\|}$ is the dislocation line vector for the slip system g in the singular surface. The quantity λ^g represents the scalar surface dislocation density associated to the slip system g drawn in black in figure (83 b). This dislocation density may induce a long-range internal stress that has to be superposed to the applied stress and the misfit stress to obtain the total stress in the microstructure. The long-range internal stress is calculated in the next section.

3.2.4 Calculation of the microscopic stresses

3.2.4.1 Principle of the calculation

The local variables will be calculated by using the same assumption of a periodic microstructure as already used in sections 2 and 3.1. In addition, homogeneous elastic properties are assumed for the γ and the γ' phases. The macroscopic stress $\boldsymbol{\Sigma}$ and the macroscopic strain $\mathbf{E}$ of the homogenised medium

can be obtained by using a volume average of the local fields (i.e. the microscopic stress $\boldsymbol{\sigma}(\mathbf{x})$, and strain $\varepsilon(\mathbf{x})$) and are written in the form (see equations 1.56):

$$\boldsymbol{\Sigma} = \langle \boldsymbol{\sigma} \rangle_V = \frac{1}{V} \int_V \boldsymbol{\sigma}(\mathbf{x}) \; dV \tag{3.35}$$

$$\mathbf{E} = \langle \varepsilon \rangle_V = \frac{1}{V} \int_V \varepsilon(\mathbf{x}) \; dV \tag{3.36}$$

where $\mathbf{x}$ is the local position vector in the computational cell. The compatibility conditions for the microscopic total strain are expressed by $\varepsilon = \frac{1}{2} \left(\nabla \mathbf{u} + \nabla \mathbf{u}^T \right)$, where $\mathbf{u}$ is the microscopic displacement vector. The elastic strain is related to the stress $\boldsymbol{\sigma}$ by Hooke's law (see equation 1.11).

The microscopic stress, total and plastic strain fields are assumed to be locally periodic. The fluctuations of the local fields are denoted with a tilde, e.g. $\tilde{\mathbf{u}}(\mathbf{x})$, $\tilde{\boldsymbol{\sigma}}(\mathbf{x})$, $\tilde{\varepsilon}(\mathbf{x})$, and $\tilde{\varepsilon}^p(\mathbf{x})$. The periodicity conditions and the relationship between macroscopic and microscopic stress and strain fields are [MAU92]

$$\mathbf{u}(\mathbf{x}) = \mathbf{E}.\mathbf{x} + \tilde{\mathbf{u}}(\mathbf{x}) \tag{3.37}$$

$$\tilde{\varepsilon}(\mathbf{x}) = \varepsilon\big(\tilde{\mathbf{u}}(\mathbf{x})\big) = \frac{1}{2} \left(\nabla \tilde{\mathbf{u}}(\mathbf{x}) + \nabla \tilde{\mathbf{u}}^T(\mathbf{x}) \right) \tag{3.38}$$

$$\boldsymbol{\sigma}(\mathbf{x}) = \boldsymbol{\Sigma} + \tilde{\boldsymbol{\sigma}}(\mathbf{x}) \tag{3.39}$$

$$\varepsilon(\mathbf{x}) = \mathbf{E} + \tilde{\varepsilon}(\mathbf{x}) \tag{3.40}$$

$$\varepsilon^p(\mathbf{x}) = \mathbf{E}^p + \tilde{\varepsilon}^p(\mathbf{x}) \tag{3.41}$$

with $\boldsymbol{\sigma}.\mathbf{n}^+ = -\boldsymbol{\sigma}.\mathbf{n}^-$ as boundary conditions on the opposite faces of the periodic cell. From equations (3.39)−(3.41) and (3.35)−(3.36), it follows that $\langle \tilde{\boldsymbol{\sigma}} \rangle_V = \mathbf{0}$, $\langle \tilde{\varepsilon} \rangle_V = \mathbf{0}$, and $\langle \tilde{\varepsilon}^p \rangle_V = \mathbf{0}$.

FE solutions of the governing field equations (3.37)−(3.41) for repeating unit cell representative of materials with periodic microstructures produce accurate estimates of the local field variables, albeit at a substantial computational cost[5]. The construction of inelastic macroscopic constitutive equations for arbitrary loading based on such analyses is not straightforward, making it difficult to embed FE based models into more general structural analysis procedures. This has given rise to the development of approximate models which employ simplifying assumptions on the form of plastic strains within the individual phases (see section 3.1.4.3). This is the subject of the two following sections.

3.2.4.2 Piece-wise uniform homogeneous plastic strains

A number of approximate analyses of a periodic cell, which employ subdomain discretisation of the unit cell to mimic the material's microstructure, has been developed to deal with the inelastic response of periodic multiphase materials. The Generalized Method of Cells [PAL92], employs a first-order representation of the displacement field in each subdomain of the repeating unit cell, producing piece-wise uniform strain and stress fields throughout the cell. The method is a generalisation of the original Method of Cells developed by Aboudi [ABO82] which is based on a limited domain discretisation. The predictive capability of the generalised method in various applications has been summarised in [ABO04].

In order to obtain a manageable constitutive law, a particular form of piece-wise homogeneous plastic strain fields applied to γ/γ' superalloys is considered [FED99] [FED02]. Obviously, the regions in which the plastic deformation are taken homogeneous must be defined by taking into the account the nature of all the deformation mechanisms illustrated in section 3.2.2. Thus, piece-wise uniform plastic strains are assumed at the microscopic level. Formally, this is written as

$$\varepsilon^p(\mathbf{x}) = \sum_K \varepsilon_K^p \, \Im_K(\mathbf{x}) \tag{3.42}$$

---

[5]The DCM calculations are a very good examples.

where $\Im_K$ is the indicator function of some subdomain $V_K \subset V$

$$\Im_K(\mathbf{x}) = \begin{cases} 1 & \text{for } \mathbf{x} \in V_K \\ 0 & \text{for } \mathbf{x} \notin V_K \end{cases} \tag{3.43}$$

Taking the averages over each subdomain, equation (3.42) gives $\varepsilon^p = \sum_K \varepsilon_K^p$. Note that the regions V_K may overlap.

3.2.4.3   Choice of the decomposition of the periodic cell

The question now arises, in which manner the periodic cell, and in particular the matrix channels should be decomposed. The choice of the decomposition is crucial because it affects the estimate of the internal stresses. For piece-wise homogeneous plastic strains, the tensor of the geometrically necessary dislocations α_{hi} vanishes inside the homogeneously plastically strained regions and it has a surface density given by $\alpha_{hi} = -\epsilon_{hlj}\left[\beta_{I\ ji}^p - \beta_{J\ ji}^p\right]\hat{n}_l$ on the boundary between the domains V_I and V_J, according to equation (3.33). These dislocations are responsible for the internal stresses.

First, it is natural to distinguish between the precipitates and the matrix because their resistance to glide is different and the interfaces are likely to represent an obstacle to dislocation glide. The existence of geometrically necessary dislocations at the γ/γ' interface accommodating the plastic strain gradient between both phases has been discussed already, and its physical counterpart, the dislocation networks at the phase boundaries have been observed many times.

Secondly, the superposition of the external and the misfit stresses leads to different plastic responses in the three channel types and thus results in different dislocation structures at the three interface types. Hence, it is also natural to divide the matrix into three different channel types.

The choice for the shape of the decomposition of the matrix into three channels is not straightforward. Figure (84) shows two natural solutions of decomposition of the one-eighth unit-cell (see figure 84 a) and of the matrix. In figure (84 b) the channels have wedge-shaped ends and do not overlap. In the following, this decomposition will be referred to as WSE for brevity. In the alternative decomposition shown in (84 c) the channels are parallelepiped-shaped and will be referred to as P in the following for brevity.

As decomposition of the matrix into subdomains leads to dislocations walls within the matrix in addition to those existing at the interface between the matrix and the precipitates, a decision must be taken about the more physically justified way to decompose the γ phase. Once again, DD simulations are a precious tool to elucidate this issue and use is made of the DCM results to identify the best representation. For instance (i) figure (85) shows a glide sequence of an individual dislocation at a crossing between two channels. Due to the anisotropy of the line tension and/or lower local stresses in the vertical channel, the loop is immobilised at the entrance of the vertical channel, roughly parallel to the γ/γ' interfaces. In addition, to give credit to the latter dislocation configuration, (ii) figure (86) shows the same effect for a

(a)   (b)   (c)
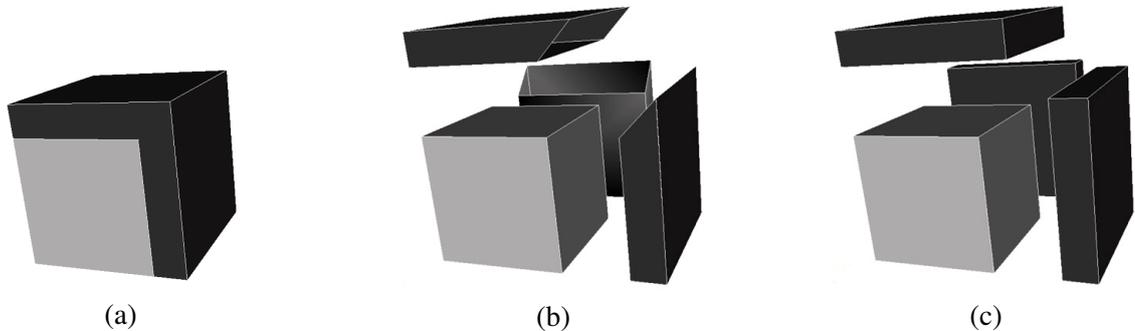
Figure 84 - (a) View of one-eighth symmetry unit-cell model. (b) Its decomposition 1 in non-overlapping subdomains in the matrix (WSE), and (c) decomposition 2 in overlapping subdomains (P).
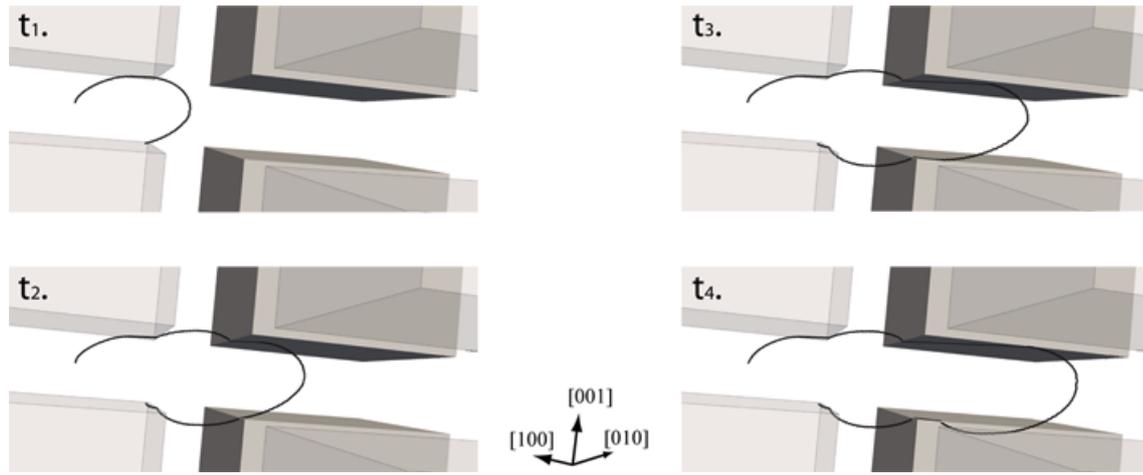
Figure 85 - Glide sequence of an individual dislocation within a horizontal γ channel at a crossing between two channels: due to the anisotropy of the line tension and/or the lower RSS in the vertical channel, the potentially mobile segment does not overcome the Orowan threshold stress and immobilises at the channel entrance, roughly parallel to the γ/γ' interfaces.

large number of dislocations illustrated in section 2.4.4.3 for the [001] case.

Clearly, both results (i) and (ii) support the P decomposition defined in figure (84 c). The internal dislocation walls of the channels separate regions in which plastic straining has a different intensity. In contrast, the oblique dislocation walls of the decomposition 1 illustrated in figure (84 b) do not correspond to any dislocation configuration reproduced by the DCM.

In addition, it has been noted by Fedelich [FED02] that the P decomposition behaves too stiffly with respect to experimental data. However, this conclusion was reached under the premise that no dislocation sources exist in the channels. In that case, dislocation multiplication is only possible if all channels are plastically strained, including channels in which dislocation glide is less favorable. The assumed presence of dislocation sources leads to a completely different situation, so that the plastic flow restricted to a single channel type becomes kinematically possible. This point will be discussed in detail in the following.

In summary, the following subdomains are defined to describe the distribution of the local plastic strains:

* V_1, V_2, and V_3 are the overlapping parallelepiped regions as shown in figure (84 c) (i.e. the P decomposition is adopted).

* V_4 is the γ' precipitate.

The volume fraction of each region V_K is denoted by f_K where $\sum_{K=1}^{4} f_K > 1$ because the regions overlap. The macroscopic plastic strain defined by $\mathbf{E}^p = \langle \varepsilon^p \rangle_V$ is then[6]

$$\mathbf{E}^p = \langle \varepsilon^p \rangle_V = \frac{1}{V} \int_V \varepsilon^p(\mathbf{x})\, \mathrm{d}V = \frac{1}{V} \sum_K \int_V \varepsilon_K^p(\mathbf{x})\, \mathrm{d}V = \frac{1}{V} \sum_K V_K \varepsilon_K^p \tag{3.44}$$

$$= \sum_{K=1}^{4} f_K \varepsilon_K^p \tag{3.45}$$

Moreover, by convention, the plastic strain in the region V_4 is taken to also include the homogeneous distribution of misfit eigenstrain, i.e. $\varepsilon_4^p = \varepsilon_4^p + \varepsilon_4^{\mathrm{misfit}}$, where $\varepsilon_4^{\mathrm{misfit}} = \delta_u \mathbf{I}$ with $\mathbf{I}$ the second rank unit tensor, and $\delta_u = 2\frac{a^{\gamma'} - a^\gamma}{a^{\gamma'} + a^\gamma}$ the unconstrained misfit.

According to equation (3.45), $\mathbf{E}^p$ is obtained by the evaluation of ε_K^p for each subdomain V_K. The plastic

---

[6]For the same elastic constants in all phases.

(a)   (b)
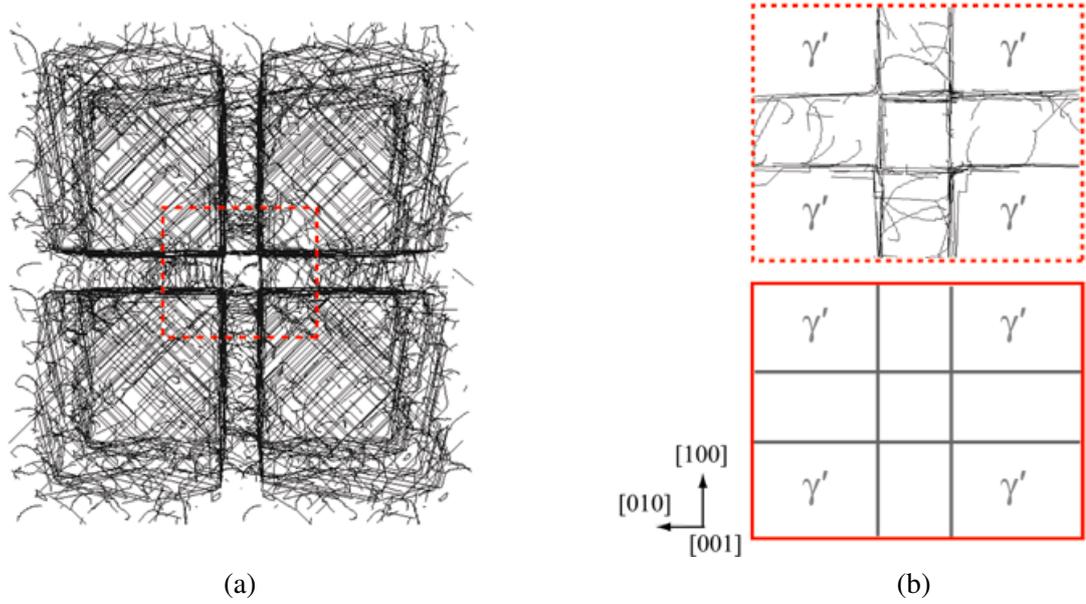
Figure 86 - Dislocation immobilisation at channel entrances observed in a massive 3D DCM calculation (see section 2.4.4). (a) Overall dislocation structure around four precipitates after 0.2% plastic strain for the [001] case. (b-up) Thin foil of 0.25 μm thickness cut perpendicularly to the [001]-directions, at a crossing between two channels and through the centre of precipitates. (b-down) Idealisation of the dislocation structure in (b-up) used in the M3RSX model.

deformation ε_K^p due to each mechanism is driven by the RSS $\hat{\tau}_{gK}$ defined by the effective local stresses $\hat{\boldsymbol{\sigma}}_K$, i.e. $\hat{\tau}_{gK} = \mathbf{m}_g.\hat{\boldsymbol{\sigma}}_K.\mathbf{n}_g$. The local stress are derived from the stored energy in the microstructure, as will be shown in the next section.

3.2.4.4 Estimate of the effective local stresses

Stored elastic energy

The elastic energy stored in the periodic cell is defined by

$$W = \frac{1}{2} \int_V \varepsilon^e : \mathbf{C} : \varepsilon^e \mathrm{d}V \tag{3.46}$$

The periodicity conditions may be applied to the elastic strain ε^e such as equations (3.37)−(3.41) and (3.35)−(3.36), so that $\varepsilon^e = \langle\varepsilon^e\rangle + \tilde{\varepsilon}^e$, where $\tilde{\varepsilon}^e$ is the fluctuation part of the ε^e defined by $\tilde{\varepsilon}^e = \varepsilon^e - (\mathbf{E} - \langle\varepsilon^p\rangle)$. By substituting into equation (3.46), the stored elastic energy can be split into a macroscopic part W_1 and a fluctuation part W_2:

$$
\begin{aligned}
W &= \frac{1}{2} \int_V \left(\langle\varepsilon^e\rangle + \tilde{\varepsilon}^e\right) : \mathbf{C} : \left(\langle\varepsilon^e\rangle + \tilde{\varepsilon}^e\right)\mathrm{d}V = \frac{1}{2} \int_V \langle\varepsilon^e\rangle : \mathbf{C} : \langle\varepsilon^e\rangle\mathrm{d}V + \frac{1}{2} \int_V \tilde{\varepsilon}^e : \mathbf{C} : \tilde{\varepsilon}^e\mathrm{d}V \\
&= \frac{1}{2} \int_V \left(\mathbf{E} - \langle\varepsilon^p\rangle\right) : \mathbf{C} : \left(\mathbf{E} - \langle\varepsilon^p\rangle\right)\mathrm{d}V + \frac{1}{2} \int_V \tilde{\varepsilon}^e : \mathbf{C} : \tilde{\varepsilon}^e\mathrm{d}V \\
&\equiv W_1 + W_2
\end{aligned}
\tag{3.47}
$$

The elastic energy W is written as the sum of two different origins: global deformation of the volume W_1, and incompatibilities between each phase W_2. Even though the term of global elastic energy is well defined, the fluctuation part is still written in terms of local quantities. Thanks to a simplified

micromechanical analysis, W_2 is approximated using a Fourier series analysis with the assumption of piece-wise uniform strain fields in the three kinds of channels and in the precipitate.

Calculation by Fourier series

The assumption of piece-wise uniform strain fields illustrated in section 3.2.4.2 has also been employed by Dvorak [DVO92] in the context of a procedure called the TFA (see section 1.2.6) or indeed in many other mean-field approaches. This approach has recently been generalised by Chaboche *et al.* [CHA01] and demonstrated to capture the local stress and (inelastic) strain fields with good accuracy in comparison to FE simulations. Alternative methods based on Fourier series approximations of the stress and strain fields in the repeating unit cell have been developed by Walker et al. [WAL94], Fotiu and Nemat-Nasser [FOT96] for periodic composites, and by Fedelich [FED99] [FED02] for periodic two-phase alloys.
Within the approximation of periodicity, the fluctuating quantities $\tilde{\mathbf{u}}(\mathbf{x})$ and $\tilde{\varepsilon}^p(\mathbf{x})$ are guaranteed by Fourier series expansions in the periodic cell following the standard procedure (see for instance [MUR87]):

$$\tilde{u}_i(\mathbf{x}) = \sum_{p_\alpha \neq 0} \bar{u}_i(p_\alpha) \ e^{i\boldsymbol{\xi}(p_\alpha).\mathbf{x}} = \sum_{\xi \neq 0} \bar{u}_i(\boldsymbol{\xi}) \ e^{i\boldsymbol{\xi}.\mathbf{x}} \tag{3.48}$$

$$\tilde{\varepsilon}^p_{ij}(\mathbf{x}) = \sum_{p_\alpha \neq 0} \bar{\varepsilon}^p_{ij}(p_\alpha) \ e^{i\boldsymbol{\xi}(p_\alpha).\mathbf{x}} = \sum_{\xi \neq 0} \bar{\varepsilon}^p_{ij}(\boldsymbol{\xi}) \ e^{i\boldsymbol{\xi}.\mathbf{x}} \tag{3.49}$$

where $i = \sqrt{-1}$, $\xi_\alpha(p_\alpha) = \frac{\pi p_\alpha}{L_\alpha}$ is the wave vector, and p_α positive or negative integers with L_α the dimensions of the cell ($\alpha = 1, 2, 3$ in 3D)[7]. The Fourier coefficients $\bar{\varepsilon}^p$ of the expansion of $\tilde{\varepsilon}^p_{ij}(\mathbf{x})$ are obtained by

$$\bar{\varepsilon}^p_{ij}(\boldsymbol{\xi}) = \frac{1}{V} \int_V \varepsilon^p_{ij}(\mathbf{x}) \ e^{-i\boldsymbol{\xi}.\mathbf{x}} \ \mathrm{d}V \tag{3.50}$$

By solving the equilibrium equations together with equations (3.41) and (3.48), the coefficients of the displacement fluctuation fields $\bar{u}_i(\boldsymbol{\xi})$ as function of the plastic strain distribution are

$$\begin{aligned} \tilde{\sigma}_{ij,j} = 0 \quad &\Rightarrow \quad C_{ijkl}\,\tilde{\varepsilon}_{kl,j} = 0 \\ &\Rightarrow \quad C_{ijkl}\,\tilde{u}_{k,lj} = C_{ijkl}\,\tilde{\varepsilon}^p_{kl,j} \\ &\Rightarrow \quad C_{ijkl}\,\bar{u}_k(\boldsymbol{\xi})\,\xi_l\xi_j = -iC_{ijkl}\,\bar{\varepsilon}^p_{kl}\xi_j \quad \forall \boldsymbol{\xi} \neq \mathbf{0} \\ &\Rightarrow \quad \bar{u}_i(\boldsymbol{\xi}) = -iV_{ij}(\boldsymbol{\xi})\,C_{jlmn}\,\bar{\varepsilon}^p_{mn}\xi_l \end{aligned} \tag{3.51}$$

with

$$V_{ij}(\boldsymbol{\xi}) = K_{ji}(\boldsymbol{\xi}) \ , \ \text{or} \ \ \mathbf{V}(\boldsymbol{\xi}) = \mathbf{K}(\boldsymbol{\xi})^{-1} \tag{3.52}$$

$$K_{ji}(\boldsymbol{\xi}) = C_{jkil}\xi_l\xi_k \tag{3.53}$$

Note that $\mathbf{V}$ and $\mathbf{K}$ are symmetric second order tensors and that $\mathbf{V}$ satisfies also $\mathbf{V}(-\boldsymbol{\xi}) = \mathbf{V}(\boldsymbol{\xi})$.
The density of the stored elastic energy can be defined by

$$\varpi = \frac{1}{V}W = \frac{1}{V}(W_1 + W_2) = \varpi_1^{\text{macro}} + \varpi_2^{\text{micro}} \tag{3.54}$$

---

[7]The interested reader should refer to more complete specialised texts such as chapter 8 of [RUD76].

where (see Appendix D.1 for the expression obtained for $W_2 = \frac{1}{V}\varpi_2^{\text{micro}}$ after some algebra)

$$\varpi_2^{\text{micro}} = \frac{1}{2}\sum_{q_\alpha \neq 0} \omega_{cdpq}(q_\alpha)\bar{\varepsilon}_{cd}^p(q_\alpha)\bar{\varepsilon}_{pq}^p(-q_\alpha) \ , \qquad \text{with} \tag{3.55}$$

$$\omega_{cdpq}(q_\alpha) = C_{cdpq} - C_{cdkl}\xi_l(q_\alpha)V_{km}(q_\alpha)\xi_n(q_\alpha)C_{mnpq} \tag{3.56}$$

or

$$\varpi_2^{\text{micro}} = \frac{1}{2}\sum_{\boldsymbol{\xi} \neq \mathbf{0}} \bar{\boldsymbol{\varepsilon}}^p(\boldsymbol{\xi}) : \boldsymbol{\omega}(\boldsymbol{\xi}) : \bar{\boldsymbol{\varepsilon}}^p(-\boldsymbol{\xi}) \ , \qquad \text{with} \tag{3.57}$$

$$\boldsymbol{\omega}(\boldsymbol{\xi}) = \mathbf{C} - \mathbf{C} : \left(\boldsymbol{\xi} \otimes \mathbf{V}(\boldsymbol{\xi}) \otimes \boldsymbol{\xi}\right) : \mathbf{C} = \left[\mathbf{I} - \mathbf{C} : \left(\boldsymbol{\xi} \otimes \mathbf{V}(\boldsymbol{\xi}) \otimes \boldsymbol{\xi}\right)\right] : \mathbf{C} \tag{3.58}$$

According to equations (3.47) and (3.54), the average density ϖ of the stored elastic energy is also expressed as function of the plastic strain distribution, and is written as

$$\varpi = \frac{1}{2}\left(\mathbf{E} - \langle\bar{\varepsilon}^p\rangle\right) : \mathbf{C} : \left(\mathbf{E} - \langle\bar{\varepsilon}^p\rangle\right) + \frac{1}{2}\sum_{\boldsymbol{\xi} \neq \mathbf{0}} \bar{\boldsymbol{\varepsilon}}^p(\boldsymbol{\xi}) : \boldsymbol{\omega}(\boldsymbol{\xi}) : \bar{\boldsymbol{\varepsilon}}^p(-\boldsymbol{\xi}) \tag{3.59}$$

Moreover, introducing the assumed piece-wise uniform plastic strain distribution given by equations (3.42) and (3.43) into the expression (3.50) of Fourier coefficients $\bar{\varepsilon}^p(\boldsymbol{\xi})$, one obtains:

$$\bar{\varepsilon}^p(\boldsymbol{\xi}) = \frac{1}{V}\int_V \varepsilon^p(\mathbf{x})\,\mathrm{e}^{-i\boldsymbol{\xi}.\mathbf{x}}\,\mathrm{d}V = \frac{1}{V}\sum_{K=1}^4\int_V \varepsilon_K^p\,\mathrm{e}^{-i\boldsymbol{\xi}.\mathbf{x}}\,\mathrm{d}V = \sum_{K=1}^4 I_K(\boldsymbol{\xi})\varepsilon_K^p \tag{3.60}$$

with $I_K(\boldsymbol{\xi}) = \dfrac{1}{V}\displaystyle\int_{V_K} \mathrm{e}^{-i\boldsymbol{\xi}.\mathbf{x}}\mathrm{d}V$.

By combining equation (3.60) and the expression of the elastic energy in the periodic cell (3.59), the latter can also be evaluated as function of the tensorial internal variables ε_K^p

$$\varpi = \frac{1}{2}\left(\mathbf{E} - \sum_{K=1}^4 f_K\varepsilon_K^p\right) : \mathbf{C} : \left(\mathbf{E} - \sum_{K=1}^4 f_K\varepsilon_K^p\right) + \frac{1}{2}\sum_{\boldsymbol{\xi} \neq \mathbf{0}}\sum_{K,L} I_K(\boldsymbol{\xi})I_L(-\boldsymbol{\xi})\varepsilon_K^p : \boldsymbol{\omega}(\boldsymbol{\xi}) : \varepsilon_L^p$$

$$= \frac{1}{2}\left(\mathbf{E} - \sum_{K=1}^4 f_K\varepsilon_K^p\right) : \mathbf{C} : \left(\mathbf{E} - \sum_{K=1}^4 f_K\varepsilon_K^p\right) + \frac{1}{2}\sum_{K,L}\varepsilon_K^p : \boldsymbol{\Omega}_{KL} : \varepsilon_L^p \tag{3.61}$$

where the $4 \times 4 = 16$ fourth order tensors $\boldsymbol{\Omega}_{KL}$ depend on the geometry and on the elastic constants. These structural tensors are given by

$$\boldsymbol{\Omega}_{KL} = \sum_{\boldsymbol{\xi} \neq \mathbf{0}} I_K(\boldsymbol{\xi})I_L(-\boldsymbol{\xi})\boldsymbol{\omega}(\boldsymbol{\xi}) = \left[\sum_{\boldsymbol{\xi} \neq \mathbf{0}} I_K(\boldsymbol{\xi})I_L(-\boldsymbol{\xi})\left[\mathbf{I} - \mathbf{C} : \left(\boldsymbol{\xi} \otimes \mathbf{V}(\boldsymbol{\xi}) \otimes \boldsymbol{\xi}\right)\right]\right] : \mathbf{C} \tag{3.62}$$

Since $\mathbf{E}^p = \sum_{K=1}^4 f_K\varepsilon_K^p$, the first term of the right-hand side of equation (3.61) is the macroscopic part of the stored energy and the second term the microscopic part associated to incompatibility of deformation between the subdomains. Note the symmetry $\boldsymbol{\Omega}_{KL} = \boldsymbol{\Omega}_{LK}$ since $\boldsymbol{\omega}(-\boldsymbol{\xi}) = \boldsymbol{\omega}(\boldsymbol{\xi})$. From equation (3.58) follow the additional symmetries $(\boldsymbol{\Omega}_{KL})_{ijkl} = (\boldsymbol{\Omega}_{KL})_{klij} = (\boldsymbol{\Omega}_{KL})_{jikl}$.

The material is described by the internal variables ε_K^p, and the associated thermodynamic forces are obtained by minimising the energy related to the internal variables, as will be shown below.

Effective local stresses and driving forces

In the theory of irreversible processes [MAU92], the driving force associated to any transformation described by a variation of the internal variable ε_J^p is the derivative of the free energy with respect to this variable. The thermodynamic forces $\mathbf{A}_J$ associated to the internal variables ε_J^p, $J = 1, 2, 3, 4$ then become[8]:

$$\mathbf{A}_J = -\frac{\partial \varpi}{\partial f_J \varepsilon_J^p} = \mathbf{C} : \left(\mathbf{E} - \sum_{K=1}^{4} f_K \varepsilon_K^p \right) - \frac{1}{f_J} \sum_{K=1}^{4} \mathbf{\Omega}_{JK} : \varepsilon_K^p \tag{3.63}$$

According to equation (3.39) the stress field is written as $\boldsymbol{\sigma}(\mathbf{x}) = \boldsymbol{\Sigma} + \tilde{\boldsymbol{\sigma}}(\mathbf{x})$ with a fluctuation field:

$$\tilde{\sigma}_{pq}(\mathbf{x}) = C_{pqik}\left(\tilde{u}_{i,k} - \tilde{\varepsilon}_{ik}^p \right) \tag{3.64}$$

Substituting equations (3.49), (D.3), and (D.4) into equation (3.64), it becomes

$$\tilde{\sigma}_{pq}(\mathbf{x}) = C_{pqik} \sum_{p_\alpha \neq 0} \left[C_{jlmn}\bar{\varepsilon}_{mn}^p(p_\alpha)\xi_l(p_\alpha)\xi_k(p_\alpha)V_{ij}(p_\alpha) - \bar{\varepsilon}_{ik}^p(p_\alpha) \right] e^{i\boldsymbol{\xi}(p_\alpha).\mathbf{x}} \tag{3.65}$$

$$= \sum_{p_\alpha \neq 0} \underbrace{\left[C_{jlmn}\xi_l(p_\alpha)\xi_k(p_\alpha)V_{ij}(p_\alpha)C_{pqik} - C_{pqmn} \right]}_{-\omega_{pqmn}(p_\alpha)} \bar{\varepsilon}_{mn}^p(p_\alpha) \, e^{i\boldsymbol{\xi}(p_\alpha).\mathbf{x}} \tag{3.66}$$

and so the local stresses (i.e. equation 3.39) are given as function of the plastic strain distribution by

$$\boldsymbol{\sigma}(\mathbf{x}) = \boldsymbol{\Sigma} - \sum_{\boldsymbol{\xi} \neq \mathbf{0}} \boldsymbol{\omega}(\boldsymbol{\xi}) : \bar{\boldsymbol{\varepsilon}}^p(\boldsymbol{\xi}) \, e^{i\boldsymbol{\xi}.\mathbf{x}} \tag{3.67}$$

The second term of equation (3.67) gives the deformation-induced back-stresses, and the first term denotes the macroscopic stress.

From equation (3.67) the average local stresses in each subdomain V_J can be calculated

$$\langle \boldsymbol{\sigma} \rangle_{V_J} = \boldsymbol{\Sigma} - \frac{1}{V_J} \sum_{\boldsymbol{\xi} \neq \mathbf{0}} \boldsymbol{\omega}(\boldsymbol{\xi}) : \bar{\boldsymbol{\varepsilon}}^p(\boldsymbol{\xi}) \int_{V_J} e^{i\boldsymbol{\xi}.\mathbf{x}}\mathrm{d}V \tag{3.68}$$

$$= \boldsymbol{\Sigma} - \frac{1}{V_J} \sum_{\boldsymbol{\xi} \neq \mathbf{0}} \sum_K I_K(\boldsymbol{\xi})\boldsymbol{\omega}(\boldsymbol{\xi}) : \varepsilon_K^p \int_{V_J} e^{i\boldsymbol{\xi}.\mathbf{x}}\mathrm{d}V \tag{3.69}$$

$$= \boldsymbol{\Sigma} - \frac{1}{f_J} \sum_{\boldsymbol{\xi} \neq \mathbf{0}} \sum_K I_K(\boldsymbol{\xi})I_J(-\boldsymbol{\xi}) : \boldsymbol{\omega}(\boldsymbol{\xi}) : \varepsilon_K^p \tag{3.70}$$

and are finally given by

$$\langle \boldsymbol{\sigma} \rangle_{V_J} = \boldsymbol{\Sigma} - \frac{1}{f_J} \sum_{K=1}^{4} \mathbf{\Omega}_{JK} : \varepsilon_K^p = \mathbf{A}_J \tag{3.71}$$

The thermodynamic forces (3.63) and the average values (3.71) which are identical can thus be regarded as the driving forces or effective stresses $\hat{\boldsymbol{\sigma}}_J = \langle \boldsymbol{\sigma} \rangle_{V_J}$ for the corresponding mechanisms necessary in the evaluation of the mobility of dislocations. Accordingly, the back-stresses $\mathbf{X}_J = \frac{1}{f_J} \sum_{K=1}^{4} \mathbf{\Omega}_{JK} : \varepsilon_K^p$ are defined here explicitly in the M3RSX model, where the $\mathbf{\Omega}_{JK}$ are calculated only once before the simulations.

---

[8]The interested reader should refer to more complete specialised works [LEM85].

To summarise, the effective stress tensors $\hat{\boldsymbol{\sigma}}_J$ ($J = 1, 2, 3, 4$) are

$$\hat{\boldsymbol{\sigma}}_J = \langle \boldsymbol{\sigma} \rangle_{V_J} = \mathbf{A}_J = \boldsymbol{\Sigma} - \frac{1}{f_J} \sum_{K=1}^{4} \boldsymbol{\Omega}_{JK} : \boldsymbol{\varepsilon}_K^p \tag{3.72}$$

$$= \boldsymbol{\Sigma} - \sum_{K=1}^{4} \underbrace{\left[\frac{1}{f_J} \sum_{\boldsymbol{\xi} \neq \mathbf{0}} I_K(\boldsymbol{\xi}) I_L(-\boldsymbol{\xi}) \left[\mathbf{I} - \mathbf{C} : \left(\boldsymbol{\xi} \otimes \mathbf{V}(\boldsymbol{\xi}) \otimes \boldsymbol{\xi} \right) \right] \right]}_{\mathbf{F}_{KJ} \text{ from equation 1.60}} : \mathbf{C} : \boldsymbol{\varepsilon}_K^p \tag{3.73}$$

and the RSS $\hat{\tau}_{gJ}$ driving each deformation mechanism are then obtained by projection on octahedral slip systems g, i.e. $\hat{\tau}_{gJ} = \mathbf{m}_g.\hat{\boldsymbol{\sigma}}_J.\mathbf{n}_g$. Note that equation (3.73) has the same form as equation (1.60) from the TFA procedure with $\mathbf{B}_K = \mathbf{I}$. The latter equality is justified here because each subdomain has the same elastic tensor.

3.2.5 Dislocation-based constitutive model

3.2.5.1 Plastic deformation in the channels

The threshold stress

The description of slip in the channels is based on the assumption that the dislocations only move when the energy released by their motion is higher than the energy of a dislocation newly deposited at the interfaces. This assumption leads to the existence of a threshold stress, which is inversely proportional to the thickness w of the channel (see equation 1.6) [BRO71]. If the acting shear stress is higher than the threshold stress, the dislocations move with a velocity increasing with the overstress. This point has been discussed in section 2.4.3.4. The threshold stress for dislocation motion in the channels plays a crucial role in the constitutive framework.

Thus, dislocation loops of the slip system g can glide in the γ channels, bowing out between the precipitates, if the work performed by the RSS $\hat{\tau}_{gK}$ in channel type K exceeds the corresponding increase of line energy of the dislocation. Note that in the following, all variables pertaining to a slip system and a channel type are referenced by the subscripts g and K, for instance the local RSS $\hat{\tau}_{gK}$. For an extension δs of the length of the deposited segments for slip system g in the channel K of width $d = 2L - 2c$, the latter condition reads:

$$2\,T_{gK}\,\delta s \leq \hat{\tau}_{gK}\,b\,w\,\delta s \tag{3.74}$$

where $w = d\sqrt{\frac{3}{2}}$ is the channel width in an octahedral plane, and T_{gK} is the line energy of the trailing segment. The trailed segments lie along the intersection of the $\{111\}$ glide planes and the $\{100\}$ interfaces, i.e. along the $\langle 110 \rangle$ directions. Their energy depends on the orientation of their line with respect to that of the Burgers vector and the crystal axes. Only two cases can occur (see figure 55):

* The trailing segments are pure screws.

* The trailing segments are of mixed type, with a $60°$ angle between line and Burgers vector.

For a square loop of width w, the line energy has the form [HIR82]:

$$T_{gK} = \frac{1}{2}\,\alpha\,K_{gK}\,b^2 \tag{3.75}$$

where $\alpha = \frac{1}{2\pi}\ln\left(\frac{w}{r_0}\right)$, and r_0 is representative of the size of the dislocation core, i.e. $0.5b \leq r_0 \leq b$. For the range of these values and $w = 60$ nm (a representative value of the channel width), the estimate $0.86 \leq \alpha \leq 1$ is obtained. However, due to its paramount importance in controlling flow in the channels

and the large uncertainties related to this simple estimate, α will be treated, in the following, as an adjustable parameter in a physical range of values.

The factor K_{gK} has been estimated by Foreman [FOR55] for both cases of interest

$$K_{gK} = K_s = \sqrt{\frac{1}{2}\left(c_{44}\left(c_{11} - c_{12}\right)\right)} \quad \text{for the screw segments} \tag{3.76}$$

$$K_{gK} = \frac{1}{4}\left(K_x + 2K_y + K_s\right) \quad \text{for the mixed segments} \tag{3.77}$$

where

$$K_x = \left(\bar{c}'_{11} + c'_{11}\right)\sqrt{\frac{c'_{66}\left(\bar{c}'_{11} - c'_{11}\right)}{c'_{22}\left(\bar{c}'_{11} + c'_{12} + 2c'_{66}\right)}}$$

$$K_y = \sqrt{\frac{c'_{22}}{c'_{11}}}\, K_x$$

$$\text{with}$$

$$c'_{11} = \frac{1}{2}\left(c_{11} + c_{12} + 2c_{44}\right)$$

$$c'_{22} = c_{11}$$

$$c'_{66} = c_{44} \tag{3.78}$$

$$c'_{12} = c_{12}$$

$$\bar{c}'_{11} = \sqrt{c'_{11}c'_{22}}$$

From equations (3.74) and (3.75), it follows that glide occurs in the channel K if the local RSS overcomes the corresponding Orowan critical shear stress given by

$$\tau_{gK}^{\text{Orowan}} = \alpha\frac{K_{gK}\, b}{w} \tag{3.79}$$

The line tension (3.75) applied to the M3RSX model is a simplification of the one used by the DCM (see equation 2.6) with the assumption that each dislocation is regarded as a rectangular loop

Dislocation mobility and plastic strain due to dislocation glide

If the acting shear stress is higher than the threshold stress $\tau_{gK}^{\text{Orowan}}$ defined in equation (3.79), the mobile dislocation segments move with a velocity increasing with the overstress $\hat{\tau}_{gK} - \tau_{gK}^{\text{Orowan}}$. Dislocation glide is thermally activated. While numerous forms have been proposed in the literature [KOC75], a simple law for the velocity v_{gK}^{glide} of a mobile dislocation segment of the system g in the channel K, which accounts for thermal activation[9] and which vanishes at the Orowan stress, is [KRA75]

$$v_{gK}^{\text{glide}} = v_0^{\text{glide}}\sinh\left[\frac{\left(\hat{\tau}_{gK} - \tau_{gK}^{\text{Orowan}}\right)V^{\text{glide}}}{k_B\, T}\right] \tag{3.80}$$

where V^{glide} is an activation volume, v_0^{glide} a temperature-dependent constant reference dislocation velocity, and k_B and T denote respectively Boltzmann's constant and the absolute temperature.

The average shear rate in the channel K produced by $\mathcal{N}_{gK}$ mobile segments of the slip system g is deduced by the Orowan equation (1.28):

$$\rho_m^g = \sum_K \rho_m^{gK} = \frac{w\, \mathcal{N}_{gK}}{V_{\text{channel}}} \tag{3.81}$$

---

[9]This is different from the one used in the DCM, because there v corresponds to the free-flight velocity, whereas here the waiting time before obstacles is taken into account as well.

Thus, the shear rate is defined by

$$\dot{\gamma}_{gK}^{\text{glide}} = \underbrace{\frac{1}{V_{\text{channel}}} \, w \, \mathcal{N}_{gK}}_{\rho_m^{gK} \text{ from equation 1.28}} \, b \, v_{gK}^{\text{glide}} \tag{3.82}$$

where $V_{\text{channel}} = 8 \, (L - c) \, L^2$ is the volume of the channel, which is taken as parallelepiped with dimensions $2(L - c) \times 2L \times 2L$ (see figure 83 a).

When dislocation segment densities are chosen as internal variables, their evolution laws generally contain multiplication/production terms (characterised by "+" in the following equations) and immobilisation terms ("−"). This is the subject of the next section.

Dislocation multiplication/production

Under load the dislocations start to multiply. In the early stages and at high temperature (above 850°C), the number of moving segments in the channels increases as the dislocation loops propagate in new channels where they continue to glide. This is the key multiplication mechanism considered by Fedelich [FED02]. In accordance, the production frequency of new segments in two channels $I \neq J$ due to moving dislocation loops in the channel K, $K \neq I$, $K \neq J$ is taken into account through

$$\dot{\mathcal{N}}_{gI}^{+ \text{ channel}} = \dot{\mathcal{N}}_{gJ}^{+ \text{ channel}} = \frac{\mathcal{N}_{gK} \, v_{gK}^{\text{glide}}}{\sqrt{2}L} \tag{3.83}$$

with $\sqrt{2}L$ is the average distance between two channels in a $\{111\}$ plane.

However, if the local stresses are not high enough to deform all channel types, this multiplication mechanism does not operate. Within this assumption, sustained plastic flow is not possible for low stresses and the previous work of Fedelich [FED02] shows that this resulted in very low values of the fitted α parameter of equation (3.79), of magnitude 0.3. This is why, in addition to dislocation multiplication as a result of existing dislocation expansion, dislocation sources are supposed to exist in each channel, similar to ideal Frank-read sources. The production frequency $f_{gK}^{+ \text{ FR}}$ of new loops in the channel K is given by

$$f_{gK}^{+ \text{ FR}} = \frac{v_{gK}^{\text{glide}}}{L_{\text{production}}} \tag{3.84}$$

where $L_{\text{production}}$ is the distance glided by a dislocation emitted from the source before emission of a new dislocation loops. $L_{\text{production}}$ will be regarded as an adjustable parameter related to the frequency of generation of new mobile segments in each channel K.

Hence, the increase of the mobile segments $\dot{\mathcal{N}}_{gK}^{+ \text{ FR}}$ of length w freshly emitted by the Frank-Read sources in channel K is assumed to be function of the plastic shear strain rate [ESS79], and is written as

$$\dot{\mathcal{N}}_{gK}^{+ \text{ FR}} = f_{gK}^{+ \text{ FR}} \, \mathcal{N}_{gK} = \frac{v_{gK}^{\text{glide}}}{L_{\text{production}}} \, \mathcal{N}_{gK} \tag{3.85}$$

The assumption that dislocation sources exist in the channels may be justified by figure (62 c). It has been shown that the collinear super-jogs which decorate the dislocation lines could act as dislocation sources within a γ channel. Leading to the self production term, $L_{\text{production}}$ is an essential difference with respect to the former model version [FED02]. Indeed, this assumption addresses some deficiencies of the first version, as will become clearer in the next sections.

Dislocation immobilisation

Dislocation loops traveling through the channels can interact with other loops gliding either on parallel slip planes or on intersecting planes. The latter interactions are not taken into account here. It has been observed in section 2.4.4.3 that the junction production rate decreases after some straining (see figure 56 b). In other words, the dislocation-dislocation interaction is assumed to be negligible with respect to the dislocation-precipitate interaction where the internal stress created by interfacial dislocations is dominant.

Nevertheless, dislocation-dislocation interaction can be phenomenologically taken into account by means of dipolar reactions. The present model considers that all mobile segments in the channels have an edge character, so the possibility of dislocation-dislocation interactions are reduced and only the immobilisation of the mobile dislocations by the formation of dislocation dipoles is taken into account (figure 87). Reactions between two dislocation loops gliding in opposite sense on adjacent parallel planes, leading to dipole formation, are assumed to take place if the distance h between these planes is smaller than a critical distance h_c (figure 87 c). An immobile dipole will be formed if the driving shear stress $\hat{\tau}_{gK} - \tau_{gK}^{\text{Orowan}}$ is counterbalanced by the maximum attraction force between two dislocations, i.e. if the distance between their glide planes is smaller than $h_c = \frac{b\, c_{44}}{4\pi\left(\hat{\tau}_{gK} - \tau_{gK}^{\text{Orowan}}\right)}$.

| (a) | (b) | (c) |
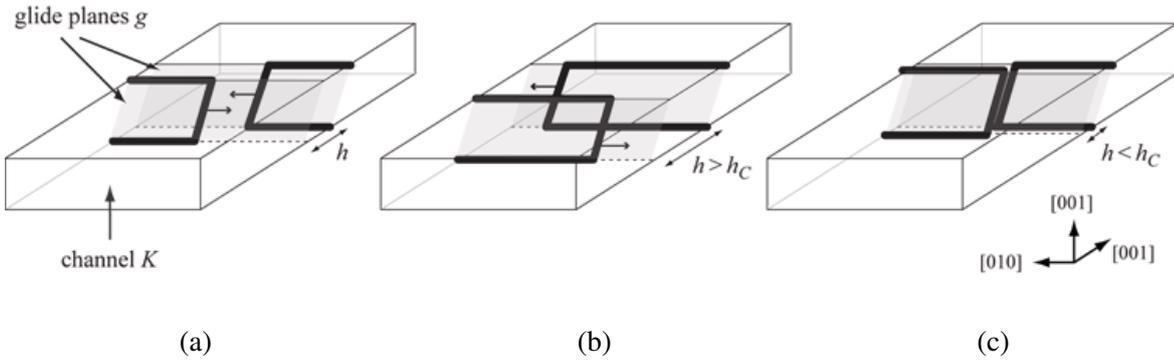
Figure 87 - (a) Illustration of two mobile dislocations within a channel K gliding on parallel slip planes. (b) These mobile dislocations do not interact of the distance h is higher than a critical value h_c (see text for an estimation of h_c), whereas (c) if the distance h is lower than h_c, the dislocations are immobilised by forming a dipole.

An estimation of the corresponding immobilisation rate has been derived in [FED02]:

$$\dot{\mathcal{N}}_{gK}^{-\text{ immobilisation}} = 2\frac{v_{gK}^{\text{glide}}\, h_c\, w\, \mathcal{N}_{gK}^2}{V_{\text{channel}}} \tag{3.86}$$

Mobile dislocation evolution

The evolution equation for the density of mobile segments resulting from addition of equations (3.83), (3.85), and (3.86) is given by

$$\dot{\mathcal{N}}_{gK} = \underbrace{\frac{1}{\sqrt{2}L}\sum_{I\neq K} v_{gI}^{\text{glide}}\mathcal{N}_{gI}}_{\sum \dot{\mathcal{N}}_{gI}^{+\text{ channel}}} + \underbrace{\frac{v_{gK}^{\text{glide}}}{L_{\text{production}}}\mathcal{N}_{gK}}_{\dot{\mathcal{N}}_{gK}^{+\text{ FR}}} - \underbrace{2\frac{v_{gK}^{\text{glide}}\, h_c\, w\, \mathcal{N}_{gK}^2}{V_{\text{channel}}}}_{\dot{\mathcal{N}}_{gK}^{-\text{ immobilisation}}} \tag{3.87}$$

The first term of the right-hand side of the equation represents the multiplication of mobile segments due to the propagation of dislocation loops in the other channels at their crossing. The second term is the production of mobile segments emitted by dislocation sources in the channel K. An important role is played by this term in the modelling of the strength of $\langle 111 \rangle$ specimens, and specially in the localisation of plastic slip in particular channels, leading to apparent slip bands on cubic planes. Finally, the third term corresponding to the dislocation-dislocation interactions in the equation is, for all orientations, always smaller than the two other contributions.

Dislocation storage at interfaces

The dislocation segments trailing those traveling through the channels are pressed against the interfaces by the local RSS. Their numbers for the system g at the interface between the channel K and the precipitate can be characterised by the scalar variable λ_{gK}, which gives the segment density in the phase boundary, measured perpendicularly, to their common line vector. The increase of the segment density resulting from the glide mechanism described in the previous sections can be calculated from equations (3.34) and (3.82):

$$\dot{\lambda}_{gK}^{+ \text{ storage}} = \sqrt{\frac{2}{3}} \frac{1}{V_{\text{channel}}} w\, \mathcal{N}_{gK}\, v_{gK}^{\text{glide}} \tag{3.88}$$

Note that $\frac{1}{\lambda_{gK}}$ is the average distance between two segments of the slip system g at the interface.

3.2.5.2   Cutting of γ' precipitates

The precipitates can be sheared by matrix dislocation pairs with overall Burgers vector $a\langle 1\bar{1}0 \rangle$ (see figure 7 b). In this case, the second dislocation is necessary to remove the APB left in the ordered γ' structure by the first dislocation (see section 2.4.2). The level of activity of each system mainly depends on the temperature and the stress.

Cutting of γ' particles is usually accomplished by dislocation segments moving through the γ channels that enter the γ' particle and pass through its whole cross-section to reach the opposite γ/γ' interfaces. Either dislocations of the opposite sign are present at the opposite side, in which case an annihilation reaction with the cutting dislocation is likely, or the cutting dislocation will cross the next channel and further shear the next precipitate. In the last case, the dislocation line length is not expected to change significantly on average. Hence, the threshold stress for cutting stems from the energy necessary to create an APB in the ordered γ' phase.

In the temperature range considered here, the glide resistance of the isolated γ' phase is much higher than that of the γ phase (see figures 8 b) [ANT94]. Accordingly, the cutting frequency f_g^{cutting} is assumed to be controlled by the average velocity of the dislocation segments in the precipitates via

$$f_g^{\text{cutting}} = \frac{v_g^{\text{cutting}}}{l_{\gamma'}} \tag{3.89}$$

where $l_{\gamma'}$ is the average size of the precipitates in octahedral planes. An estimation for this length is $l_{\gamma'} = \sqrt{\langle S_{\gamma'} \rangle}$ where $\langle S_{\gamma'} \rangle = 4\frac{c^2}{\sqrt{3}}$ is the average area of particles cut by a randomly located $\{111\}$ plane. For the average velocity of dislocation segments in the γ' phase, a relationship similar to equation (3.80) is assumed

$$v_g^{\text{cutting}} = v_0^{\text{cutting}} \sinh\left[\frac{\langle |\hat{\tau}_g^{\text{cutting}}| - \tau_g^{\text{APB}} \rangle V^{\text{cutting}}}{k_B\, T}\right] \text{sign}\left(\hat{\tau}_{gK}^{\text{cutting}}\right) \tag{3.90}$$

where $\hat{\tau}_g^{\text{cutting}}$ is the average RSS in the precipitate, v_0^{cutting} is a constant, and τ^{APB} is related to a APB-like energy E^{APB} by $\tau^{\text{APB}} = \frac{E^{\text{APB}}}{b}$ combined with the activation volume denoted V^{cutting}. As shown in [FED02], the resulting plastic shear rate has the form

$$\dot{\gamma}_{gK}^{\text{cutting}} = \frac{1}{V}\sqrt{\frac{3}{2}}\, b\, \underbrace{\frac{v_g^{\text{cutting}}}{l_{\gamma'}}}_{f_g^{\text{cutting}}} (\lambda_{g1} + \lambda_{g2} + \lambda_{g3}) \tag{3.91}$$

where $V = 8L^3$ is the volume of the computational cell.

3.2.5.3 Climb at the γ/γ' interfaces

The dislocation segments deposited at the γ/γ' interfaces can be annihilated by climbing along the interfaces and eventually by reactions with segments of opposite sign. Here again several scenarios can be considered

* As proposed by Svoboda and Lukas [SVO97], closed loops surrounding a precipitate can climb around the interface and annihilate at the apex of the precipitate.

* Long dislocation segments travel around the precipitates by combination of climb and glide until they meet a reaction partner. This deformation-recovery mechanism and its variants[10] (local climb, general climb, cooperative climb) has already been examined for particle strengthened alloys with low or medium content of the particle phase [McL85]. Mukherji and Wahi [MUK96] extended the analysis to the context of superalloys with large volume fraction of the precipitate phase.
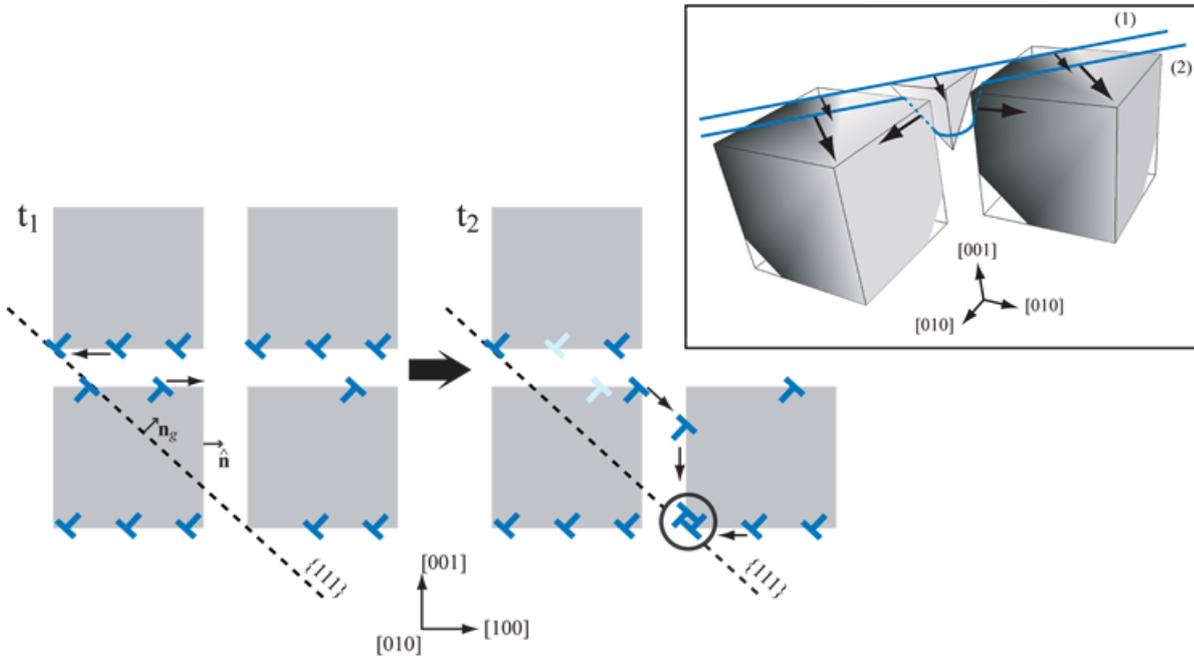
Figure 88 - Two-dimensional representation of the assumed climbing recovery. The inset shows the corresponding three-dimensional process.

The occurrence of the first mechanism requires that all channel types are plastically strained for the formation of closed loops. However, with realistic values of the Orowan stress, dislocation glide in all

---

[10]The interested reader should refer to [MUK96] for definitions of various moodes of the climb process.

channel types is impossible for sufficiently low creep stresses. For instance, equation (3.79) with $\alpha = 1$, the elastic constants of CMSX-4 at 950°C and a channel width of 67 nm, yields $\tau^{\text{Orowan}} = 248$ MPa for 60° segments, or a corresponding uniaxial theoretical tensile strength of about 620 MPa, without accounting for the effect of the misfit stresses. Indeed, this threshold is even higher in the vertical channels due to negative superposition of the misfit stresses. However, creep is already possible at 950°C for stresses around 100 MPa. As a matter of fact, under low external uniaxial tensile stresses dislocation glide is possible in the channels perpendicular to the load axis due to the positive superposition of the misfit and the external stresses in these channels.

For sustained plastic flow, recovery climb must be possible even when only one channel type is plastically deformed. Climbing of long dislocation segments originated from slip in a single channel type (second mechanism) is thus considered. The segments move around the particle by a combination of climbing and gliding until they reach annihilation partners. For simplicity, the two dimensional form of the mechanism is demonstrated in figure (88). To overcome the precipitates, the dislocations have to increase their length (see the inset in figure 88). The climb resistance $\frac{dl}{dx}$, which is defined as the increase in line length dl per glide step dx, strongly depends on the operating climb variant (local climb, general climb, cooperative climb) and is thus difficult to estimate a priori. In view of the uncertainty related to the determination of the climb resistance, the threshold resulting from the line increase $\frac{dl}{dx}$ is neglected here.

Next, the plastic strain resulting from the climb process must be estimated. At any time, parts of the dislocation will move upward or downward relative to the initial slip plane. Averaging over time and a large number of segments, it appears reasonable to assume that the out of plane (pure climb) contributions to the overall deformation compensate. This assumption considerably simplifies the estimation of the change of the internal stresses. The resulting stress state is the same as if the dislocation had sheared the precipitates in its initial plane until it reaches an annihilation partner (see the black circle in figure 88).

The preceding assumptions can be formalised as follows. Let v_{gI}^{climb} be the average out of plane component of the climb velocity of a segment initially deposited at interface I. The out of plane climb path is proportional to the height $H_{\gamma'}$ of a precipitate along the $\{111\}$ direction, with $H_{\gamma'} = 2\sqrt{3}c$. The annihilation frequency must be proportional to $f_{gI}^{\text{climb}} = \frac{4v_{gI}^{\text{climb}}}{H_{\gamma'}}$, where $\frac{H_{\gamma'}}{4}$ corresponds to the average initial distance of a segment to the apex of a precipitate. The annihilation rate of segments is then

$$\dot{\lambda}_{gI}^{-\,\text{climb}} = -\lambda_{gI}\, f_{gI}^{\text{climb}} = -4\lambda_{gI}\frac{v_{gI}^{\text{climb}}}{H_{\gamma'}} = -\frac{2}{\sqrt{3}}\lambda_{gI}\frac{v_{gI}^{\text{climb}}}{c} \tag{3.92}$$

From equations (3.34) and (3.92), the jump of the shear rate between both sides of the interface I can be deduced

$$[\![\dot{\gamma}_{gI}^{\text{climb}}]\!] = 4b\lambda_{gI}\frac{v_{gI}^{\text{climb}}}{\sin(\hat{\mathbf{n}}, \mathbf{n}^g)\ H_{\gamma'}} \tag{3.93}$$

The corresponding plastic strains are $\left(\forall\, I,\ J,\ K \in \{1,\ 2,\ 3\},\ J \neq K,\ I \neq K,\ I \neq J\right)$

$$\dot{\boldsymbol{\varepsilon}}_I^p = \mathbf{0} \tag{3.94}$$

$$\dot{\boldsymbol{\varepsilon}}_J^p = \dot{\boldsymbol{\varepsilon}}_K^p = \dot{\boldsymbol{\varepsilon}}_4^p = (\mathbf{n}^g \otimes \mathbf{m}^g)\, [\![\dot{\gamma}_{gI}^{\text{climb}}]\!] \tag{3.95}$$

and according to equation (3.61) the elastic energy is reduced by

$$\dot{\omega} = -\left(\sum_{J \neq I} f_J \hat{\boldsymbol{\sigma}}_J\right) : \langle \mathbf{m}^g \otimes \mathbf{n}^g \rangle\, [\![\dot{\gamma}_{gI}^{\text{climb}}]\!] \tag{3.96}$$

from which the thermodynamic driving force of the mechanism follows

$$\hat{\tau}_{gI}^{\text{climb}} = \left(\sum_{J \neq I} f_J \hat{\boldsymbol{\sigma}}_J \right) : \langle \mathbf{m}^g \otimes \mathbf{n}^g \rangle \tag{3.97}$$

The previous quantity is the spatial average of the RSS $\hat{\tau}_g$ in the sheared phases (the two other channels and the precipitate). Finally, a simple linear relationship for the average climb velocity is assumed:

$$v_{gI}^{\text{climb}} = D \, \hat{\tau}_{gI}^{\text{climb}} \tag{3.98}$$

3.2.6   Summary of the constitutive equations

Here the set of equations constituting the M3RSX model in terms of shear rate, mobile dislocation evolution and segment mobilities for each deformation mechanism, is summarised. The evolution of the internal variables, ε_K^p, $\dot{\rho}_{gK}$ and $\dot{\lambda}_{gK}$ depends on eight parameters listed in table (3.5). The structural tensors $\boldsymbol{\Omega}_{KL}$ depend on the elastic constants and the microstructure geometry. They relate the (microscopic) effective stress $\hat{\boldsymbol{\sigma}}_J$ for any channels J to the macroscopic stress $\boldsymbol{\Sigma}$.

Macroscopic and microscopic quantities

$$\boldsymbol{\Sigma} = \mathbf{C} : (\mathbf{E} - \mathbf{E}^p) \qquad\qquad \mathbf{E}^p = \sum_{K=1}^{4} f_K \varepsilon_K^p$$

$$\hat{\boldsymbol{\sigma}}_J = \boldsymbol{\Sigma} - \frac{1}{f_J} \sum_{K=1}^{4} \boldsymbol{\Omega}_{JK} : \varepsilon_K^p \qquad\qquad \varepsilon^p = \sum_{K=1}^{4} \varepsilon_K^p$$

Evolution equation for λ_{gK}

$$\dot{\lambda}_{gK} = \dot{\lambda}_{gK}^{+ \, \text{storage}} + \dot{\lambda}_{gK}^{- \, \text{climb}}$$

Glide in the γ channels $\big[\ K \in \{1, 2, 3\}\ \big]$

$$\dot{\varepsilon}_K^p = \frac{1}{2} \sum_{g=1}^{24} (\mathbf{n}^g \otimes \mathbf{m}^g + \mathbf{m}^g \otimes \mathbf{n}^g) \, \dot{\gamma}_{gK}^{\text{glide}}$$

$$\dot{\gamma}_{gK}^{\text{glide}} = \frac{1}{V_{\text{channel}}} \, w \, b \, \mathcal{N}_{gK} \, v_{gK}^{\text{glide}}$$

$$\dot{\mathcal{N}}_{gK} = \frac{1}{\sqrt{2}L} \sum_{I \neq K} v_{gI}^{\text{glide}} \mathcal{N}_{gI} + \frac{v_{gK}^{\text{glide}}}{L_{\text{production}}} \mathcal{N}_{gK} - 2 \frac{v_{gK}^{\text{glide}} \, h_c \, w \, \mathcal{N}_{gK}^2}{V_{\text{channel}}}$$

$$\dot{\lambda}_{gK}^{+ \, \text{storage}} = \sqrt{\frac{2}{3}} \frac{1}{V_{\text{channel}}} w \, \mathcal{N}_{gK} \, v_{gK}^{\text{glide}}$$

$$v_{gK}^{\text{glide}} = v_0^{\text{glide}} \sinh \left[\frac{\left(\hat{\tau}_{gK} - \tau_{gK}^{\text{Orowan}} \right) V^{\text{glide}}}{k_B \, T} \right]$$

$$\hat{\tau}_{gK} = \mathbf{m}^g . \hat{\boldsymbol{\sigma}}_K . \mathbf{n}^g$$

$$\tau_{gK}^{\text{Orowan}} = \alpha \frac{K_{gK} \, b}{w}$$

Cutting of the γ' precipitates $\left[\, K = 4 \, \right]$

$$\dot{\varepsilon}_4^p = \frac{1}{2} \sum_{g=1}^{24} \left(\mathbf{n}^g \otimes \mathbf{m}^g + \mathbf{m}^g \otimes \mathbf{n}^g \right) \dot{\gamma}_{g4}^{\text{cutting}} + \dot{\varepsilon}_4^{\text{misfit}}$$

$$\dot{\gamma}_{g4}^{\text{cutting}} = \frac{1}{8L^3} \sqrt{\frac{3}{2}} \, b \, \frac{v_g^{\text{cutting}}}{l_{\gamma'}} \left(\lambda_{g1} + \lambda_{g2} + \lambda_{g3} \right)$$

$$v_g^{\text{cutting}} = v_0^{\text{cutting}} \sinh \left[\frac{\langle |\hat{\tau}_g^{\text{cutting}}| - \tau_g^{\text{APB}} \rangle V^{\text{cutting}}}{k_B \, T} \right] \, \text{sign} \left(\hat{\tau}_{gK}^{\text{cutting}} \right)$$

$$\hat{\tau}_{gK}^{\text{cutting}} = \mathbf{m}^g . \hat{\boldsymbol{\sigma}}_4 . \mathbf{n}^g$$

$$\tau_g^{\text{APB}} = \frac{E^{\text{APB}}}{b}$$

Climb along the γ/γ' interfaces $\left[\, (I, J, K) \in \{1, 2, 3\}, \quad J \neq K, \quad I \neq K, \quad I \neq J \, \right]$

$$\dot{\varepsilon}_J^p = \dot{\varepsilon}_K^p = \dot{\varepsilon}_4^p = \left(\mathbf{n}^g \otimes \mathbf{m}^g \right) [\![\dot{\gamma}_{gI}^{\text{climb}}]\!] \qquad\qquad \dot{\varepsilon}_I^p = \mathbf{0}$$

$$\dot{\lambda}_{gI}^{-\,\text{climb}} = -\lambda_{gI} \, f_{gI}^{\text{climb}} = -4\lambda_{gI} \frac{v_{gI}^{\text{climb}}}{H_{\gamma'}} = -\frac{2}{\sqrt{3}} \lambda_{gI} \frac{v_{gI}^{\text{climb}}}{c}$$

$$[\![\dot{\gamma}_{gI}^{\text{climb}}]\!] = 4b\lambda_{gI} \frac{v_{gI}^{\text{climb}}}{\sin \left(\hat{\mathbf{n}}, \mathbf{n}^g \right) \, H_{\gamma'}}$$

$$v_{gI}^{\text{climb}} = D \, \hat{\tau}_{gI}^{\text{climb}}$$

$$\hat{\tau}_{gI}^{\text{climb}} = \left(\sum_{J \neq I} f_J \hat{\boldsymbol{\sigma}}_J \right) : \langle \mathbf{m}^g \otimes \mathbf{n}^g \rangle$$

Symbol	CMSX-4 at 850°C	CMSX-4 at 950°C	Unit	Reference
b	0.25	0.25	nm	
C_{11}	181823	174400	MPa	[FED02b]
C_{12}	114952	112000	MPa	[FED02b]
C_{44}	101446	97000	MPa	[FED02b]
$2c$	573	562	nm	[LIN07]
$2L$	631	631	nm	[LIN07]
δ_u	-0.00215	-0.00225	nm	[GLA94]
$\mathcal{N}_0$	0.01	0.01	-	

Table 3.4: Input material parameters for the simulations.

3.2.7 Application to the alloy CMSX-4

3.2.7.1 Experimental details

The present model was designed for single crystal superalloys in the high temperature range, essential for industrial applications in turbine components. In a collaborative work with the Bundesanstalt für Materialforschung und -prüfung (BAM), all tests reported here were performed on the alloy CMSX-4 at 850°C and 950°C, and for various specimen orientations[11]. The deviations of the specimen axes from the $\langle 001 \rangle$ crystallographic direction did not exceed 11.3° for the $\langle 001 \rangle$ oriented specimens.

Creep tests have been simulated at only 850°C, since at 950°C rafting readily occurs, a phenomenon that is not represented in the M3RSX model yet.

3.2.7.2 Input parameters

The model has been implemented as a constitutive law in the FE code ZéBuLoN. The code performs a Runge-Kutta integration scheme with automatic time stepping based on an estimate of the integration error.

Direct extensive Scanning Electron Microscope and TEM measurements of the size of the precipitates $2c$ and the channel width w have been recently performed in [LIN07]. The authors obtained $w = 58$ nm at Room Temperature (RT) and an average $2c = 573$ nm. Assuming ideal cubic precipitates and periodicity, $2L = 631$ nm and the corresponding volume fraction of the γ' phase at RT, $f_{\gamma'} = 0.75$. These values agree well with the recent measurements by Roebuck *et al.* [ROE07], $f_{\gamma'}(\text{RT}) = 0.75$ and by Serin [SER02], $w(\text{RT}) = 51$ nm.

The volume fraction of the γ' phase decreases steeply with the temperature above 850°C. The interpolating function proposed by Roebuck *et al.* [ROE07] yields $f_{\gamma'}(\text{T} = 950°\text{C}) = 0.71$. Assuming that the size of the periodic cell remains constant (no coarsening for either short term loadings at 950°C nor at 850°C), the data of corresponding size of the γ' precipitate $2c(\text{T} = 950°\text{C}) = 562$ nm and the width of the channel $w(\text{T} = 950°\text{C}) = 67$ nm are obtained.

Measurements of the unconstrained misfit were performed by Glatzel at RT, $\delta_u(\text{RT}) = -1.30\ 10^{-3}$ and at 1000°C, $\delta_u(\text{T} = 1000°\text{C}) = -2.25\ 10^{-3}$ [GLA94]. Interpolating linearly between these two values, $\delta_u(\text{T} = 850°\text{C}) = -2.15\ 10^{-3}$ and $\delta_u(\text{T} = 950°\text{C}) = -2.25\ 10^{-3}$ will be used in simulations. The elastic constants have been calculated by the resonance method [FED02b].

The table (3.4) summarises the input material parameters used for the simulations.

---

[11]Experimental results of the CMSX-4 by Alstom (Baden) and by the Institute for Materials Technology, Darmstadt University of Technology are gratefully acknowledged. The present model may be applied to similar nickel-base alloys with high volume fraction such as AM1.

Symbol	CMSX-4 at 850°C	CMSX-4 at 950°C	Unit	Used in equation
α	0.62	0.91	-	3.79
v_0^{glide}	3.75×10^{-3}	6.45	nm.s^{-1}	3.80
V^{glide}	56.64	40.17	b^3	3.80
$L_{\text{production}}$	3.47	2.23	μm	3.87
v_0^{cutting}	1.95×10^{-2}	5.13×10^{-1}	nm.s^{-1}	3.90
V^{cutting}	32.56	33.43	b^3	3.90
E^{APB}	0.024	0.016	J.m^{-2}	3.90
D	2.51×10^{-8}	1.58×10^{-5}	$\text{nm.s}^{-1}.\text{Pa}^{-1}$	3.98

Table 3.5: Fitted parameters for the alloy CMSX-4 at 850°C and 950°C.

3.2.7.3 Calibration of adjustable parameters

Table (3.5) lists the fitted parameters of the current model. The parameters have been determined by calibrating the macroscopic response of the constitutive model with tests results from $\langle 001 \rangle$ and $\langle 111 \rangle$ oriented specimens for both temperatures (850°C and 950°C). The experimental tests are listed in table (3.6). The minimisation of the objective function has been performed with the simplex algorithm [COR01]. Note that the M3RSX model has only 8 adjustable parameters for each temperature and that no cube glide systems are considered in the simulations. Most previous models [CAI87] [MER92] [NOU95] [FED02] [LEV06] [PRE08] include cubic glide systems as independent deformation mechanisms, which increases the number of adjustable parameters by a factor 2. The two simulated tests of near-[011] specimens have only been used for validation. The detailed comparisons between the model predictions and the experimental data are shown in the next section.

The pre-factor α is lower at 850°C than at 950°C. One reason of this discrepancy is due to creep tests at 850°C which were not available for 950°C. Creep tests have not been simulated at 950°C, because rafting occurs readily at this temperature [EPI08]. Indeed, creep is already possible at relatively low stresses with respect to the Orowan stress (see equation 3.79). As a matter of fact, creep is likely to occur well below this theoretical threshold stress due to the large scatter of the channel widths as well as the existence of large residual dendritic stresses [EPI05]. These effects, which probably control the magnitude of low stress creep, are not represented in the model. The value of 0.9 at 950°C is close to the value of 0.85 obtained by Busso *et al.* [BUS00] and that of 1.02 obtained by DCM calculations in section 2.4.3.3, as well as the theoretical bounds derived in section 2.4.3.4.

The respective activation volumes of the gliding and shearing processes are close for both temperatures. As expected for a thermally activated processes, the values of v_0^{glide} and D increase with temperature.

The values obtained for the glide distance $L_{\text{production}}$ between two dislocations emitted from a Frank-Read source are close at both temperatures ($\approx 3 \, \mu\text{m}$). $L_{\text{production}}$ has been considered as a fitted parameter because a reliable identification of the glide distance would require a considerable experimental effort. However, DCM analyses[12] of the possibly of super-jogs to act as a dislocation source would be useful to physically determine $L_{\text{production}}$. Here this parameter is the essential key for modelling correctly the mechanical behaviour in [111]-oriented specimens, because it imposes the value of the stress-plateau of the curves illustrated in figure (92). This point will be discussed in the next section.

The combination of the fitted value of E^{APB} and V^{cutting} determines the CRSS at which γ' precipitates are sheared. This critical stress has the same order of magnitude as values reported for superalloys in the literature (see section 3.1.3.3). This is also discussed in the next section (figure 89).

---

[12]This work is in progress.

3.2.7.4 Simulation results

Several representative simulation results with the corresponding experimental values are presented. The form of the tensile curves $\langle 001 \rangle$ orientation is characteristic for superalloys at high temperature. As shown in figures (90 a) and (91), they exhibit three stages that correspond to the elastic regime (1), the channel gliding process (2) and precipitate shearing (3). Stage (2) can be easily recognised since the deposition of dislocation segments in the precipitate interfaces is accompanied by a high level of strain hardening. The magnitude of this hardening increases with the volume fraction of the γ' phase. This has been observed in the comparison with the SC16 and the SRR99 alloys [FED02], with respective γ' content of 40% and 60%, respectively. The magnitude of hardening depends on the $\mathbf{\Omega}_{IJ}$ tensors, which contain the information about the geometry of the microstructure. The stage (3) is a roughly horizontal plateau. This steady-state stress level is essentially controlled by the APB energy E^{APB} and the activation volume V^{cutting}. The combination of both determines a CRSS at which γ' precipitates are cut. Let consider the test # 1 (of which the simulated stress-strain curve is shown in figure 91 a) and a corresponding activated glide system during the simulation (for instance, $g = A6 = (\bar{1}11)\,[0\bar{1}1]$). Figure (89) illustrates the RSS, $\hat{\tau}_{A6\ 4}$, acting on system $A6$ and the equivalent plastic strain $\varepsilon_4^{eq} = \sqrt{\frac{2}{3}\varepsilon_{ij}^p \varepsilon_{ij}^p}$ in the precipitate as function of total strain. It shows (vertical dotted line) a stress plateau at 1.6% strain, which corresponds to a saturation/limitation of the storage of dislocations at the precipitate interfaces. Indeed, at this 1.6% strain state, precipitates are plastically deformed while the ε_4^{eq} in γ' increases linearly (see figure 89). In addition, the onset of plastic strain within precipitates corresponds to a CRSS (thick horizontal line) equal to the 560 MPa. The latter stress corresponds to the classical precipitate-cutting stress expected to be of the order $\frac{\gamma^{\mathrm{APB}}}{b}$. An estimate $\gamma^{\mathrm{APB}} = 560 \times 10^6 \times 0.25 \times 10^{-9} = 140\ \mathrm{mJ.m^{-2}}$ is in good agreement with experimental values reported for superalloys in the literature (see section 2.4.2).

As schematically shown in figure (90 b), the second stage is missing in specimens strained along the $\langle 111 \rangle$ direction. The elastic regime is followed by a low hardening phase (2), often including a stress drop after an upper yield point (see, e.g. the test results reported by Bettge and Österle [BET99], or the DCM results in section 2.4.4). The absence of hardening will be discussed in the next section. Figures (92) show that the simulated results reproduce qualitatively and quantitatively well the tensile curves of the $\langle 111 \rangle$ orientation.

The comparison of simulated results and experimental data for cyclic tests is investigated for stabilised hysteresis loops for various orientations (near [001], [011], and [111]-oriented specimens). The experimental as well as the simulated hysteresis curves stabilise quickly after one or two cycles because cyclic hardening is negligible. In figures $(93 - 97)$ the presented results display the influence of strain rate, strain amplitude and orientation. Note that in contrast to the previous work [FED02], no reverse glide in the channels upon load reversal has been accounted for.
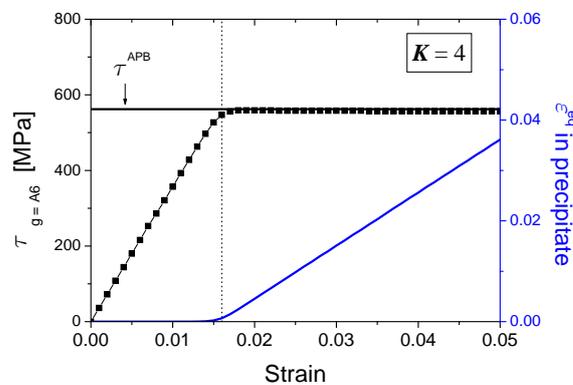
Figure 89 - Evolution of the resolved shear stress on a primary system $g = A6$ and the equivalent plastic strain in the precipitate ($K = 4$) during the test # 1.

Strain controlled multiple relaxation tests performed at 850°C for [001]- with cyclic (tensile and compressive) relaxations and [111]-oriented specimens (only tensile relaxation) have been simulated, where the constant strain rate loading at 3.10^{-5} s^{-1} was interrupted by 10h relaxation segments. The resulting stress relaxations are shown in figures $(98 - 102)$.

Finally, creep tests for different applied stress and orientations have been simulated at 850°C. Simulated creep curves are shown in figures (103) as a function of time, and for sake of comparison, as a function of log(time). Note that the current model is designed to describe the first and second creep stage and not tertiary creep.

Tensile tests				
Test #	Temperature (°C)	Crystal orientation	Strain rate (s^{-1})	Real orientation
1	850	$\langle 001 \rangle$	10^{-2}	$[0.0, 5.3, 34.0]$
2	850	$\langle 001 \rangle$	10^{-3}	$[0.0, 6.4, 16.5]$
3	850	$\langle 001 \rangle$	10^{-4}	$[0.0, 6.5, 37.6]$
4	850	$\langle 111 \rangle$	10^{-4}	$[0.0, 53.2, 42.3]$
5	950	$\langle 001 \rangle$	10^{-2}	$[0.0, 6.5, 31.2]$
6	950	$\langle 001 \rangle$	10^{-3}	$[0.0, 6.4, 16.5]$
7	950	$\langle 001 \rangle$	10^{-4}	$[0.0, 7.5, 18.5]$
8	950	$\langle 111 \rangle$	10^{-3}	$[0.0, 53.5, 42.6]$
9	950	$\langle 111 \rangle$	10^{-4}	$[0.0, 53.2, 42.3]$

Cyclic tests				
Test #	Temperature (°C)	Crystal orientation	Strain rate (s^{-1})	Real orientation
10	850	$\langle 001 \rangle$	10^{-3}	$[0.0, 6.0, 1.9]$
11	850	$\langle 011 \rangle$	10^{-3}	$[0.0, 44.2, 4.2]$
12	850	$\langle 111 \rangle$	3.10^{-5}	$[0.0, 50.4, 41.8]$
13	850	$\langle 111 \rangle$	10^{-3}	$[0.0, 52.2, 43.0]$
14	950	$\langle 001 \rangle$	10^{-4}	$[0.0, 10.5, -12.9]$
15	950	$\langle 001 \rangle$	10^{-4}	$[0.0, 8.3, -2.3]$
16	950	$\langle 001 \rangle$	3.10^{-5}	$[0.0, 7.0, -16.0]$
17	950	$\langle 001 \rangle$	10^{-3}	$[0.0, 6.7, -23.0]$
18	950	$\langle 111 \rangle$	10^{-3}	$[0.0, 44.6, -41.9]$
19	950	$\langle 111 \rangle$	10^{-3}	$[0.0, 50.6, -42.9]$
20	950	$\langle 111 \rangle$	3.10^{-5}	$[0.0, 47.0, -40.4]$

Relaxation tests				
Test #	Temperature (°C)	Crystal orientation	Strain rate (s^{-1})	Real orientation
21	850	$\langle 001 \rangle$	3.10^{-5}	$[0.0, 7.5, 21.2]$
22	850	$\langle 111 \rangle$	3.10^{-5}	$[0.0, 50.5, 37.2]$
23	950	$\langle 001 \rangle$	3.10^{-5}	$[0.0, 7.5, 17.7]$
24	950	$\langle 001 \rangle$	10^{-3}	$[0.0, 4.1, 0.0]$
25	950	$\langle 011 \rangle$	10^{-3}	$[0.0, 0.8, -42.5]$

Creep tests				
Test #	Temperature (°C)	Crystal orientation	Stress (MPa)	Real orientation
26	850	$\langle 001 \rangle$	580	$[0.0, 3.8, 12.8]$
27	850	$\langle 001 \rangle$	520	$[0.0, 0.4, 5.1]$
28	850	$\langle 001 \rangle$	470	$[0.0, 7.1, 25.1]$
29	850	$\langle 001 \rangle$	450	$[0.0, 10.7, 5.4]$
30	850	$\langle 001 \rangle$	401	$[0.0, 8.2, 2.8]$
31	850	$\langle 111 \rangle$	450	$[0.0, 53.2, 43.0]$
32	850	$\langle 111 \rangle$	400	$[0.0, 47.7, 43.8]$

Table 3.6: List of experimental tests and characterisations.

Tensile tests

(a)   (b)
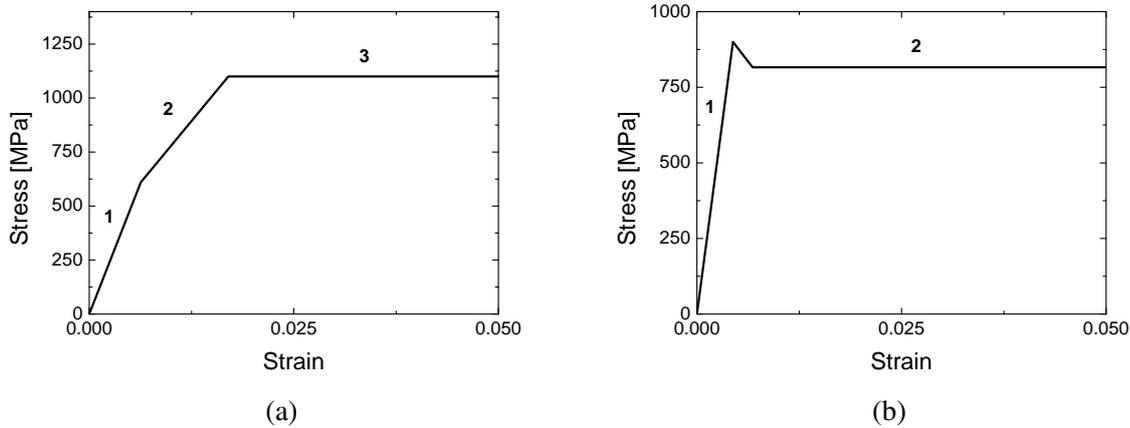
Figure 90 - Sketch of the typical stress-strain responses of a single crystal superalloy at high temperature, (a) near $\langle 001 \rangle$-oriented specimens showing three stages: the elastic regime (1), the channel gliding process (2), and precipitate shearing (3), and (b) near $\langle 111 \rangle$-oriented specimens showing two stages: the elastic regime (1), and a low hardening phase (2).

(a)   (b)
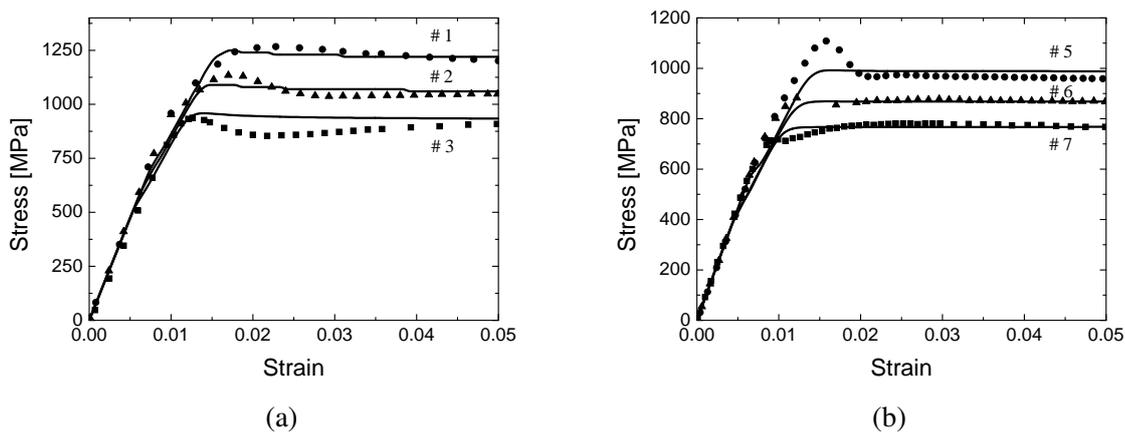
Figure 91 - Monotonic stress-strain responses: comparison of experimental data (symbols) and simulations (solid lines) near [001] orientations at (a) 850°C (tests # 1, # 2, and # 3), and at (b) 950°C (tests # 5, # 6, and # 7).

(a)   (b)
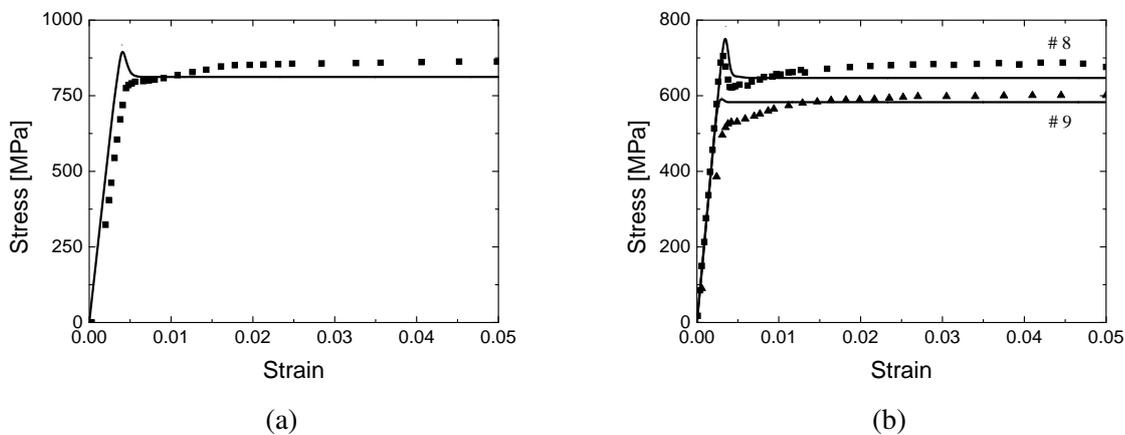
Figure 92 - Monotonic stress-strain responses: comparison of experimental data (symbols) and simulations (solid lines) near [111] orientations at (a) 850°C (test # 4), and at (b) 950°C (tests # 8, and # 9).

Cyclic tests

(a)   (b)
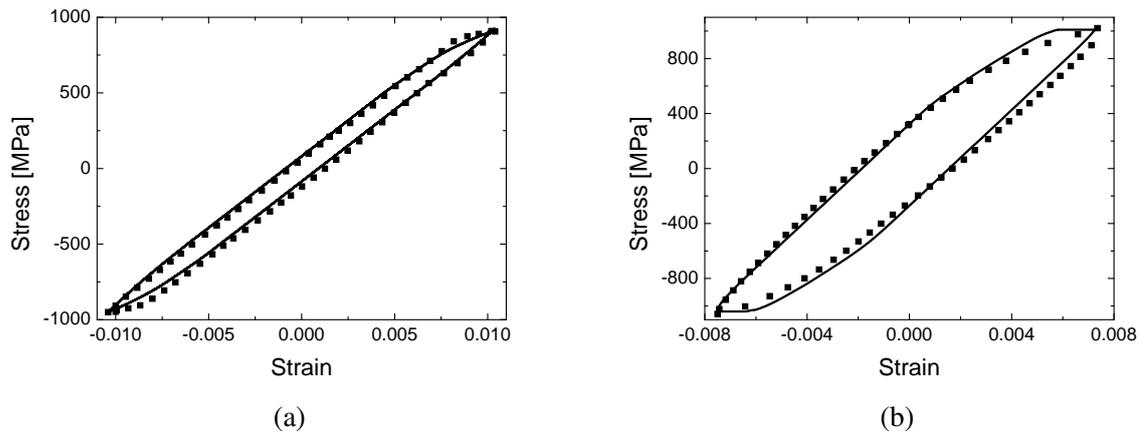
Figure 93 - Stress-strain responses of the stabilised hysteresis loop: comparison of experimental data (symbols) and simulations (solid lines) at 850°C near (a) [001]- (test # 10), and (b) [011]-oriented specimens (test # 11).

(a)   (b)
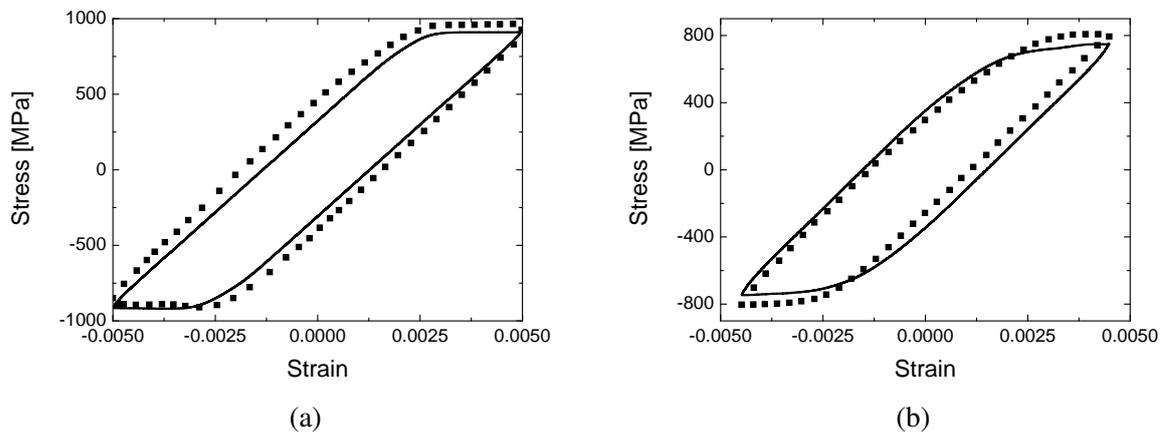
Figure 94 - Stress-strain responses of the stabilised hysteresis loop: comparison of experimental data (symbols) and simulations (solid lines) at 850°C for two near [111]-oriented specimens: (a) test # 12, and (b) test # 13.

(a)   (b)
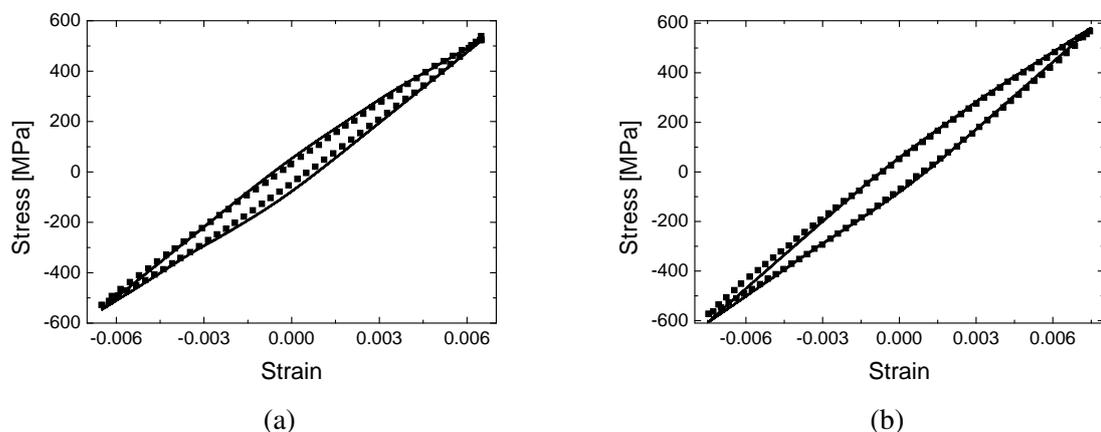
Figure 95 - Stress-strain responses of the stabilised hysteresis loop: comparison of experimental data (symbols) and simulations (solid lines) at 950°C for two near [001]-oriented specimens: (a) test # 14, and (b) test # 15.
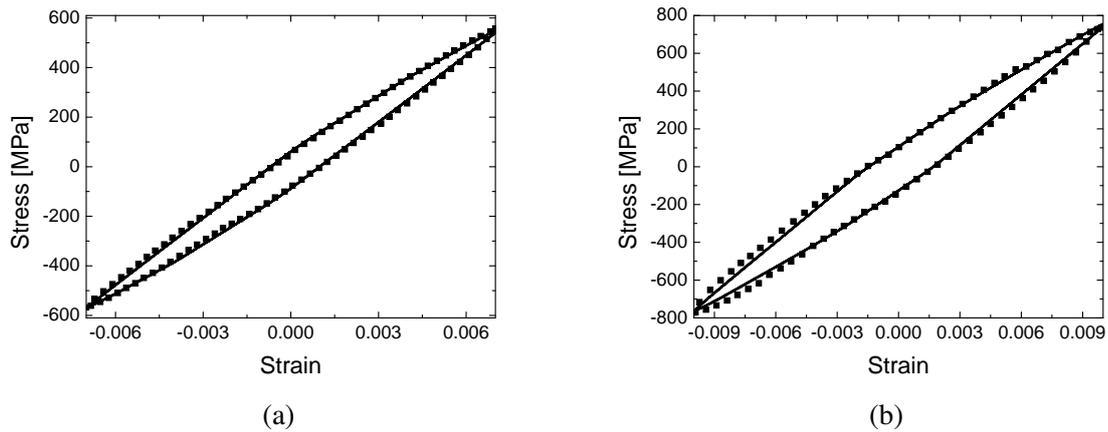
Figure 96 - Stress-strain responses of the stabilised hysteresis loop: comparison of experimental data (symbols) and simulations (solid lines) at 950°C for two near [001]-oriented specimens: (a) test # 16, and (b) test # 17.
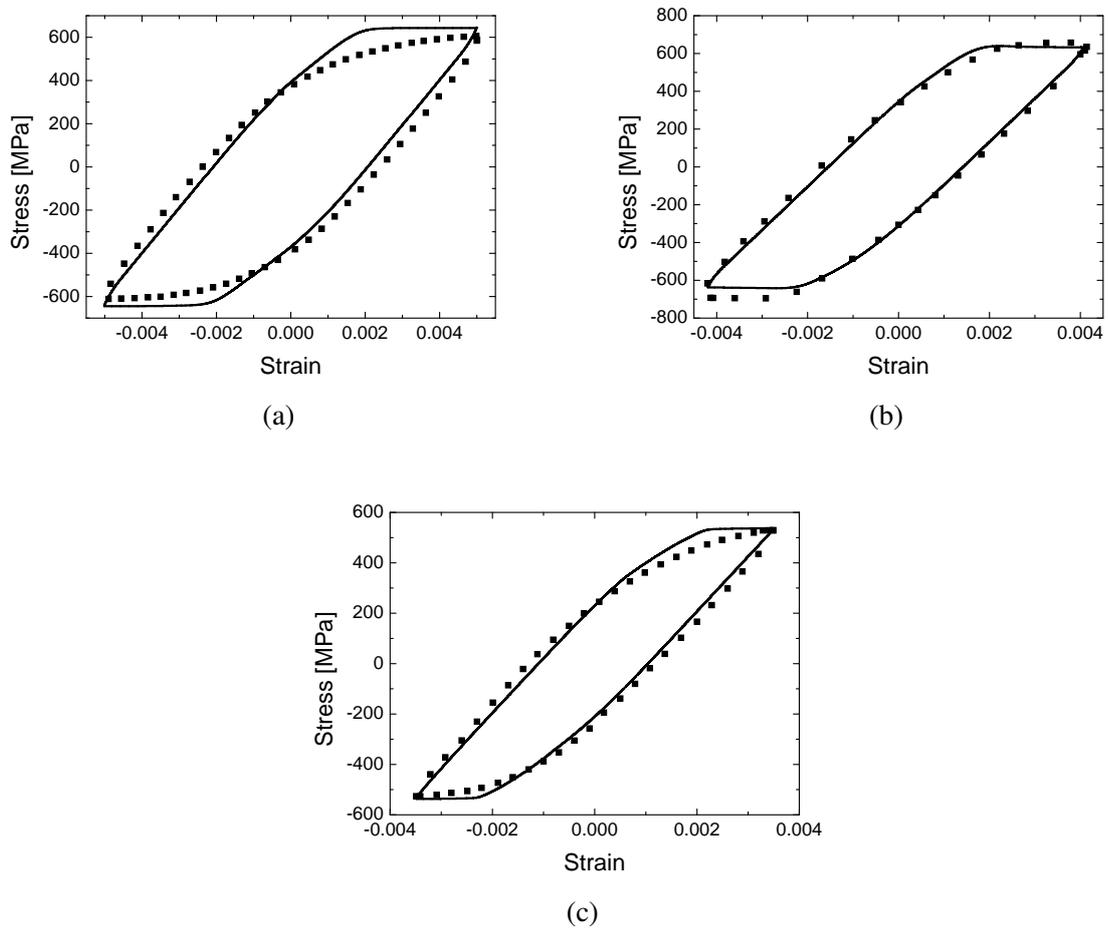
Figure 97 - Stress-strain responses of the stabilised hysteresis loop: comparison of experimental data (symbols) and simulations (solid lines) at 950°C for three near [111]-oriented specimens: (a) test # 18, (b) test # 19, and (c) test # 20.

Stress relaxation tests

(a)
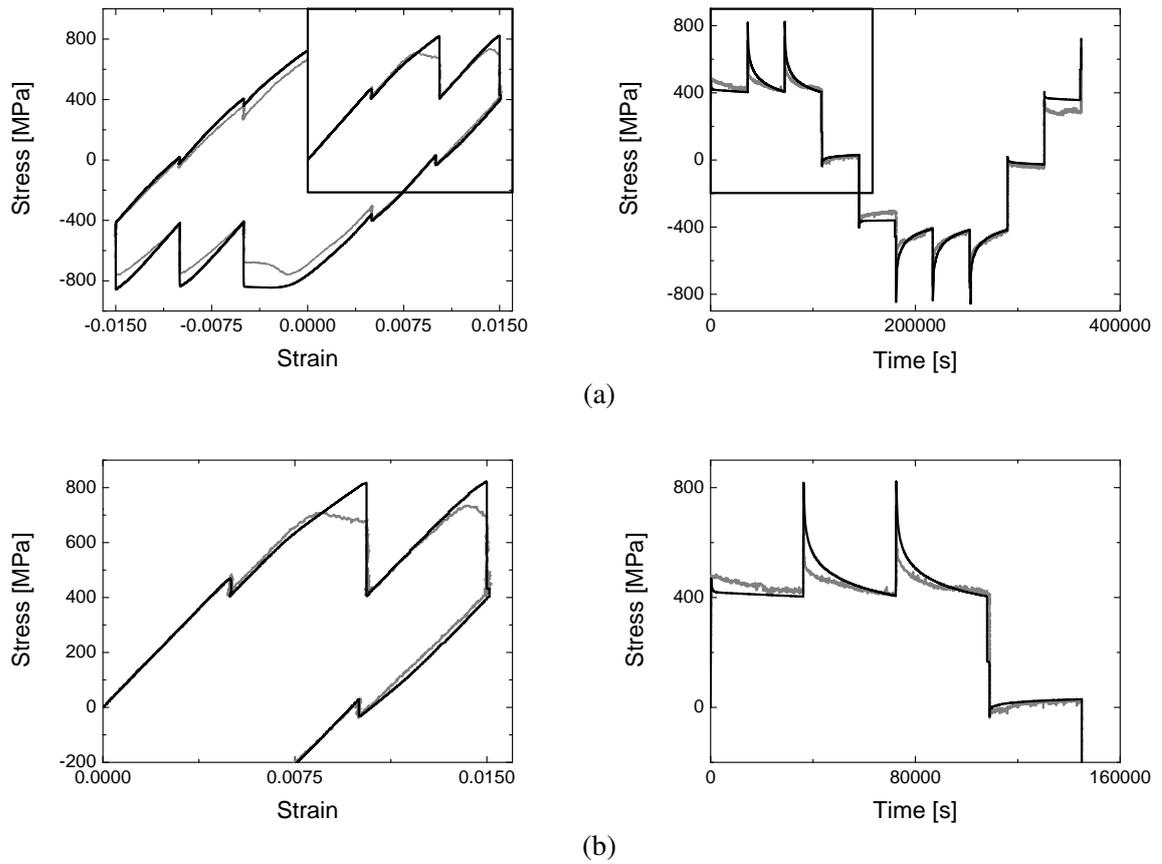
Figure 98 - Relaxation behaviour as a function of strain and time: comparison of experimental data (grey lines) and simulations (black lines) at 850°C for a (a) near [001]-oriented specimen (test # 21), and (b) is the enlarged area of (a).
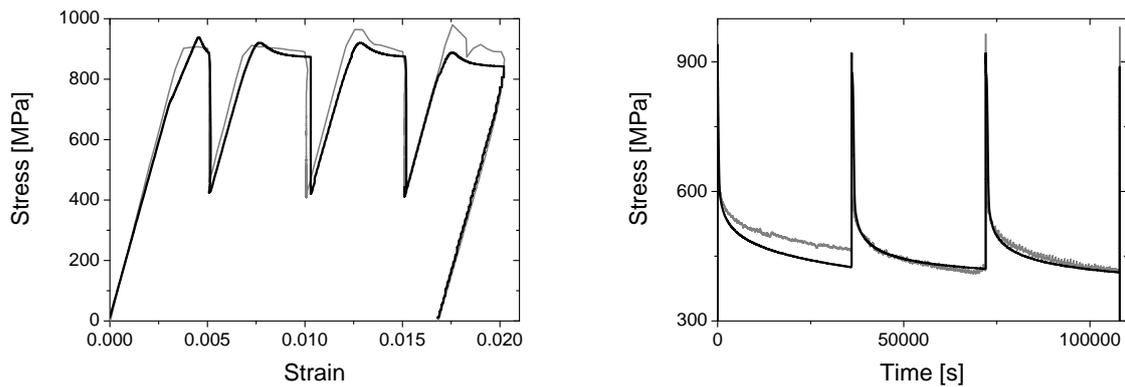
Figure 99 - Relaxation behaviour as a function of strain and time: comparison of experimental data (grey lines) and simulations (black lines) at 850°C for a near [111]-oriented specimen (test # 22).
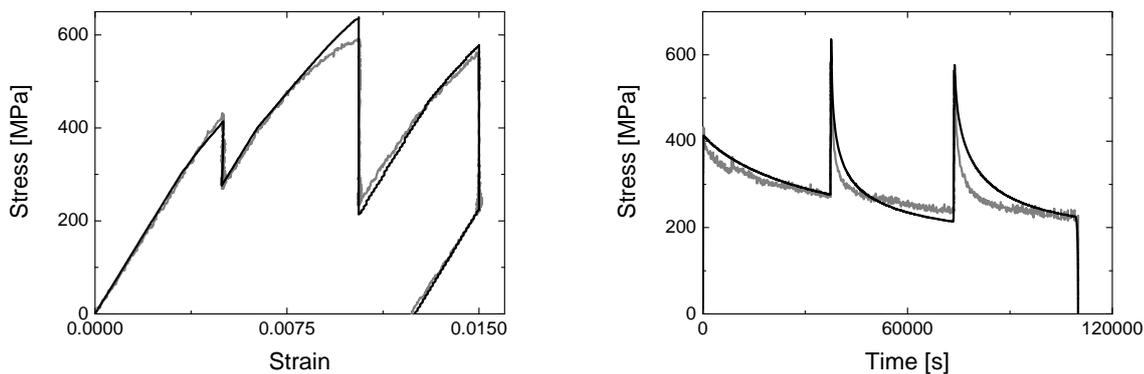
Figure 100 - Relaxation behaviour as a function of strain and time: comparison of experimental data (grey lines) and simulations (black lines) at 950°C for a near [001]-oriented specimen (test # 23).
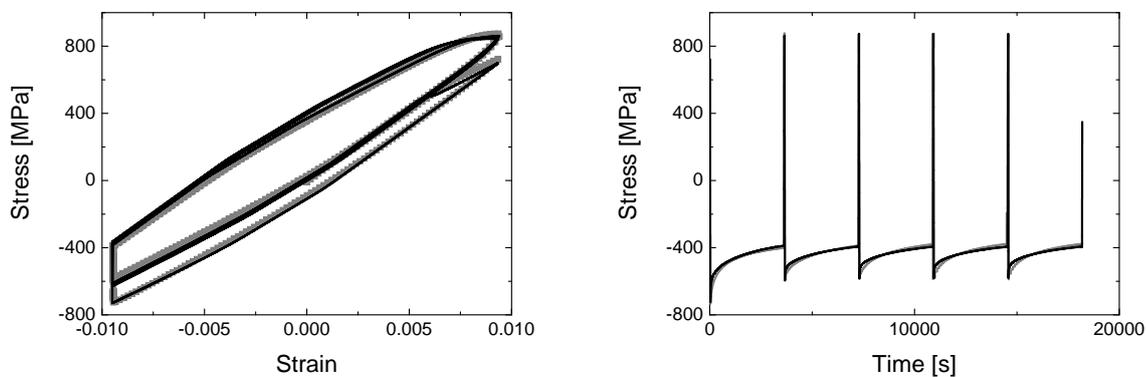
Figure 101 - Relaxation behaviour as a function of strain and time: comparison of experimental data (grey lines) and simulations (black lines) at 950°C for a near [001]-oriented specimen (test # 24).
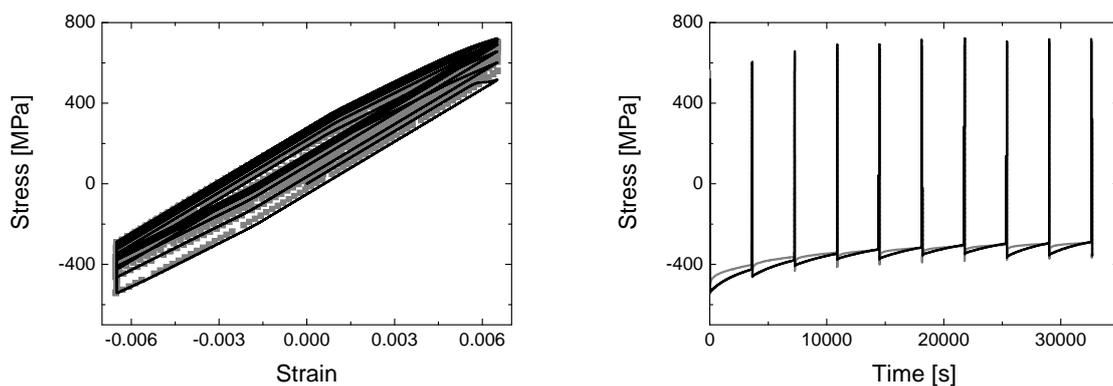
Figure 102 - Relaxation behaviour as a function of strain and time: comparison of experimental data (grey lines) and simulations (black lines) at 950°C for a near [011]-oriented specimen (test # 25).

Creep tests
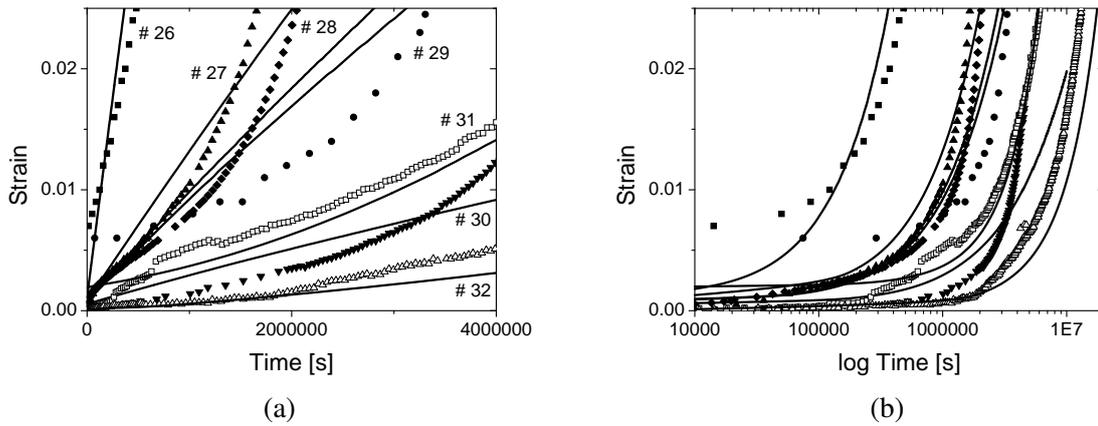
Figure 103 - Creep strain behaviour for different stress levels at 850°C: comparison of the experimental data (solid lines) and the simulations (symbols) near [001]- (full symbols: tests # 26 − # 30) and [111]-oriented specimens (filled symbols: test # 31 and # 32) as function of (a) time and (b) $\log$(time).

3.2.8 Discussion

3.2.8.1 Influence of the distribution of (geometrically necessary) dislocations

The choice of the decomposition of the matrix into 3 channels has been discussed in section 3.2.4.3 (see figure 84) and its implications are now presented. The Appendix D.2 gives the components of the influence tensors Ω_{KL} for both decomposition types. The difference is roughly an order of magnitude in the leading components. The consequences of these differences on the $\langle 111 \rangle$ tensile behaviour are observed in figure (104). In these simulations (simulated test # 4), only the channel decomposition differs while the remaining model parameters are identical. Clearly, the WSE decomposition (grey curve in figure 104) overestimates the strain hardening while the P decomposition (black curve in figure 104) exhibits no hardening, in qualitative agreement with the experiments and the results from the DCM simualtions. The absence of hardening of the black curve in figure (104) is due to two equally activated slip sys-
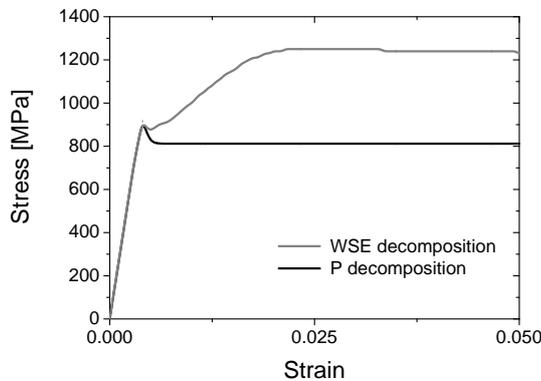
Figure 104 - Influence of the matrix decomposition on the tensile behaviour of $\langle 111 \rangle$-oriented specimens: the grey line represents the behaviour of the WSE decomposition and the black line that of the P decomposition (see figure 84 for a geometrical illustration of these decompositions).

tems, such that the superposition of the internal stresses of their interfacial dislocations vanishes, as will be shown later. This phenomenon is consistent with the DCM results discussed in section 2.4.4.4. In contrast, the WSE decomposition is accompanied by the accumulation of geometrically necessary dislocations at the channel inner-boundaries, which have no physical counterpart. The long-range internal stresses generated by these dislocation densities do not vanish for the same slip system combination. As a result, strain hardening is overestimated. It must be noted that the previous version of the model had to resort to cubic slip to remedy this excess of hardening.

Therefore, both the DCM results and the improved estimation of the internal stresses presented here question the significance of cubic slip as an effective deformation mechanism.

3.2.8.2   Evidence of the mechanism of pseudo-cubic slip

In this section, the key effects responsible for the absence of hardening in $\langle 111 \rangle$ tensile specimens (in particular, the test # 4) are summarised. At the start of the simulation, the number of dislocation segments of mixed and screw character are the same and the density λ at the γ/γ' interfaces equal zero. The stress state at that moment is given by the superposition of the applied stress and the coherency stress which is determined by the misfit parameter δ. At any time $t > 0$ the stress state is given by the applied stress, misfit parameter and the long-range stresses due to densities on the γ/γ' interfaces.

Selection of slip systems in $\langle 111 \rangle$ specimens

According to classical crystal plasticity, the six slip systems $A6$, $D6$, $A3$, $C3$, $C1$ and $D1$ (see table 3.3), are equally and maximally stressed in a homogeneous crystals under uniaxial tension along the $\langle 111 \rangle$, as in test # 4. Due to the superposition of the misfit, the external stresses and the dependence of the Orowan threshold on the orientation of the trailed dislocation segments, this model does not apply to superalloys. To facilitate the discussion, the effective RSS, i.e. $\hat{\tau}_{gK}$, the Orowan stresses τ^{Orowan}, and the driving forces $\hat{\tau}_{gK} - \tau^{\mathrm{Orowan}}$ are presented in table (3.7) for the six candidate slip systems in the three channel types during tensile test # 4, at a stress level $\Sigma = 780$ MPa before yielding.

Inspection of table (3.7) shows that in each channel only two systems will be activated at the onset of yielding (blue values in the table). These systems are those with the lowest Orowan threshold, i.e. for which screw segments are deposited at the interfaces. Finally, note that the two selected systems are conjugate with the same Burgers vector but opposite line vectors. These results are in accordance with the DCM analysis on the origin of the pseudo-cubic slip at the dislocation scale, as discussed in section 2.4.4.3.

Strain hardening in $\langle 111 \rangle$ specimens

Considering for instance the case of channel $K = 2$, table (3.7) shows that the first activated slip systems are $A3$ and $C3$ (because of their corresponding lowest Orowan threshold) which consequently induce equal stresses in channel $K = 2$. Thus $\gamma^{\mathrm{glide}}_{A3,\,2} = \gamma^{\mathrm{glide}}_{C3,\,2} = \gamma^{\mathrm{glide}}_2$, and the resulting plastic rate (equation 3.31) is written in the form:

$$\dot{\varepsilon}^p_2 = \frac{1}{2}\Big[\left(\mathbf{n}^{A3} \otimes \mathbf{m}^{A3} + \mathbf{m}^{A3} \otimes \mathbf{n}^{A3} \right)\ \dot{\gamma}^{\mathrm{glide}}_{A3,\,2} + \left(\mathbf{n}^{C3} \otimes \mathbf{m}^{C3} + \mathbf{m}^{C3} \otimes \mathbf{n}^{C3} \right)\ \dot{\gamma}^{\mathrm{glide}}_{C3,\,2} \Big] \tag{3.99}$$

$$\dot{\varepsilon}^p_2 = \frac{1}{2}\Big[\left(\mathbf{n}^{A3} \otimes \mathbf{m}^{A3} + \mathbf{m}^{A3} \otimes \mathbf{n}^{A3} \right) + \left(\mathbf{n}^{C3} \otimes \mathbf{m}^{C3} + \mathbf{m}^{C3} \otimes \mathbf{n}^{C3} \right) \Big] \dot{\gamma}^{\mathrm{glide}}_2 \tag{3.100}$$

The latter quantity is proportional to what would be produced by a cubic system on the plane $\mathbf{e}_2 = (0\bar{1}0)$ in the direction $\mathbf{m} = [10\bar{1}]$, i.e. $\dot{\varepsilon}^p_2 \propto (\mathbf{e}_2 \otimes \mathbf{m} + \mathbf{m} \otimes \mathbf{e}_2)$.

As demonstrated in the Appendix (D.3), the internal stresses generated by the plastic strain in equation (3.99) in a parallelepiped channel with faces normal to $(\mathbf{e}_2 \otimes \mathbf{m})$ vanish, i.e. $\mathbf{\Omega}_{J2} : (\mathbf{e}_2 \otimes \mathbf{m} + \mathbf{m} \otimes \mathbf{e}_2) =$

Slip system g	$A6:$ $(\bar{1}11)\langle 110\rangle$			$D6:$ $(1\bar{1}1)\langle 110\rangle$		
Channel type K	1	2	3	1	2	3
Trailed segment	M	M	S	M	M	S
τ^{Orowan} (MPa)	180.	180.	122.	180.	180.	122.
$\hat{\tau}_{gK}$ (MPa)	149.	230.	228.	241.	107.	228.
$\hat{\tau}_{gK} - \tau^{\mathrm{Orowan}}$ (MPa)	-31.	50.	**106.**	61.	-73.	**106.**

Slip system g	$A3:$ $(\bar{1}11)\langle 101\rangle$			$C3:$ $(11\bar{1})\langle 101\rangle$		
Channel type K	1	2	3	1	2	3
Trailed segment	M	S	M	M	S	M
τ^{Orowan} (MPa)	180.	122.	180.	180.	122.	180.
$\hat{\tau}_{gK}$ (MPa)	139.	227.	229.	248.	227.	101.
$\hat{\tau}_{gK} - \tau^{\mathrm{Orowan}}$ (MPa)	-41.	**105.**	49.	68.	**105.**	-79.

Slip system g	$C1:$ $(11\bar{1})\langle 011\rangle$			$D1:$ $(1\bar{1}1)\langle 011\rangle$		
Channel type K	1	2	3	1	2	3
Trailed segment	S	M	M	S	M	M
τ^{Orowan} (MPa)	122.	180.	180.	122.	180.	180.
$\hat{\tau}_{gK}$ (MPa)	224.	218.	91.	219.	95.	218.
$\hat{\tau}_{gK} - \tau^{\mathrm{Orowan}}$ (MPa)	**102.**	38.	-89.	**97.**	-85.	38.

Table 3.7: Driving force for dislocation glide for the six candidate slip systems g in the three channel types K during a monotonic tensile test of a [111]-oriented specimen.

0 for any J. Consequently, the corresponding contribution to the strain hardening rate (see equation 3.71)

$$\dot{\mathbf{X}}_J = \frac{1}{f_J}\boldsymbol{\Omega}_{J2} : \dot{\boldsymbol{\varepsilon}}_2^p = \mathbf{0} \tag{3.101}$$

also vanishes. Expression (3.101) means that the relative contributions to kinematical hardening associated to the combination of $A3$ and $C3$ in $K = 2$ compensate. Consequently, the strength (i.e. the estimation of kinematical hardening rate through expression 3.101) of $\langle 111\rangle$ specimens remains extremely low, while it remains high for $\langle 001\rangle$ specimens with $\dot{\mathbf{X}}_J \neq 0$.

Dislocation sources

At the microscopic scale, the role played by the dislocation sources in each channel, is an essential condition for the absence of work hardening in $\langle 111\rangle$ specimens at the macroscopic scale. This can indefinitely sustain plastic flow in accordance with equation (3.85). Without these sources, the dislocation multiplication mechanism expressed by equation (3.83) requires, when operating alone, the other channels to be plastically deformed, which in turn would give rise to dislocation induced internal stresses and thus work hardening.

For the $\langle 111\rangle$ orientation, dislocation sources allow removing the cubic slip systems from the model, and plastic slip tends to localise in a channel by two octahedral slip systems (e.g. one primary system and its collinear slip system), leading to apparent slip bands on cubic planes.

3.2.9 Application to the engineering problems

3.2.9.1 Validation on standard dog-bone specimen at 850°C

The first structural calculation is the tensile dog-bone test. Figure (105 a) presents the mesh geometry including 1696 prismatic FE. The dimensions of the dog-bone gauge section are confined to 60 mm (long), 21.5 (wide) and 0.15 (thick). Uniaxial tensile deformation with a $\langle 001 \rangle$-orientation is performed on the specimen at an imposed strain rate of $\dot{E}_{33} = 10^{-3}$ s^{-1}, for the single crystal superalloy CMSX-4 at 850°C. The corresponding material parameters are those of table (3.5).
Figure (105 b) and (105 c) shows the deformation E^{33} and the stress Σ^{33}, respectively. The predicted stress-strain response may be analysed by either the response given at one IP inside the homogeneous zone or by the averaged quantities of the gauge section. The comparison between both calculations is given in figure (106). It shows that the stress-strain curves are identical, and also illustrates the capability of the M3RSX model in reproducing the behaviour in experiment-like conditions obtained in laboratory.

(a)　　　　　　　　　(b)　　　　　　　　　(c)
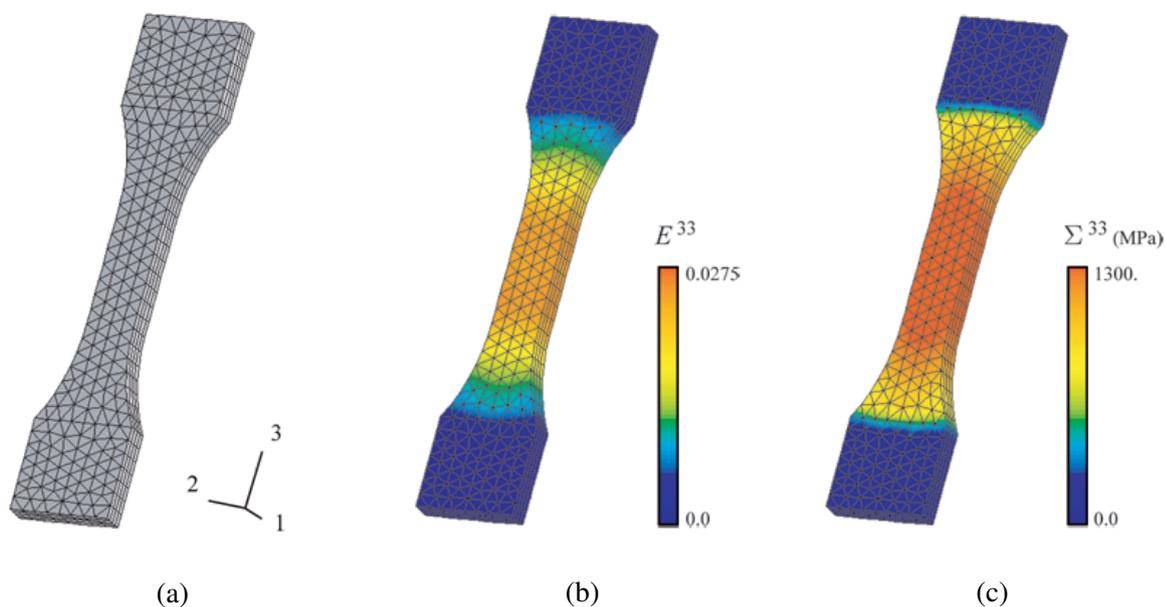
Figure 105 - (a) Finite element mesh of the specimen (1696 prismatic finite elements). (b) Strain contours E^{33} and (c) stress state Σ^{33} computed in tensile loading, along the specimen axis.

3.2.9.2 Torsion of single crystal tubes at 950°C

This example investigates the macroscopic behaviour of a single crystal superalloys under torsion loading. From an experimental point of view, after torsion tests performed on thin-walled specimen oriented along $\langle 001 \rangle$ on the CMSX-4 single crystal superalloy at 950°C, cube slip traces were observed in four zones along the circumference, near the $\langle 110 \rangle$ secondary orientations [POL90] [NOU96] [BON06]. This was a first experimental indication of a strain heterogeneity, alternating "soft zones" (type $\langle 110 \rangle$ secondary orientations) and "hard zones" (type $\langle 100 \rangle$ secondary orientations).
In FE analysis their presence is usually due to the cube slip systems which are activated in the soft zones. This case illustrates the important structural effects of the activation of cube slip systems for the constitutive laws. The aim of this example is to reproduce this strain heterogeneity with the M3RSX model without the physically unjustified cube slip systems.
As shown in figure (107 a) a 3D mesh with 4032 nodes and with $2 \times 2 \times 2$ integration points for each element is used for modelling the specimen. The lower end of the mesh is clamped, and the torsion loading
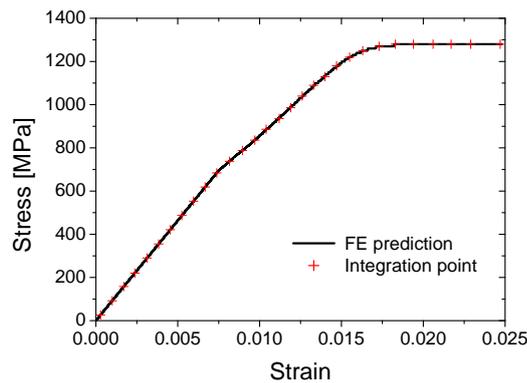
Figure 106 - Comparison of macroscopic stress-strain response at one integration point and the FE prediction averaged on the gauge section.

is applied at the other end.

Figure (107 b) shows the equivalent plastic strain E_{eq}^p at the maximum of the cycle at the surface of the specimen. In accordance with experimental investigations [POL90] [NOU96], the localisation of plastic deformation is well reproduced and very pronounced, since the minimum value in the central section is 2.1×10^{-5}, and the maximum value 0.9×10^{-1}. The M3RSX model allows to reproduce this strain heterogeneity at 950°C, even through no cubic slip systems are activated. In addition, the stress distribution is illustrated in figure (107 c) by means of equivalent stress Σ_{eq}. The zone involving the maximum stress is located in the $\langle 100 \rangle$ secondary orientations while the $\langle 110 \rangle$ zone exhibits a minimum stress, according to experimental data.
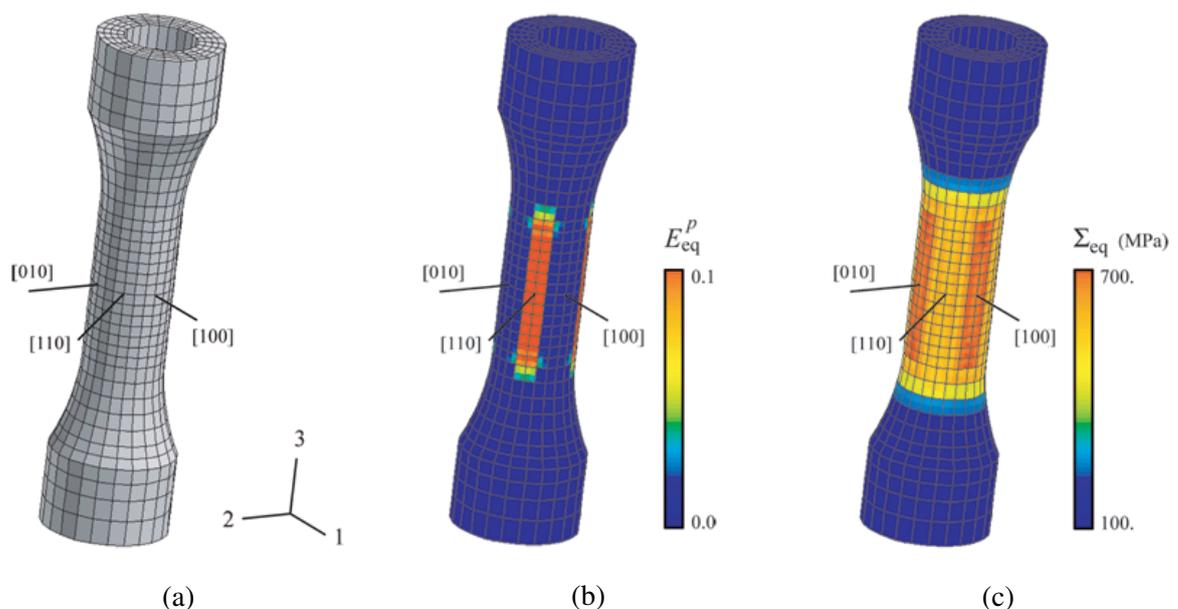
Figure 107 - (a) Finite element mesh of the specimen. (b) Equivalent plastic strain E_{eq}^p and (c) equivalent stress state Σ_{eq} computed in pure torsion loading, along the specimen axis.

Résumé

Les possibilités de la simulation numérique par EF pour évaluer des champs de déplacement ou de contraintes à différentes échelles sont nombreuses: le cas du volume élémentaire représentatif dans lequel le maillage par éléments finis prend explicitement en compte la microstructure, ou le cas d'une éprouvette monocristalline pour laquelle l'échelle macroscopique constitue le niveau pertinent pour décrire les mécanismes de déformation, en sont deux exemples classiques.

Le premier modèle développé dans cette partie se justifie par un arrangement hétérogène de dislocations à l'échelle de la microstructure mettant en évidence aux interfaces du précipité, des régions riches et pauvres en dislocations. Il a pour principal objectif de prédire les phénomènes physiques simulés par le MDC et ainsi, établir un éventuel lien entre les théories discrètes et continues de la plasticité. Au niveau continu, ce lien est fondé sur une prise en compte des densités de dislocation (statistique et géométrique). Concernant le superalliage monocristallin, le gradient de déformation plastique permet de localiser ces densités de dislocations géométriquement nécessaires (ou GND) aux interfaces. La contribution de la variable interne essentielle associée aux GND est incorporée dans l'écrouissage isotrope. Même fruste, cette nouvelle loi fait intervenir un paramètre clé facilement identifiable auprès des réponses macroscopiques acquises par le MDC et permet alors idéalement de prédire le comportement mécanique aux plus grandes déformations que celles obtenues par les simulations discrètes. Néanmoins, l'accord qualitatif et quantitatif du modèle avec les résultats du MDC sur le profil de densité de dislocation dans les couloirs reste très insuffisant. Plusieurs arguments peuvent être avancés. Un premier, d'ordre numérique, est la densité de maillage utilisée pour les calculs avec le modèle continu qui peut être trop grossière. Un second, physique, réside sur la faiblesse inhérente à "l'opérateur mathématique gradient" à traiter un problème tel que l'interaction dislocation-précipité dans les superalliages. En effet, contrairement au cas du polycristal où les dislocations sont accumulées aux joints de grains sous la forme d'empilements de dislocations, le MDC, appliqué au superalliage monocristallin, montre que l'écrouissage est intimement contrôlé par un tapissage de longs segments de dislocation aux interfaces. Ces segments s'accumulent lorsqu'une dislocation se déplace dans les couloirs de matrice et ce, sans former d'empilement de dislocations qui impliquerait une réduction du libre parcours des dislocations dans les couloirs de matrice. Dans ce sens, une approche micromécanique complémentaire développée dans un second volet s'est avérée être un tremplin naturel en vue de calcul de structures.

Ce second modèle, initialement développé par Fedelich, a été mise en oeuvre dans le cadre d'une collaboration menée avec le Bundesanstalt für Materialforschung und -prüfung (BAM, Berlin). La méthode considérée est de type micromécanique pour laquelle la réponse globale du matériau est obtenue en appliquant une technique d'homogénéisation aux réponses des constituants élémentaires. La structure hétérogène élastoviscoplastique de chacune des phases ainsi que leurs morphologies sont explicitement mises en évidence dans le modèle. Un des objectifs de la thèse a donc été de justifier physiquement le nouveau modèle appelé M3RSX. Cette justification est intimement basée sur une prise en considération des résultats issus du MDC concernant l'analyse effectuée sur les microstructures de dislocation formées et de leurs conséquences sur le comportement en traction suivant l'orientation $\langle 111 \rangle$. En effet, à travers l'identification des mécanismes de déformation et la formulation à l'écrouissage anisotrope prenant en compte la déformation plastique (uniforme) dans chaque couloir, l'expression de la contrainte locale a été déterminée en fonction de la polarisation des dislocations accumulées pendant la déformation. Les modifications apportées au modèle initial ont principalement porté sur deux points précédemment traités à l'échelle du MDC: (i) il met en évidence la localisation de la déformation plastique dans un couloir de matrice, dont (ii) les deux systèmes octaédriques actifs n'engendrent peu de contraintes internes. Le point (ii) est intrinsèquement à relier aux formes des sous-domaines considérés dans l'approche micromécanique. Justifiés par les simulations du MDC, les formes parallélépipédiques de ces sous-domaines constituent le point fort permettant de rendre compte de l'adoucissement observé en $\langle 111 \rangle$. Le modèle a ainsi été identifié à hautes températures pour le superalliage CMSX-4 sans la prise en compte de systèmes cubiques. Testé sur une large gamme d'essais sous diverses sollicitations, le modèle a ensuite été appliqué au calcul d'une éprouvette en torsion. Les résultats obtenus sont conformes à l'expérience.

Conclusion et perspectives

Une étude multi-échelles du comportement mécanique des superalliages monocristallins est présentée. Celle-ci met en jeu des simulations discrètes de la plasticité avec la méthode de la Dynamique des Dislocations (DD) et des modèles de la plasticité cristalline issues de la mécanique des milieux continus. Une caractéristique commune de ces modèles utilisés est de pouvoir prendre en considération une distribution de dislocations spatialement hétérogène dans le matériau. Les principaux objectifs de la thèse porte sur l'étude de (i) la formation des microstructures de dislocation dans les couloirs de matrice du superalliage, (ii) la nature des interactions dislocation−precipité, et (iii) l'influence des dislocations déposées aux interfaces sur les propriétés mécanique du matériau. La démarche adoptée s'appuie sur deux transitions d'échelles: une transition "discrète − continue" et "micro − macro". La première établit un lien entre les simulations de DD et des modèles continus à longueur interne. La seconde remonte aux échelles supérieures les informations pertinentes mises en évidence aux échelles fines. Dans ce contexte, les travaux rapportés dans ce mémoire montrent qu'il est possible d'alimenter et de justifier physiquement les fondements d'un modèle micromécanique à partir d'informations recueillies aux échelles des dislocations.

Les différents modèles mis en jeu dans cette étude ont fait l'objet d'une discussion dont les points essentiels sont maintenant résumés.

Le Modèle Discret-Continu (MDC) présente une simulation combinant à la fois une approche physique et mécanique de la plasticité. En effet, il permet de simuler l'évolution microstructurale de dislocation par une simulation de DD tout en satisfaisant aux équations d'équilibre en volume et en surface résolues par la méthode des Eléments Finis (EF). L'idée originale de cette simulation hybride est de substituer la loi de comportement conventionnelle d'un calcul EF par une simulation tridimensionnelle de DD qui repose principalement sur la théorie élastique des dislocations. En raison de la longue portée du champ de contrainte des dislocations, la simulation discrète (DD) joue donc le rôle d'une loi de comportement non-locale. Initié en 1999 dans le cadre de la thèse de Lemarchand, le MDC n'a cessé d'évoluer dans l'optique de décrire de façon toujours plus fidèle les propriétés élémentaires des dislocations, et la déformation plastique sous-jacente.

Dans un premier temps, l'optimisation de certaines procédures du MDC réalisée durant la thèse ont permis d'obtenir un gain considérable en terme de description de la déformation plastique et de temps de calcul. Encore inaccessibles il y a trois ans, les simulations réalisées font intervenir un grand nombre de segments de dislocation en considérant, lorsqu'il est nécessaire, le mécanisme de glissement dévié. Par ailleurs, la prise en compte des segments de caractères mixtes dans le nouveau code de DD (microMégas) améliore la description des interactions élastiques, et offre un gain CPU conséquent. Cette amélioration est d'autant plus importante que les segments déposés aux interfaces du précipité γ' sont principalement de caractère mixte $\pm 60°$. Enfin, les derniers développements réalisés sur le MDC offre la possibilité de simuler des matériaux constitués de plusieurs domaines plastiques. Par exemple, le mécanisme du cisaillement de précipités cohérents γ' par une paire de dislocations, observé expérimentalement, a été simulé et étudié.

Ce premier travail a permis d'analyser l'influence des paramètres physico-chimiques et microstructuraux mis en jeu dans chacune des deux phases constituant un superalliage. Cette étude a mis en évidence

plusieurs caractéristiques: (i) l'énergie d'antiphase et la contrainte de friction dans les couloirs de matrice sont deux paramètres durcissants importants qui conditionnent la mobilité des dislocations dans la matrice, (ii) la fraction volumique et la largeur des couloirs contrôlent la courbure de la dislocation, et par conséquent le travail mécanique nécessaire à une superdislocation pour cisailler un précipité.

D'un point de vue méthodologique du MDC, l'une perspective majeure serait d'être capable de simuler la totalité des mécanismes physiques élémentaires mis en jeu lors la déformation plastique des superalliages à hautes températures. Parmi ces mécanismes, la production et la diffusion de défauts ponctuels semblent être importantes pour modéliser le fluage. La montée des dislocations est donc certainement un mécanisme important qu'il serait opportun de pouvoir intégrer au MDC. Cet objectif atteint, une étude de différent mode de chargement permettrait de mettre en évidence le mécanisme dominant entre le glissement (déplacement conservatif) et la montée (non conservatif) des dislocations. Une étude de la dépendance en température de la mobilité des dislocations serait également possible.

Deux applications du MDC sont ensuite présentées dans le mémoire de thèse. La première a pour objet d'étudier des effets de taille induits par une variation de la largeur du couloir de matrice γ sur les propriétés mécaniques. Une seconde étude traite de l'influence de l'orientation du chargement sur le comportement mécanique du superalliage. Les microstructures de dislocations générées numériquement sont systématiquement analysées, et sont souvent comparées à des observations expérimentales tirées de la littérature.

Les simulations en traction monotone suivant l'orientation $\langle 001 \rangle$ pour les différentes morphologies (à hautes températures) mettent en évidence que:

* Macroscopiquement, l'effet de taille à la limite d'élasticité vérifie la loi d'Orowan et varie comme l'inverse de la largeur des couloirs.

* Les dislocations sont totalement stockées aux interfaces γ/γ' des précipités et leur densité croît linéairement avec la déformation plastique. L'identification d'une loi de stockage des dislocations montre que le libre parcours moyen des dislocations est intimement lié à la largeur des couloirs.

* Le réseau complexe formé de segments de dislocation accumulées aux interfaces est polarisé et se forme en l'absence d'empilement de dislocations dans les couloirs de matrice.

* La loi classique de type stockage/restauration, principalement écrite pour représenter les interactions de contact entre dislocations, semble ne pas être adaptée à la modélisation du comportement collectif des dislocations dans un superalliage. En effet, dans ce matériau, l'écoulement plastique associé au glissement des dislocations est contrôlé par les fortes contraintes internes générées par les dislocations déposées aux interfaces.

Dans la seconde application, la comparaison de l'évolution des microstructures de dislocations en fonction de l'orientation du chargement monotone, $\langle 001 \rangle$ vs. $\langle 111 \rangle$, met en évidence un mécanisme de déformation jusqu'alors inconnu. Celui-ci est caractérisé par la formation de microstructures de dislocation très particulière, qui est en bon accord avec les observations expérimentales. Il ressort de cette étude une meilleure compréhension du comportement des dislocations responsables du glissement cubique observé à l'échelle macroscopique:

* La densités de dislocation évoluent différemment pour les deux orientations de chargement et des microstructures caractéristiques peuvent être identifiées dans les deux cas. L'analyse de leur différences explique le faible taux de stockage de dislocations obtenu en chargement monotone suivant $\langle 111 \rangle$.

* L'activation de deux systèmes octaédriques singuliers (un système primaire et son dévié) lors du chargement $\langle 111 \rangle$ accommode la quasi-totalité de la déformation plastique. Cette instabilité plastique implique une violation de la loi de Schmid qui stipule théoriquement l'activation symétrique de six systèmes octaédriques.

* Les interactions entre systèmes primaire et dévié jouent un rôle majeur dans la localisation de la déformation plastique dans une direction de couloir de matrice. Des supercrans, produit de réaction entre systèmes colinéaires, se forme sur les dislocations. C'est l'accumulation de ces supercrans force les dislocations à glisser dans une direction parallèle à leur vecteur de Burgers, et ainsi, confine la plasticité aux faibles déformations dans un glissement "pseudo-cubique".

* Les multiples réactions colinéaires entre dislocations déposées aux interfaces forment des microstructures de dislocation en zig-zag comparables à celles observées par Bettge and Österle.

* La localisation de la déformation plastique en traction $\langle 111 \rangle$ se manifeste par l'accumulation aux interfaces de longs segments de caractère vis. Contrairement au réseau de dislocations formé en traction $\langle 001 \rangle$, cette microstructure n'est pas polarisée et n'induit pas d'écrouissage plastique.

Ces résultats sont d'une importance capitale dans l'écriture d'un modèle micromécanique. Il peut être souligné que la continuité logique de ces analyses serait l'étude des mécanismes élémentaires intervenant en sollicitation cyclique. Dans un premier temps, la simulation d'un cycle d'hystérésis permettrait d'identifier les mécanismes physiques contrôlant l'effet Bauschinger. Les résultats ainsi obtenus définiraient dans un deuxième temps les bases d'une modélisation de l'écrouissage cinématique pour les superalliages.

Un modèle intermédiaire à longueur interne a été implémenté dans le code EF ZéBuLoN afin de modéliser de manière continue les dislocations stockées aux interfaces simulées avec le MDC. Dans un schéma multi-échelles, ce modèle intermédiaire permet de faire le lien direct entre la nature discrète d'une population de dislocations et sa représentation dans le cadre d'une modélisation continue à une échelle caractéristique du matériau. Le modèle de plasticité cristalline de Teodosiu a été ici utilisé en introduisant une variable interne additionnelle associée à la notion de dislocations géométriquement nécessaires (ou GND). Ces GND affectent le libre parcours moyen des dislocations mobiles et induisent ainsi un durcissement plastique supplémentaire. L'objectif est de prédire le comportement mécanique en ajustant les paramètres du modèle continu aux réponses macroscopiques simulées par le MDC. Les principales conclusions à retenir de cette partie sont:

* Le calibrage d'un paramètre clé du modèle continu permet de restituer le comportement mécanique simulé par le MDC. L'évolution de la densité de dislocation reproduit par le modèle de plasticité cristalline est globalement en accord avec les résultats des simulations discrètes.

* Une limitation majeure de ce modèle réside cependant dans son inaptitude à reproduire des quantités locales telles que la densité de dislocation stockée aux interfaces. La principale explication repose sur le calcul du gradient de la déformation plastique qui implique l'existence d'empilement de dislocation contre les interfaces. Or, ce type de distribution spatiale des dislocations n'est pas conforme avec les résultats obtenus avec le MDC.

* La loi d'écrouissage isotrope identifiée semble être mal adaptée à la plasticité des superalliages. L'introduction des GND dans le libre parcours des dislocations n'est pas représentatif des études menées par le MDC qui montrent que le libre parcours moyen des dislocations est contrôlé par la largeur (fixe) des couloirs. Par ailleurs, les dislocations déposées aux interfaces génèrent en traction suivant $\langle 001 \rangle$ de fortes contraintes internes qui sont mal représentées dans ce modèle continu. Cette incohérence est corrigée dans un second modèle micromécanique.

Afin de rendre compte du champ de contrainte interne associé à la présence des dislocations qui accommodent les gradients de distorsion plastique dans le cristal, un terme d'origine cinématique pourrait être ajouté dans la loi de comportement de ce modèle intermédiaire. Une identification complémentaire avec les résultats du MDC et une comparaison des niveaux de contraintes internes dans les couloirs des deux modèles serait envisageable. Dans ce sens, il faut noter que les coefficients de la matrice d'interaction

des dislocations intervenant dans le présent modèle prennent en compte, sans en discerner les effets respectifs, l'écrouissage isotrope et cinématique. L'identification des contributions relatives à chacun des deux mécanismes d'écrouissage pourrait être réalisé avec les simulations d'essais en chargement cyclique mentionnés précédemment.

Une approche micromécanique par homogénéisation, basée sur une résolution de champs par séries de Fourier est finalement développée. Cette dernière montre la faisabilité d'un transfert d'informations pertinente de l'échelle des dislocations aux échelles supérieures. Fortes des analyses effectuées sur l'anisotropie du chargement, cette dernière partie de la thèse s'est centrée sur la question ouverte de l'intégration des systèmes cubiques dans les lois de comportement, principalement activés en traction suivant $\langle 111 \rangle$. L'objectif est de développer une modélisation réaliste capable de restituer l'ensemble des mécanismes de déformation identifiés aux échelles fines, mais pour une application de l'ingénieur utilisable dans des codes de calcul EF. Le modèle retenu, initialement développé par Fedelich, intégrait les systèmes cubiques. Il a été réécrit en ne considérant que les systèmes octaédriques. Les mécanismes locaux de déformation appréhendés de manière physique sont ici modélisés dans une phase individuelle. L'interaction mécanique entre chaque phase joue alors un rôle essentiel dans la détermination de la réponse globale du matériau. Ce modèle à variables internes est fondé sur l'existence d'une population de dislocation stockée aux interfaces du précipité induite par l'accommodation plastique dans la microstructure. Ces structures hétérogènes de dislocations génèrent des contraintes internes à longues distances qui sont calculées pour restituer le comportement macroscopique du superalliage. Structurellement, le modèle contient quatre sous-domaines: trois couloirs et un précipité. Les propriétés de chacune des phases et les propriétés macroscopiques sont liées par un tenseur d'influence $\mathbf{\Omega}$ calculé explicitement en amont de la simulation. Ce tenseur est fonction du découpage de la microstructure en sous-domaines et des propriétés élastiques du matériau. Les résultats des simulations mettent en évidence plusieurs caractéristiques, ainsi que des cohérences avec les simulations discrètes:

* Seuls huit paramètres permettent de mettre en évidence trois mécanismes de déformation (le glissement des dislocations dans les couloirs, le cisaillement des précipités et la montée des dislocations aux interfaces) et de décrire le comportement global. Les systèmes octaédriques suffisent à reproduire l'anisotropie d'écrouissage observée en traction monotone suivant $\langle 001 \rangle$ et $\langle 111 \rangle$.

* La définition de 24 systèmes octaédriques conduit à une sélection des deux systèmes singuliers primaires et déviés comme le montre le MDC. Par ailleurs, le critère de plasticité lié à la tension de ligne des dislocations potentiellement vis ou mixtes permet de reproduire fidèlement la localisation plastique observée à l'échelle des simulations discrètes.

* Le découpage des sous-domaines du modèle micromécanique est identifié sur un calcul MDC: la forme parallélépipédique est ainsi adoptée et permet de reproduire correctement le comportement macroscopique observé suivant $\langle 111 \rangle$.

* Les paramètres du modèle ont tous un sens physiques et leurs valeurs sont calibrées dans des domaines d'identification réalistes. Le "pseudo-glissement cubique" est justifié par une absence de contraintes internes associée à l'activation de deux systèmes octaédriques dans un couloir qui déposent des segments de vecteur de Burgers de signes opposés.

* Les paramètres ajustables ont été identifiés pour un alliage CMSX-4 à 850 et 950°C et les résultats montrent un bon accord entre expérience et simulation.

Une application immédiate, outre l'identification du modèle sur des superalliages de même génération comme l'AM1, serait la comparaison des champs de contraintes locaux avec les champs simulés par le MDC, et de confronter l'évolution des densités de dislocations stockées aux interfaces. Par ailleurs, il est bien connu qu'en fonctionnement la microstructure cuboïdale des précipités évolue. Une mise en radeau des précipités qui conduit à une détérioration importante des propriétés mécaniques est alors observée. Parce que le modèle micromécanique prend explicitement en considération la microstructure, une

amélioration possible du modèle micromécanique consisterait à prendre en compte cette évolution de la microstructure à travers le tenseur d'influence Ω. Une modification simple du modèle micromécanique consisterait à substituer Ω par une fonction polynomiale P(Ω), fonction de l'évolution de la microstructure.

Finalement, le présent travail de thèse montre à la fois l'intérêt scientifique et les avantages d'une modélisation multi-échelles. L'interface, et plus précisement, l'organisation des dislocations sur les interfaces, a été le phénomène essentiel à appréhender aux diverses échelles d'investigation. La méthodologie développée met en évidence aux échelles fines des propriétés originales des dislocations, et montre les difficultés liées à une description continue de la matière. Malgré ces difficultés, il est montré que pour certaines informations pertinentes, des transitions "du discret au continu" et "du micro au macro" sont possibles dans le but d'améliorer la prédiction du durcissement des superalliages monocristallins.

In this Appendix, connections between two crystal plasticity theories presented in section 1.2.4 are discussed. The tangent interaction matrices K^{gr} for both models are the link between the strain rate $\dot{\gamma}^r$ on slip plane r to the rate of the critical stress $\dot{\hat{\tau}}^g$ on the slip plane g

$$\dot{\hat{\tau}}^g = \sum_r K_{gr} |\dot{\gamma}^r| \tag{A.1}$$

On the one hand, the dislocation density-based model (section 1.2.4.2) is considered through the set of three constitutive equations defined by equations (1.29), (1.31), and (1.33). They can be rewritten in a classical form by calculating the derivative of equation (1.31) with respect to time and substituting $\dot{\rho}^g$ given by equation (1.33). This gives the tangent interaction matrix $K_\star^{gr}$ for the dislocation density-based model [TAB01]

$$K_\star^{gr} = \frac{\mu}{2} \frac{a^{gr}}{\sqrt{\sum_i a^{gi} \rho^i}} \left(\frac{\sqrt{\sum_j a^{rj} \rho^j}}{K} - y_C \rho^r \right) \tag{A.2}$$

On the other hand, the set of equations for the phenomenological approach (see section 1.2.4.3) without considering the associated kinematic hardening of equation (1.41), i.e. $X^g = 0$ is given by

$$\dot{\gamma}^g = \left(\frac{|\tau^g| - R^g}{V} \right)^n \operatorname{sign}(\tau^g) \tag{A.3}$$

$$R^g = R_0^g + Q^g \sum_r h^{gr} \left(1 - \exp^{-qp^r} \right) \tag{A.4}$$

In the phenomenological model, the dislocation density ρ^r can be introduced as a state variable in the expression of R^g (i.e. equation A.4). Thus ρ^r plays the role of the cumulated plastic strain p^r and R^g the role of the slip resistance $\hat{\tau}^g$. The relation (1.31) may also be rewritten

$$R^g = \mu b \sqrt{\sum_r a^{gr} \rho^r} \tag{A.5}$$

Thus, a step by step identification with expression (A.4) gives

$$\left(\frac{R^g}{\mu b} \right)^2 = \left(\frac{1}{\mu b} \right)^2 \left(Z^g - Q^g \sum_r h^{gr} \exp^{-qp^r} \right)^2 \tag{A.6}$$

with $Z^g = R_0^g + Q^g \sum_r h^{gr}$. Note that Z^g may be regarded as a saturation stress for $p^r \to \infty$ (or $\rho^r \to \infty$). Supposing that the matrix h^{gr} is inversible, the exponential term can be extracted as function

of the difference $Z^g - R^g$

$$\exp^{-qp^r} = \sum_l \left[\left(h^{lr} \right)^{-1} \frac{Z^l - R^l}{Q^l} \right] \tag{A.7}$$

In addition, differentiating R^g defined by equation (A.4) becomes

$$\dot{R}^g = qQ^g \left[\sum_r h^{gr} \exp^{-qp^r} \right] |\dot{\gamma}^r| = \sum_r K^{gr}_{\star\star} |\dot{\gamma}^r| \tag{A.8}$$

with $\dot{p}^r = |\dot{\gamma}^r|$. Thus, the tangent interaction matrix $K^{gr}_{\star\star}$ is expressed in the form

$$K^{gr}_{\star\star} = qQ^g h^{gr} \exp^{-qp^r} = qQ^g h^{gr} \sum_l \left[\left(h^{lr} \right)^{-1} \frac{Z^l - R^l}{Q^l} \right] \tag{A.9}$$

Substituting equation (A.5) into equation (A.9), the tangent interaction matrix gives

$$K^{gr}_{\star\star} = qh^{gr} \left(m^{gr} - b\mu \sum_l \left[\left(\frac{Q^g}{Q^l} \right) \left(h^{lr} \right)^{-1} \sqrt{\sum_k a^{lk} \rho^k} \right] \right) \tag{A.10}$$

where $m^{gr} = \sum_l \left(h^{lr} \right)^{-1} Z^l \frac{Q^g}{Q^l}$ (in MPa).

Comparing the phenomenological model of section 1.2.4.3 of the dislocation density-based model of section 1.2.4.2 through their corresponding tangent interaction matrix, $K^{gr}_{\star}$ (equation A.2) and $K^{gr}_{\star\star}$ (equation A.10), respectively, given by

$$K^{gr}_{\star} = \frac{\mu}{2} a^{gr} \left(\frac{1}{K} \sqrt{\frac{\sum_j a^{rj} \rho^j}{\sum_i a^{gi} \rho^i}} - y_C \frac{\rho^r}{\sqrt{\sum_i a^{gi} \rho^i}} \right) \tag{A.11}$$

$$K^{gr}_{\star\star} = q\mu h^{gr} \left(\frac{m^{gr}}{\mu} - b \sum_l \left[\left(\frac{Q^g}{Q^l} \right) \left(h^{lr} \right)^{-1} \sqrt{\sum_k a^{lk} \rho^k} \right] \right) \tag{A.12}$$

Three main differences are observed

* The term factors h^{gr} and a^{gr} are playing an analogous role, e.g. two dimensionless interaction matrices, but they are nevertheless defined with different means.

* The constant interaction matrix h^{gr} in the hardening term of the equation (A.12) plays the role of the ratio $\sqrt{\dfrac{\sum_j a^{rj} \rho^j}{\sum_i a^{gi} \rho^i}}$ which is variable in the equation (A.11) of the dislocation density-based model.

* The quantity $\sum_l \left(\dfrac{Q^g}{Q^l} \right) \left(h^{lr} \right)^{-1} \sqrt{\sum_k a^{lk} \rho^k}$ in equation (A.12) is homogeneous to $\sqrt{\rho}$ in a scalar formulation of the net stored density. This quantity is located in the dislocation recovery term of the equation (A.12) instead of the quantity $\dfrac{\rho^r}{\sqrt{\sum_i a^{gi} \rho^i}}$ in equation (A.11), which is also homogenuous to $\sqrt{\rho}$.

Moreover, considering the simplistic case[1] where the components of diagonal interaction matrices a^{gr} and h^{gr} are equal to 1, and 0 otherwise, i.e. $a^{gr} = h^{gr} = (h^{gr})^{-1} = \delta^{gr}$, i.e. $\delta^{gr} = 1$ if $g = r$, and zero

---

[1]This case is qualified of unrealistic because it implies that latent hardening is neglected. This assumption is only made to compare the mathematical structure of both models.

otherwise, both matrices $K_\star^{gr}$ and $K_{\star\star}^{gr}$ are reduced to

$$K_\star^{gr} = \frac{\mu}{2} \delta^{gr} \left(\frac{1}{K} - 2y_C \sqrt{\rho^r} \right) \tag{A.13}$$

$$K_{\star\star}^{gr} = \frac{\mu}{2} \delta^{gr} \left(\frac{2qZ^r}{\mu} - 2bq\sqrt{\rho^r} \right) \tag{A.14}$$

For the particular case where only the isotropic hardening is considered and no latent hardening is adopted, the above identification shows that equations (A.13) and (A.14) are similar: for instance $q = \frac{y_C}{b}$ and $K = \frac{\mu\, b}{2y_C \left(R_0^g + Q^g \right)}$. In this way, there is no reason that the mechanical predictions for both model are different.

Nevertheless, the above step by step identification does not include the kinematic hardening. This simplication is based on the fact that the kinematic hardening is most often choosen in a dislocation density-based framework in a phenomelogical form such as the equation (1.43).

A standard formulation of kinematic hardening in a dislocation density-based model is still subject of debate.

Technical notes on the DCM

B.1   Algorithme

Pour la mise en place de l'algorithme illustré par la figure 31, et son exécution, les codes existants de Dynamique des Dislocations (DD) et d'Eléments Finis (EF) sont adaptés afin de pouvoir échanger des données. Par ailleurs, les modifications des deux codes ne doivent pas en aucun cas altérer leur fonctionnement dans le cadre de calculs non-couplés. Les deux codes protagonistes, à savoir Z-SeT [ZéBuLoN] pour la partie EF et mM [MicroMégas] pour la partie DD, sont écrits dans deux langages de programmation différents, à savoir C/C++ pour Z-SeT et Fortran 95 pour mM. C'est pour celà qu'un code monolithique n'a pas été initialement envisagé.

La solution retenue est un modèle de type maître-esclave entre Z-SeT en mM, animé par la librairie pvm (Parallel Virtual Machine) [Pvm]. La principale fonction de Z-SeT est la résolution du problème mécanique global et son intégration en temps. La loi de comportement du problème étant la loi non-locale substituée par une simulation de DD, Z-SeT s'occupe également du lancement de l'exécutable de mM. Il existe donc trois entitées différentes: le code EF (Z-SeT), le code DD (mM) et une entité intermédaire qui gère les communications entre ces deux précédents codes (pvm).

Pour Z-SeT, tout le code lié au MDC s'intégre dans un plugin `zMDC`. Les fichiers source du plugin dépendent des objets C++ du code principal: dès la compilation, les chemins vers des fichiers `*.h` contenant les déclarations des objets en question sont connus. A travers cette dépendance, les fichiers source du plugin sont indépendamment maintenus du projet principal. Un autre plugin `Zpvm`, livré avec la version parallèle de Z-SeT, gère l'interfaçage entre Z-SeT et pvm dont le plugin `zMDC` dépend de `Zpvm`.

Pour mM, tout le code lié au MDC est intégré dans le projet principal qui devient actif lors la compilation. Les modifications ne perturbent donc pas le fonctionnement des autres sections du code. Le code se trouve dans des fichiers supplémentaires ou dans des fichiers existants, défini entre `#ifdef MDC` et `#endif` afin de le rendre "invisible" lors d'une compilation de DD conventionnelle.

B.2   Fichiers d'entrée et paramètres de simulations

Pvm

En ce qui concerne pvm, la machine virtuelle doit être proprement configurée avant de lancer le calcul MDC. Proprement configurée signifie ici que la machine virtuelle inclut la machine sur laquelle l'exécutable de mM est exécuté sur `localhost`. Notons que lors de la compilation des librairies pvm, autant les `libpvm.*` et `libfpvm.*` sont nécessaires.

Z-SeT

Tout d'abord, pour pouvoir lancer un calcul MDC, la variable d'environnement `ZEBU_PATH` doit pointer vers le répertoire où se trouve `libzMDC.so`. Le calcul est alors lancé dans un répertoire appelé `$MDC_ROOT/Project`. Ensuite, un calcul peut être lancé par la commande `Zrun -s MPI pvm3 -dd nom_du_calcul.inp`. L'argument `-s MPI pvm3` active l'interface (ici l'interface est pvm3) qui s'occupe du transfert des données entre les différents exécutables, et l'argument `-dd` active la partie propre à la simulation DD. Notons qu'il est possible de suivre simultanément le déroulement du calcul mM en temps réel si l'argument `-s Parallel.Pvm.Flags 4` avant `-dd` est rajouté. Ceci permet de lancer l'exécutable de mM dans une fenêtre de débogueur de type `gdb` (ou un autre débogueur).

Le fichier `nom_du_calcul.inp` contient toute la mise en données du calcul propre à Z-SeT. Ce fichier est un fichier d'entrée avec une partie spécifiquement dédiée au MDC. Le calcul MDC est effectué sur un maillage EF qui doit impérativement être dimensionné en unité de a, à savoir le paramètre de maille du réseau de simulation DD.

Dans ce fichier, se trouve tout d'abord un bloc compris entre ****dislocation et ****return dans lequel la partie "exécution" du couplage est gérée. On trouve les commandes suivantes

```
****dislocation
 ***dislocation_host nom_de_machine
 ***dislocation_binary chemin_de_executable
****return
```

où `nom_de_machine` est le nom de la machine sur laquelle l'exécutable de mM est lancé. Cette machine doit être la même que celle définie dans la machine virtuelle pvm. Par ailleurs, `chemin_de_executable` contient le chemin pointant vers l'exécutable de mM.

La seconde partie de la mise en données concerne le couplage et correspond à la mise en données classique d'un calcul EF ZéBuLoN, compris entre ****calcul et ****return. Dans ce dernier bloc, deux mots clé sont spéficiques au MDC. Tout d'abord, il faut spécifier que le maillage (ou une partie du maillage) contient des éléments de types `dislocation`, selon les conditions aux frontières souhaitées par l'utilisateur: conditions aux limites périodiques ou pas. Le second point correspond à la spécificité de la résolution globale de l'algorithme: un mot clé propre au MDC est caractéristisé afin de prendre en compte la non-localité des interactions entre les dislocations aux échelles considérées

```
***resolution newtondislo
```

Celui-ci est substitué au classique ***resolution `newton`. Il est d'ailleurs impératif d'informer Z-SeT des ordres de grandeurs du temps, de déplacement et de la déformations tant ceux-ci sont plus petits. Ces fonctionalités sont faites via la commande ****dimension.

La troisième partie concerne la mise en données du comportement du matériau à travers

```
***behavior dislocation_behavior
    elasticity isotropic
    young valeur_du_module_young
    poisson valeur_du_ratio_poisson
***return
```

Dans cet exemple, l'élasticité est isotrope, mais il est tout à fait possible d'utiliser l'élasticité anisotrope

(ce qui distingue le MDC de la méthode de superposition existante en élasticité anisotrope). Lors d'un tel calcul, le modèle anisotrope de la tension de ligne dans mM doit être activée. Cette loi est associée à un (ou plusieurs) groupe(s) d'élément(s) appelé `elset` dans Z-SeT dont les noms spéficiques des elsets commencent par `dislocation`.

mM

L'exécutable de mM dans sa version MDC, appelé `mdc`, est piloté par plusieurs fichiers d'entrée. Pour tout calcul mM, les fichiers d'entrée et de sortie se trouvent dans des endroits précis relatifs à l'endroit où se trouvent l'exécutable.

Si cet endroit est défini par $MDC_ROOT/bin, un répertoire $MDC_ROOT/in contient les fichiers d'entrée de `mdc` et un autre répertoire $MDC_ROOT/out sauvegarde les résultats simulés.

Pour un calcul conventionnel de DD, un premier fichier d'entrée $MDC_ROOT/in/input.dd contient une liste de trois spécificités contenant les paramètres matériau, le pilotage du calcul, et la configuration initiale des segments de dislocations. Pour le MDC, une quatrième ligne a été ajoutée afin de mettre en evidence les paramètres liés au couplage. Cette rigoureuse séparation est un des principaux changements dans la version Mixte par rapport au précédent modèle Coin-Vis. Cette quatrième ligne correspond aux informations suivantes

1. La clé `clef_gelule` (booléen `T` ou `F`) qui (dés)active la prise en compte des gélules dans le traitement des interactions à courtes distances.

2. Le demi-rayon $\frac{h}{2}$ de régularisation `epaidemi` (un entier, en unités de a).

3. Les dimensions `nbx`, `nby` et `nbz` (entiers en nombre d'éléments) du volume maillé.

B.3   Quantités échangées

Cette section décrit les quantités échangées entre les deux codes via pvm. Ces quantités sont regroupées dans différents blocs qui sont spécifiquement numérotés. Pour chaque bloc, l'endroit dans lequel se trouve le code correspondant est communiqué à la fois pour le module `zMDC` de Z-SeT et pour la version MDC de mM. La plupart des communications se terminent par un échange d'une clé de synchronisation. Dans un premier instant, Z-SeT lance l'exécutable de mM via pvm et attend le retour du `tid` de mM (`tid` est un identifiant de mM pour pvm, donc un entier, nécessaire à la connaissance du destinataire d'une chaîne de caractère). L'exécutable de Z-SeT possède également son propre `tid`, qui est ensuite envoyé à mM contenant le répertoire dans lequel Z-SeT calcule (à savoir $MDC_ROOT/Project). A travers cette information, mM peut alors effectuer un `chdir` vers $MDC_ROOT/out. Ce premier bloc de communication se termine avec l'envoi d'un entier $MAGIC_DISLO de mM à Z-SeT:

Z-SeT No. 0 :	PROBLEM_STATIC_MECHANICAL_DISLOCATION::open_mM
	dans zMDC/Static_dislocation.c
mM No. 0 :	15main.F90
Magic key :	MAGIC_DISLO

Ensuite, Z-SeT envoie le `nom_du_problem` (une chaîne de caractères) à mM, dont ce dernier confirme sa bonne réception par l'envoi de la clé `111`.

Z-SeT No. 1 :	PROBLEM_STATIC_MECHANICAL_DISLOCATION::load
	dans zMDC/Static_dislocation.c
mM No. 1 :	subroutine nom_du_problem dans 20gammaplas.f90
Magic key :	111

Le transfert du maillage des domaines ayant une loi de type `dislocation_behavior` de Z-SeT à mM est nécessaire. Tout d'abord sont envoyés le nombre d'éléments dans ces domaines (un entier), le nombre de noeuds par élément `nombre_noeuds_ref`, le nombre de noeuds dans le maillage, et le nombre de domaines de type `dislocation_behavior`. mM confirme la bonne récéption par l'envoi de la clé `222`:

Z-SeT No. 2 :	`PROBLEM_STATIC_MECHANICAL_DISLOCATION::send_mesh_info`
	dans `zMDC/Static_dislocation.c`
mM No. 2 :	`subroutine transformation_maillage` dans `20gammaplas`
Magic key :	`222`

Ensuite Z-SeT entre dans une boucle sur les éléments de type `dislocation_behavior`, et pour chaque élément sont envoyés dans l'ordre

1. L'ordre de chaque noeud de l'élément (`nombre_noeuds_ref`).

2. Dans une boucle sur les noeuds, les coordonées de chaque noeud en unités de *a*.

3. Le nombre de points de Gauss de l'élément `nombre_gauss`.

4. Dans une boucle sur les points de Gauss de l'élément, les coordonées de chaque point de Gauss.

Après cette boucle sur les éléments, mM confirme la bonne réception par un second envoi de la clé `222`, et le tenseur d'élasticité associé à chaque domaine de type `dislocation_behavior` est transféré à mM (mM confirmera sa bonne réception par l'envoi d'une clé `333`):

Z-SeT No. 3 :	`MCEDSI::matrix_of_elasticity_for_dislocation`
	dans `zMDC/Mcesd_std_dislocation.c`
mM No. 3 :	`subroutine matrice_elasticity_gauss` dans `20gammaplas`
Magic key :	`333`

Z-SeT envoie une clé `clef_rede` (un entier `i`) à mM, indiquant s'il s'agit d'un redémarrage d'un précédent calcul (`i = 1`) ou s'il s'agit d'un nouveau calcul (`i = 0`). mM confirme réception par l'envoi de la clé `444`. Il s'agit là du dernier échange avant le début du calcul à proprement dit, c'est à dire avant de rentrer dans la boucle d'intégration du temps t:

Z-SeT No. 4 :	`PROBLEM_STATIC_MECHANICAL_DISLOCATION::load`
	dans `zMDC/Static_dislocation.c`
mM No. 4 :	`subroutine redemarrage` dans `20gammaplas.f90`
Magic key :	`444`

Ensuite est donné à mM l'incrément du tenseur de déformation totale pour un point de Gauss. Les composantes du tenseur sont envoyés dans l'ordre standard de Z-SeT (11, 22, 33, 12, 23, 31). Cette routine est appelée depuis une boucle sur les tous points de Gauss de tous les éléments des elsets avec un comportement associé de type `dislocation_behavior`. Contrairement à une loi de comportement usuelle, tous les incréments sont envoyés ensemble, sans attendre le résultat de l'intégration:

Z-SeT No. 5 :	`DISLOCATION_BEHAVIOR::get_strain_dislocation`
	dans `zMDC/Dislocation_behavior.c`
mM No. 5 :	`subroutine increment_deformation_iteration`
	dans `20gammaplas.f90`
Magic key :	`555`

Le résultat de l'intégration de la loi de comportement est alors envoyé à Z-SeT. Ceux sont l'incrément du tenseur de la déformation plastique et le tenseur de contrainte qui sont envoyés pour chaque point de Gauss. Ce dernier tenseur est nécessaire afin de décrire les interactions à courtes distances des dislocations. C'est donc entre la communication **No 5** et **6** que la DD évolue:

Z-SeT No. 6 :   `INTEGRATION_RESULT* DISLOCATION_BEHAVIOR::integrate`
dans `zMDC/Dislocation_behavior.c`

mM No. 6 :   `subroutine  resultats_calcul` dans `20gammaplas.f90`

Magic key :   `666`

Z-SeT envoie son incrément de temps `delta_zeb` à mM, et mM répond par l'envoie d'une clé de synchronisation `777`:

Z-SeT No. 7 :   `PROBLEM_STATIC_MECHANICAL_DISLOCATION::make_increment`
dans `zMDC/Static_dislocation.c`

mM No. 7 :   `subroutine  increment_de_temps` dans `20gammaplas.f90`

Magic key :   `777`

Une partie communique le résultat de la boucle de Newton-Raphson à mM.
Un entier `nouvel_increment` est envoyé par Z-SeT défini par "-1" → Convergence OUI: incrément suivant, "0" → Convergence NON: itération suivante, ou "1" → Convergence NON: nombre maximum d'itérations atteint et le calcul s'arrête.
mM renvoie la clé `888` pour confirmer la bonne réception de `nouvel_increment`:

Z-SeT No. 8 :   `MECHANICAL_QUASI_NEWTON::convergence_loop`
dans `zMDC/Algorithm_mqn_dislocation.c`

mM No. 8 :   `subroutine  poursite_calcul` dans `20gammaplas.f90`

Magic key :   `888`

Enfin Z-SeT envoie la décision de la suite du calcul via un entier `continue_calcul` défini par "0" → Calcul terminé, ou "1" → Calcul non terminé: nouvel incrément de temps.
mM renvoie la clé `999` pour confirmer la bonne réception de `continue_calcul`:

Z-SeT No. 9 :   `PROBLEM_STATIC_MECHANICAL_DISLOCATION::make_increment`
dans `zMDC/Static_dislocation.c`

mM No. 9 :   `subroutine  fin_calcul` dans `20gammaplas.f90`

Magic key :   `999`

Leading and trailing dislocations during the cutting process into the DD code

One of the developments made during this thesis, in the mM code, is the modelling of cutting process of ordered γ' precipitates by pairs of dislocations (see figures 108 and C). The key parts of such modelling are presented in the following. One must differentiate three stages, which are (i) the localisation of segments with respect to precipitate interfaces, (ii) the identification of the leading and trailing dislocation of a superdislocation, and (iii) the definition of the mobilities of each dislocation inside the precipitates.

t₁.   t₂.

t₃.   t₄.
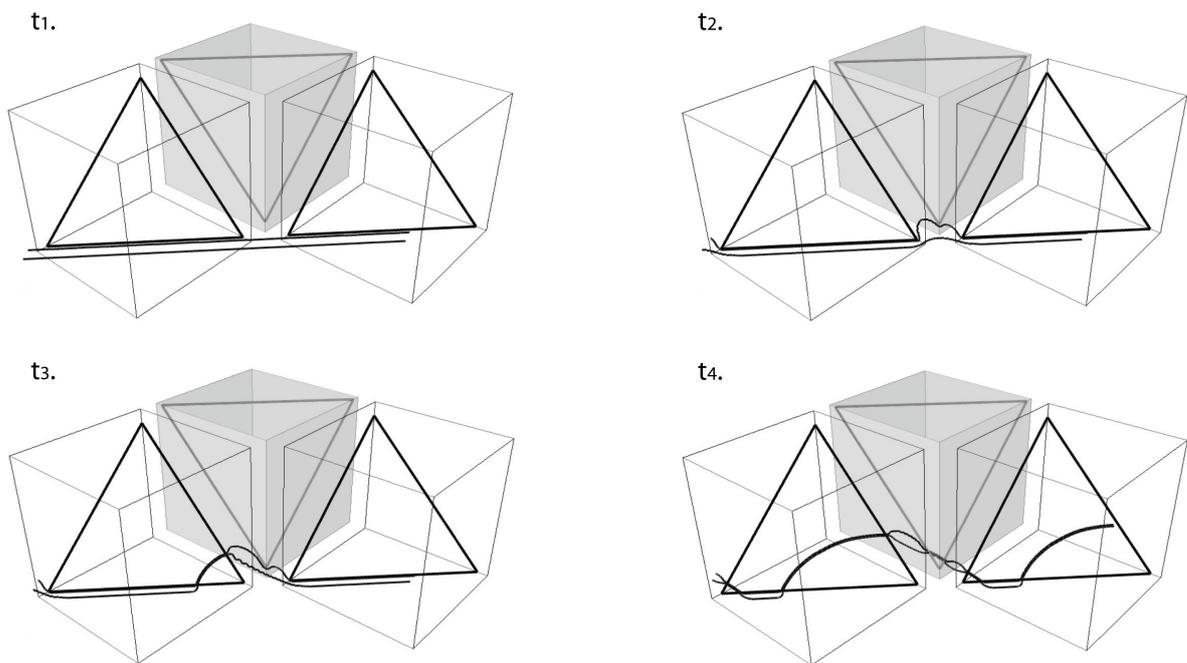
Figure 108 - Illustration of the cutting process of γ' precipitates by a superdislocation.

(i) Test of localisation of one segment (in the subroutine `11topolo.f90`)

```
do i = 1, nsegm
  ! Identification of the initial plastic phase
  if ((InclExcl) .and. (seg(i)%norme /= izero))  then
    Oi(:) = seg(i)%O(:)
    Ei(:) = seg(i)%O(:) + seg(i)%norme * Bveclin(:, seg(i)%veclin)
    Segcub(1, nbplanDom) = .false.
    ! Repeated test of segment position with respect to the interface boundary planes
    do jj = 1, nbplanDom
      inormT(:) = Plan(jj)%miller(:)
      normT(:) = real(inormT(:), DP)
      InterSO(:) = InterP(inormT(:), Plan(jj)%pos, Oi(:), inormT(:))
      InterSE(:) = InterP(inormT(:), Plan(jj)%pos, Ei(:), inormT(:))
      ! Normal projection vector
      Vect1O(:) = real(Oi(:), DP) − InterSO(:)
      Vect1E(:) = real(Ei(:), DP) − InterSE(:)
      if ((DOTproduct(Vect1O, normT) > zero)  .or.      &
        (DOTproduct(Vect1E, normT) > zero))  then
          Segcub(jj) = .true.
      endif
    enddo
    ! Final test of inclusion of one segment into precipitates
    if (all(Segcub) .eqv. InclExcl) seg(i)%Nphase = iun
  endif
enddo
```
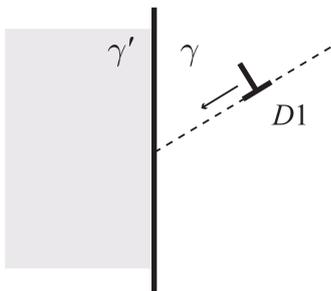

(a) seg(i)% Nphase = 0
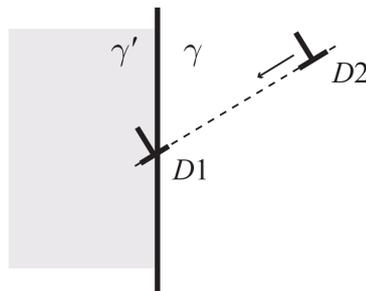
(b) seg(i)% Nphase = 1
TAUeff < TAUkw
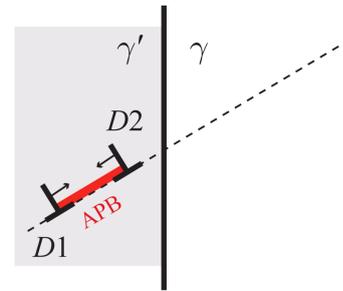
(c) seg(i)% Nphase = 1
TAUeff > TAUkw
abs(TAUint(i)) > sigAPB

Figure 84 - Schematic of the procedure in the DD simulations to simulate the formation of superdislocations. (a) Step 1: one dislocation moves toward the precipitate interface. (b) Step 2: the first dislocation is arrested at the interface because the effective stress is smaller than the Kear-Wilsdorf stress and a second dislocation arrives in the same glide plane. (c) Step 3: internal interaction between the two dislocations is large enough to form a superdislocation made of a leading and a trailing dislocation bounding an APB defect.

(ii) Identification of the leading and trailing dislocations and dispatch of the APB stress (in the subroutine `09elasti.f90`)

do $i = 1, nsegm$
  if $(i ==$ seg(i)%voiso .and. $i ==$ seg(i)%voise$)$ CYCLE
  if LoiSeg$(i) ==$ izero **then**
    ! Choice of the mobility law according to the segment position
    LoiSeg$(i) =$ numeroLOI(VLi)
  endif
  if $($VLcs$(i) <=$ izero .and. seg(i)%wait$) <$ itrois
    signe $=$ sign $($un, TAUapp$(i))$
    SigneTAUapp $($SYSseg(i)%VEClin$) =$ signe
    TAUtot $=$ TAUtl$(i) +$ TAUapp$(i) +$ TAUint(i)
    conditionAPB $=$ seg(i)%Nphase
    if $($conditionAPB$)$ **then**
      ! If the segment into the γ' is the trailing one: the APB stress helps mobility
      if $\big(($abs(TAUint(i))$) >$ sigAPB$)$ .and.   &
        $($TAUapp$(i) *$ TAUint$(i) < 0)\big)$ **then**
        TAUint$(i) =$ TAUint$(i) + 2 *$ signe $*$ TAUapb(i)
      endif
    ! The default solution is an isolated segment entering the precipitate
      TAUint$(i) =$ TAUint$(i) -$ signe $*$ TAUapb(i)
    endif
    TAUtot $=$ TAUtl$(i) +$ TAUapp$(i) +$ TAUint(i)
  endif
enddo

(iii) Mobility criteria into the precipitates (in the subroutine `12contact.f90`)

do $i = 1, nsegm$
  ! Into the precipitates, the effective stress on one segment must be
  ! larger than the Kear-Wilsdorf stress to move
  if $\big(($seg(i)%Nphase $/ =$ izero$)$ .and. $($TAUeff $<$ TAUkw$)\big)$ **then**
    ABSdep $=$ izero
  endif
enddo

On the unit cell for micromechanical analyses

D.1 Formulation of the stored elastic energy

Here some algebra are given in order to obtain the fluctuation part of the elastic energy W_2, and then the analytic expression for the local stress.

Inserting the values of the Fourier coefficients (3.51) in equation (3.48)

$$\tilde{u}_i\left(\mathbf{x}\right) = \sum_{p_\alpha \neq 0} -iC_{jlmn}\,\bar{\varepsilon}^p_{mn}\left(p_\alpha\right)\xi_l\left(p_\alpha\right)V_{ij}\left(p_\alpha\right)\,e^{i\boldsymbol{\xi}(p_\alpha).\mathbf{x}} \tag{D.1}$$

$$\tilde{u}_{i,k}\left(\mathbf{x}\right) = \sum_{p_\alpha \neq 0} C_{jlmn}\,\bar{\varepsilon}^p_{mn}\left(p_\alpha\right)\xi_l\left(p_\alpha\right)\xi_k\left(p_\alpha\right)V_{ij}\left(p_\alpha\right)\,e^{i\boldsymbol{\xi}(p_\alpha).\mathbf{x}} \tag{D.2}$$

$$\tilde{u}_{i,k}\left(\mathbf{x}\right) = \sum_{p_\alpha \neq 0} \bar{u}_{ik}\left(p_\alpha\right)\,e^{i\boldsymbol{\xi}(p_\alpha).\mathbf{x}} \tag{D.3}$$

with

$$\bar{u}_{ik}\left(p_\alpha\right) = C_{jlmn}\bar{\varepsilon}^p_{mn}\left(p_\alpha\right)\xi_l\left(p_\alpha\right)\xi_k\left(p_\alpha\right)V_{ij}\left(p_\alpha\right) \tag{D.4}$$

After these mathematical considerations, let us introduce equation (3.51) into the fluctuation part of the elastic energy defined by equation (3.48)

$$W_2 = \frac{1}{2}C_{ijkl}\int_V \tilde{\varepsilon}^e_{ij} : \tilde{\varepsilon}^e_{kl}\mathrm{d}V = \frac{1}{2}C_{ijkl}\int_V \tilde{u}_{i,j} : \tilde{\varepsilon}^{pl}_{kl}\mathrm{d}V \tag{D.5}$$

According to equations (3.49) and (D.3)

$$W_2 = \frac{1}{2}C_{ijkl}\sum_{\substack{q_\alpha \neq 0 \\ m_\alpha \neq 0}}\left[\bar{u}_{ij}\left(q_\alpha\right) - \bar{\varepsilon}^p_{ij}\left(q_\alpha\right)\right]\left[\bar{u}_{kl}\left(m_\alpha\right) - \bar{\varepsilon}^p_{kl}\left(m_\alpha\right)\right]$$

$$\times \int_V e^{i\frac{\pi(q_1+m_1)x_1}{L_1}}\,e^{i\frac{\pi(q_2+m_2)x_2}{L_2}}\,e^{i\frac{\pi(q_3+m_3)x_3}{L_3}}\,\mathrm{d}V \tag{D.6}$$

$$W_2 = \frac{8L_1L_2L_3}{2}C_{ijkl}\sum_{q_\alpha \neq 0}\left[\bar{u}_{ij}(q_\alpha) - \bar{\varepsilon}^p_{ij}(q_\alpha)\right]\left[\bar{u}_{kl}(-q_\alpha) - \bar{\varepsilon}^p_{kl}(-q_\alpha)\right] \tag{D.7}$$

$$W_2 = \frac{8L_1L_2L_3}{2}C_{ijkl}\sum_{\boldsymbol{\xi} \neq \mathbf{0}}\left[\bar{u}_{ij}\left(\boldsymbol{\xi}\right) - \bar{\varepsilon}^p_{ij}\left(\boldsymbol{\xi}\right)\right]\left[\bar{u}_{kl}\left(\boldsymbol{\xi}\right) - \bar{\varepsilon}^p_{kl}\left(\boldsymbol{\xi}\right)\right] \tag{D.8}$$

$$W_2 = \frac{8L_1L_2L_3}{2}C_{ijkl}\sum_{\boldsymbol{\xi}\neq\mathbf{0}}\left[C_{abcd}\bar{\varepsilon}^p_{cd}(\boldsymbol{\xi})\xi_b\xi_j V_{ia}(\boldsymbol{\xi}) - \bar{\varepsilon}^p_{ij}(\boldsymbol{\xi})\right]$$

$$\times \left[C_{mnpq}\bar{\varepsilon}^p_{pq}(-\boldsymbol{\xi})\xi_n\xi_l V_{km}(-\boldsymbol{\xi}) - \bar{\varepsilon}^p_{kl}(-\boldsymbol{\xi})\right] \tag{D.9}$$

$$W_2 = \frac{8L_1L_2L_3}{2}C_{ijkl}\sum_{\boldsymbol{\xi}\neq\mathbf{0}}\left[C_{abcd}\xi_b\xi_j V_{ia}(\boldsymbol{\xi}) - \delta_{ic}\delta_{jd}\right]$$

$$\times \left[C_{mnpq}\xi_n\xi_l V_{km}(-\boldsymbol{\xi}) - \delta_{km}\delta_{lq}\right]\bar{\varepsilon}^p_{cd}(\boldsymbol{\xi})\,\bar{\varepsilon}^p_{pq}(-\boldsymbol{\xi})) \tag{D.10}$$

In addition, because $\mathbf{V}(-\boldsymbol{\xi}) = \mathbf{V}(\boldsymbol{\xi})$

$$W_2 = \frac{8L_1L_2L_3}{2}C_{ijkl}\sum_{\boldsymbol{\xi}\neq\mathbf{0}}\left[C_{abcd}\xi_b\xi_j V_{ia}(\boldsymbol{\xi}) - \delta_{ic}\delta_{jd}\right]\left[C_{mnpq}\xi_n\xi_l V_{km}(\boldsymbol{\xi}) - \delta_{km}\delta_{lq}\right]$$

$$\times \bar{\epsilon}^p_{cd}(\boldsymbol{\xi})\,\bar{\epsilon}^p_{pq}(-\boldsymbol{\xi}) \tag{D.11}$$

$$W_2 = \frac{8L_1L_2L_3}{2}\sum_{\boldsymbol{\xi}\neq\mathbf{0}}\omega_{cdpq}(\boldsymbol{\xi})\bar{\varepsilon}^p_{cd}(\boldsymbol{\xi})\,\bar{\varepsilon}^p_{pq}(-\boldsymbol{\xi}) \tag{D.12}$$

with

$$\omega_{cdpq} = C_{ijkl}\left[C_{abcd}\xi_b\xi_j V_{ia}(\boldsymbol{\xi}) - \delta_{ic}\delta_{jd}\right]\left[C_{mnpq}\xi_n\xi_l V_{km}(\boldsymbol{\xi}) - \delta_{km}\delta_{lq}\right] \tag{D.13}$$

Thus

$$\omega_{cdpq} = C_{cdab}\xi_b V_{ai}(\boldsymbol{\xi})\xi_j C_{ijkl}\xi_l V_{km}(\boldsymbol{\xi})\xi_n C_{mnpq} - C_{cdab}\xi_b V_{ai}(\boldsymbol{\xi})\xi_j C_{jikl}\delta_{ic}\delta_{lq}$$

$$- \delta_{ic}\delta_{jd}C_{ijkl}\xi_l V_{km}(\boldsymbol{\xi})\xi_n C_{mnpq} + \delta_{ic}\delta_{jd}C_{ijkl}\delta_{kp}\delta_{lq} \tag{D.14}$$

$$\omega_{cdpq} = C_{cdab}\xi_b V_{ai}(\boldsymbol{\xi})K_{ik}(\boldsymbol{\xi})V_{km}(\boldsymbol{\xi})\xi_n C_{mnpq}$$

$$- C_{cdab}\xi_b V_{ai}(\boldsymbol{\xi})\xi_j C_{jipq} - C_{cdkl}\xi_l V_{km}(\boldsymbol{\xi})\xi_n C_{mnpq} + C_{cdpq}$$

$$\omega_{cdpq} = C_{cdab}\xi_b V_{am}(\boldsymbol{\xi})\xi_n C_{mnpq} - C_{cdab}\xi_b V_{ai}(\boldsymbol{\xi})\xi_j C_{jipq} - C_{cdkl}\xi_l V_{km}(\boldsymbol{\xi})\xi_n C_{mnpq} + C_{cdpq}$$

$$\omega_{cdpq} = C_{cdpq} - C_{cdkl}\xi_l V_{km}(\boldsymbol{\xi})\xi_n C_{mnpq} \tag{D.15}$$

D.2   Component of the Ω_{IJ} tensors at 850° C (in MPa)

The influence tensors associated to the WSE decomposition are denoted by $\boldsymbol{\Omega}^{\mathrm{WSE}}_{IJ}$ and those associated to the P decomposition are denoted by $\boldsymbol{\Omega}^{\mathrm{P}}_{IJ}$

D.2.1   Tensors $\Omega^{\mathrm{WSE}}_{IJ}$ associated to the WSE decomposition

$$\boldsymbol{\Omega}^{\mathrm{WSE}}_{11} = \begin{bmatrix} 414.89 & 197.30 & 197.30 & 0. & 0. & 0. \\ & 8404.21 & 3237.40 & 0. & 0. & 0. \\ & & 8404.21 & 0. & 0. & 0. \\ & & & 7595.68 & 0. & 0. \\ & & & & 297.72 & 0. \\ & & & & & 297.72 \end{bmatrix}$$

$$\Omega_{12}^{\text{WSE}} = \begin{bmatrix} -403.42 & 5.83 & -163.16 & 0. & 0. & 0. \\ & -403.42 & -163.16 & 0. & 0. & 0. \\ & & -827.91 & 0. & 0. & 0. \\ & & & -388.43 & 0. & 0. \\ & & & & -388.43 & 0. \\ & & & & & 14.99 \end{bmatrix}$$

$$\Omega_{13}^{\text{WSE}} = \begin{bmatrix} -403.42 & -163.16 & 5.83 & 0. & 0. & 0. \\ & -827.91 & -163.16 & 0. & 0. & 0. \\ & & -403.42 & 0. & 0. & 0. \\ & & & -388.41 & 0. & 0. \\ & & & & 14.99 & 0. \\ & & & & & -388.43 \end{bmatrix}$$

$$\Omega_{14}^{\text{WSE}} = \begin{bmatrix} 391.95 & -39.97 & -39.97 & 0. & 0. & 0. \\ & -7172.86 & -2911.07 & 0. & 0. & 0. \\ & & -7172.86 & 0. & 0. & 0. \\ & & & -6818.82 & 0. & 0. \\ & & & & 105.71 & 0. \\ & & & & & 105.71 \end{bmatrix}$$

$$\Omega_{22}^{\text{WSE}} = \begin{bmatrix} 8404.21 & 197.30 & 3237.40 & 0. & 0. & 0. \\ & 414.89 & 197.30 & 0. & 0. & 0. \\ & & 8404.21 & 0. & 0. & 0. \\ & & & 267.72 & 0. & 0. \\ & & & & 7595.68 & 0. \\ & & & & & 267.72 \end{bmatrix}$$

$$\Omega_{23}^{\text{WSE}} = \begin{bmatrix} -827.91 & -163.16 & -163.16 & 0. & 0. & 0. \\ & -403.42 & 5.83 & 0. & 0. & 0. \\ & & -403.42 & 0. & 0. & 0. \\ & & & 14.99 & 0. & 0. \\ & & & & -388.43 & 0. \\ & & & & & -388.43 \end{bmatrix}$$

$$\Omega_{24}^{\text{WSE}} = \begin{bmatrix} -7172.86 & -39.97 & -2911.07 & 0. & 0. & 0. \\ & 391.95 & -39.97 & 0. & 0. & 0. \\ & & -7172.96 & 0. & 0. & 0. \\ & & & 105.71 & 0. & 0. \\ & & & & -6818.82 & 0. \\ & & & & & 105.71 \end{bmatrix}$$

$$\Omega_{33}^{\text{WSE}} = \begin{bmatrix} 8404.21 & 3237.40 & 197.30 & 0. & 0. & 0. \\ & 8404.21 & 197.30 & 0. & 0. & 0. \\ & & 414.89 & 0. & 0. & 0. \\ & & & 267.72 & 0. & 0. \\ & & & & 267.72 & 0. \\ & & & & & 7595.68 \end{bmatrix}$$

$$\Omega_{34}^{\text{WSE}} = \begin{bmatrix} -7172.86 & -2911.07 & -39.97 & 0. & 0. & 0. \\ & -7172.86 & -39.97 & 0. & 0. & 0. \\ & & 391.95 & 0. & 0. & 0. \\ & & & 105.71 & 0. & 0. \\ & & & & 105.71 & 0. \\ & & & & & -6818.82 \end{bmatrix}$$

$$
\boldsymbol{\Omega}_{44}^{\mathrm{WSE}} =
\begin{bmatrix}
13953.80 & 2991.02 & 0. & 0. & 0. & 0. \\
 & 0. & 0. & 0. & 0. & 0. \\
 & & 0. & 0. & 0. & 0. \\
 & & & 0. & 0. & 0. \\
 & & & & 0. & 0. \\
 & & & & & 6607.38
\end{bmatrix}
$$

D.2.2 Tensors Ω_{IJ}^{P} associated to the P decomposition

$$
\boldsymbol{\Omega}_{12}^{\mathrm{P}} = \boldsymbol{\Omega}_{13}^{\mathrm{P}} = \boldsymbol{\Omega}_{23}^{\mathrm{P}} = \mathbf{0}
$$

$$
\boldsymbol{\Omega}_{11}^{\mathrm{P}} =
\begin{bmatrix}
0. & 0. & 0. & 0. & 0. & 0. \\
 & 9364.39 & 3627.18 & 0. & 0. & 0. \\
 & & 9364.39 & 0. & 0. & 0. \\
 & & & 8703.58 & 0. & 0. \\
 & & & & 0. & 0. \\
 & & & & & 0.
\end{bmatrix}
$$

$$
\boldsymbol{\Omega}_{14}^{\mathrm{P}} =
\begin{bmatrix}
0. & 0. & 0. & 0. & 0. & 0. \\
 & -7652.60 & -2964.14 & 0. & 0. & 0. \\
 & & -7652.60 & 0. & 0. & 0. \\
 & & & -7112.59 & 0. & 0. \\
 & & & & 0. & 0. \\
 & & & & & 0.
\end{bmatrix}
$$

$$
\boldsymbol{\Omega}_{22}^{\mathrm{P}} =
\begin{bmatrix}
9364.39 & 0. & 3627.18 & 0. & 0. & 0. \\
 & 0. & 0 & 0. & 0. & 0. \\
 & & 9364.39 & 0. & 0. & 0. \\
 & & & 0 & 0. & 0. \\
 & & & & 8703.58 & 0. \\
 & & & & & 0.
\end{bmatrix}
$$

$$
\boldsymbol{\Omega}_{24}^{\mathrm{P}} =
\begin{bmatrix}
-7652.60 & 0. & -2964.14 & 0. & 0. & 0. \\
 & 0. & 0. & 0. & 0. & 0. \\
 & & -7652.60 & 0. & 0. & 0. \\
 & & & 0. & 0. & 0. \\
 & & & & -7112.59 & 0. \\
 & & & & & 0.
\end{bmatrix}
$$

$$
\boldsymbol{\Omega}_{33}^{\mathrm{P}} =
\begin{bmatrix}
9364.39 & 3627.18 & 0 & 0. & 0. & 0. \\
 & 9364.39 & 0 & 0. & 0. & 0. \\
 & & 0 & 0. & 0. & 0. \\
 & & & 0. & 0. & 0. \\
 & & & & 0. & 0. \\
 & & & & & 8703.58
\end{bmatrix}
$$

$$
\boldsymbol{\Omega}_{34}^{\mathrm{P}} =
\begin{bmatrix}
-7652.60 & -2964.14 & 0. & 0. & 0. & 0. \\
 & -7652.60 & 0. & 0. & 0. & 0. \\
 & & 0. & 0. & 0. & 0. \\
 & & & 0. & 0. & 0. \\
 & & & & 0. & 0. \\
 & & & & & -7112.59
\end{bmatrix}
$$

$$
\boldsymbol{\Omega}_{44}^{\mathrm{P}} =
\begin{bmatrix}
13953.80 & 2991.02 & 0. & 0. & 0. & 0. \\
 & 0. & 0. & 0. & 0. & 0. \\
 & & 0. & 0. & 0. & 0. \\
 & & & 0. & 0. & 0. \\
 & & & & 0. & 0. \\
 & & & & & 6607.38
\end{bmatrix}
$$

D.3 Proof of the statement (3.99)

In order to prove that $\boldsymbol{\Omega}_{J\,2} : (\mathbf{e}_2 \otimes \mathbf{m}) = \mathbf{0}$, first let consider the integral

$$
I_2(\boldsymbol{\xi}) = \frac{1}{V} \int_{V_2} e^{i\boldsymbol{\xi}(p_\alpha).\mathbf{x}}
\tag{D.16}
$$

The integration domain V_2 consists of two parallel plates (see figure 109). For any positive or negative integers $(p_1, p_2, p_3) \neq (0,0,0)$, it is established that

$$
\begin{aligned}
I_2(p_1, p_2, p_3) &= \frac{1}{8L^3} \int_{-L}^{L} e^{\frac{-i\pi p_1 x_1}{L}}\, \mathrm{d}x_1 \times \left[\int_{-L}^{-c} e^{\frac{-i\pi p_2 x_2}{L}}\, \mathrm{d}x_2 + \int_{c}^{L} e^{\frac{-i\pi p_2 x_2}{L}}\, \mathrm{d}x_2 \right] \\
&\quad \times \int_{-L}^{L} e^{\frac{-i\pi p_3 x_3}{L}}\, \mathrm{d}x_3 \\
&= \begin{cases} 0 & \text{if} \quad p_1 \neq 0 \text{ or } p_3 \neq 0 \\ -\dfrac{1}{p_2 \pi} \sin\left(\dfrac{p_2 \pi c}{L}\right) & \text{if} \quad p_1 = p_3 = 0 \end{cases}
\end{aligned}
\tag{D.17}
$$

Hence, the sum (3.62) reduces to
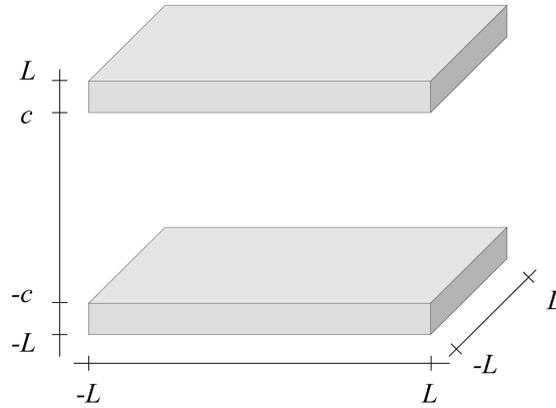
Figure 109 - View of the domain V_2.

$$
\boldsymbol{\Omega}_{J\,2} = 2 \sum_{p_2 > 0} I_J(0, p_2, 0) I_{K=2}(0, p_2, 0) \boldsymbol{\omega}(0, p_2, 0)
\tag{D.18}
$$

The second rank tensor $\mathbf{K}(0, p_2, 0)$ defined in equation (3.53) has the components $K_{ik}(0, p_2, 0) = C_{i2k2}\frac{\pi^2 p_2^2}{L^2}$ since $\xi_i(0, p_2, 0) = \delta_{i2}\frac{\pi p_2}{L}$ and its inverse is $V_{ik} = C_{i2k2}^{-1}\frac{L^2}{\pi^2 \xi_2}$. The components of the fourth rank tensor $\boldsymbol{\omega}(0, p_2, 0)$ defined in equation (3.58) become

$$
\begin{aligned}
\omega_{cdpq}(0, p_2, 0) &= C_{cdpq} - C_{cdkl}\xi_l(0, p_2, 0) V_{km}(0, p_2, 0)\xi_n(0, p_2, 0) C_{mnpq} \\
&= C_{cdpq} - C_{cdk2} C_{k2m2}^{-1} C_{m2pq}
\end{aligned}
\tag{D.19}
$$

For the product $\boldsymbol{\omega}(0, p_2, 0) : (\mathbf{e}_2 \otimes \mathbf{m})$, it follows

$$
\begin{aligned}
\omega_{cdpq}(0, p_2, 0) \left(\mathbf{e}_2 \otimes \mathbf{m}\right)_{pq} &= \omega_{cdpq}(0, p_2, 0)\delta_{2p}m_q \\
&= \omega_{cd2q}(0, p_2, 0)m_q \\
&= \left(C_{cdpq} - C_{cdk2}C^{-1}_{k2m2}C_{m2pq}\right)\delta_{2p}m_q \\
&= \left(C_{cd2q} - C_{cdk2}C^{-1}_{k2m2}C_{m22q}\right)m_q \\
&= \left(C_{cd2q} - C_{cdk2}\delta_{kq}\right)m_q \\
&= 0
\end{aligned}
\qquad (\text{D.20})
$$

Bibliography

[Douin] http://www.cemes.fr/Personnel/Douin/Simulations.html

[MicroMégas] http://zig.onera.fr/mm\home_page/index.html

[MSM] http://www.cam.ac.uk/phase-trans/2003/Superalloys/superalloys.html

[Pvm] http://www.csm.ornl.gov/pvm/

[ZéBuLoN] http://www.nwnumerics.com/Zebulon/Capabilities.html

[ACH00] A. Acharya, J.L. Bassani, Incompatibility and crystal plasticity. Journal of the Mechanics and Physics of Solids, **48**, 1565-1595, 2000.

[ACH01] A. Acharya, A model of crystal plasticity based on the theory of continuously distributed dislocations. Journal of the Mechanics and Physics of Solids, **49**, 761-784, 2001.

[ACH04] A. Acharya, Constitutive analysis of finite deformation field dislocation mechanics. Journal of the Mechanics and Physics of Solids, **52**, 301-316, 2004.

[AIF84] E.C. Aifantis, Towards a continuum approach to dislocation pattern. In: Markenscoff, X. (Ed.), Dislocations in Solids - Recent Advances, AMD-63, ASME, 23-33, 1984.

[AIF87] E.C. Aifantis, The physics of plastic deformation. International Journal of Plasticity, **3**, 211-248, 1987.

[AIF99] E.C. Aifantis, Gradient deformation models at nano, micro and macro scales. Journal of Engineering Materials and Technology, **121**, 189-202, 1999.

[ABO82] J. Aboudi, A continuum theory for fiber-reinforced elastic-viscoplastic composites. International Journal of Engineering Science, **20**, 605-621, 1982.

[ABO04] J. Aboudi, The generalized method of cells and high-fidelity generalized method of cells micromechanical models − a review. Mechanics of Advanced Materials and Structures, **11**, 329-366, 2004.

[ANT94] D. Anton, Ni_3Al in Nickel-Based Superalloys. In: J.H. Westbrook, R.L. Fleisher (Eds.), Intermetallic Compounds, **2**, Practice, John Wiley & Sons, New York, 3-15, 1994.

[ARM66] P. J. Armstong, C. O. Frederick, A mathematical representation of the multiaxial Bauschinger effect. CEGB Report No. RD/B/N 731.

[ARS99] A. Arsenlis, D. M. Parks, Crystallographic aspects of geometrically-necessary and statistically-stored dislocation density. Acta Meterialia, **47**, 1597-1611, 1999.

[ASA83] R. Asaro, Micromechanics of crystals and polycrystals. Advances in Applied Mechanics, **23**, 1-115.

[ASH70] M. F. Ashby, The deformation of plastically non-homogeneous materials. Philosophical Magazine A, **21**, 399-424, 1970.

[AZA00] A. El-Azab, Statistical mechanics treatment of the evolution of dislocation distributions in single crystals. Physical Review B, **61**, 11956-11966, 2000.

[BAL91] N. Baluc, H.P. Karnthaler, M.J. Mills, TEM observation of the fourfold dissociation of superlattice dislocations and the determination of the fault energies in $Ni_3(Al,Ta)$. Philosophical Magazine A, **64**, 137-150, 1991.

[BEA69] P. Beardmore, R.G. Davies, T.L. Johnson, On the temperature dependence of flow stress of Nickel-based alloys. Transactions of the Metallurgical Society of TMS-AIME, **245**, 1537-1545, 1969.

[BEL07] T. Belytschko, R. Gracie, On XFEM applications to dislocations in problems with interfaces. International Journal of Plasticity, **23**, 1721-1738, 2007.

[BEN04] A. A. Benzerga, Y. Bréchet, A. Needleman, E. Van der Giessen, Incorporing three-dimensional mechanisms into two-dimensional dislocation dynamics. Modelling and Simulation in Materials Science and Engineering, **12**, 159-196, 2004.

[BET99] D. Bettge, W. Österle, "Cube slip" in near-[111] oriented specimens of a single-crystal nickel-base superalloy. Scripta Materialia, **40**, 389-395, 1999.

[BON06] V. Bonnand, Etude de l'endommagement d'un superalliage monocristallin en fatigue thermo-mécanique multiaxiale. PhD-thesis, Ecole des Mines de Paris, 2006.

[BRO64] L.M. Brown, The self-stress of dislocations and the shape of extended nodes. Philosophical Magazine, 441-466, 1964.

[BRO71] L.M. Brown, R.K. Ham, Dislocation-Particle Interactions. Strenthening Methods in Crystals. A. Kelly and R.B. Nicholson, Elsevier, Amsterdam, 1971.

[BRO77] L.M. Brown, D.R. Clarke, The work hardening of fibrous composites with particular reference to the copper-tungsten system. Acta Metallurgica, **25**, 563-570, 1977.

[BRU02] G. Bruno, H.C. Pinto, W. Reimers, γ' nucleation and growth in the nickel based superalloy SC16. Journal of Applied Physics A, **74**, 940-942, 2002.

[BUL98] V.V. Bulatov, F.F. Abraham, L.P. Kubin, B. Devincre, S. Yip, Connecting atomistic and mesoscale simulations of crystal plasticity. Nature, **391**, 669-672, 1998.

[BUL56] R. Bullough, B.A. Bilby, Continuous distributions of dislocations and the crystallography of martensitic transformation. Proceedings of the Physical Society B, **69**, 1276-1286, 1956.

[BUS00] E. P Busso, F. T. Meissonnier, N. P. O'Dowd, Gradient-dependent deformation of two-phase single crystals. Journal of the Mechanics and Physics of Solids, **48**, 2333-2361, 2000.

[CAI06] W. Cai, A. Arsenlis, C. Weinberger, V. Bulatov, A non-singular continuum theory of dislocations. Journal of the Mechanics and Physics of the Solids, **54**, 561-587, 2006.

[CAI87] G. Cailletaud, Une approche micromécanique phénoménologique du comportement inélastique des métaux. PhD-thesis, Ecole des Mines de Paris, 1987.

[CAN91] G. R. Canova, L. P. Kubin, Dislocation microstructures and plastic flow: a three-dimensional simulation. Continuum models and discrete systems, ed. by Maugin G. A., 1991.

[CAR87] P. Caron, T. Khan, 'Advanced Materials and Processing Techniques for Structural Applications', T. Khan and A. Lasalmonie, ONERA internal report, 59, 1987.

[CAR99] P. Caron, T. Khan, Evolution of Ni-based superalloys for single crystals gas turbine blade applications. Aeropace Science and Technology, **3**, 513-523, 1999.

[CAR77] C. Carry, J.L. Strudel, Apparent and effective creep parameters in single crystals of a nickel base superalloy - I. Incubation period. Acta Metallurgica, **25**, 767-777, 1977.

[CER01] P. Cermelli, M. E. Gurtin, On the characterization of geometrically necessary dislocations in finite plasticity. Journal of the Mechanics and Physics of Solids, **49**, 1539-1568, 2001.

[CHA77] J.L. Chaboche, Viscoplastic constitutive equations for the description of cyclic and anisotropic behavior of metal. S. Bull. Acad. Polon. Sci., Série Sci. Tech. XXV (1), 33-39, 1977.

[CHA89] J.L. Chaboche, Constitutive Equations for Cyclic Plasticity and Cyclic Viscoplasticity. International Journal of Plasticity, **5**, 247-302, 1989.

[CHA01] J.L. Chaboche, S. Kruch, J.F. Maire, J. Pottier, Towards a micromechanics based inelastic and damage modeling of composites. International Journal of Plasticity, **17**, 411-439, 1992.

[CHI02] D. Chidambarrao, X.H. Liu, K.W. Schwarz, Combined dislocation and process modeling for local oxidation of silicon structure, **92**, 6278-6286, 2002.

[CHO05] Y.S. Choi, T.A. Parthasarathy, D.M. Dimiduk, M.D. Uchic, Numerical study of the flow responses and the geometric constraint effects in Ni-base two-phase single crystals unsing strain gradient plasticity. Materials Science and Engineering A, **397**, 69-83, 2005.

[CLE96] N. Clément, A. Coujou, M. Jouiad, P. Caron, H.O.K. Kirchner, T. Khan, Local order and mechanical properties of the γ matrix of nickel-base superalloys. Superalloys 1996, 239-248, 1996.

[CLE97] H.H.M Cleveringa, E. Van Der Giessen, A. Needleman, Comparison of discrete dislocation and continuum plasticity predictions for a composite material. Acta Materialia, **45**, 3163-3179, 1997.

[CLE98] H.H.M Cleveringa, E. Van Der Giessen, Discrete dislocation simulations and size dependent hardening in single slip. Journal de Physique, **8**, 83-92, 1998.

[COR01] T.H. Cormen, C.E. Leiserson, R.L. Rivest, C. Stein, Introduction to Algorithm, Second Edition. MIT Press and McGraw-Hill, 29.3: The simplex algorithm, 790-804, 2001.

[COS09] E. Cosserat, F. Cosserat, Théorie des corps déformables. Libraire scientifique A, Hermann et fils, Paris, 1909.

[DAI97] H. Dai, Geometrically-Necessary Dislocation density in continuum plasticity theory, FEM Implementation and Applications. PhD-thesis, Massachusetts Institute of Technology, 1997.

[DAV65] R.G. Davies, N.S. Stoloff, On the yield stress of aged Ni-Al alloys. Transactions of the Matellurgical Society of AIME, **233**, 714-719, 1965.

[DEC84] B. Décamps, M. Condat, P. Caron, T. Khan, Dissociated matrix dislocations in a γ/γ' Ni-based single crystal superalloy. Scripta Metallurgica, **18**, 1171-1174, 1984.

[DEC04] B. Décamps, S. Raujol, A. Coujou, F. Pettinari-Sturmel, N. Clément, D. Locq, P. Caron, On the shearing mechanism of γ' precipitates by a single $\frac{a}{6}\langle 112 \rangle$ Shockley partial in Ni-based superalloys. Philosophical Magazine, **84**, 91-107, 2004.

[DEM07] M. Demura, D. Golberg, T. Hirano, An athermal deformation model of the yield stress anomaly in Ni$_3$Al. Intermetallics, **15**, 1322-1331, 2007.

[DEN08] J. Deng, A. El-Azab, B.C. Larson, On the elastic boundary value problem of dislocations. Philosophical Magazine, **30**, 3527-3548, 2008.

[DEP04] C. Déprés, Modélisation physique des stades précurseurs de l'endommagement en fatigue dans l'acier inoxydable austénitique 316L. Ph. D. Thesis, Institut National Polytechnique de Grenoble, Laboratoire G énie Physique et Mécanique des Matériaux, 2004.

[DEP08] C. Déprés, M. Fivel., L. Tabourot, A dislocation-based model for low-amplitude fatigue behaviour of face-centred cubic single crystals. Scripta Materialia, **58**, 1086-1089, 2008.

[DeS07] C. de Sansal, Plasticité et effet de taille dans les polycristaux à grains micrométriques: simulations mésoscopiques et modélisation. PhD-thesis, Ecole Centrale Paris, 2007.

[DeS10] C. de Sansal, B. Devincre, L. Kubin, Grain size strengthening in microcrystalline copper: a three-dimensional dislocation dynamics simulation, Key Ingineering Materials, **423**, 25-32, 2010.

[DEV95] B. Devincre, Three dimensional stress fields expressions for straight dislocation segments, Solid State Communications, **93**, 875-878, 1995.

[DEV96] B. Devincre. Mesoscale simulation of the dislocation dynamics, in: H.O. Kirchner, V. Pontikis, L.P. Kubin (Eds.). Computer Simulation in Materials Science, North-Holland, Amsterdam, 309-323, 1996.

[DEV97] B. Devincre, P. Veyssière, L. P. Kubin, and G. Saada, A simulation of dislocation dynamics and of the flow stress anomaly in L1$_2$ alloy. Philosophical Magazine A, **75**, 1263, 1997.

[DEV99] B. Devincre, P. Veyssière, and G. Saada, Simulation of the plastic flow in Ni$_3$Al: work hardening and strain-rate sensitivity. Philosophical Magazine A, **79**, 1609, 1999.

[DEV01] B. Devincre, L. P. Kubin, C. Lemarchand, R. Madec, Mesoscopic simulations of plastic deformation. Materials Science and Engineering, **309**, 201-219, 2001.

[DEV03] B. Devincre, A. Roos, S. Groh, Boundary problems in DD simulations. In: Thermodynamics, Microstructures and Plasticity, A. Finel *et al.*, Nato Sciences Series II: Mathematics, Physics and Chemistry, **108**, p. 275, Eds (Kluwer, NL-Dordrecht), 2003.

[DEV05] B. Devincre, T. Hoc, L. Kubin, Collinear interactions of dislocations and slip systems. Materials Science and Engineering A, **400-401**, 182-185, 2005.

[DEV06] B. Devincre, L. Kubin, T. Hoc, Physical analyses of crystal plasticity by DD simulations, Scripta Materialia, **5**, 741-746, 2006.

[DEV07] B. Devincre, L. Kubin, T. Hoc, Collinear superjogs and the low-stress response of fcc crystals. Scripta Materials, **57**, 905-908, 2007.

[DEV08] B. Devincre, T. Hoc, L. Kubin, Dislocation mean free paths and strain hardening of crystals. Science, **320**, 1745-1748, 2008.

[DEW67] R. de Wit, Some relations for straight dislocations. Phys Stat Sol, **20**, 567-573, 1967.

[DIM91] D.M. Dimiduk, Dislocation structures and anomalous flow in L1$_2$ compounds. Journal de Physique, **1**, 1025-1053, 1991.

[DUH87] D. N. Duhl, Directionally solidified superalloys. High temperature materials for aerospace and industrial power. In Superalloys II, C. T. Sims, N. S. Stoloff, and W. C. Hage, John Wiley and Sons Ltd, New York, 1987.

[DVO92] G.J. Dvorak, Transformation field analysis of inelastic composite materials. Proceedings of the Physical Society of London, A**431**, 89-110, 1992.

[EMB71] J. Embury, Strengthening Methods in Crystals. A. Kelly, R.B. Nicholson (Eds), Applied Science Publishers, London, 1971.

[EPI05] A. Epishin, T. Link, U. Brückner, B. Fedelich, Residual stresses in the dendritic structure of single-crystal nickel-based superalloys. Fizika metallov i metallovedenie, **100**, 104-112, 2005.

[EPI08] A. Epishin, T. Link, M. Nazmy, M. Staubli, H. Klingelhoffer, G. Nolze, Microstructural degradation of CMSX-4: kinetics and effect on mechanical properties. Superalloys 2008, The Minerals, Metals and Materials Society, Champion, Pennsylvania, USA, 2008.

[ERI64] A.C. Eringen, E.S. Suhubi, Nonlinear theory of simple micro-elastic solids - I. International Journal of Engineering Science, **2**, 189-203, 1964.

[ESH51] J.D. Eshelby, The force on an elastic singularity. Philosophical Transactions of the Royal Society, **A62**, 307-314, 1951.

[ESH56] J.D. Eshelby, The continuum theory of lattice defect. In Solid State Physics 3, eds. F. Seitz and D. Turnbull, Academic Press, 79-144, 1956.

[ESP96] L. Espié, Etude expérimentale et modélisation numérique du comportement mécanique de monocristaux de superalliages. PhD-thesis, Ecole des Mines de Paris, 1996.

[ESS79] U. Essmann, H. Mughrabi, Annihilation of dislocations during tensile and cyclic deformation and limits of dislocation densities. Philosophical Magazine, **40**, 731-756, 1979.

[EVE04] L. P. Evers, W. A. M. Brekelmans, M. G. D. Geers, Scale dependent crystal plasticity framework with dislocation density and grain boundary effects. International Journal of Solids and Structures, **41**, 5209-5230, 2005.

[FED99] B. Fedelich, A microstructure based constitutive model for the mechanical behavior at high temperatures of nickel-base single crystal superalloys. Computational Materials Science, **16**, 248-258, 1999.

[FED02] B. Fedelich, A microstructural model for the monotonic and the cyclic mechanical behavior of single crystals of superalloys at high temperatures. International Journal of Plasticity, **18**, 1-49, 2002.

[FED02b] B. Fedelich; J. Beckman, M. Finn, M. Zelewski, J. Olschewski, Determination of temperature dependent elastic constants of anisotropic materials by Resonance Method, Materials Week 2002, DGM.eV., Munich, 2002.

[FED08] B. Fedelich, G. Künecke, A. Epishin, T. Link, P.D. Portella, Constitutive modelling of creep degradation due to rafting in single crystal Ni-base superalloys. Creep 2008, Bayreuth, Germany, 2008.

[FED09] B. Fedelich, G. Künecke, A. Epishin, T. Link, P.D. Portella, Constitutive modelling of creep degradation due to rafting in single crystal Ni-base superalloys. Materials Science and Engineering A, **510-511**, 273-277, 2009.

[FEL89] M. Feller-Kniepmeier, T. Link, Dislocation structures in $\gamma - \gamma'$ interfaces of the single-crystal superalloy SRR99 after annealing and high temperature creep. Science and Engineering A **113**, pp. 191-195, 1989.

[FEY00] F. Feyel, J.L. Chaboche, FE^2 multiscale approach for modelling the elastoviscoplastic behaviour of long fibre SiC/Ti composite materials. Computer Methods in Applied Mechanics and Engineering, **183**, 309-330, 2000.

[FIV99] M. Fivel, G. R. Canova, Developing rigorous boundary conditions to simulations of discrete dislocation dynamics. Modelling and Simulation in Materials Science and Engineering, 7, 753-768, 1999.

[FIV04] M. Fivel, S. Forest, Plasticité cristalline et transition d'échelle : cas du monocristal. Techniques de l'ingénieur. Matériaux métalliques ISSN 1762-8733, **M4016**, pp. M4016.1-M4016.20, 2004.

[FLE94] N. A. Fleck, G. M. Müller, M. F. Ashby, J.W. Hutchinson, Strain gradient plasticity: theory and experiment. Acta Materialia, **42**, 475-487.

[FLE97] N. A . Fleck, J. W. Hutchinson, Strain gradient plasticity. Advances in Applied Mechanics, **33**, 195-361, 1997.

[FLE01] N. A. Fleck, J.W. Hutchinson, A reformulation of strain gradient plasticity. Journal of the Mechanics and Physics of Solids, **49**, 2245-2271, 2001.

[FLE63] R.L. Fleischer, Substitutional solution hardening. Acta Metallurgica, **11**, 203-209, 1963.

[FLE96] G. Fleury, F. Schubert, H. Nickel, Modelling of the thermo-mechanical behaviour of the single crystal superalloy CMSX-4. Computaional Materials Science, **7**, 187-193, 1996.

[FLO04] S. Flouriot, Détermination expérimentale et simulation numérique des phénomènes de localisation de la déformation en pointe de fissure dans un monocristal C.F.C. Ph. D. Thesis, Ecole des Mines de Paris, 2004.

[FOE97] R. Foerch, J. Besson, G. Cailletaud, P. Pilvin. Polymorphic constitutive equations in finite element codes. Computer Methods in Applied Mechanics and Engineering **7**, 187-193, 1997.

[FOR55] A.J.E. Foreman, Dislocation energies in anisotropic crystals. Acta Metallurgica, **3**, 322-330, 1955.

[FOR67] A. J. E. Foreman, The bowing of a dislocation segment. Philosophical Magazine, **15**, 1011-1021, 1967.

[FOR00] S. Forest, F. Barbe, G. Cailletaud, Cosserat modelling of size effects in the mechanical behavior of polycrystals and multi-phase materials. International Journal of Solids and Structures, **37**, 7105-7126, 2000.

[FOR01] S. Forest, P. Boubidi, R. Sievert, Strain localization patterns at a crack tip in generalized single crystal plasticity. Scripta Materialia, **44**, 953-958, 2001.

[FOR03] S. Forest, R. Sedláček, Plastic slip distribution in two-phase laminate microstructures: Dislocation-based vs. generalized-continuum approaches. Philosophical Magazine, **83**, 245-276, 2003.

[FOR06] S. Forest, Milieux continus généralisés et matériaux hétérogènes. Presses de l'Ecole des Mines de Paris, 2006.

[FOT96] P.A. Fotiu, S. Nemat-Nasser, Overall properties of elastic-viscoplastic periodic composites. International Journal of Plasticity, **12**, 163-190, 2996.

[FRA80] P. Franciosi, M. Berveiller, Latent hardening in copper and aluminium single crystams. A. Zaoui, Acta Materialia, **28**, 273-283, 1980.

[FRA82] P. Franciosi, A. Zaoui, Multislip in F.C.C. crystals; a theoretical approach compared with experimental data. Acta Metallurgica, **30**, 1627-1637, 1982.

[FRA51] F. C. Frank, Crystal dislocations - Elementary concepts and definitions. The Philosophical Magazine, **42**, 809-819, 1951.

[FRA91] D. François, A. Pineau, A. Zaoui, Comportement mécanique des matériaux: élasticité et plasticité. Hermès, Paris, 1991.

[FRE87] A. Fredholm, Monocristaux d'alliage base Nickel: Relation entre composition, microsctructure et comportement mécanique á hautes températures. PhD-thesis, Ecole des Mines de Paris, 1987.

[FRE09] C. Fressengeas, A. J. Beaudoin, D. Entemeyer, T. Lebedkina, M. Lebyodkin, V. Taupin, Dislocation transport and intermittency in the plasticity of crystalline solids. Phys. Rev, **79**, 2009.

[GAO99] H. Gao, Y. Huang, W.D. Nix, J.W. Hutchinson, Mechanism-based strain gradient plasticity - I. Theory. Journal of the Mechanics and Physics of Solids, **47**, 1239-1263, 1999.

[GER73] Cours de M/'ecanique des Milieux Continus. Volume **I**, Masson, Paris, 1973.

[GHO99] N.M. Ghoniem, L.Z. Sun, Fast-sum method for the elastic field of three-dimensional dislocation ensembles. Physical Review B, **60**, 128-140, 1999.

[GHO00] N. M. Ghoniem, B. N. Singh, L.Z. Sun, T. D. de la Rubia, Interaction and accumulation of glissile defect clusters near dislocations. Journal Nucl. Mater., **276**, 166-177, 2000.

[GIL93a] J. Gil Sevillano, Flow stress and work hardening. In Mughrabi H, editor. Plastic deformation and fracture of materials. Weinheim: VCH, 19, 1993.

[GIL93b] G. Sevillano, Low stress and work hardening. In: Cahn, R.W. Haasen, P. Kramer, E. Mughrabi (Eds), Materials Science and Technology, **6**, 19-88, 1993.

[GLA89] U. Glazel, M. Feller-Kniepmeier, Calculations of internal stresses in the γ/γ' microstructures of a nickel-base superalloy with high volume fraction of γ'-phase. Scripta Metallurgica, **23**, 1839-1844, 1989.

[GLA94] U. Glazel, Microstructure and internal strains of undeformed and creep deformed samples of a nickel-base superalloy. Verlag Dr. Köster, Berlin, 1994.

[GOM99] D. Gómez-García, B. Devincre, L. Kubin, Dislocation dynamics in confined geometry. Journal of Computer-Aided Materials Design, **6**, 157-164, 1999.

[GOM00] D. Gómez-García, B. Devincre, L. Kubin, Forest hardening and boundary conditions in 2D simulations of dislocation dynamics. In: Multiscale Phenomena in Materials-Experiments and Modeling, MRS Warrendale, Pennsylvania, **578**, 131-136, 2000.

[GOM06] D. Gómez-García, B. Devincre, L. Kubin, Dislocation patterns and the similitude principle: 2.5d mesoscale simulations. Physical Review Letters, **12**, 125503, 2006.

[GRA07] R. Gracie, G. Ventura, T. Belytschko, A new fast finite element method for dislocations based on interior discontinuities. International Journal for Numerical Methods in Engineering, 69, 423-441, 2007.

[GRA08] R. Gracie, J. Oswald, T. Belytschko, On a new extended finite element method for dislocations: Core enrichment and nonlinear formulation. Journal of the Mechanics and Physics of Solids, **56**, 200-214, 2008.

[GRO03a] Simulation de la plasticité des matériaux cristallins par le modèle discret-continu. PhD-thesis, University of Orsay, Paris XXI, 2003.

[GRO03b] S. Groh, B. Devincre, L.P. Kubin, A. Roos, F. Feyel, J.L. Chaboche, Dislocations and elastic anisotropy in heteroepitaxial metallic thin films. Philosophical Magazine Letters, **83**, p. 303, 2003.

[GRO04] S. Groh, B. Devincre, F. Feyel, L.P. Kubin, A. Roos, J.L. Chaboche, Discrete-Continuum Modeling of Metal Matrix Composites Plasticity. In: Mesoscopic Dynamics in Fracture Process and Strength of Materials, Y. Shibutani, H. Kitagawa, Eds (Kluwer, NL-Dordrecht), **115**, 235-244, 2003.

[GRO97] I. Groma, Link between the microscopic and mesoscopic length-scale description of collective behavior of dislocations. Physical Review B, **56**, 5807-5813, 1997.

[GRO03] I. Groma, F.F. Csikor; M. Zaiser, Spatial correlations and higher-order gradient terms in a continuum description of dislocation dynamics. Acta Materialia, **51**, 1271-1281, 2003.

[GUR00] M.E. Gurtin, On the plasticity of single crystals: free energy, microforces, plastic-strain gradients. Journal of the Mechanics and Physics of Solids, **48**, 898-1036, 2000.

[GUR02] M.E. Gurtin, A gradient theory of single-crystal viscoplasticity that accounts for geometrically necessary dislocations. Journal of the Mechanics and Physics of Solids, **50**, 5-32, 2002.

[GUR07] M.E. Gurtin, L. Anand, S.P. Lele, Gradient single-crystals plasticity with free energy dependent on dislocation densities. Journal of the Mechanics and Physics of Solids, **55**, 1853-1878, 2007.

[GUR08] P. J. Guruprasad, W. J. Carter, A. A. Benzerga, A discrete dislocation analysis of the Bauschinger effect in microcrystals. Acta Materialia, **56**, 5477-5491.

[HAL51] E.O. Hall, The deformation and aging of mild steel. Part III: discussion and results. Proceedings of the Physical Society of London, **64**, 747-753, 1951.

[HAN91] F. Hanriot, G. Cailletaud, L. Rémy, Mechanical behaviour of a nickel based superalloy single crystal. In A. Freed, K. Walker, Editeurs : High temperature constitutive modelling - Theory and application, ASME, New-York, pp. 139-150. ASME, 1991.

[HAR98] J. Harder, A crystallographic model for the study of local deformation processes in polycrystals. International Journal of Plasticity, **15**, 605-624, 1998.

[HEL03] D. Helm, P. Haupt, Shape memory behavior: modelling within continuum thermomechanics. International Journal of Solids and Structure, 40, 827-849, 2003.

[HIL66] R. Hill, Generalized constitutive relations for incremental deformation of metal crystals by multislip. Journal of the Mechanics and Physics of Solids, **14**, 95-102, 1966.

[HIR82] J.P. Hirth, J. Lothe, Theory of Dislocations. John Wiley & Sons, New York, 1982.

[HIR60] P.B. Hirsch, A. Howie, M.J. Whelan, A kinematical theory of diffraction constrast of electron transmission microscope images of dislocations and other defects. Philosophical Transactions of the Royal Society, **A252**, 499-529, 1960.

[HIR92] P.B. Hirsch, A new theory of the anomalous yield stress in $L1_2$ alloys. Philosophical Magazine A, **65**, 569-612, 1992.

[HOC06] T. Hochrainer, M. Zaiser, P. Gumbsch, A three-dimensional continuum theory of dislocation systems: Kinematics and mean-field formulation. Philosophical Magazine, **87**, 1261-1282, 2006.

[HOR91] E. Hornbogen, H. Warlimont, Aufbau und Eigenschaften von Metallen und Legierungen. Metallkunde (Berlin: Springer), 134-144, 1991.

[HUT76] J. W. Hutchinson, Bounds and self-consistent estimates for creep of polycrystalline materials. Proceedings of the Royal Society of London, Series A, **348**, 101-127, 1076.

[JIL50] D.C. Jillson, Quantitative Stress-Strain Studies on Zinc Single Crystals in Tension. Transactions of the Metallurgical Society of AIME, Journal of Metals, **188**, 1129-1133, 1950.

[JUM94] K. Jumonji, S. Ueta, S. Kato, A. Sato, Temperature dependence of strain-rate sensitivity, work hardening and dislocation structure in Ni_3Al single crystals. Philosophical Magazine A69, 1111-1124, 1994.

[KEA62] B.H. Kear, H.G.F. Wilsdorf, Dislocation configurations in plastically deformed Cu_3Au alloys. Transactions of the Metallurgical Society of AIME, **224**, 382-386, 1962.

[KEL93] R.R. Keller, H.J. Maier, H. Mughrabi, Characterization of interfacial dislocation networks in a creep-deformed nickel-base superalloy. Scripta Metallurgica et Materialia, **28**, 23-28, 1993.

[KHA83] A.G. Khachaturyan, Theory of Structural Transformations in Solids. John Wiley and Sons, New York, 1983.

[KHA95] A. S. Khan, S. Huang, Continuum Theory of Plasticity. A Wiley-Interscience Publication. John Wiley & Sons, New York, 1995.

[KRA07] J. Kratochvíl, M. Kružík, R. Sedláček, Statistically based continuum model of misoriented dislocation cell structure formulation. Physical Review B, **75**, 2007.

[KRA75] A.S. Krauss, H. Eyring, Deformation kinetics. John Wiley & Sons, New York, 1975.

[KRA96] A.S. Krauss, K. Krauss, Unified Constitutive Laws of Plastic Deformation. Academic Press Inc., 1996.

[KRO58] E. Kröner, Kontinuumstheorie der Versetzungen und Eigenspannungen. In L. Collatz, F. Lösch (Editors): Ergebnisse der angewandten Mathematik, **5**, Springer, 1958.

[KRO94] F. Kroupa, Short range interaction between dislocations. Key Engineering Materials, **97-98**, 377-382, 1994.

[KOC75] U.E. Kocks, A. S. Argon, M. F. Ashby, Thermodynamics and kinetics of slip. Progress in Materials Science, ed by L. P. Kubin, R. L. Selinger, J. L Bassani, K. Cho, 1975.

[KOC76] U. E. Kocks, Laws for work-hardening and low-temperature creep. Journal of Engineering Materials and Technology, **98**, 16-85.

[KOC03] U.F. Kocks, H. Mecking, Physics and phenomenology of strain hardening: the FCC case. Progress in Materials Science, **48**, 171-273, 2003.

[KON52] K. Kondo, On the geometrical and physical foundations of the theory of yielding. Proceedings of the Japan National Congress of Applied Mechanics, **2**, 41, 1952.

[KUB90a] L.P. Kubin, G. Canova, The formation of ordered dislocation microstructures. In: U. Messerschmidt *et al.* (Eds), Electron Microscopy in Plasticity and Fracture Research of Materials, Akademie Verlag, Berlin, 23-32, 1990.

[KUB90] L.P. Kubin, Y. Estrin, G. Canova, Defects and materials instabilities. In D. Walgraef and N. M. Ghoniem, editors, NATO ASI series, 277, Kluwer, Dordrecht, Netherlands, 1990.

[KUB91] L.P. Kubin, Y. Estrin, C. Perrier, On static strain ageing. Acta Metallurgica et Materialia, **40**, 1037-1044, 1991.

[KUB92] L. Kubin, G. Canova, M. Condat, B. Devincre, V. Pontikis, Y. Bréchet, Dislocation microstructures and plastic flow: a 3D simulations. Solid State Phenomena, **23/24**, 455-472, 1992.

[KUB03] L. Kubin, R. Madec, B. Devincre, Dislocations interactions and reactions in FCC and BCC crystals. Multiscale Phenomena in Materials-Experiments and Modeling Related to Mechanical Behavior, H. Zbib *et al.* (Eds.), Materials Research Society Symposium Proceeding, **779**, 25-36, 2003.

[KUB06] L.P. Kubin, B. Devincre, T. Hoc, Inhibited dynamic recovery and screw dislocation annihilation in multiple slip of fcc single crystals. Philosophical Magazine, **86** (25-26), 4023-4036, 2006.

[KUB08] L.P. Kubin, B. Devincre, T. Hoc, Modeling dislocation storage rates and mean free paths in face-centered cubic crystals. Acta Materialia, **20**, 6040-6049, 2008.

[KUB09] L.P. Kubin, T. Hoc, B. Devincre, Dynamic recovery and its orientation dependence in face-centered cubic crystals. Acta Materialia, **57**, 2567-2575, 2009.

[KUT98] T. Kuttner, R.P. Wahi, Modelling of internal stress distribution and deformation behaviour in the precipitation hardened superalloy SC16. Materials Science and Engineering A, **242**, 259-267, 1998.

[LEE69] E.H. Lee, Elastic-plastic deformation at finite strains. Journal of Applied Mechanics, ASME, **39**, 1-9, 1969.

[LEF06] S. Lefèbvre, Etude expérimentale et simulation numérique du comportement mécanique de structures sub-micromécaniques de cuivre: application aux interconnexions dans les circuits intégrés. PhD-thesis, Ecole Centrale Paris, 2006.

[LEM85] J. Lemaître, J.L. Chaboche, Mécanique des Matériaux Solides. Dunod, Paris, 1985.

[LEM99] De la dynamique des dislocations à la mécanique des milieux continus: Développement et application d'une simulation micro-macro. PhD-thesis, University of Orsay, Paris XXI, 1999.

[LEM99a] C. Lemarchand, B. Devincre, L.P. Kubin, J.L. Chaboche, Coupled meso-macro simulations of plasticity: Validation tests. In Multiscale Modelling of Materials, V. Bulatov, T. Diaz de la Rubia, T. Phillips, R. andKaxiras, and N. Ghoniem, Eds., MRS, Warrendale, Pennsylvania, **538**, 63-68, 1999.

[LEM99b] C. Lemarchand, J.L. Chaboche, B. Devincre, L.P. Kubin, Multiscale modelling of plastic deformation. Journal de Physique, IV **9**, 271, 1999.

[LEM00] C. Lemarchand, B. Devincre, L.P. Kubin, J.L. Chaboche, Dislocations and internal stressses in thin films: a discrete continuum simulation. In Multiscale Phenomena in materials experiments and modeling, R. et al., Ed., MRS, Warrendale, Pennsylvania, **578**, 87-92, 2000.

[LEM01] C. Lemarchand, B. Devincre, L. P. Kubin, Homogenization method for discrete-continuum simulation of dislocation dynamics. Journal of the Mechanics and Physics of Solids, **49**, 1969-1982, 2001.

[LEP87] J. Lépinous, L. P. Kubin, The dynamic organization of dislocation structures: a simulation. Scripta Metallurgica, **21**, 833-837, 1987.

[LEV06] V. Levkovitch, R. Sievert, B. Svendson, Simulation of deformation and lifetime behavior of a fcc single crystal superalloy at high temperature under low-cycle fatigue loading. International Journal of Fatigue, **28**, 1791-1802, 2006.

[LI64] J. C. M. Li, Stress field of a dislocation segment. The Philosophical Magazine, **10**, 1097-1098, 1964.

[LIM99] Y. Y. Lim, M. M. Chaudhri, The effect of the indenter load on the nanohardness of ductile metals: An experimental study on polycrystalline work-hardened and annealed oxygen-free copper. Philosophical Magazine A, **79**, 2979-3000, 1999.

[LIN07] T. Link, P. Portella, Microstructural degradation of the single-crystal superalloy CMSX-4 during annealing under load: Implementation of rafting kinetics in mechanical modelling. Interim report of the DFG project, PO 405/10- LI 494/4-1, 2007.

[LIU09] Z. L. Liu, X. M. Liu, Z. Zhuang, X. C. You, A multi-scale computational model of crystal plasticity at submicron-to-nanometer scales. International Journal of Plasticity, **25**, 1436-1455, 2009.

[LOT59] J. Lothe, J.P. Hirth, Dislocation dynamics at low temperatures. Physical Review, **115**, 543-550, 1959.

[MA06] A. Ma, F. Roters, D. Raabe, A dislocation density based constitutive model for crystal plasticity FEM including geometrically necessary dislocations. Acta Materialia, **54**, 2169-2179, 2006.

[MAC01] D.W. MacLachlan, L. W. Wright, S. Gunturi, D.M. Knowles, Constitutive modelling of anisotropic creep deformation in single crystal blade alloys SRR99 and CMSX-4, International Journal of Plasticity, **17**, 441-467, 2001.

[MAD01] R. Madec, B. Devincre, L.P. Kubin, New line model for optimized dislocation dynamics simulations. In "Multiscale Modeling of Materials-2000", L. Kubin *et al.* (Eds.), Materials Research Society Symposium Proceedings, **653**, 2001.

[MAD02] R. Madec, B. Devincre, L.P. Kubin, From Dislocation Junctions to Forest Hardening. Physical Review Letters, **89**, 255508, 2002.

[MAD03] R. Madec, B. Devincre, L.P. Kubin, T. Hoc, D. Rodney, The role of collinear interaction in dislocation-induced hardening. Science, **301**, 1879-1882, 2003.

[MAD04] R. Madec, B. Devincre, L.P. Kubin, On the use of periodic boundary conditions in dislocation dynamics simulation. Mesoscopic Dynamics in Fracture Process and Strength of Materials, ed. by Y. Shibutani, H. Kitagawa, 2004.

[MAD05] R. Madec, L.P. Kubin, Dislocation dynamics in BCC metals: interaction strengths in the athermal regime. In: Vincenzini, P. Lami (Eds.), Third International Conference Computational Modeling and Simulation of Materials - Part A, 671-680, 2005.

[MAN65] J. Mandel, Une généralisation de la théorie de la plasticité de W.T. Koiter. International Journal of Solids and Structures, **1**, 173-195, 1965.

[MAR61] M.J. Marcinkowski, N. Brown, R.M. Fisher, Dislocation configurations in $AuCu_3$ and AuCu type superlattices. Acta Metallurgica, **9**, 129-137, 1961.

[MAR06] N. Marchal, Propagation de fissure en fatigue-fluage à haute température de superalliages monocristallins à base de nickel. PhD-thesis, Ecole des Mines de Paris, 2006.

[MAU92] G. Maugin, The Thermomechanics of Plasticity and Fracture. Cambridge University Press, Cambridge, 1992.

[McD92] D. McDowell, A Nonlinear Kinematic Hardening Theory for Cyclic Thermoplasticity and Thermoviscoplasticity. International Journal of Plasticity, **8**, 695-728, 1992.

[McL85] M. McLean, On the threshold stress for dislocation creep in particle strengthened alloys. Acta Metallurgica, **33**, 545-556, 1985.

[MEI01] F.T. Meissonnier, E.P. Busso, N.P. O'Dowd, Finite element implementation of a generalised non-local rate-dependent crystallographic formulation for finite strains. International Journal of Plasticity, **17**, 601-640, 2001.

[MER91] L. Méric, P. Poubanne, G. Cailletaud, Single crystal modeling for structural calculations: part 1-model presentation. Journal of Engineering Materials and Technology, **113**, 162-170, 1991.

[MER92] L. Méric, G. Cailletaud, Finite element implementation of a model for crystals at finite strain. In: P. Ladeveze, O. C. Zienkewicz (Editors), New Adv Comp Struc Mech, 1992.

[MIN64] R.D. Mindlin, Microstructure in linear elasticity. Archive for Rational Mechanics and Analysis, **16**, 51-78, 1964.

[MIN68] R.D. Mindlin, N.N. Eshel, On first strain gradient theories in linear elasticity. International Journal of Solids and Structures, **4**, 109-124, 1968.

[MIN86] R.V. Miner, T.P. Gabb, J. Gayda, K.J. Hemker, Orientation and temperature dependence of some mechanical properties of the single-crystal nickel-base superalloy René N4 : Part III. Tension-compression anisotropy. Metallurgical and Materials Transactions A, **17**, pp. 507-512, 1986.

[MIU98] S.Miura, S. Ochiai, Y. Oya, Y. Mishima, T. Suzuki, in: High Temperature Ordered Intermetallic Alloys III, MRS Symp. Proc., Volume **133**, eds C.T. Liu, A.I. Taub, N.S. Stoloff and C.C. Koch (Materials Res. Soc., Pittsburgh), 241, 1989.

[MOH99] V. Mohles, D. Ronnpagel, E. Nembach, Simulations of dislocation glide in precipitation hardened materials. Computational Materials Science, **16**, 144-150, 1999.

[MOH01] V. Mohles, Computer simulations of particle strengthening: lattice mismatch strengthning.Materials Science and Engineering A, **319-321**, 201-205, 2001.

[MOH04] V. Mohles, The critical resolved shear stress of single crystals with long-range ordered precipitates calculated by dislocation dynamics simulations. Materials Science and Engineering A, **365**, 144-150, 2004.

[MON06] G. Monnet, B. Devincre, Solute friction and forest interaction. Philosophical Magazine, **11**, 1555-1565, 2006.

[MOR98] A. Mortensen, O. Pedersen, H. Lilholt, On the work hardening of fiber reinforced copper. Scripta Materialia, **38**, 1109-1115, 1998.

[MUK96] D. Mukherji, R.P. Wahi, Some implications of the particle and climb geometry on the climb resistance in nickel-base superalloys. Acta Materialia, **44**, 1529-1539, 1996.

[MUR63] T. Mura, Continuous distribution of moving dislocations. Philosophical Magazine, **8**, 843, 1963.

[MUR87] T. Mura, Micromechanics of defects in solids. Kluwer Academic Publishers, Dordrecht, The Netherlands, 1987.

[NAB51] F.R.N. Nabarro, The synthesis of elastic dislocation fields. Philosophical Magazine, **42**, 1224-1231, 1951.

[NAB97] P. Veyssière, G. Saada, Microscopy and plasticity of the L1$_2$ γ' phase, in "Dislocations in Solids", **10**, p 253, 1997.

[NAT89] M.V. Nathal, J.O. Diaz, R.V. Miner, High temperature creep behavior of single crystal gamma prime and gamma alloys. In High Temperature Ordered Intermetallic Alloys III, C.T. Liu, A.I. Taub, N.S. Stoloff, C.C. Koch (Eds.), Materials Research Society, Pittsbourg, PA, 269-274, 1989.

[NEM85] E. Nembach, G. Neite, Precipitation Hardening of Superalloys by Ordered γ'-Particles. In J.W. Christian, P. Haasen, T.B. Massalski (Eds.). Progress in Materials Science, Pergamon Press, U.K., 177-319, 1985.

[NEM00] E. Nembach, Order strengthening: recent developments, with special reference to aluminium-lithium-alloys. Progress in materials science, **45**, 275-338, 2000.

[NOU89] D. Nouailhas, Unified modelling of cyclic viscoplasticity. International Journal of Plasticity, **5**, 501-520, 1989.

[NOU95] D. Nouailhas, G. Cailletaud, Finite element analysis of the mechanical behavior of two-phase single-crystal superalloys. Scripta Metallurgica, **34**, 565-571, 1995.

[NOU96] D. Nouailhas, G. Cailletaud, Tension-Torsion behavior of single-crystal superalloys: experiment and finite element analysis. International Journal of Plasticity, 11, 451-470, 1996.

[NOU97] D. Nouailhas, S. Lhuillier, On the micro-macro modelling of γ/γ' single crystal behavior. Computational Materials Science, **9**, 177-187, 1997.

[NYE53] J. F. Nye, Some geometrical relations in dislocated crystals. Acta Metallurgica, **1**, 153-162, 1953.

[OHA97] T. Ohashi, Finite element analysis of plastic slip and evolution of geometrically necessary dislocations in fcc crystals. Philosophical Magazine Letters, **75**, 51-58, 1997.

[OHA04] T. Ohashi, Three dimensional structures of the geometrically necessary dislocation in matrix-inclusion systems under uniaxial tensile loading. International Journal of Plasticity, **20**, 1093-1109, 2004.

[OHN93] N. Ohno, J. Wang, Kinematic hardening rules with critical state of dynamic recovery. Part I: Formulation and basic features for ratchetting behavior. International Journal of Plasticity, **9**, 375-390, 1993.

[ORO48] E. Orowan, Discussion on Internal Stresses. Symposium on Internal Stresses in Metals, Institute of Metals, London, 451-453, 1948.

[OST99] W. Österle, D. Bettge, B. Fedelich, H. Klingelhöffer, Modelling the orientation and direction dependence of the critical resolved shear stress of nickel-base superalloy single crystals. Acta Materialia, **48**, 689-700, 1999.

[OST00] W. Österle, D. Bettge, B. Fedelich, H. Klingelhöffer, Modelling the orientation and direction dependence of the critical resolved shear stress of nickel-base superalloy single crystals. Acta Materialia, **48**, pp. 689-700, 2000.

[PAI84] V. Paidar, D.P. Pope, V. Vitek, A theory of the anomalous yield behavior in L1$_2$ ordered alloys. Acta Metallurgica, **435**, 1984.

[PAL92] M. Paley, J. Aboudi, Micromechanical analysis of composites by the generalized method of cells. Mechanics of Materials, **14**, 127-139, 1992.

[PAR04] T.A. Parthasarathy, S.I. Rao, D.M. Dimiduk, A fast spreadsheet model for the yield strengh of superalloys, Superalloys 2004 edited by TMS (The Minerals, Metals & Materials Society), 2004.

[PET99] F. Pettinari, Mécanismes élémentaires de la déformation de phases γ d'une nouvelle génération de superalliages base nickel. Rôle du Rhénium et du Ruthénium. PhD-thesis, Université Paul Sabatier de Toulouse, 1999.

[PIE67] B.J. Piearcey, B.H. Kear, R.W. Smashey, Correlation of structure with properties in a directionally solidified nickel-base superalloy. Transactions of the American Society for Metals, **60**, 634-643, 1967.

[PIE82] D. Pierce, R. Asaro, A. Needleman, An analysis of nonuniform and localized deformation in ductile single crystals. Acta Metallurgica, **30**, 1087-1119, 1982.

[PIP08] J.M. Pipard, N. Nicaise, O. Bouaziz, M. Berveiller, A new mean field micromechanical approach to capture grain size effects. Computational Materials Science, **45**, 604-610, 2008.

[POL90] H. Policella, P. Paulmier, D. Pacou, Mechanical behavior of the Single-Crystal Alloy CMSX2 at High Temperature: Experimental Results. La Recherche Aérospatiale, **4**, French and English eds., 1990.

[POL92] T.M. Pollock, A.R. Argon, Creep resistance of CMSX-3 nickel base superalloy single crystals. Acta Metallurgica et Materialia, **40**, 1-30, 1992.

[POP84] D.P. Pope, S.S. Ezz, Mechanical properties of Ni_3Al and nikel-base alloys with high volume fraction of γ'. International metals reviews, **29**, 136-167, 1984.

[POU89] P. Poubanne, Etude et modélisation du comportement mécanique d'un superalliage monocristallin pour aube de turbine. PhD-thesis, Ecole Centrale de Paris, 1989.

[PRA49] W. Prager, Recent developments in the mathematical theory of plasticity. Journal of Applied Physics, **20(3)**, 235-241, 1949.

[PRE08] J. Preussner, Y. Rudnik, H. Brehm, R. Völkl, U. Glatzel, A dislocation density based material model to simulate the anisotropic creep behavior of single-phase and two-phase single crystals. International Journal of Plasticity, **25**, 973-994, 2008.

[PRE09] J. Preussner, Y. Rudnik, H. Brehm, R. Völkl, U. Glatzel, A dislocation density based material model to simulate the anisotropic creep behavior of single-phase and two-phase single crystals. International Journal of Plasticity, **25**, 973-994, 2009.

[PRO04] B.C. Prorok, Y. Zhu, H.D. Espinosa, Z. Guo, Z. Bazant, Y. Zhao, B.I. Yakobson, Micro- and nanomechanics. In: H.S. Nalwa, Editor, Encyclopedia of Nanoscience and Nanotechnology, American Scientific Publishers, **5**, 555-600, 2003.

[QUE09a] S. Queyreau, B. Devincre, Bauschinger effect in precipitation-strengthened materials: a dislocation dynamics investigation, Philosophical Magazine Letters, **7**, 419-430, 2009.

[QUE09b] S. Queyreau, G. Monnet, B. Devincre, Slip systems interactions in α-iron determined by dislocation dynamics simulations. International Journal of Plasticity, **25**, 361-377, 2009.

[RAO04] S.I. Rao, T.A. Parthasarathy, D.M. Dimiduk, P.M. Hazzledine, Discrete dislocation simulations of precipitation hardening in superalloys. Philosophical Magazine, **84**, 3195-3215, 2004.

[RAO06] S.I. Rao, T.A. Parthasarathy, D.M. Dimiduk, P.M. Hazzledine, Discrete dislocation simulations of precipitation hardening in inverse superalloys. Philosophical Magazine Letters, **86**, 215-225, 2006.

[RAU93] E. Rauch, Etude de l'écrouissage des métaux: Aspects microstructuraux et lois de comportement. PhD-thesis, Institut National Polytechnique de Grenoble, 1993.

[REE06] R.C. Reed, The Superalloys: Fundamentals and Applications, Cambridge University Press, 2006.

[REP93] B. Reppich, in: H. Mughrabi (Eds.), Plasticity and fracture of materials. Materials Science and Technology, Volume **6**, VCH-Weinheim, New York, Basel, Cambridge, p. 321, 1993.

[RIC70] J.R. Rice, On the structure of stress-strain relations for time-dependent plastic deformation in metals. Journal of Applied Mechanics, **37**, 728-737, 1970.

[RIC71] J.R. Rice, Inelastic constitutive relations for solids: an internal-variable theory and its application to metal plasticity. Journal of the Mechanics and Physics of Solids, **19**, 433-455, 1971.

[RIC83] R.A. Ricks, A.J. Porter, R.C. Ecob, The growth of gamma prime precipitates in nickel-base superalloys. Acta Metallurgica, **31**, 43-53, 1983.

[ROD01] D. Rodney, A. Finel, Phase field methods and dislocations. In: Influences of interface and dislocation behavior on microstructure evolution, **652**, Y4.9.1-Y4.9.6, Materials research society symposium proceedings, 2001.

[ROD03] D. Rodney, Y. Le Bouar, A. Finel, Phase field methods and dislocations. Acta Materialia, **51**, 17-30, 2003.

[ROE07] B. Roebuck, D. Cox, R. Reed, The temperature dependence of γ' volume fraction in a Ni-based single crystal superalloy from resistivity measurements. Scripta Materialia, **44**, 917-921, 2001.

[ROY05] A. Roy, A. Acharya, Finite element approximations of field dislocation mechanics. Journal of the Mechanics and Physics of Solids, **53**, 143-170, 2005.

[ROY95] A. Royer, P. Bastie, D. Bellet, J.L. Strudel, Temperature dependence of the lattice mismatch of the AM1 superalloy: influence of the γ' precipitates morphology. Philosophical Magazine, **72**, pp. 669-689, 1995.

[RUD76] W. Rudin, Principles of mathematical analysis. Third edition. McGraw-Hill, Inc. New York, 1976.

[SAA04] G. Saada, J. Douin, Pile-ups in thin foils: application to tranmission electron microscopy analysis of short-range-order. Philosophical Magazine, **84**, 807-824, 2004.

[SAS97] V. Sass, Untersuchung der Anisotropie im Kriechverhalten der einkristallinen Nickelbasis-Superlegierung CMSX-4: Mechanische Prüfung und Aufklärung der Mikrostruktur. PhD-thesis, Der Technischen Universität Berlin, 1997.

[SAS98] V. Sass, M. Feller-Kniepmeier, Orientation dependence of dislocation structures and deformation mechanisms in creep deformed CMSX-4 single crystals. Materials Science and Engineering A, **245**, 19-28, 1998.

[SCH35] E. Schmid, W. Boas, Kristallplastizität. Springer, 1935.

[SCH96] K.J. Schwarz, J. Tersov, Interaction of threading and misfit dislocations in a strained epitaxial layer. Applied Physics Letters, **69**, 1220-1222, 1996.

[SCH99] K.W. Schwartz, Simulation of dislocations on the mesoscale: I. Methods and examples. Journal of Applied Physics, **85**, 108-119, 1999.

[SCH07] C. Schwarz, R. Sedlácek, E. Werner, Toward a 2D Finite Element implementation of a continuum-dislocation based model. Computational Materials Science, **39**, 85-90, 2007.

[SED00] R. Sedlácek, S. Forest, Non-local plasticity at microscale: A dislocation-based and a cosserat model. Physica status solidi B, **221**, 583-596, 2000.

[SED03] R. Sedláček, J. Kratochvíl, E. Werner, The importance of being curved: Bowing dislocations in continuum description. Philosophical Magazine, **83**, 3735-3752, 2003.

[SER02] K. Serin, Werkstoffwissenschaftliche Untersuchungen zum mechanischen Verhalten und zur Gefügestabilität der einkristallinen Superlegierung CMSX-4. PhD-thesis, Der Technischen University of Bochum, 2002.

[SHA83] D.M. Shah, Orientation dependence of creep behavior of single crystal γ' (Ni$_3$Al), Scripta Materialia, **8**, pp. 997-1002, 1983.

[SHA84] D.M. Shah, D.N. Duhl, The effect of orientation, temperature and γ' size on the yield strength of a single nickel base superalloy, in Superalloys'84, ed. M. Gall *et al*. ASM, Metals Park, OH, 105-114, 1984.

[SHI06] C. Shin, M. Fivel, M. Verdier, S. Kwon, Numerical methods to improve the computing efficiency of discrete dislocation dynamics simulations. Journal of Computational Physics, **215**, 417-429, 2006.

[SHU01] J.Y. Shu, N.A. Fleck, E. Van Der Giessen, A. Needleman, Boundary layers in constrained plastic flow: comparison of nonlocal and discrete dislocation plasticity. Journal of the Mechanics and Physics of Solids, **49**, 1361-1395, 2001.

[SIE99] D. Siebörger, U. Glazel, Orientation-dependent creep behavior and microstructure of nickel solid solution single crystals. Acta Metallurgica, **47**, 397-406, 1999.

[SIM72] C.T. Sims, The superalloys. Edited by C.T. Sims and W.C. Hagel, John Wiley Pub., New York, 1972.

[STA75] A.E. Staton-Bevan, R.D. Rawlings, The deformation behavior of single crystal Ni$_3$(Al, Ti). Physica Status Solidi, **29A**; 613-622, 1975.

[STR80] T. Strangman, G. Hoppin, C. Philipps, K. Harris, R. Schwer, Development of exothermically cast single-crystal Mar-M247 and derivative alloys. Superalloys 1980, (ed.) J.K. Tien *et al.*, American Society for Metals, Metals Park, USA, 215-224, 1980.

[SVO96] J. Svoboda, P. Lukas, Modelling of kinematics of directional coarsening in Ni-superalloys. Acta Materialia, **44**, 2557-2565, 1996.

[SVO97] J. Svoboda, P. Lukas, Modelling of recovery controlled creep in nickel-base superalloy single crystals. Acta Materialia, **45**, 125-135, 1997.

[TAB97] L. Tabourot, M. Fivel, E. Rauch, Generalised constitutive laws for f.c.c. single crystals. Materials Science and Engineering, A **234-236**, 639-642, 1997.

[TAB01] L. Tabourot, Vers une vision unifiée de la plasticité cristalline. Mémoire pour l'Habilitation á Diriger des Recherches, Université de Savoie, 2001.

[TAK71] S. Takeuchi, E. Kuramoto, Anomalous temperature dependence of yield stress in Ni$_3$Ga single crystals. Journal of the Physical Society of Japan, **31**, **1282**, 1971.

[TAK73] S. Takeuchi, E. Kuramoto, Temperature and orientation dependence of the yield stress in Ni$_3$Ga single crystals. Acta Metallurgica, **21**, **415**, 1973.

[TAN06] M. Tang, W. Cai, G. Xu, V. Bulatov, A hybrid method for computing forces on curved dislocations intersecting free surfaces in three-dimensional dislocation dynamics. Modelling and Simulation in Materials Science and Engineering, **14**, 1139-1151, 2006.

[TAU07a] V. Taupin, S. Varadhan, J. Chevy, C. fressengeas, A.J. Beaudouin, M. Montagnat, P. Duval, Effects of size on the dynamics of dislocations in ice single crystals. Physical Review Letters, **99**, 155507, 2007.

[TAU07b] V. Taupin, Incompatibilité de réseau et organisation collective des dislocations. PhD-thesis, Université Paul Verlaine de Metz, 2007.

[TAY34] G. I. Taylor, The mechanism of plastic deformation in crystals. Part I + II. Proceedings of the Royal Society of London, Series A, **145**, 362-404, 1934.

[TEO70] C. Teodosiu, A dynamic theory of dislocations and its applications to the theory of the elastic-plastic continuum, in Fundamental Aspects of Dislocation Theory, eds. J. A. Simmons, R. de Wit, R. Bullough, National Bureau of Standards Special Publications, **317**, 307-324, 1970.

[TEO75] C. Teodosiu, A physical theory of the finite elastic-viscoplastic behaviour of single crystals. Eng. Trans., **23**, 157-183, 1975.

[TEO93] C. Teodosiu, J.L. Raphanel, L. Tabourot, in Large Plastic Deformations, C. Teodosiu, J.L. Raphanel, F. Sidoroff, Eds. (A. A. Balkema, Rotterdam, Netherlands), 153-168, 1993.

[THO70] P.H. Thornton, R.G. Davies, T.L. Johnson, The temperature dependence of the flow stress of the γ' phase based upon Ni_3Al. Metall. Trans. A **1**, **207**, 1970.

[TIN08] T. Tinga, W.A.M. Brekelmans, M.G.D Geers, Incorporating strain-gradient effects in a multi-scale constitutive framework for nickel-based superalloys. Philosophical Magazine, **88**, 3793-3825, 2008.

[VAN95] E. Van der Giessen, A. Needleman, Discrete dislocation plasticity: a simple planar model. Modelling and Simulation in Materials Science and Engineering, **3**, 689-735, 1995.

[VAN03] E. Van der Giessen, A. Needleman, GNDs in nonlocal plasticity theories: lessons from discrete dislocation simulations, Scripta Materialia, **48**, 127-132, 2003.

[VAR07] S. Varadhan, Modeling collective behavior of dislocations in crystalline materials. PhD-thesis, University of Illinois at Urbana-Champaign, 2007.

[VAT09a] A. Vattré, B. Devincre, A. Roos, Dislocation Dynamics simulations of precipitation hardening in Ni-based superalloys with high γ' volume fraction, Intermetallics, **17**, 988-994, 2009.

[VAT09b] A. Vattré, B. Devincre, A. Roos, A solution for elastic boundary value problems in dislocation dynamics simulations: the Discrete-Continuous Model. To be submitted (Modeling and Simulation in Materials Science and Engineering).

[VAT09c] A. Vattré, B. Devincre, A. Roos, Orientation dependence of plastic deformation in nickel-base single crystal superalloys: a Discrete-Continuous Model simulation. Accepted in Acta Materialia.

[VAT09d] A. Vattré, B. Fedelich, The cube slip in Nickel-base superalloys single crystals revisited. To be submitted (International Journal of Plasticity).

[VAT09e] A. Vattré, B. Devincre, A. Roos, Frédéric Feyel, Channel width strengthening in single-crystal superalloys: a Discrete-Continuous Model simulation. Accepted in European Journal of Computational Mechanics.

[VER98] M. Verdier, M. Fivel, I. Groma, Mesoscopic scale simulation of dislocation dynamic in fcc metals: principle and applications. Modelling and Simulation in Materials Science and Engineering, **6**, 755-770, 1998.

[VER96] M. Véron, Y. Bréchet, F. Louchet, Strain induced directional coarsening in Ni based superalloys. Scripta Materialia, **34**, 1883-1886, 1996.

[VER60] F.I. Versnyder, R.W. Guard, Directional grain structure for high temperature strength. Transactions of the American Society for Metals, **52**, 1960.

[VER70] F.I. Versnyder, M.E. Shank, The development of columnar grain and single crystal high temperature materials through directional solidification. Materials Science and Engineering, **6**, 213-247, 1970.

[VEY98] P. Veyssière, The mechanical anomaly of L1$_2$ alloys: a review of recent experiments and models. Intermetallics, **6**, 587-592, 1998.

[VOL94] R. Völkl, U. Glatzel, M. Feller-Kniepmeier, Analysis of matrix and interfacial dislocations in the nickel based superalloy CMSX-4 after creep in [$\bar{1}$11] direction. Scripta Materialia, **31**, pp. 1481-1486, 1994.

[VOL07] V. Volterra, Sur l'équilibre des corps élastiques multiplement connexes. Annales Scientifiques de l'Ecole Normale Supérieure, Paris, **24**, 401-517, 1907.

[WAG03] G. Wagner, W. Kam Liu, Coupling of atomistic and continuum simulations unsing a bridging scale decomposition. Journal of Computational Physics, **190**, 249-274, 2003.

[WAL94] K.P. Walker, A.D. Freed, E.H. Jordan, Thermoviscoplastic analysis of fibrous periodic composites by the use of triangular subvolumes. Composites Sciences and Technology, **50**, 71-84, 2001.

[WAN01] Y.U. Wang, Y.M. Jin, A.M. Cuitiño, A.G. Khachaturyan, Nanoscale phase field microelasticity theory of dislocations: model and 3D simulations. Acta Materialia, **49**, 1847-1857, 2001.

[WAN04] Z. Wang, N.M. Ghoniem, R. Lesar, Multipole representation of the elastic field of dislocation ensembles. Physical Review B, **69**, 174102, 2004.

[WAN09] L.N. Wang, Y. Liu, J.J. Yu, Y. Xu, X.F. Sun, H.R. Guan, Z.Q. Hu, Orientation and temperature dependence of yielding and deformation behavior of a nickel-base single crystal superalloy. Materials Science and Engineering A 505, 144-150, 2009.

[WES67] J.H. Westbrook, Intermetallic Compounds, John Wiley, New York, 1967.

[WAR05] N. Warnken, D. Ma, M. Mathes, I. Steinbach, Investigation of eutectic island formation in SX superalloys. Materials Science and Engineering A, **413-414**, 267-271, 2005.

[WEY01] D. Weygand, L.H. Friedman, E. Van der Giessen, A. Needleman, Discrete Dislocation modeling in three dimensional confined volumes. Materials Science and Engineering, **309**, 420-424, 2001.

[WEY02] D. Weygand, L.H. Friedman, E. van der Giessen, A. Needleman, Aspects of boundary-value problem solutions with three-dimensional dislocation dynamics. Modelling and Simulation in Materials Science and Engineering, **10**, 437-468, 2002.

[XIA03] Y. Xiang, L.T. Cheng, D.J. Srolovitz, D.J. Weinan, A level set method for dislocation dynamics. Acta Materialia, 18, 5499-5518, 2001.

[XIN09] Y. Xingfu, T. Sugui, W. Minggang, A. Shu, L. Xudong, C. Shu, Creep behaviors and effect factors of single crystal nickel-base superalloys, Materials Science and Engineering A, **499**, 352-359, 2009.

[YOO86] M. H. Yoo, On the theory of anomalous yield behavior of Ni_3Al - Effect of elastic anisotropy. Scripta Metallurgica, **20**, 915-920,1897.

[ZAI06] M. Zaiser, T. Hochrainer, Some steps towards a continuum representation of 3D dislocation systems. Scripta Materialia, **54**, 717-721, 2006.

[ZAO01] A. Zaoui, Plasticité: Approches en champs moyens (chapitre I). Dans: Homogénéisation en mécanique des matériaux (vol. 2): comportements non linéaires et problèmes ouverts. M. Bornert, T. Bretheau, P. Gilormini (eds.), Hermès, Paris, France, 17-44, 2001.

[ZBI98] H.M. Zbib, M. Rhee, J.P. Hirth, On plastic deformation and the dynamics of 3D dislocations, International Journal of Mechanical Sciences, **2-3**, 113-127, 1998.

Publications

[1] A. Vattré, B. Devincre, A. Roos, Dislocation Dynamics simulations of precipitation hardening in Ni-based superalloys with high γ' volume fraction, **Intermetallics**, **17**, 988-994, 2009.

[2] A. Vattré, B. Devincre, A. Roos, A solution for elastic boundary value problems in dislocation dynamics simulations: the Discrete-Continuous Model. To be submitted in **Modeling and Simulation in Materials Science and Engineering**.

[3] A. Vattré, B. Devincre, A. Roos, Orientation dependence of plastic deformation in nickel-base single crystal superalloys: a Discrete-Continuous Model simulation. Accepted in **Acta Materialia**.

[4] A. Vattré, B. Fedelich, The cube slip in Nickel-base superalloys single crystals revisited. To be submitted in **International Journal of Plasticity**.

[5] A. Vattré, B. Devincre, A. Roos, Frédéric Feyel, Channel width strengthening in single-crystal superalloys: a Discrete-Continuous Model simulation. Accepted in **European Journal of Computational Mechanics**.